STUDIES IN SONOELECTROCHEMISTRY

A Thesis Submitted for the Degree of

D. Phil. In Chemistry

in Trinity Term 1999

by

RICHARD P. AKKERMANS

St. John's College

Oxford University

ABSTRACT

STUDIES IN SONOELECTROCHEMISTRY – A THESIS SUBMITTED FOR THE DEGREE OF D. PHIL. IN CHEMISTRY BY RICHARD P. AKKERMANS, ST. JOHN'S COLLEGE, OXFORD UNIVERSITY, TRINITY TERM 1999.

The work described in this thesis employs 'dual activation' methodologies and in particular sonovoltammetry to study a variety of electrochemical systems. First, the effect of 20 kHz power ultrasound on the electrochemistry of simple redox systems in both water and acetonitrile is explored and characterised for different cell geometries. A simple Nernst diffusion layer model is validated.

Second, the use of insonation for efficient pre-concentration of target species in anodic stripping voltammetry (ASV) is reported. 'Sonotrodes', where the electrodes are incorporated into the ultrasonic horn tips are shown to offer particularly high rates of mass transport and additionally cause ablation of mercury from plated platinum electrodes. The key benefits of sonication are shown to be electrode depassivation and extraction plus rapidity and ease of determination, coupled with the lack of any sample pre-treatment for the detection of lead in both wine and petrol by ASV. Lead levels determined by this method and calibrated by use of standard microaddition are in excellent agreement with those obtained 'blind' by atomic absorption spectroscopy performed at independent laboratories.

Third, the novel use of ultrasonically formed emulsions is examined for both analytical and synthetic purposes. The possibility of extracting species both out of an organic phase for analysis and into an organic phase for the synthesis of water-insoluble redox products is realised.

Fourth, the sonovoltammetric determination of ascorbic acid in both aqueous solution and the fruit drink Ribena®, is compared with results obtained by laser activated electroanalysis, where low level laser illumination of an electrode is employed to maintain a fresh electrode surface. Small amounts of laser-induced thermal convection at the electrode result in steady-state voltammetry. The level of agreement is excellent between the two methods and also agrees very well with independent chemical analysis.

Fifth, laser activated voltammetry (LAV) is further explored and a simple mass transport model verified. Damage caused by high power laser ablation is evidenced by atomic force microscopy (AFM). Applications of the technique for depassivation are illustrated by the reduction of toluidine blue dye and oxidation of ferrocyanide in the presence of blood proteins. The technique is further employed under channel flow conditions to elucidate an unambiguous mechanism for aqueous iodide oxidation at platinum electrodes in the absence of the usual build up of bulk iodine (as evidenced by AFM).

Finally, the reduction of methylene green dye at platinum electrodes is used to compare and contrast sonovoltammetry and LAV with thermal and microwave dual activation techniques. The build-up of the passivating reduced form of the dye on the electrode surface, again seen by AFM, is removed by sono-emulsion and laser activation but not by microwave heating. However, greater conductivity is observed at higher temperatures and an electron-hopping mechanism is postulated.

ACKNOWLEDGEMENTS

First of all, I would like to thank my supervisor, Professor Richard Compton, for being a great supervisor, full of ideas and enthusiasm, ruthlessly efficient and being prepared to kick me into action when required. Second, thanks to 'the second line of defence' Frank and Barry for helping to solve countless experimental headaches.

Outside of the PTCL, I thank the EPSRC for a studentship and I am grateful for expert discussions with, and advice from, Professor Iwao Watanabe and Dr. Teruo Hinoue of Osaka University about laser ablation voltammetry, Professor Pankaj Vadgama of Hope Hospital, Salford about blood proteins and Eric Cordemans of Undatim Ltd., Belgium about sonotrodes. I would also like to thank Dr. Alison Rodger of Warwick Analytical Service for independent ascorbic acid and lead analyses and Lembit Nei for an introduction to conferences I will never forget.

Back in the department, Colin Bain deserves mention for his expert laser tutelage and John Freeman has my total gratitude for the countless hours of figure drawing. Stores, Electronics, Workshops and Lab Services have all been great throughout my time as a D. Phil. student, whatever the bizarre request!

On to my partners in crime within the group, I would especially like to thank Jon 'Coops' Cooper for being a good mate over the last three years and asking me to be his best man – I'm honoured. Thanks to all the part IIs, past and present, Jon B for his computer tips and tales of nicotine and alcohol abuse, Marco for the AFM, Qiu for his computer programs and laser antics, and all the other post docs (César and Andreas in particular) for their help and amusing mannerisms. I wish the 'next generation' of James, Andy, Yu-Chen, Shelley, Javier, Gavin, Jo (thanks for the chapter dividers!) and Ben all the best for their future in the Compton Group.

Away from the lab, I'd like to acknowledge my good friend Tom 'Rebs' Rebbitt for golf, Ibiza and proof that life still goes on when you leave the Compton Group. For keeping me constantly entertained, I thank Blake, Roswell, Mike, Nik and all my Sulkido and Taekwondo mates.

Becs deserves special mention for always being there for me and keeping me on the straight and narrow (you're great!) and finally I am very grateful to my family for all their support and encouragement and for helping to smooth the transition from Oxford to working life. Mars awaits!

CONTENTS

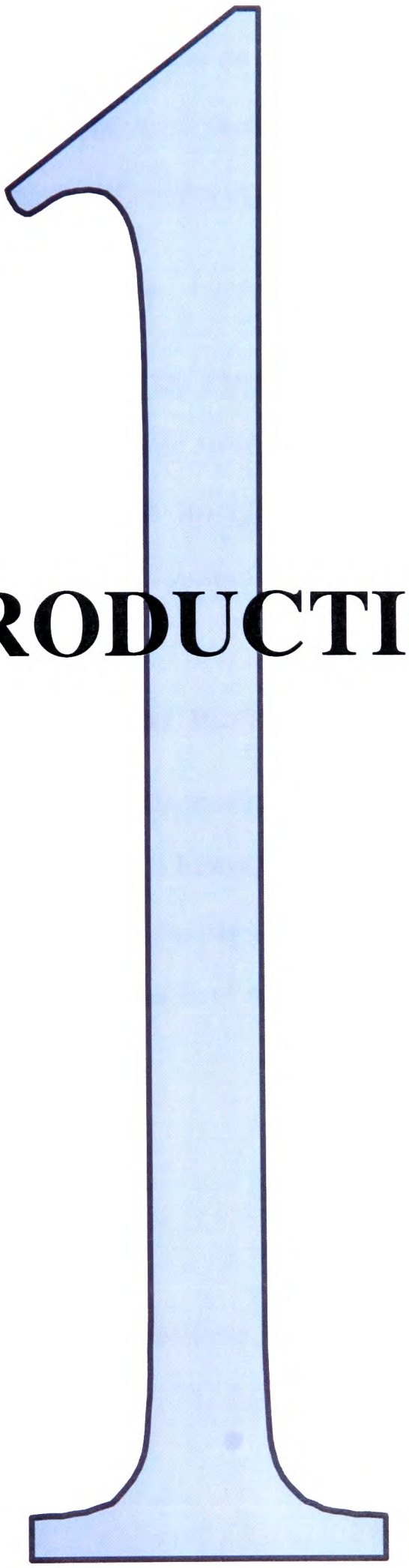

INTRODUCTION

CHAPTER 1: INTRODUCTION

This chapter introduces the fundamental principles underpinning the work presented in this thesis. First we address the electrochemical techniques employed before second moving on to 'dual activation' methodologies and reviewing the current state of the field.

1.1 DYNAMIC ELECTROCHEMISTRY

Dynamic electrochemistry is the study of electron transfer reactions between electrodes and reactant molecules induced by passing an electric current through the system, usually in a solution phase. When studying this discipline we are concerned with the development and application of techniques which probe the rate and mechanisms of these reactions.

1.1.1 NOTATION FOR ELECTROCHEMICAL PROCESSES

When discussing reaction mechanisms in this thesis, the Testa and Reinmuth notation will be used as far as possible. In this convention, a heterogeneous electron transfer between the electrode and the electroactive molecule is denoted by the symbol E, and a homogeneous kinetic step is indicated by the symbol C. One example of this is the general ECE mechanism shown below:

$$A + e^- \rightleftharpoons B \qquad E$$

$$B \rightarrow C \qquad C$$

$$C + e^- \rightleftharpoons \text{Products} \qquad E$$

Here, the electroactive species A takes up an electron forming B (E step) and then B undergoes a chemical change to form C (C step). In the last step C takes up another electron forming the final product (E step).

A specific example of the ECE mechanism is the reduction of nitroethane [1], which, after reduction, undergoes a homogeneous reaction with H^+. The product can then undergo a further reduction to yield the corresponding nitroso compound.

$$C_2H_5NO_2(aq) + e^- \rightleftharpoons C_2H_5NO_2^{\bullet -}(aq) \qquad E$$

$$H^+ + C_2H_5NO_2^{\bullet -}(aq) \rightarrow C_2H_5NO_2H(aq) \qquad C$$

$$C_2H_5NO_2H(aq) + e^- \rightleftharpoons C_2H_5NO(aq) + OH^-(aq) \qquad E$$

1.1.2 MODES OF MASS TRANSPORT

In order for electrolysis to proceed reactant molecules must be transported from the bulk solution to the electrode surface. Thus various physical processes may contribute to the overall kinetics of any particular reaction. Therefore it is important to understand mass transport effects and their quantitative description is essential for the successful interpretation of experimental observations. There are three modes of mass transport of an electroactive species to and from an electrode; diffusion, convection and migration.

***i) Diffusion*:** Macroscopically, diffusion is the movement of species under the influence of a concentration gradient which acts to maximise entropy by smoothing out inhomogeneities in composition. In microscopic terms, it is the statistical response of a system to an imbalance in the number of molecules in different regions of the system. A 'random walk' model [2] can be used to explain the movement of the molecules and a quantitative description is provided by Fick's Laws [3].

Fick's First Law describes the diffusive flux of material under the influence of a concentration gradient:

$$J_d(x,t) = -D\frac{\partial}{\partial x}[c(x,t)] \qquad (1.1)$$

where D is the diffusion coefficient in $cm^2\ s^{-1}$, c(x, t) is the concentration of the electroactive species in mol cm^{-3} and $J_d(x, t)$ is the diffusional flux in mol $cm^{-2}\ s^{-1}$ to the electrode in the x direction which is normal to the electrode surface.

Fick's Second Law describes rates of change of concentration:

$$\frac{\partial}{\partial t}c(x,t) = D\frac{\partial^2}{\partial x^2}[c(x,t)] \qquad (1.2)$$

and is readily derived from the First Law (see Appendix 1).

***ii) Convection*:** Movement due to convection occurs when a mechanical force acts on or within a solution. Two types of convection may be usefully distinguished, natural convection and forced convection. Natural convection may be present in any solution and arises from thermal gradients and/or density differences within the solution. This type of convection is difficult to predict and is therefore undesirable. Forced convection arises from external forces such as pumping, stirring or hydrodynamic flow. This may be arranged to provide well defined hydrodynamic behaviour which allows the pattern of mass transport to the electrode to be rigorously predicted. In some electrochemical experiments forced convection may be introduced to swamp effects due to natural convection [4], allowing more reliable and reproducible data. Alternatively current measurements may be taken rapidly before the onset of natural convection, as in cyclic voltammetry.

Quantitatively, the one-dimensional (x) convective flux is given by :

$$J_c(x,t) = c(x,t)v(x) \tag{1.3}$$

where $J_c(x, t)$ is the convective flux and $v(x)$ is the velocity of the solution in the x direction. The convective analogue of Fick's Second Law is therefore:

$$\frac{\partial c}{\partial t} = -\left[v_x \frac{\partial c}{\partial x}\right] \tag{1.4}$$

***iii) Migration*:** Migration is the movement of charged species due to electrical potential gradients [5] and it is by this mechanism that charge passes through the bulk electrolyte. The migratory flux due to a potential gradient $\partial\varphi / \partial x$ is given by:

$$J_m(x,t) = -\frac{zF}{RT} Dc(x,t) \frac{\partial \varphi}{\partial x} \tag{1.5}$$

where J_m is the flux due to migration in the x direction, z is the charge on the ion, F is the Faraday constant in C mol^{-1}, R is the Universal Gas Constant in J K^{-1} mol^{-1} and T is the temperature in K.

In a voltammetric experiment the combination of migration and electrolysis produces complex mass transport effects which are difficult to interpret. These effects are rendered negligible by use of an excess of electrolytically inert ions, known as the background

electrolyte. Excess can then be defined in the context that in order to reduce the migration flux to one percent of the diffusive flux, a 33-fold excess of background electrolyte is required [6]. This results in the nullification of the $\partial\varphi / \partial x$ term in the equation, hence simplifying the mathematical treatment of electrochemical systems as only diffusion and convection need be considered. The addition of background electrolyte provides further advantages:

(i) It increases the solution's conductivity, thereby making the bulk solution less resistive to the flow of current. If this were not so then the response of the cell might be limited by the flow of current through the bulk solution and not by the phenomena of interest occurring at the electrode / solution interface.

(ii) It reduces the size of the double layer across which the interfacial potential drop occurs to approximately 10-20 Å. This permits electron transfer between electrode and electroactive species via quantum mechanical tunnelling.

(iii) The ionic strength of the solution remains the same throughout the experiment and this means that the activity coefficients of the reactants remain constant throughout the electrolysis. In the following, concentrations are reported under fixed salt concentrations. Standard electrode potentials are thereby replaced by 'formal' electrode potentials. The formal potential of a reaction, $E^{0\prime}$, is related to the standard potential, $E^{\ominus}$ by the following equation [7]:

$$E^{0\prime} = E^{\ominus} + \frac{RT}{nF} \ln \frac{\Pi \gamma_{O_i}^{\nu_i}}{\Pi \gamma_{R_i}^{\nu_i}} \tag{1.6}$$

where n is the number of electrons transferred, $\gamma_{O_i}^{\nu_i}$ and $\gamma_{R_i}^{\nu_i}$ are the activity coefficients of the i^{th} oxidised and reduced species respectively in relation to molarity (mol dm^{-3}) and ν_i is the stoichiometry to which the i^{th} species appears in the reaction.

1.1.3 LINEAR SWEEP VOLTAMMETRY

Linear sweep voltammetry (LSV) [1] is conducted in a stationary solution, so relies only on diffusion for transport to and from the electrode, which is predicted by Equations

(1.1) and (1.2). The potential of the working electrode is swept from an initial value E_1 at which the electroactive species cannot undergo redox reaction, to a final potential E_2, where the electron transfer is driven rapidly. The rate at which this is swept, v_s, can be varied and the potential at time t is described by the formula:

$$E(t) = E_1 - v_s t \tag{1.7}$$

Figure 1.1 shows the resulting voltammogram, a plot of current against voltage, for a solution of a single reducible species X. The form of the current voltage behaviour can be understood as follows. Initially, no current is passed since the applied potential is not great

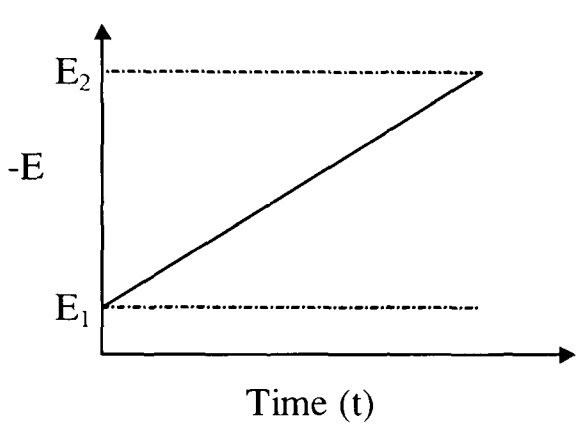

Figure 1.1a The potential sweep.

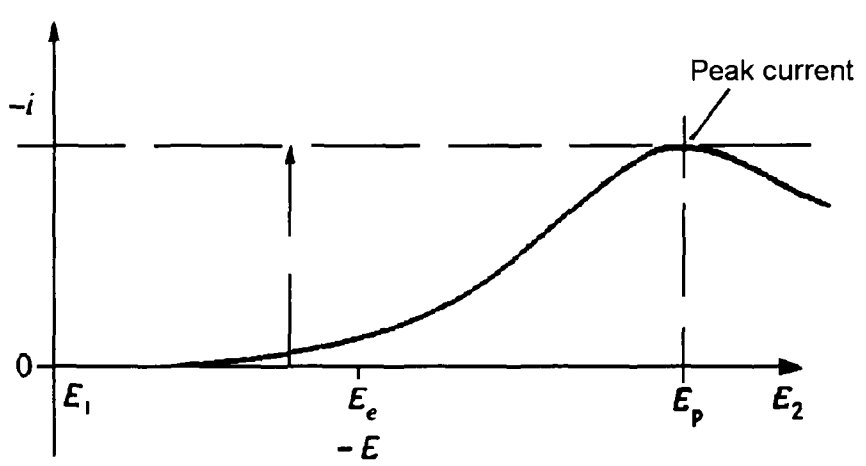

Figure 1.1b Linear sweep voltammogram (LSV) for an irreversible electron transfer reaction where E_e is the equilibrium electrode potential [1].

enough to induce electron transfer. However, as the potential is swept negative, to more reducing potentials, the reduction becomes more favourable and current starts to flow. As the potential is swept more negative still the current reaches a maximum known as the peak current, i_p and then starts to fall off. This arises because the current flow reflects not only the rate of electron transfer, k_{red}, but also the surface concentration, $[X]_0$ of the reactant X. At more negative potentials though k_{red} increases, $[X]_0$ steadily decreases as electrolysis consumes X, which is only partially replenished by diffusion of fresh X from bulk solution. Hence the current is controlled by the rate at which X can diffuse to the electrode. The region of substrate depletion near the electrode is then referred to as a diffusion layer. Thus the overall current response is a balance of electron transfer kinetics and diffusion rates.

For reversible reactions the peak current, i_p, is described by the following equation [1]:

$$|i_p| = 0.318AFD^{1/2}v_s^{1/2}[X]_{bulk}\left(\frac{F}{RT}\right)^{1/2} \quad (1.8)$$

where A is the electrode area in cm^2 and $[X]_{bulk}$ is the bulk concentration of X in mol cm^{-3}.

Alternatively for an irreversible electrode reaction [1];

$$|i_p| = 2.99\times10^5\alpha^{1/2}AD^{1/2}v_s^{1/2}[X]_{bulk} \quad (1.9)$$

where α is the transfer coefficient [7].

The diffusion layer in a solution may be considered as the distance from the electrode where the concentration of the solution deviates from that of the bulk solution. As the scan rate is increased there is less time for electrolysis and the depletion of X near the electrode is reduced, hence the diffusion layer is thinner. This leads to a larger concentration gradient and increased flux (see Equation (1.1)) and hence, the value of i_p increases. Thus, as shown in Equations (1.8) and (1.9), i_p is dependent on $v_s^{1/2}$.

1.1.4 CYCLIC VOLTAMMETRY

Cyclic voltammetry (CV) involves the application of a triangular potential cycle to the working electrode (Figure 1.2). As with LSV the current is recorded as a function of the applied voltage, and generally scan rates of 10 – 1000 mV s^{-1} are used although rates as fast as 10^6 V s^{-1} have been attained [8]. In the case of reduction where

$$X(aq) + e^- \rightarrow Y(aq)$$

as the potential becomes more negative, the cathodic current due to the reduction of electroactive substrate X(aq) at the electrode surface, often limited by electrode kinetics [4], rises approximately exponentially with applied potential. The current then passes through a maximum, after which the current falls as the supply of X in the region of the electrode becomes exhausted, and additional sources of X must diffuse from the bulk solution. When the direction of the potential sweep is reversed the reductive current decays to zero, whilst the anodic current rises approximately

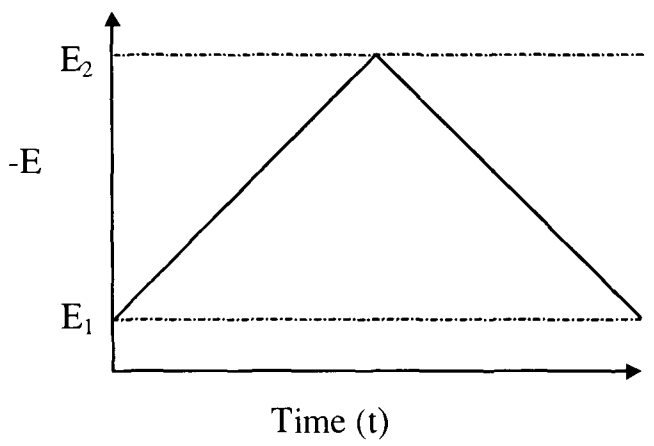

Figure 1.2 Variation of applied potential.

exponentially due to the reoxidation of the reduction product Y. After passing through a maximum, the current decays ultimately to zero. The shape of the resulting CV depends upon the reversibility of the redox couple and may be modified by homogeneous kinetic processes [4]. Figure 1.3b shows a cyclic voltammogram for a reversible couple. Here significant oxidative current flow is seen at potentials immediately anodic of $E^{\ominus}$, the standard electrode potential. In this case peak separation is independent of scan rate. Figure 1.3a shows the cyclic voltammogram for an irreversible electrode couple.

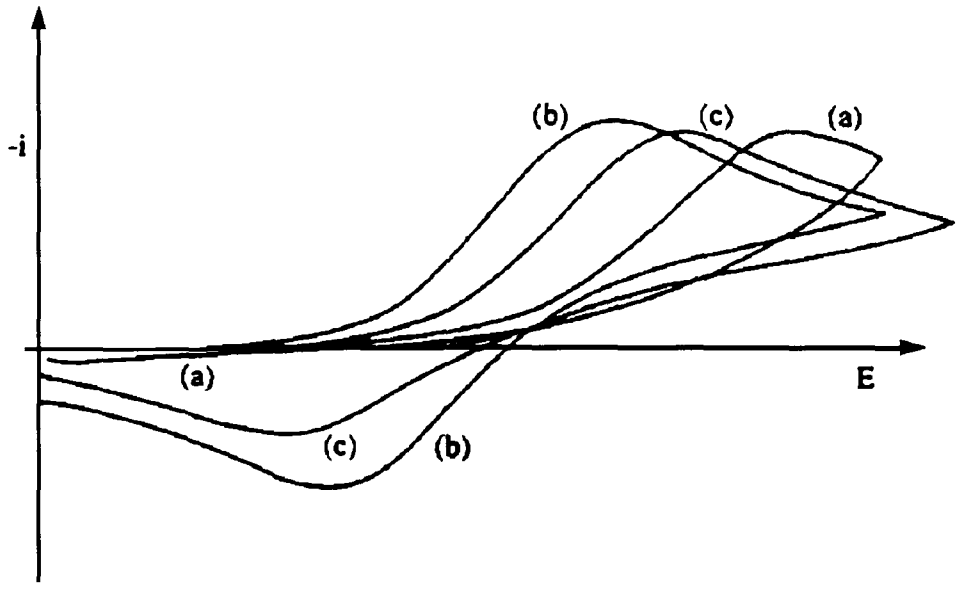

Figure 1.3 Cyclic voltammograms for (a) irreversible, (b) reversible and (c) quasi-irreversible electron transfer reactions.

Regardless of reversibility, the absolute magnitudes of the peak currents for both forward and reverse scans depend on the voltage sweep rate. However, in the irreversible case, as for LSV, the potentials of both the forward and reverse peaks are voltage sweep rate dependent, this contrasts with the reversible case, being diagnostic of the nature of the electrode kinetics. In addition, in the irreversible case, the size of the reverse peak relative to the forward peak will depend upon voltage scan rate.

1.1.5 POTENTIAL STEP CHRONOAMPEROMETRY

This type of voltammetry is a limiting case of cyclic or linear sweep voltammetry. In such experiments the potential of the working electrode is instantaneously stepped from E_1 to E_2. These values correspond, respectively, to no electrolysis and to complete conversion of X to Y at the electrode surface (see Figure 1.4).

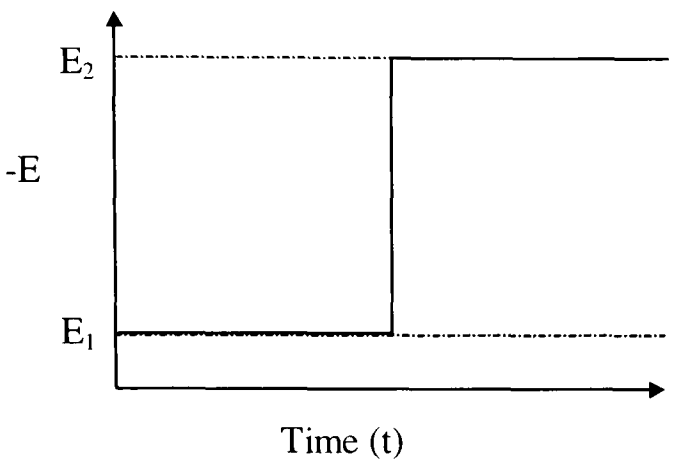

Figure 1.4 The variation in applied potential in a potential step experiment.

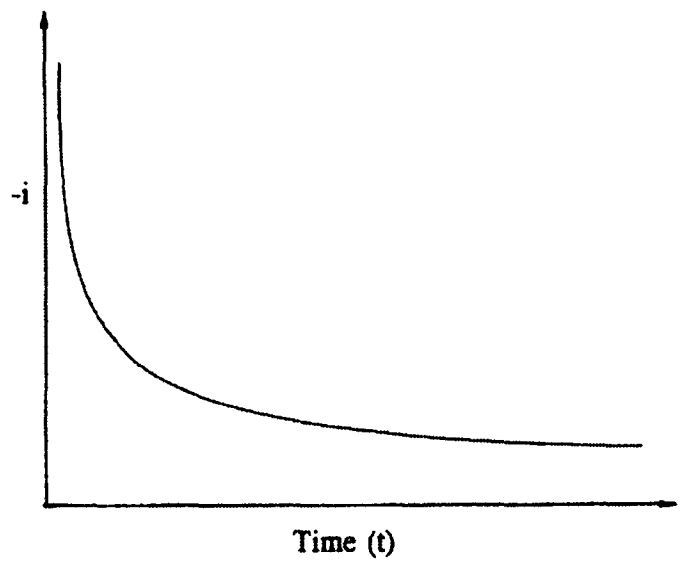

Figure 1.5 The current response in a potential step experiment.

Immediately after the step, a large current is detected which falls steadily with time. This arises because the magnitude of the current is controlled by the rate of diffusion of X to the electrode. Shortly after the step the concentration gradients are extremely large as there has been little time for any depletion of the electroactive material. Thus the initial currents flowing are very large. Gradually, as depletion occurs, the diffusion layer thickness increases and the current decreases, eventually reducing to zero, as shown in Figure 1.5. The Cottrell equation [7,9], derived from Fick's Second Law, describes the current response as a function of time;

$$|i| = \frac{nFAD^{1/2}[X]_{bulk}}{\pi^{1/2}t^{1/2}} \qquad (1.10)$$

where n is the number of moles of electrons moved, and t is time in seconds. The equation shows that potential step experiments can be used to measure diffusion coefficients.

1.1.6 MICROELECTRODES

At the edge of an electrode both radial and linear diffusion occur. In the case of macroelectrodes the contribution of radial diffusion is negligible, as the ratio of edge compared to overall surface area is small. However, for small electrodes where the converse is true, the contribution of radial diffusion is significant as shown in Figure 1.6, and hence both linear and radial diffusion must be taken

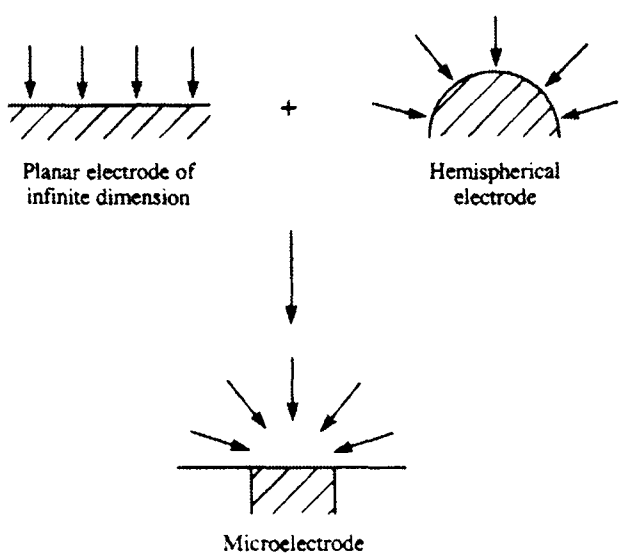

Figure 1.6 Diffusion to a microelectrode.

into account. In practice this occurs for electrodes which have at least one dimension which is between 0.1 and 50 μm. Hence, such electrodes are known as microelectrodes.

Approximations are made to solve the radial diffusion contribution [7] resulting in the following equation for the limiting current, I_{lim}, for a microdisc of radius, r:

$$I_{lim} = 4nFrD[X]_{bulk} \tag{1.11}$$

This additional contribution from radial diffusion leads to much thinner diffusion layers when compared with macroelectrodes and hence the corresponding concentration gradients are very high. Therefore, the rate of mass transport to microelectrodes is much greater than for macroelectrodes and they can be used to study very fast processes. This also results in the current-voltage waves recorded being mass transport limited, as for channel flow cells (see section 1.2.1).

One further advantage of microelectrodes is that the small electrolysis percentage permits the attainment of steady states in situations such as in the absence of added electrolyte or in non-polar solvents like hexane not possible with larger electrodes [1].

The small size of microelectrodes has its own advantages, allowing reactions to be carried out in small volumes. In addition, as the current measured at an electrode is a function of size, they have low total currents which is why the percentage of electrolysis is small.

Another important consequence of decreased electrode area is a much smaller contribution of capacitive charging current. Thus, the accessible time scales for microelectrodes are short, allowing fast transient studies to be carried out.

1.2 HYDRODYNAMIC VOLTAMMETRY

Hydrodynamic voltammetry [10-12] involves both convective mass transport of the reactant solution and relative motion between the electrodes and the solution. Practically this may be achieved either by moving the electrode in a stationary solution, or forcing solution to flow over a fixed electrode. An example of the former is the rotating disc electrode [13], and of the latter the channel flow electrode [14]. In this section only channel flow and rotating disc electrodes are discussed and later, in section 1.5 another form of hydrodynamic

electrochemistry, sono-electrochemistry will be discussed. There are three main advantages in using these hydrodynamic electrodes. First, as steady-state conditions are reached rapidly measurements can be made without the problem of double layer charging [15] which lowers the accuracy of other types of experiments. Second, conditions are reproducible unlike for example diffusion only systems which natural convection renders highly unpredictable, except over short time scales [16]. Third, the rates of mass transport to the electrode may be altered, increasing the dynamic range of the experimental conditions and hence providing a probe of electrode reaction mechanisms and kinetics.

1.2.1 CHANNEL FLOW CELL

The basic design of a channel flow cell is shown in Figure 1.7. The channel flow electrode is an electrode smoothly embedded in one wall of a rectangular duct through which electrolyte flows [17,18].

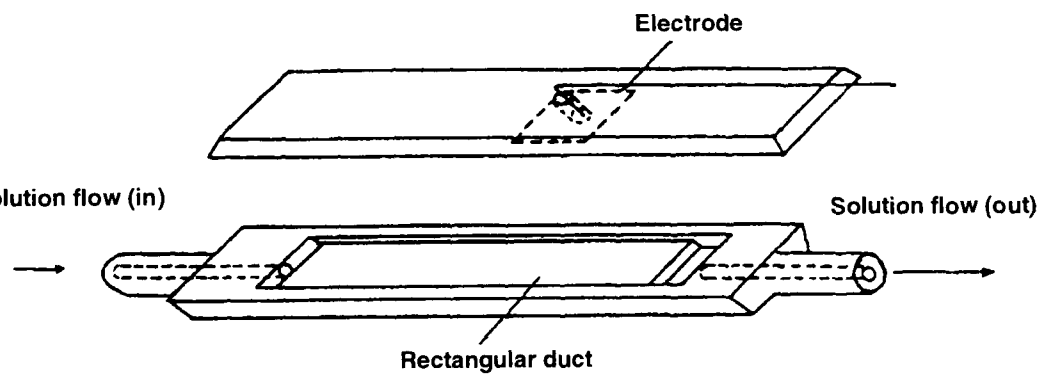

Figure 1.7 The channel flow cell assembly.

In channel flow voltammetry the transport of material to and from the electrode derives both from convection and diffusion, hence differing from linear sweep voltammetry. Convection results in a continuous supply of fresh electroactive material and a significantly increased rate of mass transport which means that current-voltage curves can be measured under steady-state conditions. This gives rise to a different form of current-voltage curve where in the case of a reduction, the current reaches a plateau at high reducing potentials (Figure 1.8). This corresponds to the transport limited current (I_{lim}) and contrasts with the maximum seen in the diffusion only case.

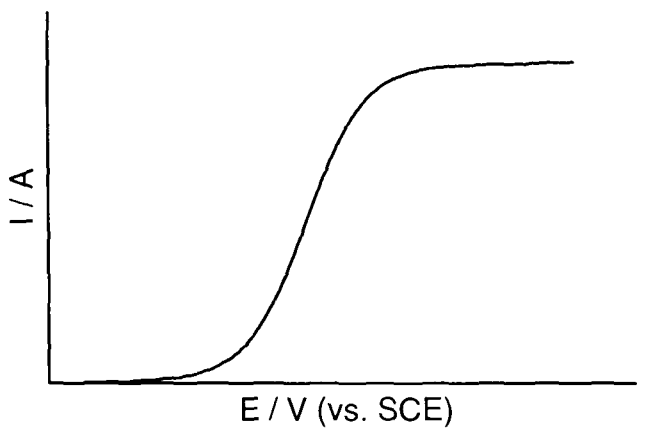

Figure 1.8 A typical steady-state hydrodynamic voltammogram.

The solution properties and the flow rate strongly influence the nature of the flow through the channel. The dimensionless Reynold's number [19] combines these factors, given by the equation:

$$R_e = 2h\frac{v_0}{\nu} \tag{1.12}$$

where ν is the kinematic viscosity of the solution, h is the channel half-height and v_0 is the centre line velocity of the solution. During experiments it is important that the flow is laminar, as this is well defined and mathematically describable. In practice [20] this is achieved when $R_e < 2000$. In typical experimental conditions, except for 'fast' flow experiments, R_e is found to be less than 10. The volume flow rate, V_f, can then be related to v_0 by the equation [19]:

$$v_0 = \frac{3V_f}{4hd} \tag{1.13}$$

where d is the width of the channel.

Figure 1.9 shows the flow profile under laminar conditions. Thus solution entering the flow cell will ultimately adopt a parabolic velocity profile, provided the lead-in section, L_e, is sufficiently long [21,22] where L_e is given by:

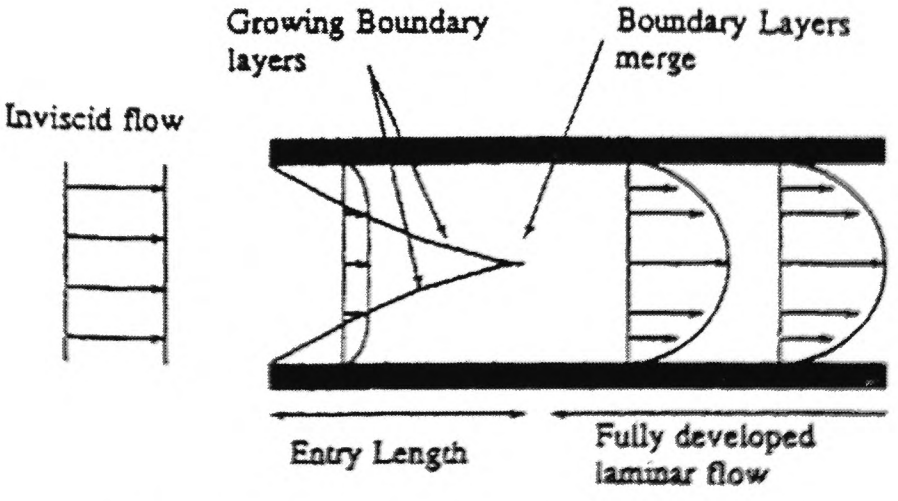

Figure 1.9 The development of laminar flow.

$$L_e = (0.1)hR_e \tag{1.14}$$

The convective flow can then be described by the following:

$$v_x = v_0\left(1 - \frac{(h-y)^2}{h^2}\right);\ v_y = v_z = 0 \tag{1.15}$$

where the co-ordinates used are those defined in Figure 1.10.

If the flow pattern within the cell is known, then the mass transport within the cell can be predicted. Generally measurements are taken in the presence of sufficient supporting electrolyte to negate migration effects, thus the convective-diffusion equation is:

$$\frac{\partial[X]}{\partial t} = D\nabla^2[X] - \left(v_x \frac{\partial[X]}{\partial x} + v_y \frac{\partial[X]}{\partial y} + v_z \frac{\partial[X]}{\partial z} \right) \tag{1.16}$$

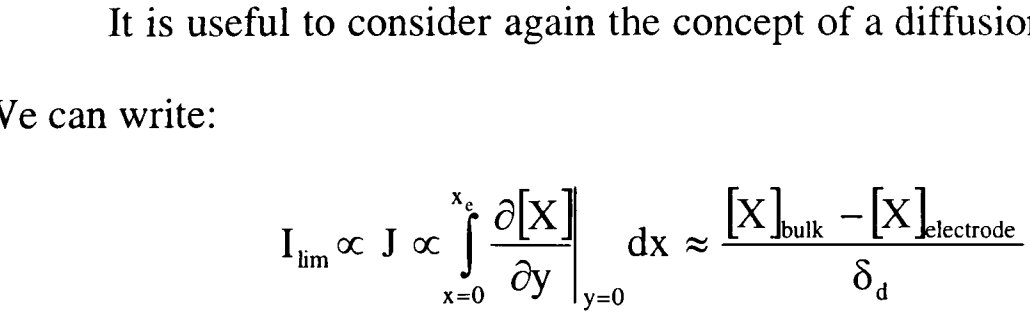

Figure 1.10 Schematic diagram with co-ordinate system.

Equation (1.16) can be simplified, as the parabolic flow pattern makes $v_y = v_z = 0$. Under steady state conditions the derivative on the left hand side is zero, and as $v_x \frac{\partial[X]}{\partial x} >> D\left(\frac{\partial^2[X]}{\partial x^2} + \frac{\partial^2[X]}{\partial z^2} \right)$ for all cases except microelectrodes [23], Equation (1.16) becomes [24]:

$$0 = D\frac{\partial^2[X]}{\partial y^2} - v_x \frac{\partial[X]}{\partial x} \tag{1.17}$$

This equation shows that there are only two forms of mass transport in the channel flow cell, convection axial, and diffusion normal to the electrode surface. From this Levich [25] derived an expression relating the limiting current, $I_{lim,}$ to known or measurable experimental and geometrical quantities:

$$I_{lim} = 0.925nF[X]_{bulk}\, w(x_e D)^{2/3} \left(\frac{V_f}{h^2 d} \right)^{1/3} \tag{1.18}$$

where x_e, h, d, w are all as shown in Figure 1.10.

It is useful to consider again the concept of a diffusion layer thickness, δ_d (see 1.1.3). We can write:

$$I_{lim} \propto J \propto \int_{x=0}^{x_e} \left. \frac{\partial[X]}{\partial y} \right|_{y=0} dx \approx \frac{[X]_{bulk} - [X]_{electrode}}{\delta_d} \tag{1.19}$$

where J is the total flux of material to the electrode and $[X]_{electrode}$ is the concentration of the species near the vicinity of the electrode. If the electrode potential is sufficient to reduce/oxidise the species, then $[X]_{electrode} = 0$, therefore;

$$I_{lim} \propto \frac{[X]_{bulk}}{\delta_d} \tag{1.20}$$

Comparing Equations (1.18), (1.19) and (1.20), we see that:

$$\delta_d \propto x^{1/3} \tag{1.21}$$

which shows that the diffusion layer is not uniform along the x-direction of the electrode. The non-uniform accessibility of the channel electrode makes it ideal for mechanistic studies.

This can be understood by considering a simple ECE mechanism (see 1.1.1). It is the variation of the effective number of electrons transferred in the reaction, N_{eff}, with flow rate, which contains the kinetic information. This reflects the competition between the intermediates (B and C) being swept downstream or diffusing back to the electrode surface to undergo further heterogeneous electron transfer. At high rates of mass transport, it is observed that only one electron is seen to be transferred, as the reaction intermediates are swept away from the electrode, preventing electron transfer to any reaction product. At slower rates, not all the material is removed from the electrode vicinity and so there can be further electron transfer. Thus for an ECE process, $1 \leqslant N_{eff} \leqslant 2$. At the upstream edge of the channel flow electrode, the diffusion layer is very thin and the concentration gradients steep. This promotes loss of reaction intermediates from the electrode surface, whilst further downstream the concentration gradients are shallower and the diffusion layer is thicker, hence the intermediates are more likely to undergo another heterogeneous

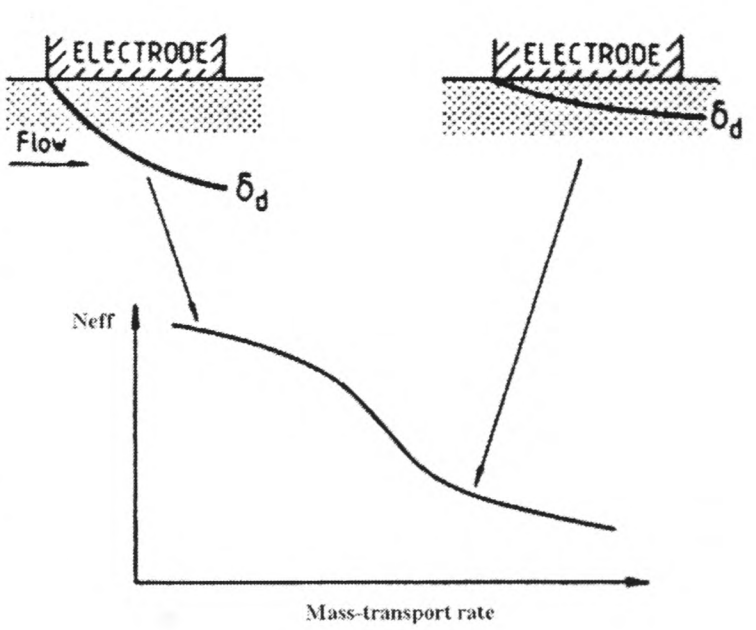

Figure 1.11 The diffusion layer of the channel flow electrode and the consequent effect on the number of electrons transferred at the electrode as a function of the mass transport.

electron transfer. Thus N_{eff} varies slowly as a function of flow rate, providing kinetic information [26] about the electrode reactions.

Figure 1.11 shows the diffusion layer of a channel flow electrode and its effect on the number of electrons transferred at the electrode as a function of mass transport.

1.2.2 ROTATING DISC ELECTRODE

The rotating disc electrode (RDE) is a commonly used hydrodynamic electrode. The electrode, as its name suggests, is rotated at a fixed rate such that a steady supply of electroactive material to the electrode is attained. The flow pattern under laminar conditions is shown in Figure 1.12. The velocity of the flow can be shown to be:

$$v_z \approx -Cz^2 \text{ where } C = 0.510\omega^{3/2}\nu^{1/2}D^{-1/3}$$

where ν is the solution viscosity and ω is the rotation speed in rad s^{-1}. The voltammograms obtained from the RDE yield a limiting current analogous to that obtained in channel flow voltammetry (see Figure 1.8). This is due to a constant influx of fresh material to the electrode removing the transport limitation of LSV in a stationary solution. The limiting current, I_{lim}, is described by the Levich [25] equation for laminar conditions:

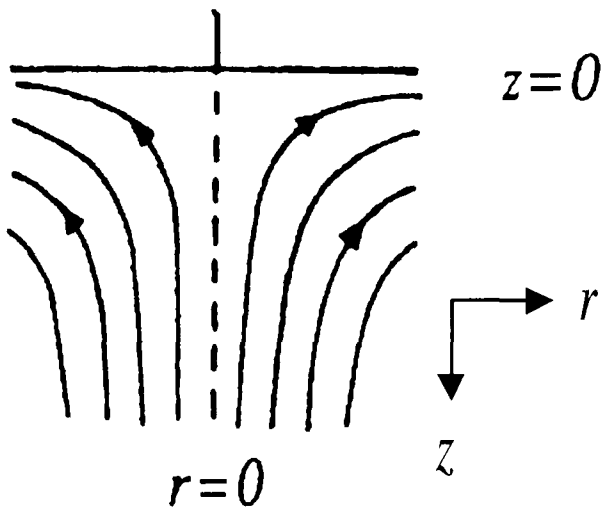

Figure 1.12 Laminar flow towards the RDE. z is the co-ordinate perpendicular to the electrode surface and r is the co-ordinate along the radius of the electrode.

$$I_{lim} = 0.62nFA[X]_{bulk} D_B^{2/3} \nu^{-1/6} \omega^{1/2} \tag{1.22}$$

From Equation (1.22) it is obvious that the limiting current will increase with rotation speed. This is due to the fact that as the speed of rotation increases then the diffusion layer thickness is reduced according to the following equation [7]:

$$\delta = \frac{1.61 D_B^{1/3} \nu^{1/6}}{\omega^{1/2}} \tag{1.23}$$

According to Equation (1.23) the flux to the electrode is greater when the diffusion layer is thinner and hence a larger limiting current is observed.

The rotating disc is a very useful tool for obtaining diffusion coefficients of electroactive materials in general and will be employed in this thesis almost exclusively to this end.

1.3 ANODIC STRIPPING VOLTAMMETRY

1.3.1 HISTORY AND USES

Anodic stripping voltammetry is an analytical technique which involves first the reduction of a target metal ion in solution usually at a mercury electrode such that an amalgam is formed in which the target is pre-concentrated. The electrode potential is then swept anodically such that the metal in the amalgam is oxidised at some potential giving rise to a characteristic peak which permits quantification of the trace ion.

The cell typically employed for anodic stripping voltammetry (ASV) is a three electrode cell as used in most electrochemistry experiments. The nature of the electrode is usually a mercury thin-film electrode (MTFE) [27].

The MTFE's geometry gives it a large surface area to volume ratio and the resolution that can be obtained from the MTFE is also much improved compared with a DME as the diffusion through the film is extremely fast. The former electrode is prepared by plating the mercury onto either a glassy carbon or platinum electrode. For the work using ultrasound reported in this thesis a platinum electrode is used as mercury adhesion under insonation is stronger than that for glassy carbon electrodes (Chapter 4). Mercury only forms thin uniform films on metals with which it easily amalgamates [28] e.g. silver or gold. The usual method for achieving this is to lay down a thin layer of silver or gold on a glassy carbon, graphite or steel substrate electrode and then plating further with mercury. The disadvantage of plating mercury in this way is that it is almost impossible to know the exact composition of the film [28]. This problem does not present itself with either platinum or glassy carbon substrates. The former has a thin oxide layer which is insoluble in mercury [29] and in the latter case an amalgam is not formed as carbon, like platinum oxide, is insoluble in mercury. The mercury

films on both platinum and glassy carbon are not uniform but consist of many mercury droplets [30].

The property of an amalgam is dependent upon the following three things [29].

1. The solubility of the target metal in mercury.
2. Interactions between dissolved metals if more than one are present.
3. Complications arising due to additional amalgamation with the substrate electrode.

Amalgams can be easily formed with the following metals: Tl, In, Ga, Zn, Cd, Pb, Al, Cu, Ag, the metals of the first and second main groups of the periodic table and the rare earths [29]. Amalgams may also be formed with W, V, Ti and U and also an unstable amalgam can be formed with NH_4^+ [29]. This provides a wide range of metals / cations that may be detected.

1.3.2 SPECTRUM OF METALS DETECTABLE BY ASV

There is a large range of metals that maybe detected by ASV as mentioned in section 1.3.1. A survey of the literature enabled a spectrum of electrode potentials to be compiled [31-39]. This is shown in Figure 1.13 and demonstrates the versatility of ASV as an analytical detection technique.

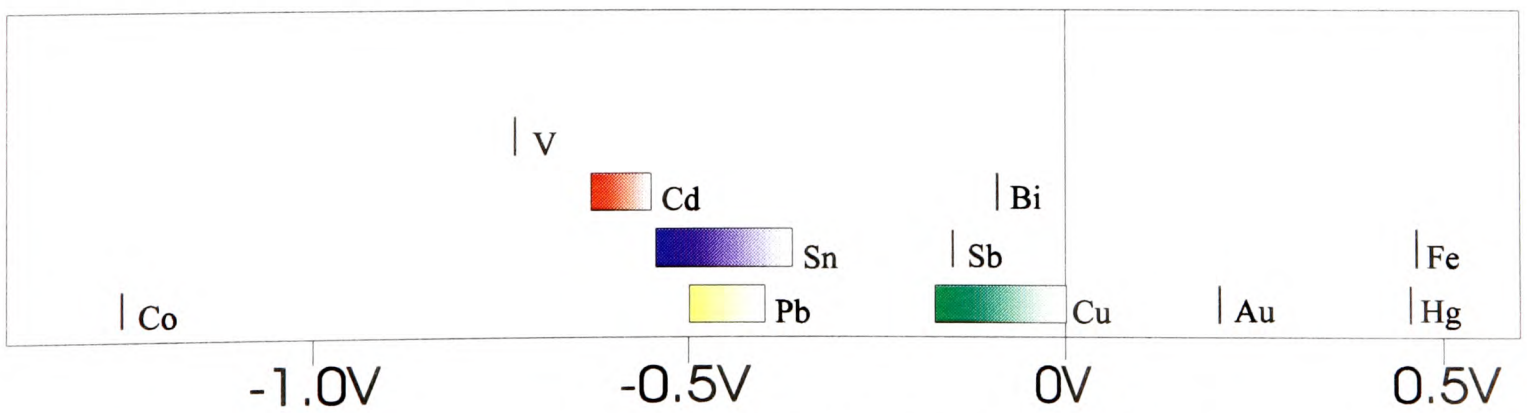

Figure 1.13 Spectrum of stripping potentials (vs. SCE) for metals detected by ASV.

1.4 DUAL ACTIVATION OF ELECTROCHEMICAL PROCESSES

The use of *dual activation* where a physical not chemical surface activating technique is employed in tandem with voltammetric methodology to produce a surface activated electrochemical protocol has many benefits. In this thesis, special emphasis is put on ultrasonic activation, which gives rise to agitation of the electrode surface and its adjacent

diffusion layer either before or during the electrochemical procedure. Experimental and fundamental aspects are addressed and illustrated with wide ranging applications. Additionally, thermal, microwave and laser activation methods are discussed and compared with corresponding sono-electrochemical techniques.

1.4.1 WHY DUAL ACTIVATION?

To perform meaningful electrochemical measurements it is of the utmost importance that the detecting electrode is both clean and reproducible. The hanging drop mercury electrode (HDME) has enjoyed extremely wide use for the simple reason that each drop has a renewed surface which is devoid of 'memory' effects and has a reproducible electrochemical response. However the harmful environmental impact of mercury electrode substrates (mercury is now or will shortly be entirely prohibited in Japan and Sweden for example) has led to its decline in electroanalytical applications. While solid electrodes have the advantage of low environmental impact, high durability and a larger potential 'window' than mercury, they can suffer badly from changes in heterogeneous electron-transfer rate, surface adsorption and 'memory' effects. In extreme cases solid electrodes can become entirely passivated resulting in extremely poor electroanalytical responses. Physical processes that can alleviate surface adsorption, electron-transfer passivation and irreproducibility would therefore facilitate the use of more robust electrode substrates for electroanalytical experiments which previously would have required a hanging mercury drop experimental procedure. The later chapters of this thesis (7-12) concentrate on the physical modification of electrode surfaces to produce reproducible electroanalytical measurements and in particular dual activation caused by ultrasonic, thermal, microwave and laser stimulation. Each of these is now introduced. Chemical and electrochemical surface activation aspects have been reviewed previously [40].

1.5 SONOCHEMISTRY

Sonochemistry is chemistry employing ultrasonic waves. Key concepts of ultrasound are introduced below and its interactions with aqueous and non-aqueous media explained with particular attention paid to acoustic streaming, cavitational phenomena and the possible chemical effects on the system.

1.5.1 ULTRASOUND

Ultrasound is a high frequency longitudinal wave which is transmitted through the liquid in exactly the same manner as any other sound wave. Longitudinal waves are waves that travel in the same direction as the oscillation of the solution molecule. This causes the molecules to be pulled apart, known as 'rarefaction' and then pushed together, known as 'compression'. The pressure created at any point along the wave can be described by the sinusoidal equation below:

$$P = P_0 \sin(2\pi ft) \tag{1.24}$$

where P_0 is the applied pressure from the transducer, f is the frequency of the ultrasound and t is the time.

There are two distinct types of ultrasound which operate at very different frequencies: power ultrasound (20-100 kHz) and diagnostic ultrasound (1-10 MHz). The former is the one commonly employed in sonochemistry and the one that this thesis is exclusively concerned with. The latter is a non-invasive technique used in medicine for scanning the human body. The most common use is the scanning of foetuses during pregnancy [41].

Ultrasound is also widely employed in industrial processes; it can be used to degas molten glass and metal; for producing finer and smaller crystals than that of silent conditions [42]; in the food industry for sterilisation processes [42] and for environmental use by coagulating airborne particles [42] thereby reducing polluting mists. A final application is the assistance of drilling, grinding and cutting of brittle materials such as glass or ceramics [42].

1.5.2 PHYSICAL EFFECTS OF ULTRASOUND

The phenomenon of cavitation occurs when the soundwave undergoes rarefaction and the acoustic pressure P_0 is large enough to create a separation distance between the solution particles, approximately twice the Van der Waal's separation [43,44], such that the liquid structure breaks down to form a cavity or bubble. These bubbles may survive many cycles (stable cavitation) or collapse after one or two cycles (transient cavitation). The energy required to create these bubbles is large so when these bubbles collapse the energy is released in the form of heat, causing a temperature rise in the solution, or in the form of light - termed sonoluminescence [45] (see Appendix 2). There are many different types of cavitation in solution and to understand the chemistry observed within these a full understanding of the nature of the bubble must be known. The following can be differentiated:

1. an empty cavity (true cavitation),
2. a solvent vapour filled cavity,
3. a dissolved gas filled cavity, or
4. a combination of gas and vapour filled cavity.

Cavitation in water requires large amounts of energy to obtain the critical separation - approximately 4 Å. To achieve this an acoustic pressure of 4000 atm [43] is required or an ultrasound intensity of 5 MW cm^{-2}. Whilst this is for true cavitation, in contrast if the cavitation bubble is filled with water vapour the required pressure is only 25% of that required before. Cavitation is also observed at much lower pressures due to 'weak spots' in the solution arising from dissolved gases and particles.

The amount of cavitation is related to a number of factors:

1. Frequency - If the frequency of the ultrasound is increased then cavitation will be reduced as bubbles have less time to form.
2. Temperature - Increasing temperature raises the vapour pressure of the liquid and cavitation will occur at lower intensities.
3. Viscosity - The greater the intermolecular forces the more difficult it is to pull the molecules apart.

4. Type of dissolved gases - The greater the specific heat ratio ($\gamma = C_P / C_V$) the less the energy of cavitation will be absorbed and more marked effects will be seen.
5. External Pressure - A higher external pressure means that less bubbles will be formed but also increases the probability that the bubbles will collapse causing chemical reactions [44].
6. Intensity - The number of molecules cavitationally displaced varies with ultrasound intensity.

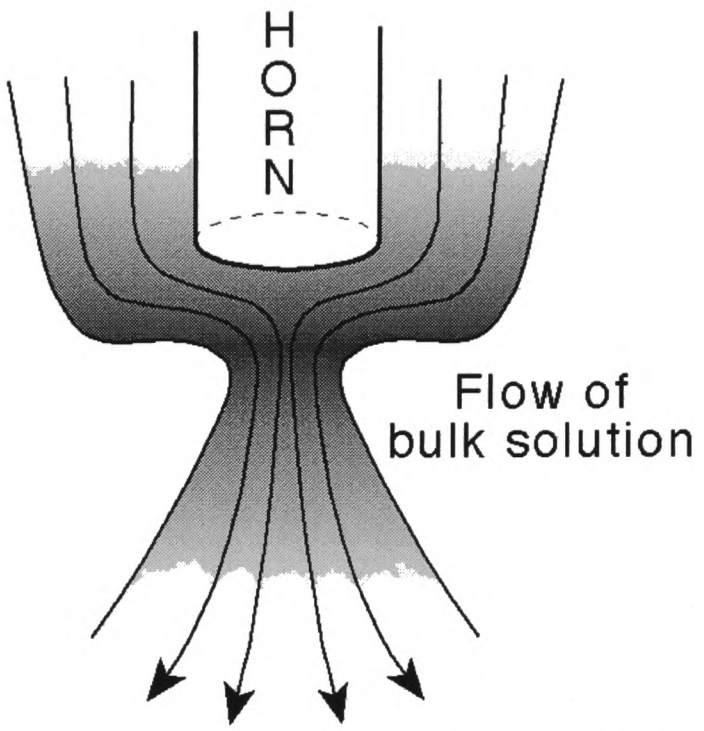

Figure 1.14 Schematic depiction of the flow pattern generated by the sonic horn.

Acoustic streaming [46] occurs when ultrasound enters a liquid and is dissipated by conversion into kinetic energy creating a shock wave in the bulk solution thereby increasing the convective motion of the solution away from the horn tip. The effect is visible to the naked eye and is dependent upon the intensity of the ultrasound (see Figure 1.14).

Microjet formation, or *microstreaming*, results from the asymmetric collapse of the cavitation microbubbles and is seen in Figure 1.15. The result is to enhance the local mass transport as the jets of liquid may be travelling at speeds of up to 100 m s^{-1}.

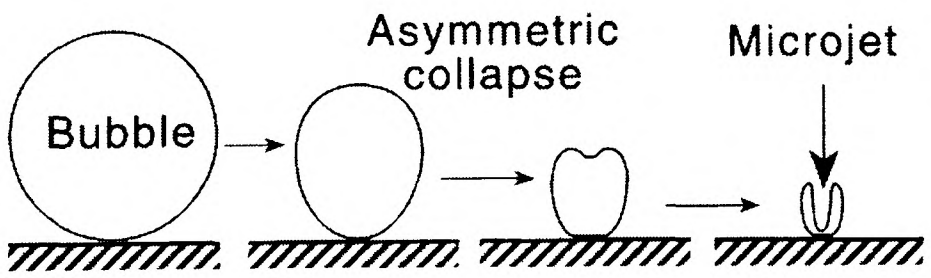

Figure 1.15 A cartoon of the collapse of a cavitation bubble causing a microjet [47].

1.5.3 CHEMICAL EFFECTS OF ULTRASOUND

Ultrasound can have many different effects on solutions depending on the frequency of the ultrasound and whether the solution is homogeneous or heterogeneous. The effects of frequency are considered first.

When cavitation occurs very high local temperatures may arise [48-51]. This in turn enables a more facile radical production. A common feature of ultrasound in chemistry is that it promotes radical reactions. In water the bubbles formed due to cavitation are filled with vapour and dissolved gas; and are transient. The internal pressure and temperature can reach several hundred bars and several thousand degrees [48-51]. Under these extreme conditions the water molecule can cleave to give $H^{\bullet}$ and $OH^{\bullet}$ radicals respectively. If molecular oxygen is present it can also cleave to give O atoms:

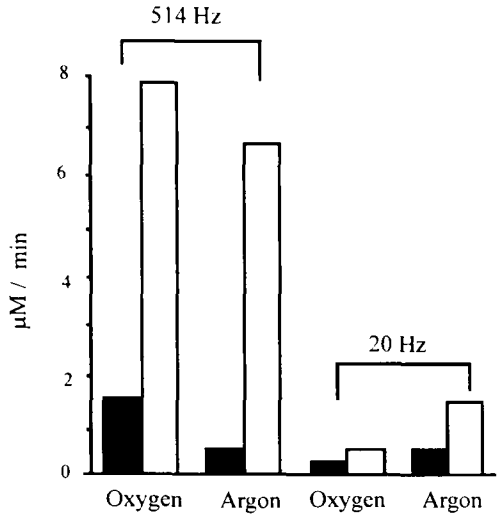

Figure 1.16 showing the rate of production of hydrogen peroxide ( ) and that of the I_3^- ion (■). Power for each is adjusted such that the rate of I_3^- production in argon is 0.45 µM min^{-1}. Data taken from [52]

$$H_2O \rightarrow H^{\bullet} + OH^{\bullet}$$

$$O_2 \rightarrow 2O$$

The transient radicals can either escape from the bubble to react with dissolved molecules or recombine.

$$2OH^{\bullet} \rightarrow H_2O_2$$

The dependence of this on frequency has been monitored using aqueous KI solution and monitoring iodide ion oxidation and hydrogen peroxide production [52]. At higher frequency (514 kHz) hydrogen peroxide is more efficiently produced under oxygen but at lower frequency (20 kHz) the opposite is seen suggesting that the recombination reaction in the bubble is promoted by oxygen and, conversely, the transport out of the bubble is hindered by the presence of oxygen at higher frequencies [52]. This is illustrated in Figure 1.16.

The influence of ultrasound on solutions varies according to whether the reacting mixture is homogeneous or heterogeneous and can give different products compared to the analogous mechanically stirred reactions. The following guidelines for the effect on reactions have been summarised by Luche [53]:

Homogeneous reactions: The chemistry of the reactions is influenced by the use of ultrasound by the collapse of the cavitation bubbles creating hot spots and introducing novel intermediates such as co-ordinately unsaturated species or free radicals and thereby changing the course of the reaction.

Heterogeneous reactions: In heterogeneous reactions three types of ultrasonic influence are observed:

i) If the reaction involves surface catalysis then the rate of reaction is increased as the ultrasound cleans the surface and promotes the reaction (e.g. Reaction 1.1).

ii) If the reaction involves a radical intermediate or Single Electron Transfer (SET) this pathway is promoted [53] (e.g. Reaction 1.2).

iii) If the inhomogeneity comes from the immiscibility of two liquids ultrasound will enhance the rate of transport across the phase boundary.

In Reaction 1.1 ultrasound activates the reaction between benzyl bromide and insoluble potassium cyanide at the alumina surface via an S_N2 type mechanism [54]; the normal solution reaction goes via an S_N1 type mechanism [54]. In Reaction 1.2 the ultrasound serves both to promote the rate of the second SET and to provide radicals to trap the intermediate after the radical re-arrangement. Under insonation the more easily formed 5-membered ring (5-exo-trig) is trapped forcing the reaction to be irreversible and resulting in a kinetic product whereas in the mechanically stirred reaction the second SET is reversible and the thermodynamic 6-membered ring product results [54].

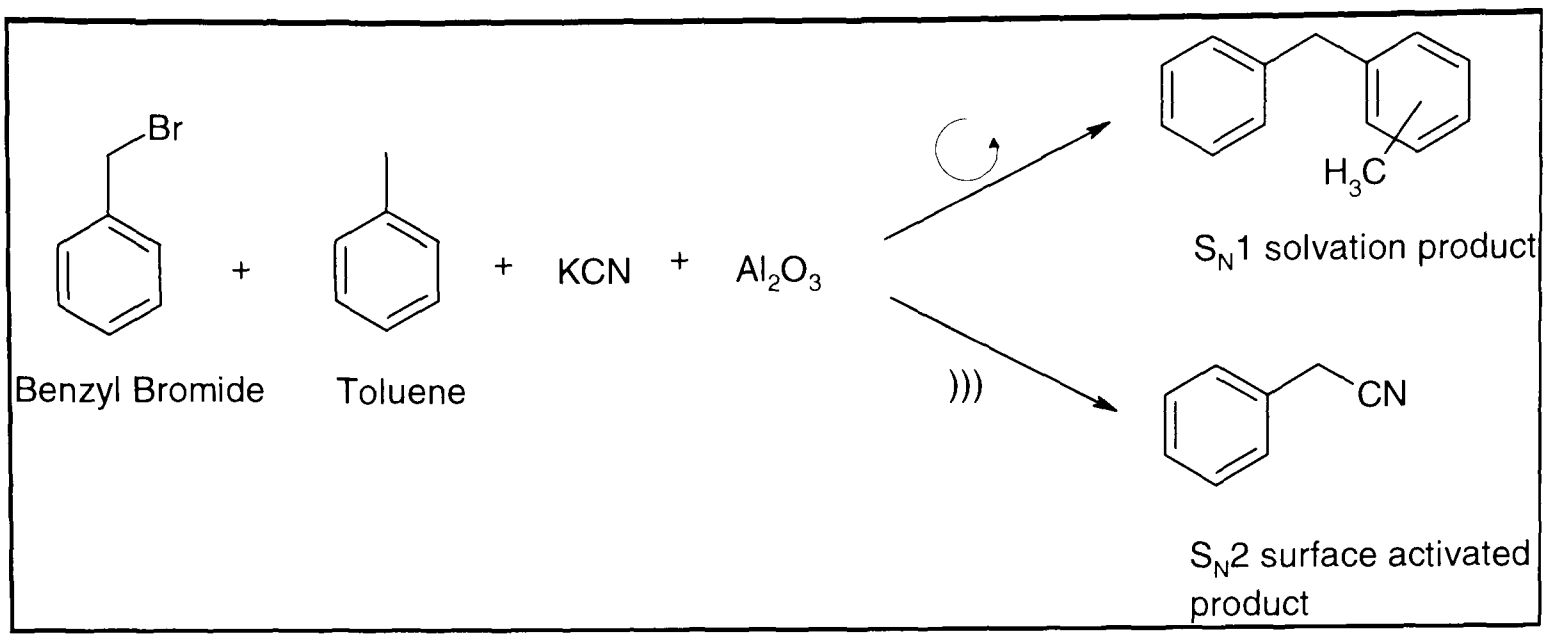

Reaction 1.1 The surface activation effect of ultrasound. ↻ and))) denote mechanical and ultrasonic stirring respectively.

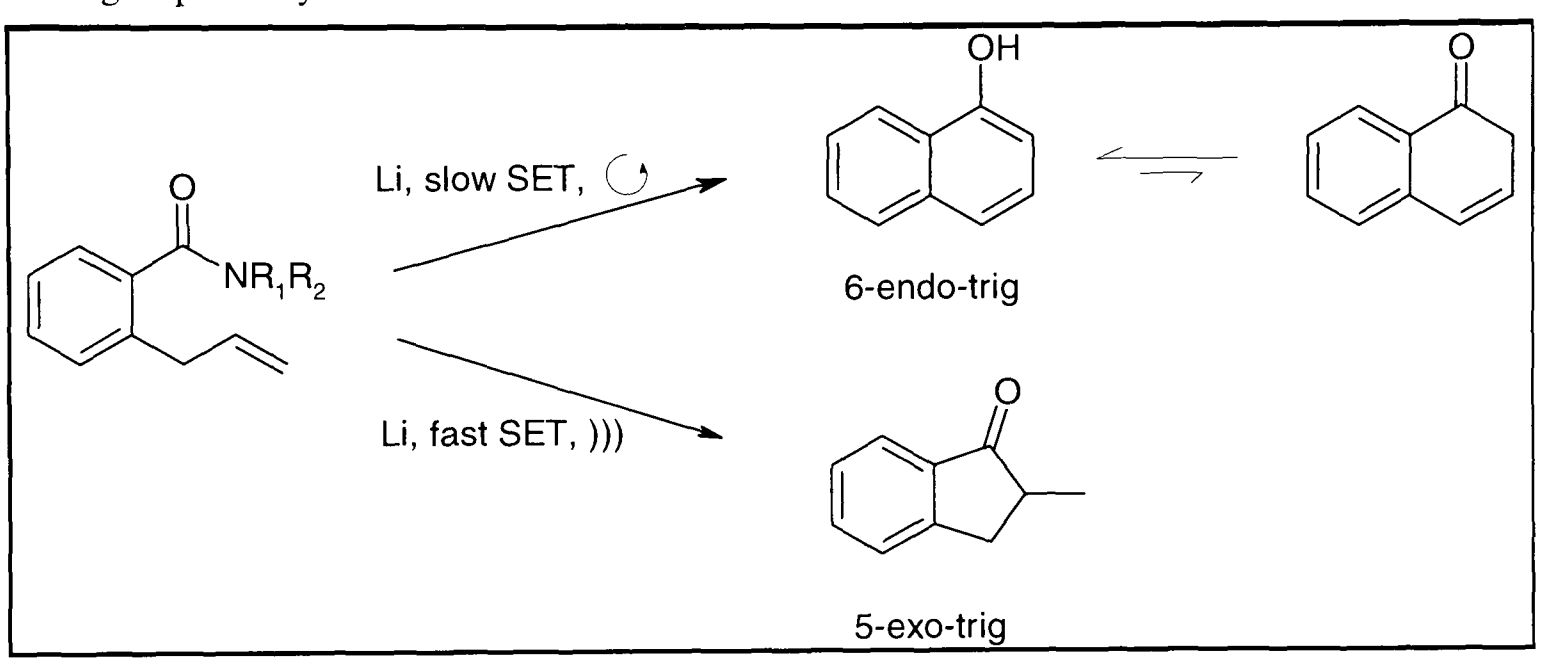

Reaction 1.2 The radical promotion effect of ultrasound.

In heterogeneous solutions that contain an alkali metal irradiation by ultrasound causes an emulsion of the metal to be produced [55]. If a piece of potassium metal is placed in xylene or toluene and exposed to ultrasound at approximately 10°C a silvery blue colour is obtained and the metal fragment disappears. This will not occur for lithium and will only occur for sodium in xylene [55]. Alkali metals are not the only metals to be emulsified by ultrasound; it has been shown that the irradiation of a thin mercury film will yield an emulsion [56,57]. The powerful effect of ultrasound on heterogeneous reactions immediately suggests its use in electrochemistry to which we next turn.

1.6 SONO-ELECTROCHEMISTRY

Having introduced separately sonochemistry and electrochemistry the concept of ultrasonic 'dual activation' is now explained in which the two are combined to give the relatively new field of *sono-electrochemistry* [58,59]. Early work in the field was carefully summarised by Yeager and Hovorka [60] and by Littlewood [61]. Some of the advantages of sono-electrochemistry over traditional electrochemistry are given below.

- The collapse of the cavitation bubbles near an electrode surface may have a cleaning effect which may render otherwise passivated or poisoned electrode surfaces active. For example Ni electrodes form an oxide overlayer and become deactivated when scanned positive. Under ultrasound they are cleaned allowing oxidation processes to be studied [62].
- Ultrasound will very considerably increase the mass transport to the electrode compared to that under silent and non-stirred solutions [63].
- Ultrasound promotes the formation of high energy intermediates and radicals and this may affect the outcome of a process and introduce novel electrochemical syntheses [64,65].
- The ability of ultrasound to degas solutions ensures that any gaseous products formed at the electrode are efficiently removed ensuring no surface effects alter the system being studied. This has been shown using ultrasound on the electrolysis of hydrochloric acid; an increase in the yield of chlorine was obtained [66].
- Ultrasound can be employed to form emulsions between aqueous and non-aqueous phases. The electrochemical implications of this are explored in Chapters 6 and 7.

The simplest method for performing sono-electrochemistry is by placing the electrochemical cell within an ultrasonic bath. However this method can be very irreproducible as the results are strongly dependent on the precise placement of the cell within the bath and the specific geometry of the cell being used [67]. The work in this thesis employs an ultrasonic horn transducer to direct the ultrasound as discussed in the next section.

1.6.1 CELL GEOMETRIES

There are four distinct types of sono-electrochemical cell set-up (shown in Figure 1.17).

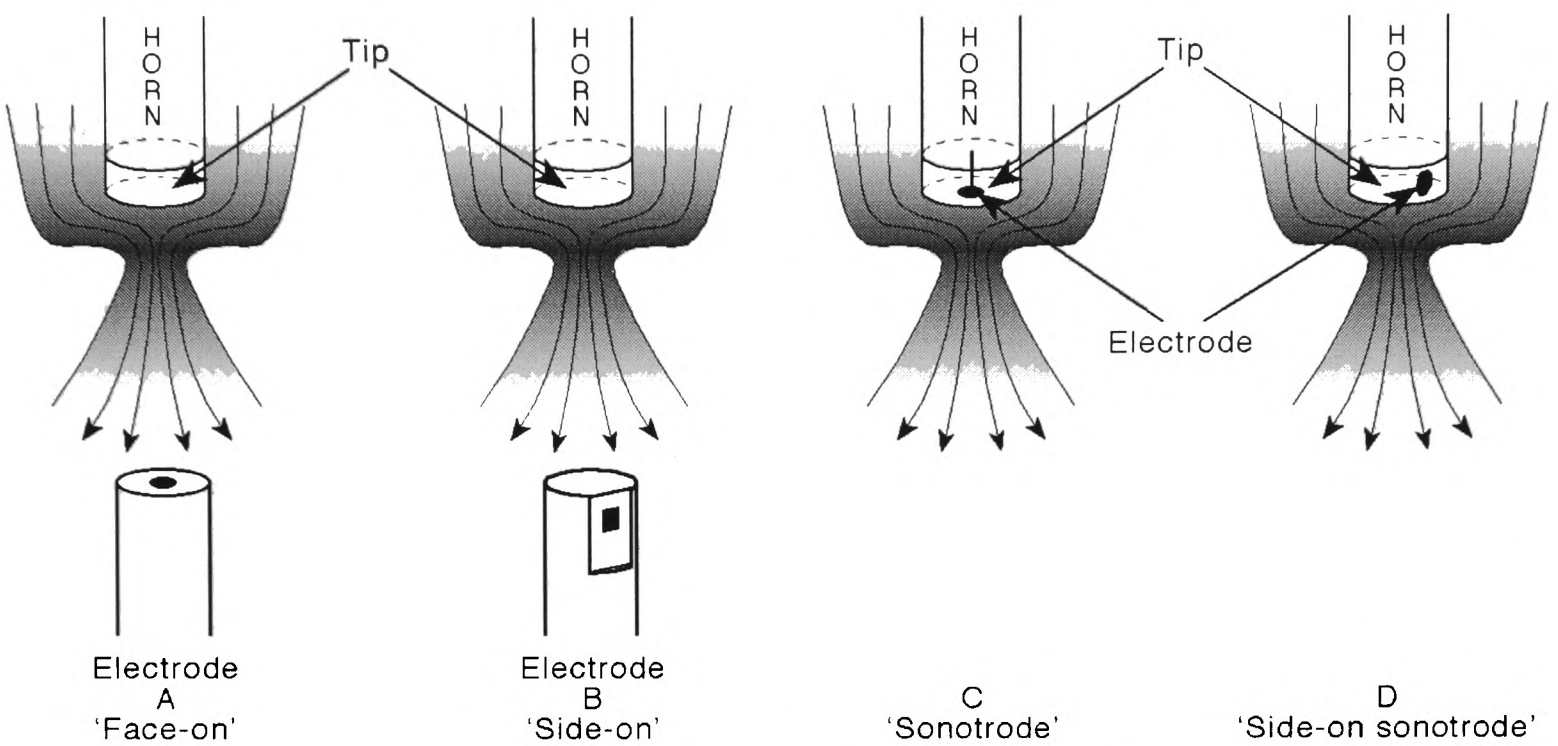

Figure 1.17 Schematic depiction of A) the 'face-on', B) the 'side-on', C) the 'sonotrode' and D) the 'side-on sonotrode' cell geometries.

A) The 'face-on' approach [68]: the working electrode is placed directly opposite the sonic horn at a known horn-electrode distance.

B) The 'side-on' approach [69]: the working electrode is placed perpendicular to the sonic horn.

C) The 'sonotrode' approach [70-72]: the working electrode is embedded in the horn such that the former acts as part of the latter (see Figure 1.18).

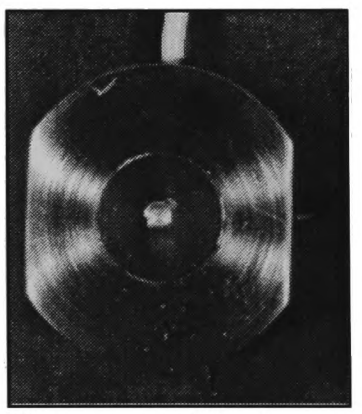

Figure 1.18 1 mm platinum 'sonotrode'.

D) The 'side-on sonotrode' approach [this work]: the working electrode is embedded in the side edge of the horn tip.

The 'face-on' approach is the most versatile as the separation of the horn and the electrode can be varied as well as the power. The 'side-on' geometry is similar to a fast flow-cell [73] but with the addition of ultrasonic effects. The 'sonotrode' is effectively a zero separation face-on set-up but is restricted to use at relatively low powers. Similarly, the 'side-on sonotrode' has similar characteristics to the 'side-on' approach and is also used at

low ultrasonic intensities. Characterisation of the different geometries is discussed further in Chapter 3.

1.6.2 MASS TRANSPORT

Eklund conducted experiments in the face-on mode studying the oxidation of ferrocene [63]. Results for silent and insonated cases are shown in Figure 1.19. It is clear that under silent conditions a conventional cyclic voltammogram is observed whereas in the presence of ultrasound the current is much higher and a steady transport limited current is observed, as with a RDE. The effect of ultrasound is to promote a substantial flux of electroactive material to the electrode by the virtue of enhanced mass transport (due to acoustic streaming, microstreaming and local cavitational bubble collapse). The current can be approximately predicted by the Nernst Diffusion Law [7]:

$$I_{lim} = \frac{nFAD[X]}{\delta} \qquad (1.25)$$

where n is the no. electrons transferred and δ is the diffusion layer thickness. The typical range of diffusion layers obtained are 0.85 - 3.00 μm which at an RDE would require a rotation speed of in the range of 5500-440 Hz! The former value is clearly impractical. The basis of Equation (1.25) is given schematically in Figure 1.20.

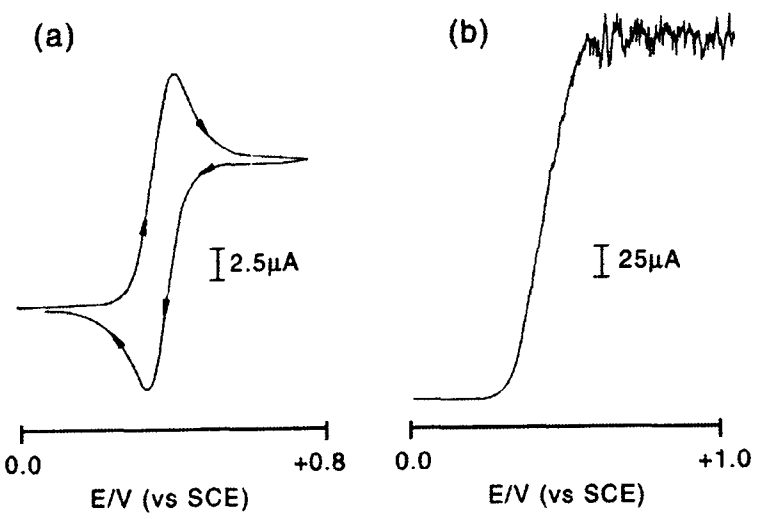

Figure 1.19 (a) Cyclic voltammogram of 2 mM ferrocene in acetonitrile (0.1M TBAP) at a 2 mm Pt disc electrode with v_s = 20 mV s^{-1} (b) Equivalent voltammogram under 50 W cm^{-2} of 20 kHz ultrasound and a horn-to-electrode separation of 40 mm.

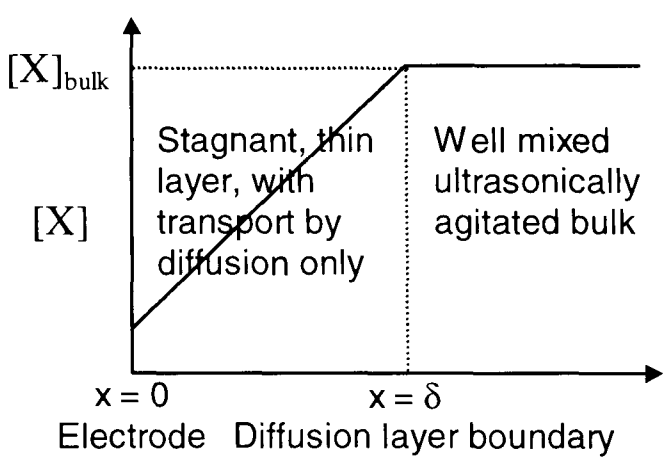

Figure 1.20 Simple model of a diffusion layer under ultrasonic conditions.

Consideration of Figure 1.20 shows that the basis of Equation (1.25) is a thin 'entirely' stagnant layer adjacent to the electrode. Such a model has been used to approximately describe the behaviour of a RDE and other hydrodynamic electrodes. However more detailed consideration, as discussed in Chapter 3, suggests that although diffusion may dominate nevertheless there will be some residual convection related to the acoustic streaming. In practice for a very large number of different hydrodynamic electrodes it is found that:

$$I_{lim} \propto D^{2/3}$$

suggesting:

$$\delta \propto D^{1/3}$$

which is comparable to Equation (1.25) and implies that the diffusion layer thickness is in reality a balance between diffusion and convection. Careful experiments on the 'face-on' geometry [74] in aqueous solution have shown that:

$$I_{lim} \propto D^{2/3} A[X] \qquad (1.26)$$

suggesting that the system behaves effectively as a hydrodynamic electrode. This is explored further in Chapter 3 for all the electrode geometries shown in Figure 1.17.

1.7 DUAL ACTIVATION BY LASER

1.7.1 ELECTRODE ILLUMINATION BY LASER

Electrode surface treatment by laser irradiation is generally considered as entirely attributable to the heat produced when the solid electrode material absorbs laser energy. The use of lasers for producing a rapid temperature jump at an electrode was investigated for the study of the electric double-layer in the early 1980s by Benderskii *et al.* [75] whilst Smalley *et al.* used a similar technique to explore heterogeneous rate processes for the ferro/ferricyanide couple at a 25 μm platinum thin foil electrode illuminated on the dielectric (non-solution) face [76]. For continuous lasers it is simple to measure the incident laser intensity but for pulsed lasers it is important to distinguish between the average *pulse* intensity (with laser pulses typically lasting hundredths of a microsecond) and the average

laser intensity which takes the 'dark' time between pulses into account. At low *pulse* intensities (typically < 100 MW cm^{-2}) for short periods, only enough energy is absorbed to cause thermal lattice vibrations of most types of solid electrode. This is known as the 'thermoelastic effect' and can be applied to thermally desorb surface adsorbed species with little or no damage to the electrode surface. As more light energy is applied, a threshold is reached where localised lattice vibration is sufficiently vigorous to cause electrode melting or, under even more extreme cases, electrode vaporisation [77]. The phenomenon is known as 'laser ablation' and was recently mathematically modelled for organic solids using a 'breathing sphere' model by Zhigilei *et al.* [78]. Ablation results in the electrode surface being permanently physically altered. Both Watanabe *et al.* and McCreery *et al.* have used this effect for cleaning electrodes for electrochemical measurements. The former used 1064 nm (infra-red) pulses at 0.5 Hz from a Nd:YAG laser to continuously refresh a gold electrode surface for ascorbic acid oxidation by stripping off the surface atoms [79]. The latter used both in-situ and ex-situ laser pulses to modify electrode kinetics of glassy carbon electrodes [80].

1.7.2 LASER ACTIVATED VOLTAMMETRY

The critical difference between 'activation' and 'ablation' lies in the effect on the electrode surface. An 'activated' surface is defined here as one where only passivating, surface-adsorbed species have been removed to reveal the same original 'fresh' surface. This can be theoretically maintained indefinitely provided the laser intensity is 'tuned' to the right strength. Surface species may vary from oxide and hydroxide layers to polymer films and redox products. An 'ablated' surface is refreshed by physical removal of one or more layers of electrode surface atoms, along with anything else that was adhered to them. If this takes place rapidly in comparison with the time taken for passivating layers to reform then a fresh but reproducible surface can be produced after every laser pulse at the cost of a small amount of electrode erosion.

In laser activated voltammetry (hereafter referred to as LAV) the illumination does not lead to direct chemical effects as in photoelectrochemistry. In this process a pulsed laser light source is used [79] which leads to activation of the electrode surface. Thus under favourable conditions it is able to retain its electrochemical reactivity in the presence of species which would generally lead to passivation through the adsorption of reactants, intermediates or products onto the electrode surface.

When the surface of the electrode is struck by a laser pulse various phenomena may occur simultaneously, such as intense optical emission, sound and heat generation and the generation of fine metal particles and gas bubbles. With the use of a low power density laser beam, the increases in temperature at the electrode surface are sufficiently small to avoid any change of state in the solid material, and elastic stresses are generated by bulk thermal expansion (thermoelastic effect [81,82]). It is these effects which lead to surface depassivation. With a high power density laser pulse, the increases in temperature give rise to melting and then to vaporisation of a small quantity of material at the surface (ablation effect [82]). Thus we can distinguish between laser ablation voltammetry (hereafter termed LAbV) [79] associated with electrode damage, and laser activated voltammetry (LAV), in which depassivation and current enhancement effects are achieved while maintaining an essentially undamaged electrode. Additionally, ultrasound may also be generated within the electrode material by laser irradiation [82].

1.8 MICROWAVE ACTIVATED VOLTAMMETRY

This is a further example of the in-situ activation of electrochemistry by external sources of radiation. Until very recently the interaction of microwave radiation with electrochemical processes [83] was entirely unexplored, despite the widespread interest in microwave enhanced chemistry. The use of low power microwave radiation in electrochemical systems is of considerable importance in areas of research such as in-situ electrochemical EPR [84] (typically X-band, 9.5 GHz) and microwave reflectance characterisation [85] of semi-conducting electrodes. In these cases the activation of the

electrochemical system due to absorption of microwave radiation can usually be ignored due to the low intensities used. However, microwave radiation is known to interact not only with molecules in the gas phase but also with condensed materials and interfaces with sufficient dielectric loss [86] and may therefore be employed to activate an electrochemical system.

The use of microwave radiation as an activation source leads to a considerable current enhancement, arising from a rapid heating effect which causes the temperature in the liquid phase at the electrode/solution interface to locally superheat [83].

1.9 DETAILED AIMS AND CONTENTS OF THIS THESIS

The chief aim of this thesis is to exploit the dramatic effect of power ultrasound on electrochemistry, namely the field of sono-electrochemistry. Ultrasound will be employed in the pre-concentration stage of ASV in order to achieve greater mass transport to the electrode and hence detect smaller amounts of target metal or reduce the timescale of the experiment by shortening the pre-concentration time required. Additionally the extraction and surface cleaning properties of ultrasound will be examined in 'real' systems with the aim of establishing new techniques for the detection of heavy metals and redox active organic molecules in, for example, food stuffs where matrix effects diminish the effectiveness of conventional electroanalytical techniques.

The secondary theme of this thesis is to explore the use and develop new approaches to the following additional dual activation techniques; laser activated electrochemistry, thermal electrochemistry and microwave activated electrochemistry. In addition it seeks to investigate the relative merits of these processes in terms of electrode depassivation/activation.

The maintenance of a clean, reproducible electrode surface is of critical importance in making meaningful electroanalytical measurements. Indeed the limited use of such methodology in real-world analytical usage likely derives substantially from the fact that in many non-model systems typically encountered outside of the research laboratory the inevitable presence of surface active materials can lead to significant interference and

electrode passivation problems. Moreover since as little as *monolayer* coverage is often sufficient to perturb the path of electrode processes it follows that only trace amounts of the adsorbing interferent may be significant.

Classically such problems were alleviated by use of a dropping mercury electrode (DME) but this device is less suitable than solid electrodes for many (such as on-line) analytical techniques and entirely inapplicable if significant oxidising potentials are required. In addition mercury is environmentally compromising, thus the development of methods to facilitate the wider and more general use of solid electrodes would be timely.

In Chapters 8 to 11 one such method is explored; laser activated electrochemistry and its applications to passivating systems. These chapters seek to show how the use of laser activation can lead to current enhancement and depassivation effects without damage to the electrode surface and are compared and contrasted with sono-electrochemical techniques. A limiting current is observed in laser activated voltammetry because the diffusion layer and electrode surface are periodically renewed via laser activation. Thus, in principle, a reproducible voltammogram can be obtained for many kinds of solid electrodes.

Previously the use of power ultrasound and in particular that transmitted directionally via a horn-type transducer probe has been successfully utilised as a method for electrode depassivation. In this thesis in addition to the conventional coupling of power ultrasound to electrochemical processes, a novel sono-emulsification technique will also be discussed in Chapter 7. In this process a two-phase solution is used, consisting of an aqueous phase and an organic phase, the electroactive species being in the aqueous phase, while the electrolysis products are partially soluble/insoluble in the aqueous phase and soluble in the organic phase. The power ultrasound applied leads to the emulsification of the solution, allowing the reaction products to be taken up by the organic phase and not deposit on the electrode surface thus leading to passivation.

One further technique briefly investigated in this work is the use of microwave activation. In Chapter 12 the current enhancement seen is calibrated by comparison with temperature activation techniques. In addition the effects of thermal activation of the

methylene green system are discussed and compared with laser activation and sono-emulsion experiments.

1.10 CHAPTER 1: REFERENCES

[1] A. C. Fisher, *Electrode Dynamics*, OUP, Oxford, **1996**.

[2] P. H. Reiger, *Electrochemistry*, Chapman and Hall, New York, **1994**, pgs. 128-129.

[3] A. Fick, *Philosophical Magazine and Journal of Science* **1855**, *10*, 30.

[4] A. J. Bard, L. R. Faulkner, *Electrochemical Methods*, Wiley, New York, **1980**, pg. 280.

[5] M. S. Wrighton, D. L. Morse, L. Pdungsap, *J. Am. Chem. Soc.* **1970**, *97*, 3603.

[6] K. B Oldam, C. G. Zoski, *Comprehensive Chemical Kinetics*, Elsevier, Oxford, **1986**, Vol. 26, pg. 122.

[7] C. M. A. Brett, A. M. O. Brett, *Electrochemistry Principles, Methods, and Applications*, OUP, Oxford, **1993**.

[8] R. Muller, J. Heinze, *J. Electrochem. Soc.* **1998**, *145*, 1227.

[9] F. G. Cottrell, *Z. Physik. Chem.* **1902**, *42*, 385.

[10] R. B. Bird, W. E. Stuart, E. N. Lightfoot, *Transport Phenomena*, Wiley, New York, **1960.**

[11] J. Newman, *Electroanal. Chem.* **1973**, *6*, 187.

[12] R. G. Compton, P. R. Unwin, *J. Electroanal. Chem.* **1986**, *205*, 1.

[13] R. N. Adams, *Electrochemistry at Solid Electrodes*, Marcel Dekker, New York, **1969.**

[14] R. G. Compton, A. M. Waller, *Comprehensive Chemical Kinetics*, Elsevier, Oxford, **1989**, Vol. 29, pg. 173.

[15] Southampton Electrochemistry Group, *Instrumental Methods in Electrochemistry*, Ellis Horward, Chichester, **1985.**

[16] W. J. Albery, *Electrode Kinetics*, Clarendon Press, Oxford, **1975.**

[17] A. M. Waller, R. G. Compton, *Comprehensive Chemical Kinetics*, Elsevier, Oxford, **1989**, Vol. 29, pg. 297.

[18] R. A. W. Dryfe, R. G. Compton, *Prog. Reaction Kinetics* **1995**, *20*, 245.

[19] R. C. Ackerberg, R. D. Patel, S. K. Gupta, *J. Fluid Mech.* **1978**, *86*, 49.

[20] W. Zhang, H. A. Stone, J. D. Sherwood, *J. Phys. Chem.* **1996**, *100*, 9462.

[21] R. G. Compton, B. A. Coles, *J. Electroanal. Chem.* **1983**, *144*, 87.

[22] W. J. Albery, S. Bruckenstein, *J. Electroanal. Chem.* **1983**, *144*, 105.

[23] R. G. Compton, R. A. W. Dryfe, J. A. Alden, N, V. Rees, P. J. Dobson, P. A. Leigh, *J. Phys. Chem.* **1994**, *98*, 1270.

[24] M. B. Glauert, *J. Fluid Mech.* **1965**, *1*, 625.

[25] V. G. Levich, *Physicochemical Hydrodynamics*, Prentice-Hall, New York, **1962**.

[26] P. R. Unwin, R. G. Compton, *J. Electroanal. Chem.* **1988**, *245*, 287.

[27] A. M. Bond, *Modern Polarographic Methods in Analytical Chemistry*, Marcel Dekker, New York, **1980**.

[28] Kh. Z. Brainina, E. Neyman, *Electroanalytical Stripping Analysis*, Wiley, New York, **1993**.
[29] F. Vydra, K. Stulík, E. Juláková, *Electrochemical Stripping Analysis*, Ellis Horwood, Chichester, **1976**.
[30] F. Marken, T. O. Rebbitt, J. Booth, R. G. Compton, *Electroanalysis* **1997**, *9*, 19.
[31] C. M. G. Van Der Berg, A. M. Harbin, *Anal. Chem.* **1993**, *65*, 3411.
[32] Z. Gao, K. S. Siow, *Talanta* **1996**, *43*, 727.
[33] H. Ping Wu, *Anal. Chem.* **1996**, *68*, 1639.
[34] B. J. Feldman, J. D. Osterloh, B. H. Hata, A. Dalessandro, *Anal. Chem.* **1994**, *66*, 1983.
[35] Z. Gao, K. S. Siow, *Talanta* **1996**, *43*, 255.
[36] Kh. Z. Brainina, A. M. Bond, *Anal. Chem.* **1995**, *67*, 2586.
[37] G. Henze, S. Sander, *Anal. Chim. Acta* **1996**, *319*, 19.
[38] C. Locatelli, E. Vasca, C. Bighi, F. Fagioli, T. Garai, *Electroanalysis* **1996**, *8*, 165.
[39] I. Turyan, D. Mandler, *Anal. Chem.* **1993**, *65*, 2089.
[40] K. Štulík, *Electroanalysis* **1992**, *4*, 829.
[41] J. C. Birnholtz, E. E. Farrell, *American Scientist* **1984**, *72*, 608.
[42] T. J. Mason, J. P. Lorimer, *Sonochemistry: Theory, Applications and Uses of Ultrasound in Chemistry*, Ellis Horwood, Chichester, **1988**.
[43] T. J. Mason, *Sonochemistry: the Uses of Ultrasound in Chemistry*, Royal Society of Chemistry Publications, London, **1990**.
[44] A. Henglein, M. Gutiérrez, *J. Phys. Chem.* **1993**, *97*, 11368.
[45] R. Hiller, K. Weninger, S. J. Putterman, B. P. Barber, *Science* **1994**, *266*, 248.
[46] F. Marken, R. P. Akkermans, R. G. Compton, *J. Electroanal, Chem.* **1996**, *415*, 55.
[47] J. Klima, C. Bernard, C. Degrand *J. Electroanal. Chem.* **1995**, *399*, 147.
[48] K. S. Suslick, *Ultrasound, Its Chemical, Physical and Biological Effects*, VCH Weinheim, New York, **1988**, pg. 138.
[49] A. J. Walton, G. T. Reynolds, *Adv. Phys.* **1987**, 239.
[50] P. K. Chendke, H. S. Fogler, *J. Phys. Chem.* **1985**, *89*, 1673.
[51] K. S. Suslick, S. J. Cokktycz, E. B. Flint *Ultrasonics* **1990**, *28*, 280.
[52] C. Petrier, A. Jeunet, J.-L. Luche, G. Reverdy, *J. Am. Chem. Soc.* **1992**, *114*, 3148.
[53] J. L. Luche, C. Einhorn, J. Einhorn, J. V. Sinisterra-Gago, *Tetrahedron Let.* **1990**, *31*, 4125.
[54] S. G. Davies, *Private Communication*, Oxford, March **1997**.
[55] J.-L. Luche, C. Petrier, C. Dupuy, *Tetrahedron Let.* **1984**, *25*, 753.
[56] K. Söllner, C. Bondy, *Trans. Faraday Soc.* **1936**, *32*, 616.
[57] W. T. Richards, *J. Am. Chem. Soc.* **1929**, *51*, 1724.
[58] D. J. Walton, S. S. Phull, *Adv. Sonochem.* **1996**, *4*, 205.
[59] R. G. Compton, J. C. Eklund, F. Marken, *Electroanalysis* **1997**, *7*, 509.
[60] E. Yeager, F. Hovorka, *J. Acoust. Soc. Am.* **1953**, *25*, 443.
[61] K. Littlewood, *J. Royal. Inst. Chem.* **1962**, *86*, 78.
[62] R. G. Compton, J. C. Eklund, S. D. Page, G. H. W. Sanders, J. Booth, *J. Phys. Chem.* **1994**, *98*, 12410.

[63] R. G. Compton, J. C. Eklund, S. D. Page, T. J. Mason, D. J. Walton, *J. Appl. Electrochem.* **1996**, *26*, 775.

[64] J. C. Eklund, D. N. Waller, T. O. Rebbitt, F. Marken, R. G. Compton, *J. Chem. Soc. Perkin Trans. 2* **1995**, 1981.

[65] R. G. Compton, J. C. Eklund, S. D. Page, T. O. Rebbitt, *J. Chem. Soc. Dalton Trans.* **1995**, 389.

[66] F. Cataldo, *J. Electroanal. Chem.* **1992**, *332*, 325.

[67] D. J. Walton, S. S. Phull, A. Chyla, J. P. Lorimer, T. J. Mason, L. D. Burke, M. Murphy, R. G. Compton, J. C. Eklund, S. D. Page, *J. Appl. Electrochem.* **1995**, *25*, 1083.

[68] J. C. Eklund, *D. Phil. Thesis*, Oxford University, **1995.**

[69] J. C. Eklund, F. Marken, D. N. Waller, R. G. Compton, *Electrochimica Acta.* **1996**, *41*, 1541.

[70] A. Durant, H. Francois, J. Reisse, A. Kirsch-de Mesmaeker, *Electrochimica Acta* **1996**, *41*, 277.

[71] J. Reisse, H. Francois, J. Vandercammen, O. Fabre, A. Kirsch-de Mesmaeker, C. Maerschalk, J.-L. Delplancke, *Electrochimica Acta* **1994**, *39*, 37.

[72] R. G. Compton, J. C. Eklund, F. Marken, D. N. Waller, *Electrochimica Acta* **1996**, *41*, 315.

[73] N. V. Rees, R. A. W. Dryfe, J. A. Cooper, B. A. Coles, R. G. Compton, S. G. Davies, T. D. McCarthy, *J. Phys. Chem.* **1995**, *99*, 7096.

[74] H. A. O. Hill, Y. Nakagawa, F. Marken, R. G. Compton, *J. Phys. Chem.* **1996**, *100*, 17395.

[75] V. A. Benderskii, G. I. Velichko, *J. Electroanal. Chem.* **1982**, *140*, 1.

[76] J. F. Smalley, C. V. Krishnan, M. Goldman, S. W. Feldberg, I. Ruzic, *J. Electroanal. Chem.* **1988**, *248*, 255.

[77] W. W. Duley, *Laser Processing and Analysis of Materials*, Plenum Press, New York, **1983**.

[78] L. V. Zhigilei, P. B. S. Kodali, B. J. Garrison, *J. Phys. Chem. B* **1998**, *102*, 2845.

[79] T. Hinoue, I. Watanabe, H. Watarai, *Chem. Lett.* **1996**, 329.

[80] E. Hershenhart, R. L. McCreery, R. D. Knight, *Analytical Chem.* **1984**, *56*, 2256.

[81] R. Oltra, G. M. Indrianjafy, J. P. Boquillon, *J. Phys. IV Colloque C7 769 Suppl. J. Phys. III* **1991**, 12.

[82] J. D. Aussel, A. Le Brun, J. C. Baboux, *Ultrasonics* **1988**, 26, 245.

[83] R. G. Compton, B. A. Coles, F. Marken, *J. Chem. Soc. Chem. Comm.* **1998**, 2595.

[84] R. G. Compton, A. M. Waller, *Spectroelectrochemistry: Theory and Practice*, Plenum Press, New York, **1988**, pg. 349.

[85] G. Schlichthörl, E. A. Ponomarev, L. M. Peter, *J. Electrochem. Soc.* **1995**, *142*, 3062.

[86] C. Gabriel, S. Gabriel, E. H. Grant, B. S. J. Halstead, D. M. P. Mingos, *Chem. Soc. Rev.* **1998**, *27*, 213.

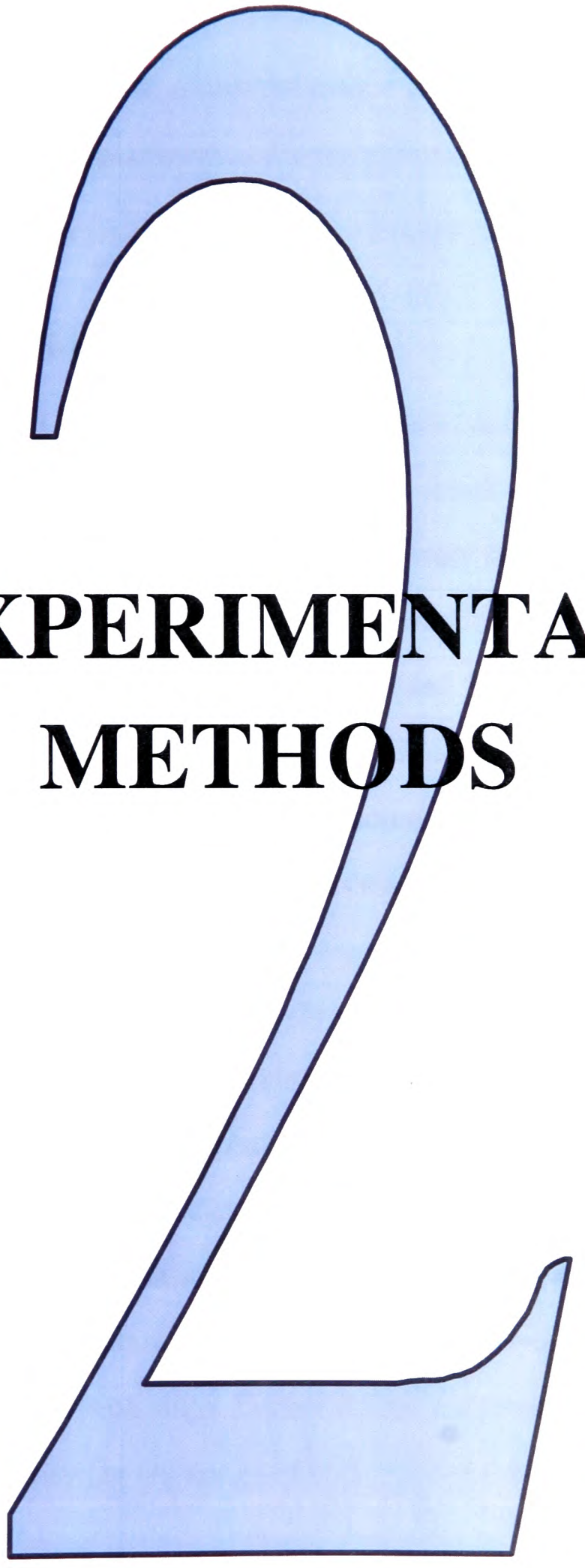

EXPERIMENTAL METHODS

CHAPTER 2: EXPERIMENTAL METHODS

This chapter describes the experimental procedures used in the work reported throughout the thesis; both standard apparatus and equipment designed specially in the course of the work are described. The details of the chemicals employed are also given.

2.1 ELECTRODE PREPARATION

A saturated calomel electrode (SCE) (Radiometer, Copenhagen) acted as a reference in all experiments throughout this work unless where stated while a graphite rod usually acted as the counter electrode. Platinum or gold coils were occasionally also used for this purpose. The platinum, gold, copper and glassy carbon working electrodes employed were all measured to 0.01 mm using a travelling microscope and were polished before use using diamond lapping compounds (Kemet, Kent, UK) of decreasing size down from 25 to 1 μm. In order to eliminate the introduction of lead into solution from the electrode, the platinum disc electrode was welded to a platinum wire and then onto a brass rod without the need for the use of any solder in its construction.

The mercury electrodes used in anodic stripping voltammetry experiments were usually formed by coating a platinum working electrode with mercury droplets. This was done by cathodically plating onto the platinum [1] from an aqueous solution of 0.15 M mercury nitrate and 0.12 M potassium cyanide using a 1.5 V cell for 30 seconds.

In order to maximise the transmission of ultrasound when sonotrodes were employed for sono-electroanalytical experiments (see section 1.6.1), the working electrode was set in Araldite which was hardened with silica. Further details are given in the next chapter, along with schematic diagrams showing the design of both types of sonotrode.

2.2 SONO-ELECTROCHEMISTRY

2.2.1 SONO-ELECTROCHEMICAL CELL DESIGNS

A well-characterised [2] three-electrode electrochemical cell was used in most sonovoltammetry experiments. The cell volume was approximately 250 cm^3 (Figure 2.1). A photograph of a typical experimental set-up is shown in Appendix 3. The working electrode was either positioned directly opposite the ultrasonic horn tip and close to the bottom of the cell or was integrated into the horn tip itself ('sonotrode' geometry). In some experiments a smaller cell was used shown in Figure 2.2 with a volume of approximately 20 cm^3 and in this cell a platinum wire acted as the counter electrode. The horns employed were supplied by Sonics & Materials (Model VCX400). In the large cell a titanium tipped horn probe of diameter 13 mm was used, whilst in the small cell a stepped titanium horn probe of diameter 3 mm was used. The above both operated at 20 kHz and were made of a titanium alloy (Ti 90%, Al 6% and V 4%) for the following reasons:

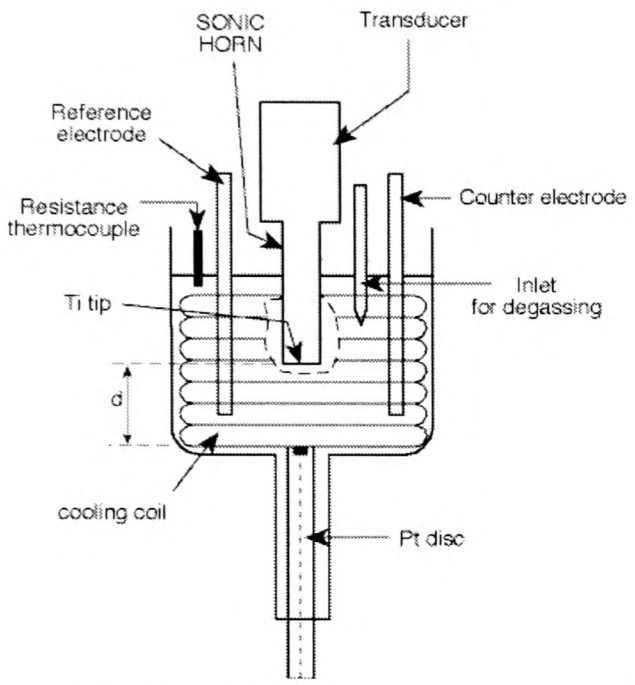

Figure 2.1 Large sono-electrochemical cell.

- High fatigue strength
- Low acoustic loss
- Chemical inertness (very significant as the horn tip must be immersed in the solution whilst operating).

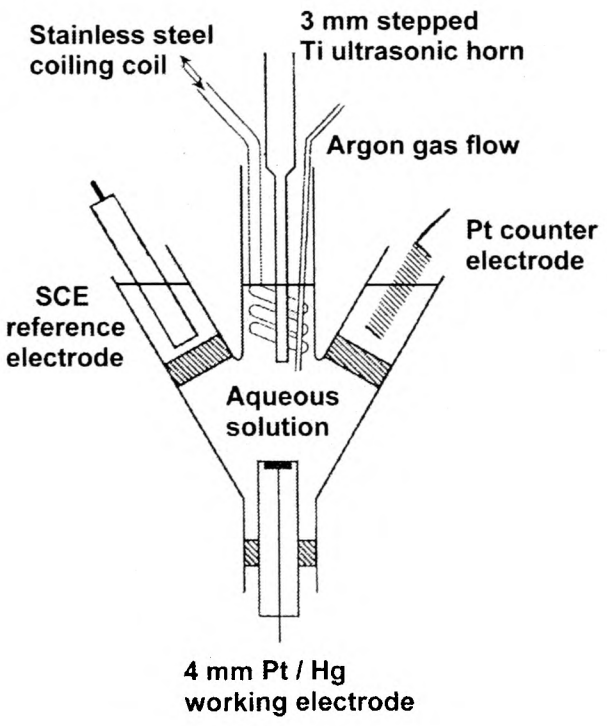

Figure 2.2 The initial sono-emulsion electrochemical cell.

The 13 mm diameter probe had a threaded end to allow the tip to be replaced when worn (see Figure 2.3). It also allowed the insertion of in-house modified tips with platinum,

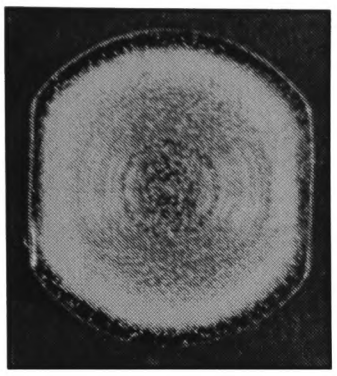

Figure 2.3 A horn tip showing considerable cavitational damage.

gold or copper inserts to give 'sonotrodes' (see 1.6.1). The horn had to be tuned for each power setting to ensure that the unit was drawing the minimum electrical power and also to make the results more reproducible. If the horn was difficult to tune then there was usually a fault within the system such as a worn tip or loose connection.

The ultrasound is generated by a piezoelectric crystal transducer [3-5]. When a rapidly alternating potential is applied to a piezoelectric material (e.g. $BaTiO_3$ or $PbNb_2O_6$) mechanical distortion occurs which is translated into vibrations of whatever is in contact with the material (most commonly metal blocks which additionally conduct away heat and protect the crystal). Transducers are of half wavelength multiples long such that the power is focused at the horn tip.

Ultrasound (US) power levels up to 50 Wcm^{-2} were employed for the 13 mm horn and up to 150 W cm^{-2} for the 3 mm horn. Intensity calibration is discussed in the next section. Thermostatting of the electrochemical cell to 25 ± 2°C was accomplished by means of a stainless steel cooling coil inserted in the solution through which water was circulated from a constant temperature bath. Generally the sonication time was limited to less than four minutes to enable the voltammetric measurements to be conducted in the essentially constant temperature range quoted above. However, during the emulsification experiments, when the cell was sonicated for up to an hour at a time, heating of the cell contents by up to 10°C was experienced. Temperature readings were taken with a thermometer consisting of a Pt 102 resistance thermocouple probe and control box.

The well-characterised sono-electrochemical cell [6] employed in the initial stages of the analysis of lead in petrol (Chapter 6) is shown in Figure 2.2. (Optimisation through the course of the project led to the development of a modified cell shown in Figure 6.1). Again, the same essentially constant temperature for voltammetric analysis was maintained by limiting the length of any single sonication period to a maximum time of 4 minutes.

2.2.2 CALORIMETRIC CALIBRATION OF ULTRASONIC HORN INTENSITY

The transducer used with the horn worked in arbitrary "%" amplitude units. It was necessary to calibrate the horn in order to be able to quote the corresponding intensities in W cm^{-2}. The intensity calibrations for the various ultrasonic horns employed were performed according to the methods of Margulis *et al.* [7] and Mason *et al.* [8] over a range of 0-544 W cm^{-2}. The intensity of the ultrasonic horn is simply related to the horn tip area and the power supplied as follows:

$$\text{Intensity} = \frac{\text{Power}}{\text{Area}} \tag{2.1}$$

The power is dependent on the mass, m, in kg, the specific heat capacity of the water, C_p, in J K^{-1} mol^{-1} and on the initial slope of the temperature (T)-time (t) graph according to:

$$\text{Power} = C_p m \left(\frac{dT}{dt}\right)_{t=0} \tag{2.2}$$

where t is the time in seconds following horn activation. The horn was activated and the temperature of a fixed quantity of water in a lagged container was measured every 30 seconds over the following 5 minutes. A plot of temperature versus time enabled an initial slope, $(dT/dt)_{t=0}$, to be determined. This was then repeated for amplitudes in the range 2% to 100% for the 13 mm diameter horns, 10% to 35% for the 3 mm diameter horns and 2% to 10% for 13 mm diameter horns fitted with 'sonotrode' tips (see 1.6.1). Calibration curves were then drawn up allowing ultrasonic intensities to be quoted. This gave typical intensities of 25 ± 1 W cm^{-2} for the 13 mm diameter horn at 40% amplitude, 52 ± 1 W cm^{-2} for the 3 mm horn at 10 % amplitude and 6 ± 1 W cm^{-2} for sonotrodes at 10% amplitude.

2.3 LASER ACTIVATED VOLTAMMETRY

2.3.1 LAV CELL DESIGN

The three electrode electrochemical cell used in the initial laser activated voltammetry (LAV) experiments is shown in Figure 2.4. A Teflon cylinder with a quartz window in the end was included to allow the path length of the laser light through the solution to the

electrode to be adjusted for use in coloured solutions. The modified apparatus is shown in Figure 2.5.

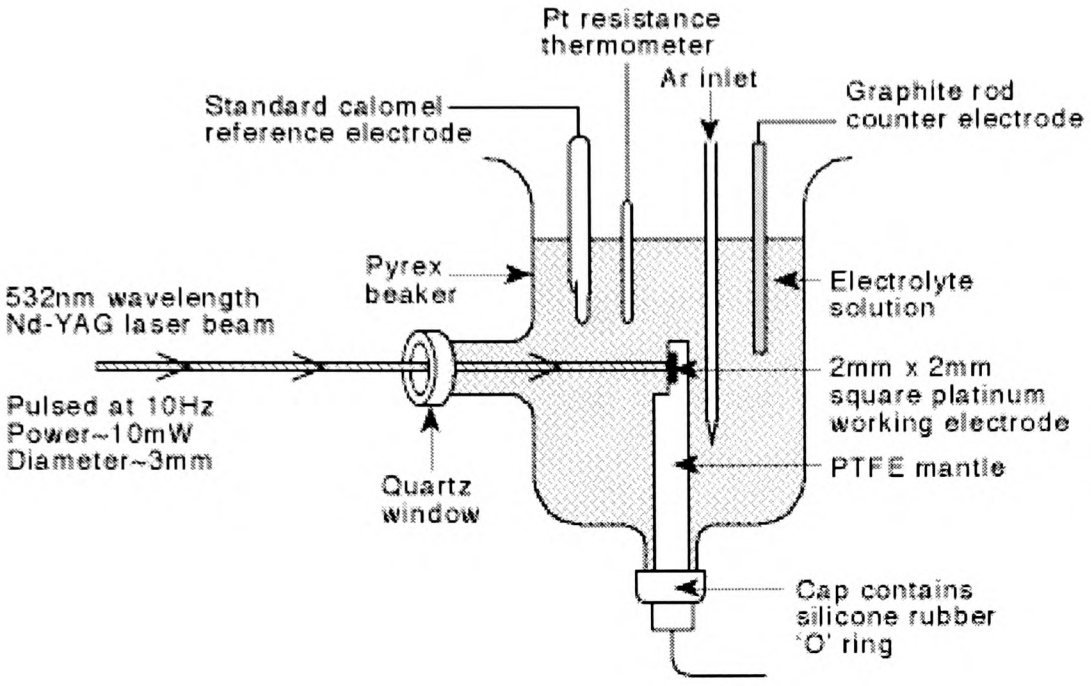

Figure 2.4 Large volume LAV cell.

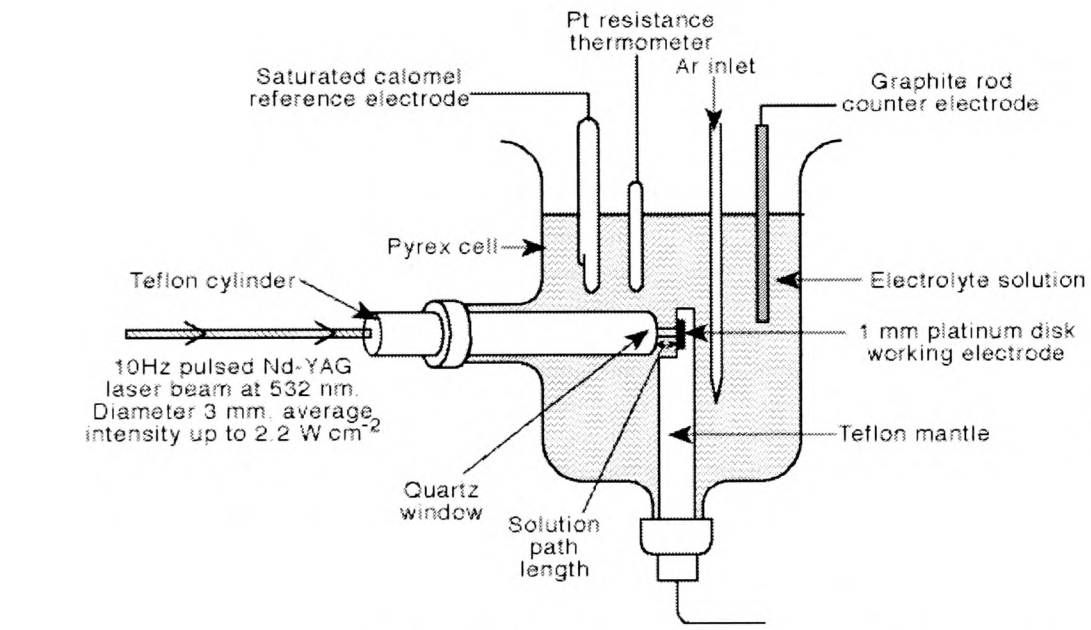

Figure 2.5 Modified LAV cell for coloured solutions.

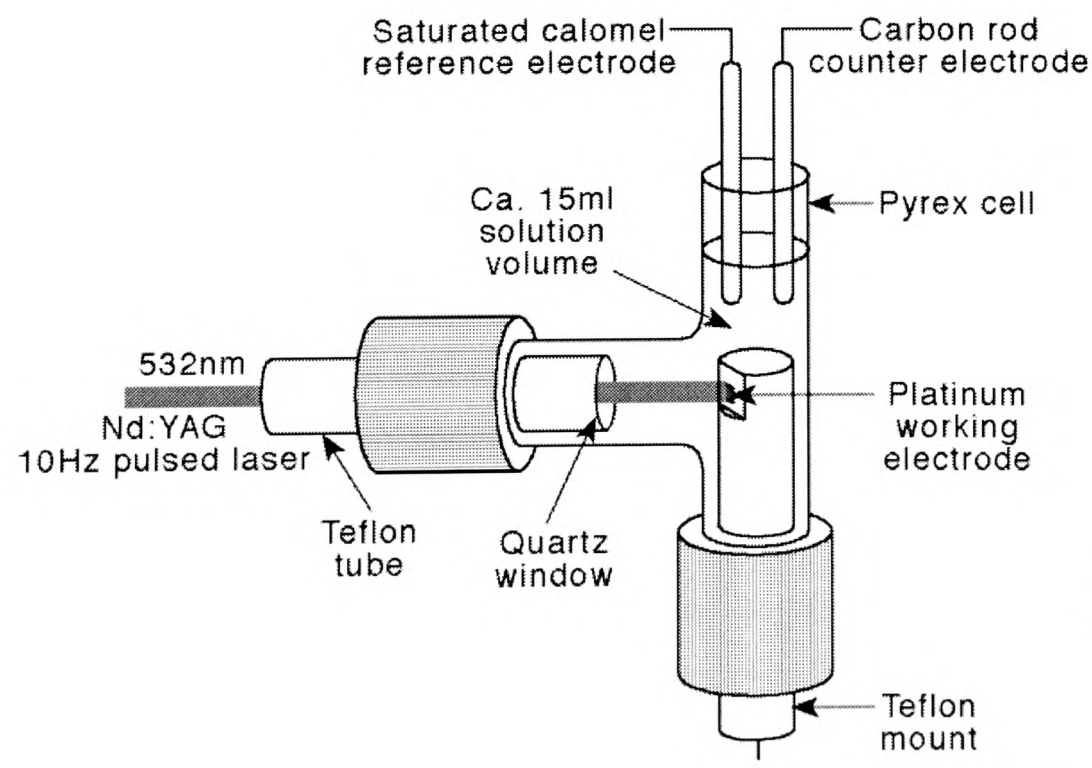

Figure 2.6 Small volume LAV cell.

Initial LAV experiments utilised a 2 mm x 2 mm platinum square electrode. In order to maximise electrode illumination however, most subsequent experiments utilised a 1 mm diameter platinum disc working electrode. Two such electrodes were prepared by the Mechanical Workshop in the PTCL, Oxford University; one for use in aqueous solutions was mounted in Perspex, and another for use in non-aqueous solutions which was mounted in soda glass. Additional laser activated voltammetry in nominally stationary solution was conducted in a small volume three-electrode cell as shown in Figure 2.6. The cell volume was approximately 15 cm^3.

The bulk solution temperature in all LAV experiments was measured using a platinum resistance thermometer and was 20 ± 2°C in all cases. The temperature during individual runs was found to increase by less than 0.2°C demonstrating a minimal overall bulk heating effect by the laser. Voltammetry under flow conditions utilised optically transparent channel flow cells as detailed in section 2.6.1.

The light source employed was a GCR 130 or subsequently a LAB 130 Q-switched Nd-YAG laser (Spectra Physics Lasers Inc., CA, USA) operating in a frequency doubled mode at a wavelength of 532 nm and pulsed at 10 Hz. Lenses and optics housings were supplied by the Newport Corporation and mirrors obtained from Comar Instruments (Cambridge, UK). The beam was reduced to 3.0 mm in diameter (except where stated) by passage through a fixed diameter aperture before being passed into the LAV cell. The laser power was determined with a Gentec ED-200LA detector head in conjunction with a Gentec SUN Series EM-1 Energy Meter (Gentec, CA, USA). The power recorded by the meter was a time average reading and not the power associated with the individual laser pulses which have a half-height width of ca. 8 ns and a pulse repetition rate of 10 Hz. Using the fixed diameter of the beam it was then possible to calculate laser intensities averaged over the full electrode area. Good homogeneity of illumination was achieved for the 1 mm diameter

electrode but in ablation mode some 'ringing' of the beam output due to Fresnel diffraction through the fixed aperture of the laser cavity was evident on the larger electrodes. Typical experiments were performed in the range 0.1 - 0.8 W cm^{-2}. High power ablation experiments employed intensities of up to 2 W cm^{-2}. Experiments to verify the area dependence of the laser activated voltammetry also used 2 mm, 3 mm and 4 mm square platinum electrodes and a larger laser beam diameter (ca. 5 mm with an approximate but fixed intensity of 150 mW cm^{-2}).

2.3.2 SONO-LASER ACTIVATED VOLTAMMETRY ARRANGEMENT

Sono-laser activated voltammetry (Sono-LAV) experiments utilised a 13 mm diameter ultrasonic horn, as discussed in 2.2.1, introduced from the top of the cell shown in Figure 2.4 in a 'side-on' arrangement [9] as shown in Figure 2.7. The distance, d, from the horn tip to the centre of the electrode was 16 ± 1 mm. The two platinum electrodes employed were 2 x 2 mm and 3 x 3 mm squares.

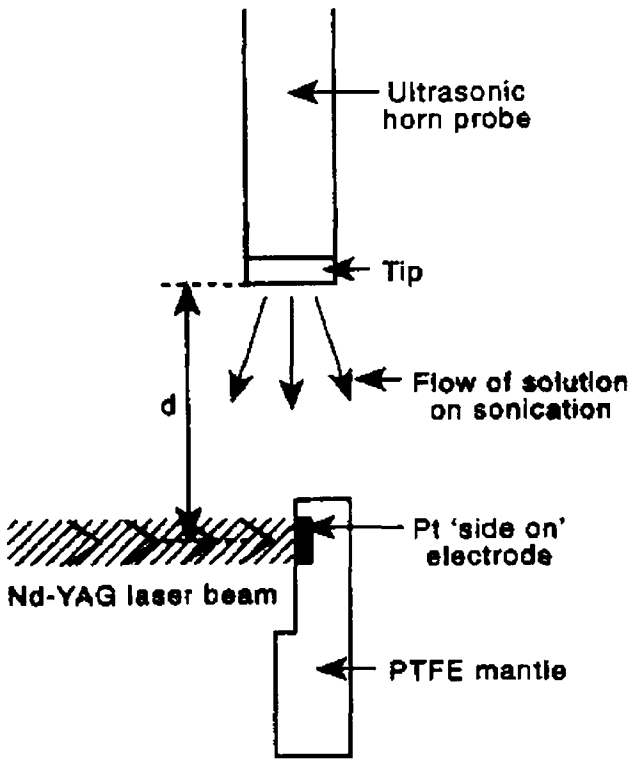

Figure 2.7 'Side-on' arrangement.

2.4 THERMALLY ACTIVATED VOLTAMMETRY

The temperature dependence of the ferrocene / ferrocenium, ferri/ocyanide and $Ru(NH_3)_6^{3+}$ / $Ru(NH_3)_6^{2+}$ redox couples was determined as follows. 1 mM solutions were made up in acetonitrile / 0.1 M TBAH for the first system and aqueous 1 M KCl for the other two. The divided cell shown in Figure 2.8 was used employing a 25 μm diameter platinum disc as the working electrode in tandem with a combined reference and counter saturated calomel electrode connected via a salt bridge. The SCE was kept at a fixed temperature which was in the range 18 ± 2°C for all experiments. The temperature of the platinum

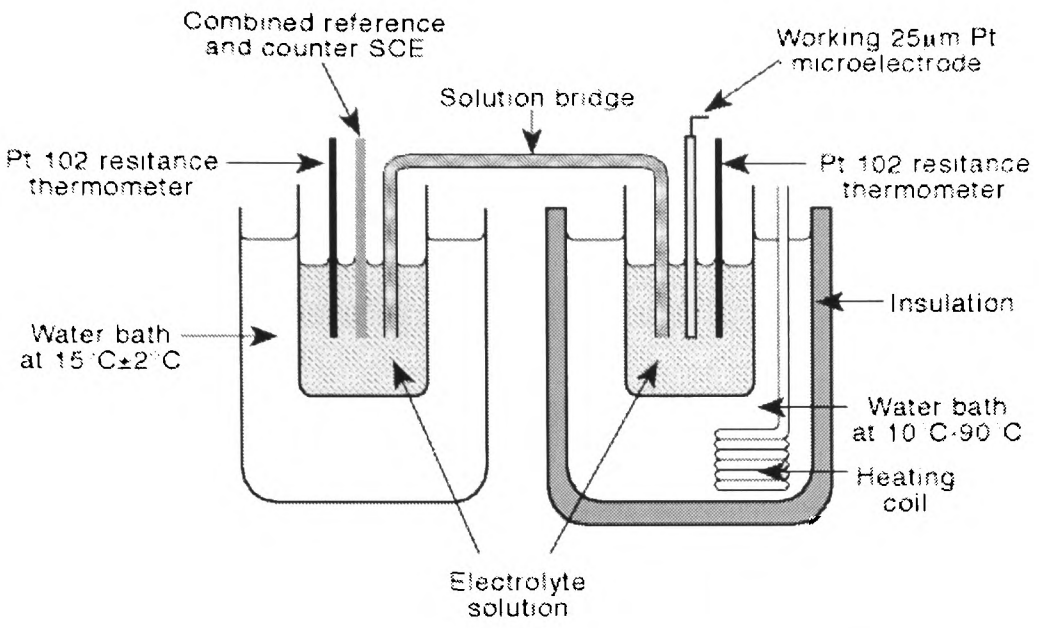

Figure 2.8 Thermally activated voltammetry apparatus.

electrode was raised in ca. 10°C steps by means of a small heating coil in a surrounding water bath. After each temperature rise the system was allowed to equilibrate before a cyclic voltammogram was measured at 10 mV s^{-1}. The limiting currents and half-wave potentials were measured in the range 10 - 90°C. The dependences of the half-wave potential on temperature for the three systems above are tabulated in Chapter 10.

2.5 MICROWAVE ACTIVATED VOLTAMMETRY

2.5.1 CELL DESIGN

The two electrode cell used in the microwave activated experiments is shown in Figure 2.9. The cell volume was approximately 5 cm^3. In this cell a platinum microelectrode was used (made by Dr. B. A. Coles of the PTCL, Oxford University), and positioned at a specific height in the cell, the ideal height being found by maximising the current response. In addition, the cell was filled with a solution to a specific height, the ideal solution height also being found by

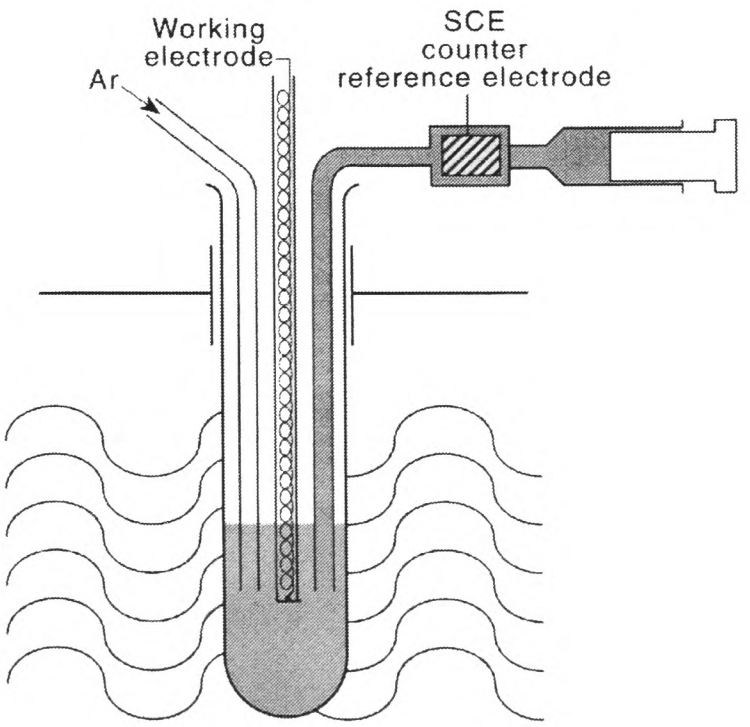

Figure 2.9 Schematic representation of the electrochemical cell used in the microwave oven.

experimentation. The reference electrode was a saturated calomel electrode (SCE) in all experiments and, due to the use of a microelectrode and the small currents involved this also acted as the counter electrode. In order to prevent bulk heating of the solution and reduce thermal convection within the cell the solution in the cell was connected to a pump system, which slowly and continually pumped solution around the system from a reservoir kept at room temperature. The inlet and outlet tubes were positioned near the top of the solution in the cell, again to reduce convection and movement of solution in the region of the electrode surface.

2.5.2 MICROWAVE OVEN MODIFICATION

An 800 W, 2.45 GHz domestic multi-mode microwave oven was modified by the Electronics Workshop in the PTCL, Oxford University to supply constant power or pulsed microwave radiation of variable power and to allow an electrochemical cell to be inserted into a high intensity region. To apply intense microwave radiation to the working electrode in a reproducible manner the intensity distribution in a Panasonic NN-3456 multi-mode microwave oven fitted with a water load was mapped. A hole through the cavity wall extended by a 14.7 mm inner diameter brass tube, 50 mm long, which acted as a waveguide below 'cut off', allowed a 1.41 cm diameter electrochemical cell to be inserted into a high intensity region. A special working electrode design with a range of Pt disc electrodes of 25, 50 and 1000 μm diameter sealed in glass was used to prevent both sparking and radiation escaping through the inlet. The lead-out from the microelectrode was in the form of a helix made by winding 0.19 mm diameter platinum wire on a 0.46 mm diameter mandrel with 28 turns per cm. A test with a radiation meter (Apollo XI microwave monitor, Apollo Ltd.) confirmed that this design acted as a filter to stop microwave radiation from being conducted out of the cavity. A capillary inlet and outlet connected to a peristaltic pump served to quickly renew the solution phase. The microwave power level of the modified oven was

continuously adjustable. The energy absorbed by the solution in the cell was governed by the dielectric loss of the sample and was considerably smaller than the microwave radiation actually present. To calibrate the power of the microwave, temperature readings were taken at set time intervals during microwave exposure for each microwave setting. The temperature rise between each reading was then plotted against exposure time and the gradient calculated for a tangent taken through zero. The latter was converted to the power in watts by multiplying by the heat capacity and mass of the whole cell.

2.6 CHANNEL FLOW ELECTRODES

2.6.1 CELL CONSTRUCTION AND CALIBRATION

The channel electrode employed, as described in section 1.2.1, consisted of a platinum working electrode (disc or square) embedded in a Teflon base of width 6 mm and length 80 mm. The precise dimensions of the platinum electrode was determined to an accuracy of ± 0.01 mm by use of a travelling microscope. The channel unit and the cover plate were made from optical grade fused synthetic quartz and were joined together using a low-melting inert wax ('Wax-Away', Adelaide Grey Ltd.).

The exact cell height of each freshly assembled cell was calibrated using an acetonitrile solution of a known concentration of ferrocene, in the presence of a supporting electrolyte, typically 0.1 M TBAH. Ferrocene has a known diffusion coefficient [10] of 2.3×10^{-5} $cm^2 s^{-1}$ in this medium and undergoes a clean, simple one-electron oxidation with no complicating homogeneous kinetics. The cell height was calculated from the slope of a *Levich plot* (Equation (1.17)) of limiting current for this system against (Volume flow rate)$^{1/3}$.

2.6.2 LASER ACTIVATED CHANNEL FLOW VOLTAMMETRY

A gravity fed flow system was used as shown in Figure 2.10. The solution flowed through Pyrex tubing of internal diameter 2 mm from a 250 cm^3 reservoir toward the channel.

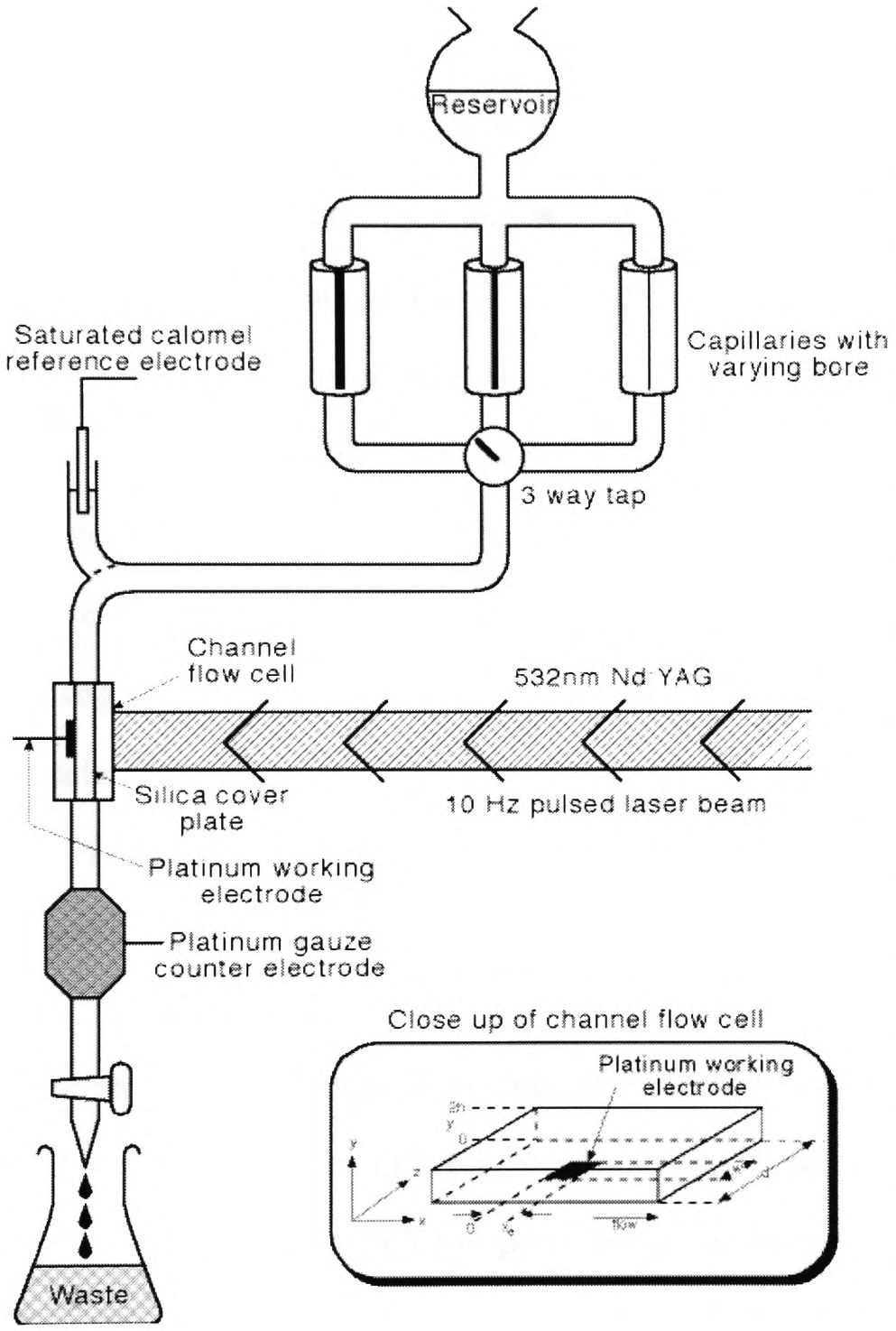

Figure 2.10 The gravity-fed channel flow system.

The cell was connected to the Pyrex tubing with small lengths of silicone tubing. A lead-out wire from the back of the Teflon base formed the connection to the potentiostat. The platinum gauze counter electrode was situated downstream of the cell and the saturated calomel electrode (SCE) reference electrode was in a compartment out of the main flow but still in electrical contact with the solution. The downstream section of the system consisted of PVC tubing of internal diameter 3 mm. This enabled viewing of the solution, especially the presence of gas bubbles, in almost all sections of the flow system. Any gas bubbles were carefully removed before all experiments as they hindered flow giving rise to regions of high electrical resistance. The flow rate was controlled by passing solution through one of four capillaries of different bore and by adjusting the vertical height of the outlet tip relative to the height of the reservoir. Flow rates in the range 10^{-4} to 0.4 $cm^3\ s^{-1}$ could be obtained with this set-up. The

Nd:YAG laser beam was carefully positioned so that the whole of the working electrode was illuminated.

2.7 ROTATING DISC ELECTRODE

The rotating disc electrode (RDE) was employed for the experimental determination of diffusion coefficients. The 6.75 mm diameter platinum working electrode was identical to the stationary electrodes described above except that it had a brass thread to allow connection to the motor for rotation. The electrode was rotated at different speeds (0-30 Hz) about the vertical axis. The temperature was monitored to ensure that there was no change in solution viscosity, which would influence the magnitude of the diffusion coefficient. The voltage was scanned until a limiting current was achieved. This was repeated for different angular frequencies. Using Equation 1.21 by plotting the limiting current, I_{Lim}, vs. the square root of the angular frequency, $\omega^{1/2}$, the diffusion coefficient, D, of the electroactive species could be calculated from the gradient of the *Levich plot* [11] given that all other values in the equation were known. If the electrode process was not limited by diffusion through the bulk solution then this was apparent from a zero gradient in the Levich plot.

The diffusion coefficients for decamethyl ferrocene, *p*-chloranil and tris(*p*-bromophenyl)amine were calculated as above from the rotation speed dependence of the transport limited current [12] for their one-electron transfers at half-wave potentials of ca. -0.12, +0.02 and +1.06 V (vs. SCE) respectively at a rotating disc electrode. The values are quoted in the next chapter and employed in the characterisation of mass transport for both sono-electrochemical and laser activated electrochemical geometries. The experiments used 5 mM solutions in acetonitrile / 0.1 M TBAH and employed a 6.75 mm diameter platinum electrode.

2.8 CONTROL ELECTRONICS

A computer controlled PGSTAT20 Autolab potentiostat (Eco-Chemie, Utrecht, Netherlands) was employed to control the potential applied at the working electrode during most sono, LAV, thermal and microwave activated experiments. The need for

bipotentiostatic [13] control of the titanium ultrasonic horn itself during sono-experiments was eliminated by insulating the transducer from the probe with a thin Teflon disc and connecting the two with a screw thread machined from Delrin instead of titanium. This prevented any unwanted electrolysis of the solution at the submerged section of the horn.

During the temperature calibration and rotating disc experiments, an Oxford Electrodes potentiostat and a linear potential scan generator were used to obtain the voltammetric measurements and the current-voltage scans were recorded on a Lloyd Instruments PL3 chart recorder.

2.9 CHEMICALS USED

NAME	FORMULA	SOURCE	GRADE / PURITY
Acetonitrile	CH_3CN	Fisher Scientific[a]	Dried, distilled
Argon	Ar	BOC[b]	99.99+%
Ascorbic acid	$C_6H_8O_6$	BDH[a]	99.7+%
Boric acid	$B(OH)_3$	Aldrich	99.5+%
Bovine albumin (fraction V)	-	Sigma[c]	96+%
p-Bromonitrobenzene	$C_6H_4NO_2Br$	Aldrich[d]	99+%
p-Chloranil	$C_6Cl_4O_2$	Aldrich	97+%
Copper (II) nitrate	$Cu(NO_3)_2.3H_2O$	Aldrich, BDH	99.5+%
Copper (II) sulphate	$CuSO_4.5H_2O$	Aldrich	99.5+%
Decamethyl ferrocene	$C_{20}H_{30}Fe$	Fluka[e]	99+%
Ferrocene	$C_{10}H_{10}Fe$	Aldrich	99+%
Fibrinogen (fraction I, type IV from bovine plasma)	-	Sigma	95+%
α-Glucose	$C_6H_{12}O_6$	BDH	99.5+%
Gold	Au	Aldrich	99.8+%
Hydrochloric acid	HCl	Aldrich, BDH	1.0 M
Iodine	I_2	BDH	99.9+%
Lead (II) nitrate (volumetric standard)	$Pb(NO_3)_2$	Aldrich	1 ml = 0.1 mg Pb
Mercury	Hg	Aldrich	99.9+%

NAME	FORMULA	SOURCE	GRADE / PURITY
Mercury (II) nitrate	$Hg(NO_3)_2$	Aldrich	98+%
Methyl viologen dichloride	$C_{12}H_{14}N_2^{2+}.2Cl^-.2H_2O$	Aldrich	98+%
Methylene blue	$C_{16}H_{18}N_3S^+.Cl^-.3H_2O$	Aldrich	95+%
Methylene green	$C_{16}H_{17}N_4O_2S^+.Cl^-$	Fluka	95+%
Nitric acid	HNO_3	BDH, Aldrich	0.1 M
n-Octane	C_8H_{18}	Aldrich	99.8+%
Platinum (foil, wire)	Pt	Aldrich	99.8+%
Potassium chloride	KCl	Aldrich	99+%
Potassium ferricyanide	$K_3[Fe(CN)_6]$	BDH, Aldrich	99+%
Potassium ferrocyanide	$K_4[Fe(CN)_6].3H_2O$	BDH	99+%
Potassium hydroxide	KOH	Aldrich	99+%
Potassium iodide	KI	BDH	99.8+%
Potassium nitrate	KNO_3	Aldrich	99+%
Potassium phosphate	KH_2PO_4	Aldrich	99.9+%
Ruthenium hexaammine trichloride	$[Ru(NH_3)_6]Cl_3$	Aldrich	95+%
Silver nitrate	$AgNO_3$	Aldrich	99+%
Sodium sulphate	Na_2SO_4	Aldrich	99+%
Sodium citrate	$Na_3C_6H_5O_7.2H_2O$	Aldrich	99+%
Sulphuric acid	H_2SO_4	BDH, Aldrich	1.0 M
Tetrabutylammonium hexafluorophosphate	$(C_4H_9)_4N.PF_6$	Fluka	99.8+%
Tetrabutylammonium perchlorate	$(C_4H_9)_4N.ClO_4$	Fluka	99.8+%
Tetrahexylphenylenediamine	$C_6H_4N_2(C_6H_{13})_4$	Prof. S. G. Davies[e]	97+%
Toluene	C_7H_8	Aldrich	99+%
Toluidine blue	$(C_{15}H_{16}N_3S)_2.ZnCl_2$	Fluka	95+%
Tris(p-bromophenyl)amine	$N(C_6H_4Br)_3$	Aldrich	97+%

[a] Loughborough, [b] Guildford, Surrey, [c] Poole, Dorset, [d] Gillingham, Dorset, [e] Dyson Perrins Laboratory, Oxford University.

2.10 PREPARATION OF SOLUTIONS

All aqueous solutions were prepared with Elgastat (High Wycombe, Bucks) UHQ grade water of resistivity 18 MΩ and potassium chloride, potassium nitrate or sulphuric acid acted as the supporting electrolyte. All masses were measured to an accuracy of 0.1 mg with

a Unimatic CL41 balance. For experiments where dissolved oxygen (which is electrochemically active and readily combines with any radical intermediates) was undesirable, the solution was thoroughly purged with pre-dried argon for up to half an hour before experimentation. Aqueous buffer solutions used in the range pH 6.0 - 7.5 contained between 0.1 and 0.2 M KH_2PO_4, with KOH being added as required to adjust to the desired value. These are termed 'phosphate buffer solutions' (PBS). Other buffer systems used for pH regions of around 4 and 9 were citric acid and boric acid respectively.

Acetonitrile (dried and distilled) was also used as a solvent, with 0.1 M tetrabutylammonium hexafluorophosphate (TBAH) or tetrabutylammonium perchlorate (TBAP) as the supporting electrolyte. Additionally dimethylformamide (DMF), toluene, dichloromethane and n-octane were employed in experiments.

2.11 ATOMIC FORCE MICROSCOPY (AFM)

Atomic force microscopy surface imaging of a platinum disc before and after the ultrasonic, laser and electrochemical procedures described later was performed on a Topometrix TMX 2000 Discoverer system in contact mode (typically 3 Hz scan rate) with probe type 1520-00 (Topometrix, CA, USA). Pyramidal silicon nitride tips (Topometrix AFM E-Chem probes 1750) were employed. The microscope cantilever deflection was measured by means of laser beam detection. This was accomplished by directing a laser beam (wavelength 670 nm and power 3 mW) onto the back of the cantilever, which was then reflected from the surface. The reflected beam was trained on a position sensitive detector (PSD) which consisted of two photoactive segments. Movement of the cantilever shifted the path of the reflected beam, hence the PSD could detect tiny movements of the foil. The size of the scans ranged from 5 x 5 μm to 50 x 50 μm. The Topometrix software employed was also used for calculation of surface roughness by comparing how much larger the actual measured surface area was than the projected area (e.g. a 5 x 5 μm scan = 25 μm^2).

2.12 UV-VISIBLE SPECTROSCOPY

Most of the ultraviolet-visible spectroscopy employed in this thesis was carried out on a Unicam UV2 spectrometer with a quartz cuvette of path length 0.1 or 1 cm. Additonally, a Perkin-Elmer Lambda-5 ultraviolet-visible spectrometer was used to obtain the absorption spectra of methylene green in toluene, the leuco base of methylene green in octane and iodine in dichloromethane, also in a standard quartz cuvette of 1 cm path length.

2.13 COMPUTING

Computer programs for the modelling of iodide oxidation in Chapter 11 were written by Dr. Qiu Fulian of the PTCL, Oxford University using FORTRAN 77 and executed on a Silicon Graphics workstation.

2.14 CHAPTER 2: REFERENCES

[1] C.-W. Lee, R. G. Compton, J. C. Eklund, D. N. Waller, *Ultrasonics Sonochemistry* **1995**, 2, S59.

[2] R. G. Compton, J. C. Eklund, F. Marken, *Electroanalysis* **1997**, *7*, 509.

[3] T. J. Mason, J. P. Lorimer, *Practical Sonochemistry, User's Guide to Applications in Chemistry and Chemical Engineering*, Ellis Horwood, Chichester, **1989**.

[4] T. J. Mason, *Sonochemistry: the Uses of Ultrasound in Chemistry*, Royal Society of Chemistry Publications, London, **1990**.

[5] T. J. Mason, J. P. Lorimer, *Sonochemistry: Theory, Applications and Uses of Ultrasound in Chemistry*, Ellis Horwood, Chichester, **1988**.

[6] H. A. O. Hill, Y. Nakagawa, F. Marken, R. G. Compton, *J. Phys. Chem.* **1996**, *100*, 17395.

[7] M. A. Margulis, A. N. Mal'tsev, *Russ. J. Phys. Chem.* **1969**, *43*, 592.

[8] T. J. Mason, J. P. Lorimer, D. M. Bates, *Ultrasonics* **1992**, *30*, 140.

[9] J. C. Eklund, F. Marken, D. N. Waller, R. G. Compton, *Electrochim. Acta* **1996**, *41*, 1541.

[10] P. Sharp, *Electrochimica. Acta* **1983**, *28*, 301.

[11] P. H. Rieger, *Electrochemistry*, Prentice-Hall, New York, **1987**.

[12] W. J. Albery, *Electrode Kinetics*, OUP, Oxford, **1975**.

[13] F. Marken, R. G. Compton, *Ultrasonics Sonochemistry* **1996**, 2, S131.

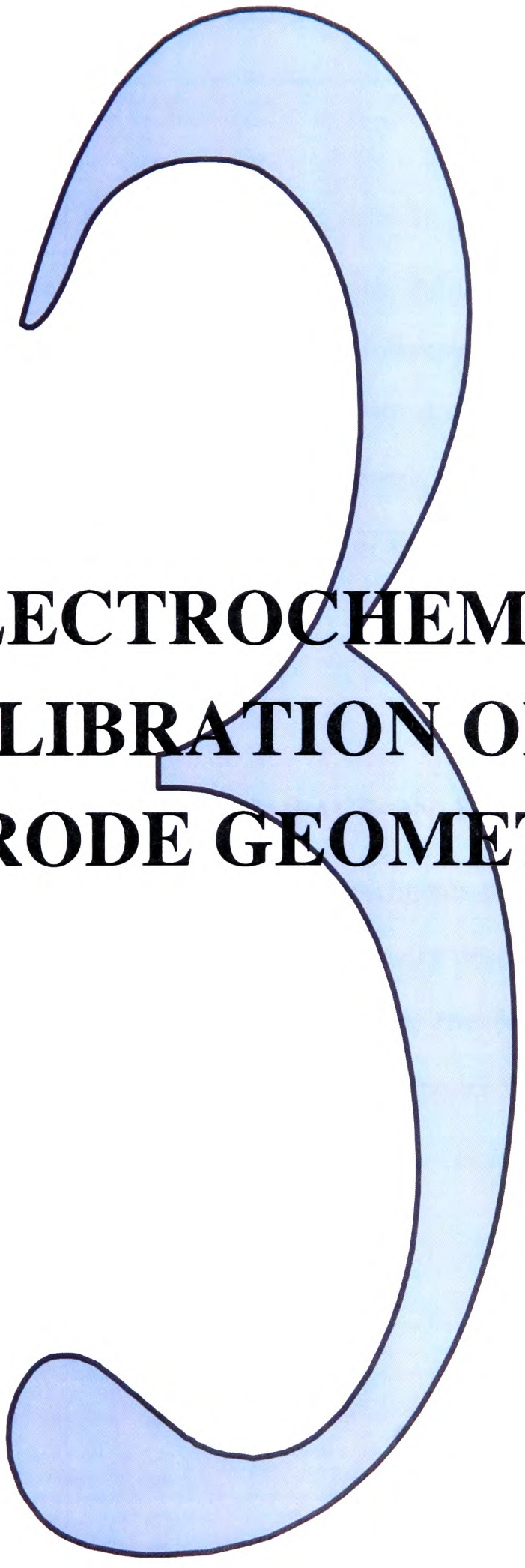

SONO-ELECTROCHEMISTRY: CALIBRATION OF ELECTRODE GEOMETRIES

CHAPTER 3: SONO-ELECTROCHEMISTRY: CALIBRATION OF ELECTRODE GEOMETRIES

3.1 CONTENTS

In this chapter, the work of Compton *et al.* [1] concerning the characterisation of mass transport within sono-electrochemical cells is built upon and expanded to cover the four different electrode geometries outlined in section 1.6.1. Theory is developed for transport models applicable to an electroactive species close to an electrode surface under the different conditions of insonation. The characterisation and optimisation of ultrasonically induced mass transport is essential to the efficiency and repeatability of the electrosynthetic and analytical procedures described in the following chapters.

3.2 BACKGROUND

3.2.1 MASS TRANSPORT TO INSONATED 'FACE-ON' ELECTRODES

By far the majority of sono-electrochemical experiments employing ultrasonic horn transducers have been performed using the 'face-on' geometry described in section 1.6.1, in which, at least under some conditions, a uniformly accessible electrode is maintained chiefly by *acoustic streaming* [2,3]. The Nernst diffusion layer model for calculating transport limiting currents arising from the discharge of an electroactive species X at a uniformly accessible electrode predicts that

$$I_{lim} = \frac{nFAD_X[X]}{\delta_X^*} \tag{3.1}$$

where I_{lim} is the limiting current, n is the number of electrons transferred, F is the Faraday constant, A is the electrode area and D_X, [X] and δ_X^* are the diffusion coefficient, concentration and limiting diffusion layer thickness at a given ultrasonic intensity of species X respectively. Aqueous calibration of the 'face-on' geometry for a 13 mm diameter ultrasonic horn to verify the model proposed in Equation 3.1 was performed in a similar

fashion to that previously reported for a 3 mm ultrasonic horn tip [4] and is further elaborated in section 3.4.1 below. Characterisation in acetonitrile solution has been performed previously [1].

3.2.2 MASS TRANSPORT TO INSONATED 'SIDE-ON' ELECTRODES

The mass transport properties of an electrode arranged in a 'side-on' geometry in an ultrasonic field, as illustrated in Figure 3.1, have been demonstrated to be approximated by those of a flow over a plate [5]. The expression relating the transport limited current, I_{lim}, to various experimental parameters which are shown in Figure 3.2 is as follows:

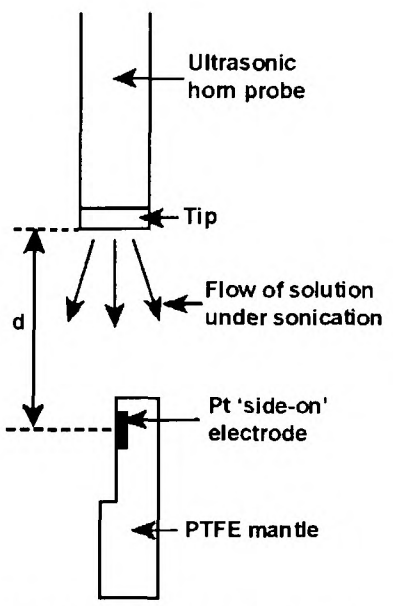

Figure 3.1 'Side-on' geometry

$$I_{lim} = \frac{0.34FD^{2/3}U^{1/2}w[X]}{\nu^{1/6}} \int_{h_0}^{h_0+xe} x^{-1/2}\left[1-\left(\frac{h_0}{x}\right)^{3/4}\right]^{-1/3} dx \qquad (3.2)$$

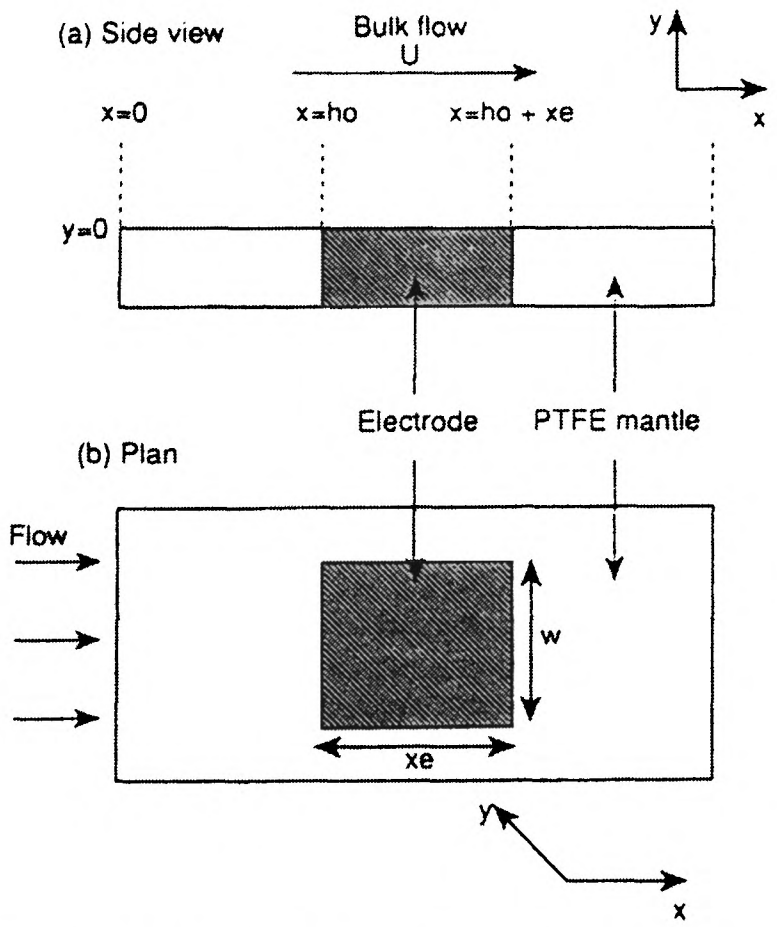

Figure 3.2 'Side-on' flow experimental parameters.

In this equation, D, [X], the kinematic viscosity, ν, an ultrasound power dependent bulk flow constant, U and the electrode geometry parameters of width, w, length xe and distance from the edge of the plate, h_0, all influence the magnitude of the resulting current. This approximate model was found to work well in spite of the fact that much of the flow was highly turbulent.

3.2.3 MASS TRANSPORT TO SONOTRODES

In the 'sonotrode' geometry (shown in Figure 1.17), the tip of the ultrasonic horn itself is used as the electrode [6,7] or is modified such that an electrode is physically introduced into the tip of the horn [8], as shown in Figure 3.3. This experimental set-up, although in one sense the limiting case of the 'face-on' geometry, has many different characteristics. As well as cavitational cleaning the vigorous 'shaking' of the horn can enhance the detachment of bulk electrodeposited surface species, as will be further investigated in the next chapter. Effective diffusion layer sizes of less than 1 μm, as calculated by using Equation 3.1, can be obtained at a sonotrode even for relatively low ultrasound intensities. Hence the high level of mass transport allows very fast electrode reactions to be easily perturbed. The mass transport in aqueous solution has been briefly reported previously [2]. Optimisation of the sonotrode design throughout the course of the project revealed that both the electrode lifetime and the transmission of ultrasound into the solution could be increased by both incorporating silica into the Araldite to make it harder and by shrinking the aperture of the hole in which the electrode was set [9].

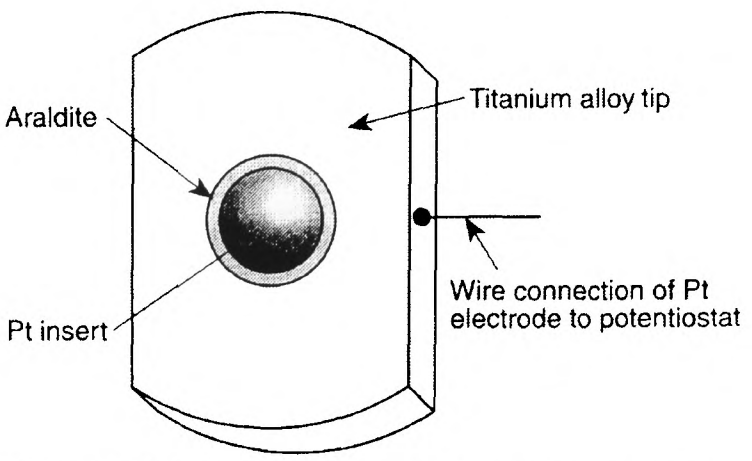

Figure 3.3 Schematic of a platinum sonotrode.

3.2.4 MASS TRANSPORT TO 'SIDE-ON' SONOTRODES

The incorporation of an electrode into the side of an ultrasonic horn transducer tip is illustrated in Figure 3.4. Unlike the 'side-on' geometry where ultrasound causes a flow of bulk solution past the electrode, the 'side-on sonotrode' geometry (also shown in Figure 1.17) is much more akin to a high speed vibrating electrode. Work performed by Atobe *et al.* investigated the differing

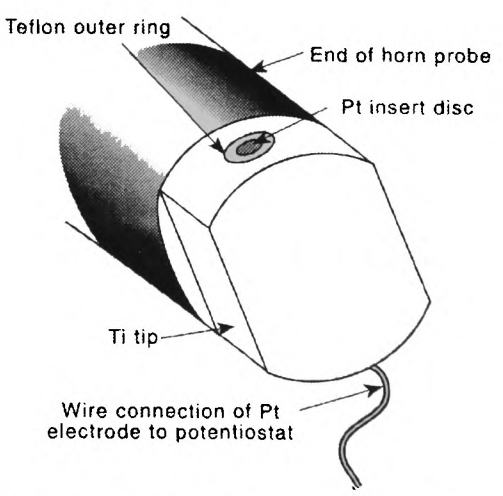

Figure 3.4 Schematic of a platinum 'side-on sonotrode'.

levels of mass transport at the nodes and antinodes of a 20 kHz horn also found a substantial increase in mass transport [10]. Voltammetry using 'side-on sonotrodes' is described later in this chapter in section 3.4.3.

3.3 EXPERIMENTAL

The well characterised [11] and thermostatted (25 ± 2°C) sono-electrochemical cell employed in 'face-on' and 'side-on' experiments is shown in Figure 2.1. The cell volume is ca. 250 cm^3. The ultrasonic immersion horn used in this chapter had a titanium alloy tipped horn probe of diameter 13mm, extended by 127 mm, and operated at 20 kHz. The ultrasonic intensity was calibrated calorimetrically according to the procedure of Margulis *et al.* and Mason *et al.* [12,13] over the range of 3 - 60 W cm^{-2}, as detailed in section 2.2.2.

The electroactive species employed in the calibration of diffusion layer thicknesses for the 'face-on' geometry are shown in Table 3.1 along with their aqueous diffusion coefficients (D) at 25°C.

Species	Electrode Reaction	D x 10^5 / cm^2 s^{-1}	Reference
$K_4[Fe(CN)_6]$	1 e^- oxidation	0.65 ± 0.01	[14]
$K_3[Fe(CN)_6]$	1 e^- reduction	0.763 ± 0.005	[14]
$CuSO_4.5H_2O$	2 e^- reduction	0.76 ± 0.02	[11]
$Hg(NO_3)_2$	2 e^- reduction	0.83 ± 0.01	[15]
$[Ru(NH_3)_6]Cl_3$	1 e^- reduction	0.91 ± 0.02	[16]
$AgNO_3$	1 e^- reduction	1.60 ± 0.05	[14]
$MVCl_2$[a]	1 e^- reduction	1.70 ± 0.05	see text
HCl	1 e^- reduction	7.42 ± 0.22	[14]

Table 3.1 Aqueous diffusion coefficients for the chemicals used in calibration of the Nernst model for the 'face-on' sono-electrochemical cell. [a] Methyl viologen dichloride hydrate.

The diffusion coefficient for methyl viologen dichloride hydrate, $MVCl_2$, was calculated from the rotation speed dependence of the transport limited current [17] for its one-electron reduction at ca. -0.07 V (vs. SCE) at a rotating disc electrode as outlined in section 2.7. This

experiment used a 1 mM solution of $MVCl_2$ in 0.05 M Na_2SO_4 and employed a 6.75 mm diameter platinum electrode. For mass transport calibration experiments with the other species, the background electrolyte used was either 0.1 M KCl in the case of the ferrocyanide, ferricyanide, hexaammineruthenium (III) chloride and HCl or 0.1 M KNO_3 in the case of the copper (II), silver (I) and mercury (II) ions.

The working electrodes used were 0.8, 1, 1.3, 2, 3, 4 and 7 mm diameter platinum discs of various design and 1 and 3 mm diameter glassy carbon discs. In 'face-on' and 'side-on' experiments, the working electrode was placed opposite a sonic horn at various horn-to-electrode separations for the calibration. The arrangement was calibrated by observing the effects of changing electrode area, horn-to-electrode distance, diffusion coefficient and concentration of electroactive species in accordance with Equation (3.1). For 'sonotrode' experiments of both types, a slightly different cell design was employed and is shown in Figure 3.5. Typically, the horn tip containing the electrode was submersed to a depth of ca. 2.5 cm, as this value gave the lowest signal noise due to acoustic reflections.

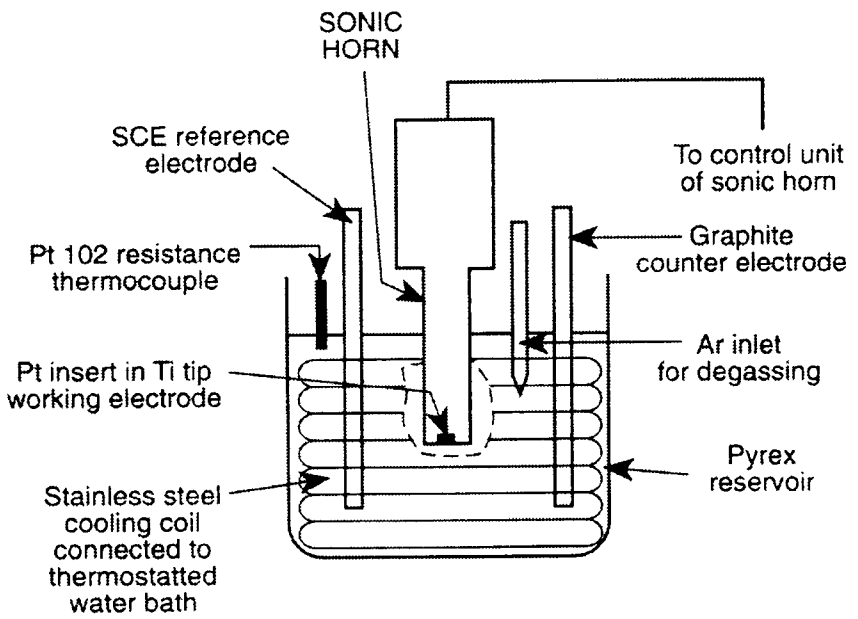

Figure 3.5 Apparatus for 'sonotrode' experiments.

3.4 GEOMETRY CALIBRATION

3.4.1 'FACE-ON' GEOMETRY

The mass transport to the insonated 'face-on' electrode was characterised as follows. The mass transport limited currents due to oxidation or reduction of the various electroactive species listed in Table 3.1 under insonation were measured for a range of different parameters. These parameters were substrate concentration, electrode area, diffusion coefficient, horn-to-electrode distance and ultrasonic intensity. Typical voltammograms are

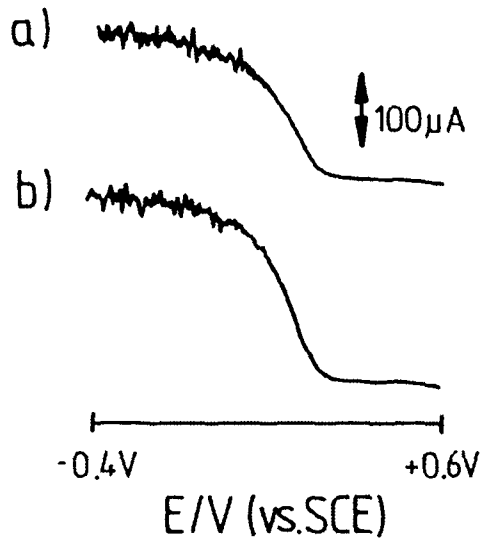

Figure 3.6 LSVs at 20 mV s^{-1} showing the US limiting current for the reduction of $K_3[Fe(CN)_6]$ / 0.1 M KCl(aq) at a 4 mm diameter Pt disc. The horn-to-electrode separation was 30 mm and the ultrasonic intensity was a) 26 W cm^{-2} and b) 57 W cm^{-2}.

shown in Figure 3.6. The variation of sono-limiting current with area and concentration at fixed ultrasound intensity and horn-to-electrode distances is seen in Figures 3.7 and 3.8 respectively. Excellent linear dependence is observed in agreement with Equation (3.1). The effect of altering the horn-to-electrode distance at two different ultrasound intensities is seen in Figure 3.9 where the diffusion layer thicknesses were calculated from the limiting currents using Equation (3.1) and tend to approximately the same limit for different intensities as the horn-to-electrode separation approaches zero.

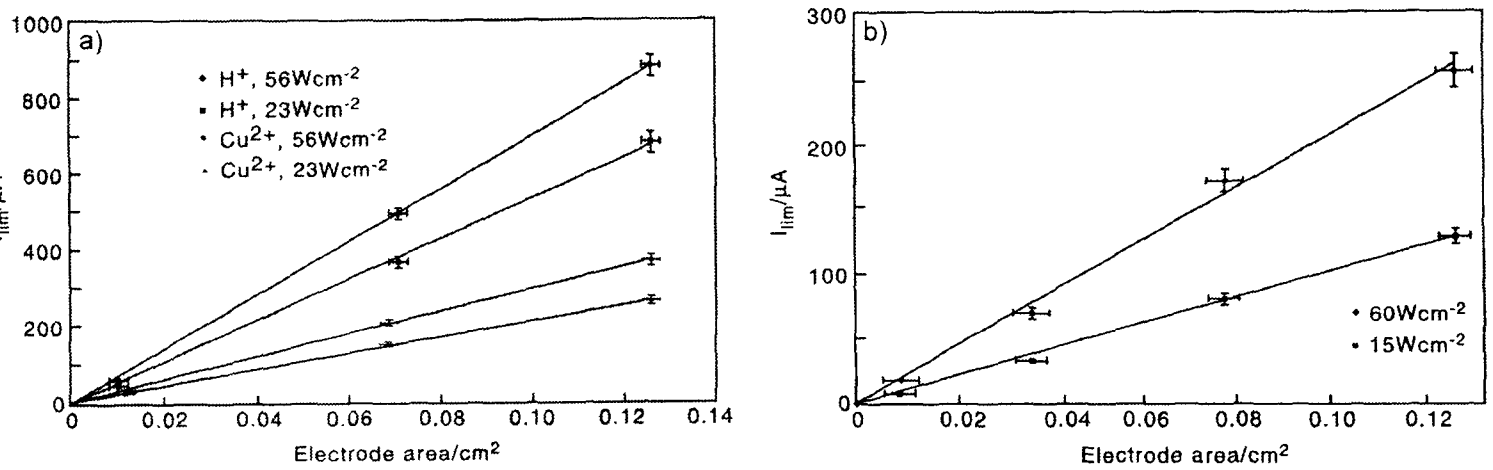

Figure 3.7 Variation in US limiting current with electrode area at two different US intensities for a) 1 mM H^+(aq) / 0.1 M KCl (◆, ■), 1 mM Cu^{2+}(aq) / 0.1 M KNO_3 (●, ▲) and b) 1 mM $[Fe(CN)_6]^{3-}$ (aq) / 0.1 M KCl. All data was measured at a horn-to-electrode distance of 35 mm.

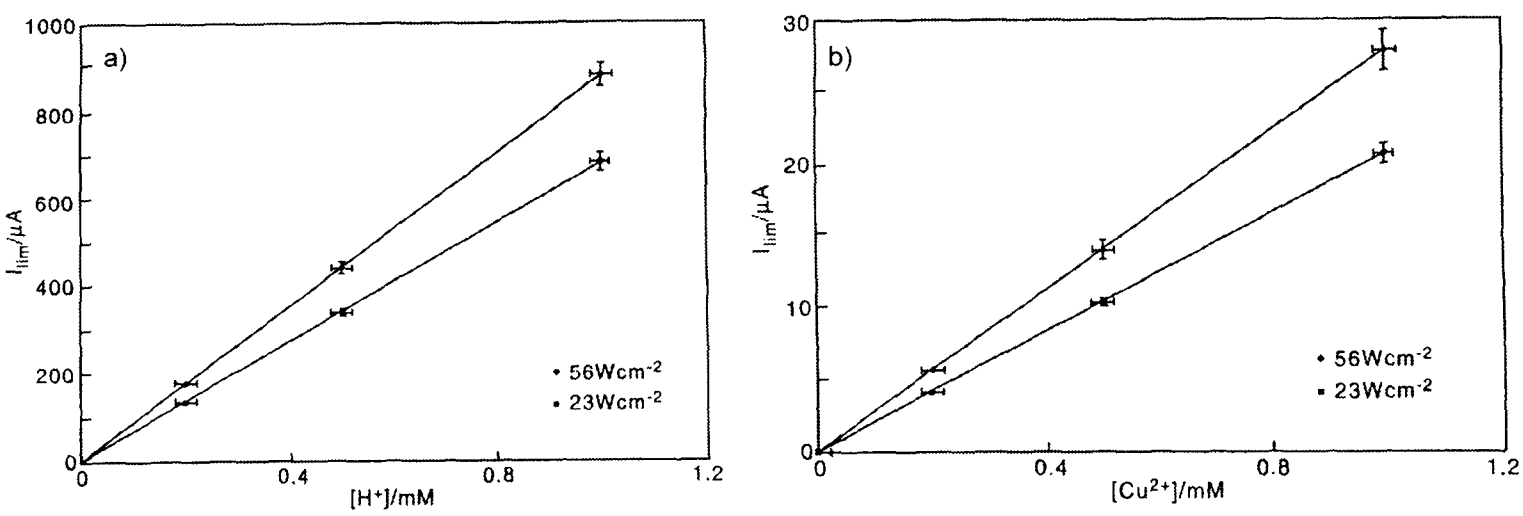

Figure 3.8 Variation in US limiting current with concentration of electroactive species at two different US intensities for a) H^+(aq) / 0.1 M KCl at a 4 mm Pt electrode and b) Cu^{2+}(aq) / 0.1 M KNO_3 at a 1 mm Pt electrode. All data were measured at a horn-to-electrode distance of 35 mm.

Next the dependence of the limiting current on diffusion coefficient for different electroactive species was analysed by normalising all the sono-limiting current data to that for a one electron transfer at a fixed concentration and electrode area using the demonstrated linear dependence upon these variables. A log-log plot of the resulting limiting currents against the diffusion coefficient shows the power to which D should be raised in Equation (3.1). The plots for two different ultrasound intensities (23 and 56 Wcm^{-2}) are seen in Figure 3.10 and have gradients of 0.666 ± 0.007 and 0.660 ± 0.009 respectively. Thus under the

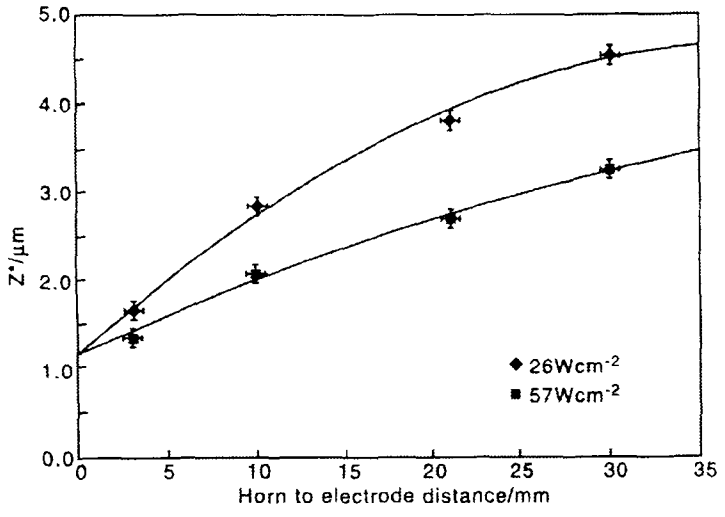

Figure 3.9 The variation in diffusion layer thickness as calculated from equation (1) with the horn to electrode separation for two different US intensities. The solution was 1 mM $K_3[Fe(CN)_6]$ / 0.1 M KCl(aq) and the working electrode a 4 mm diameter Pt disc.

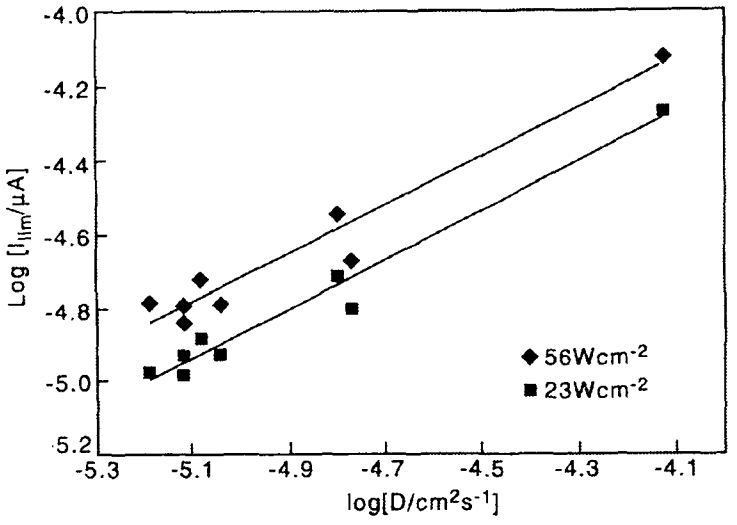

Figure 3.10 Log_{10} plot of sono-limiting current against diffusion coefficient at two different US intensities. All limiting currents were calculated for a 1 mM concentration, 0.985 mm^2 electrode area, a one electron transfer and a horn-to-electrode distance of 35 mm.

hydrodynamic conditions of the 'face-on' geometry and in aqueous media, I_{lim} was found to be proportional to $D^{2/3}$. This is as expected for hydrodynamic electrodes where $\delta^* \propto D^{1/3}$ and has been reported and discussed previously for insonated electrodes albeit with different cell geometries [4]. Accordingly, after suitable calibration, δ^*_X can be estimated for any species of interest provided the relevant diffusion coefficient data is available, as summarised in Table 3.1. This result extends the naïve uniformly accessible electrode model introduced in Equation 3.1 and implies a strong downward flow over the electrode induced by acoustic streaming.

Next, extensive measurements were undertaken to determine δ^* as a function of the horn-to-electrode separation, d, for different ultrasound powers. This was accomplished by measuring the limiting current of the sono-reduction of 1 mM potassium ferricyanide in

0.1 M potassium chloride supporting electrolyte. The diffusion coefficient of the ferricyanide anion is well-established [14] as 0.763 (± 0.005) x 10^{-5} cm^2 s^{-1} at 25°C and the reduction was found to have a half-wave potential, $E_{1/2}$, of -0.04 V (vs. SCE). Three platinum electrodes (1 mm, 2 mm and 4 mm diameter) and one glassy carbon electrode (1 mm diameter) were calibrated for four different horn-to-electrode separations, d, (5 mm, 10 mm, 22 mm and 32 mm) and for different intensity settings. The diffusion layer thickness, δ, was calculated using the relationship described by Equation (3.1). Illustrative results for the 1 mm diameter platinum electrode are shown in Table 3.2. Similar results were obtained for the other electrodes but as the size of the electrode increases so does the diffusion layer thickness. Note that the relationship in Equation (3.1) describes the average diffusion layer thickness.

Horn-to-electrode separation / mm		32	22	10	5	32	22	10	5
Amplitude / %	Intensity (± 0.5) / W cm^{-2}	I_{lim} (± 0.5) / μA				δ (± 0.1) / μm			
5	3	4	5	10	19	15.9	12.7	6.4	3.4
10	7	6	10	17	31	10.6	6.4	3.7	2.1
20	13	9	15	21	38	7.1	4.3	3.0	1.7
30	20	13	18	24	41	4.9	3.5	2.7	1.6
40	26	15	19	27	44	4.3	3.4	2.4	1.5
50	32	16	20	28	49	4.0	3.2	2.3	1.3
60	37	17	21	29	51	3.8	3.0	2.2	1.2
70	43	18	22	30	56	3.5	2.9	2.1	1.1
80	48	19	24	30	60	3.4	2.7	2.1	1.1
90	53	19	24	30	61	3.4	2.7	2.1	1.0
100	57	19	24	30	62	3.4	2.7	2.1	1.0

Table 3.2 Data for the electrochemical reduction of 1 mM $Fe(CN)_6^{3-}$ in 0.1M KCl under 'face-on' insonation at a 1 mm diameter Pt electrode.

Once the cell has been thoroughly calibrated for one electroactive species, the above theory can be employed to gain accurate estimates for the diffusion layer thickness, δ^*, at any ultrasonic intensity and horn-to-electrode distance for any species, X, provided its diffusion coefficient is known, by use of the following equation:

$$\delta_X^* = \delta_{Fe(III)}^* \left(\frac{D_X}{D_{Fe(III)}} \right)^{1/3} \qquad (3.3)$$

where $\delta^*_{Fe(III)}$ is the sono-limiting diffusion layer thickness for the ferricyanide anion as tabulated in Table 3.2.

3.4.2 'SONOTRODE' GEOMETRY

Calibration of 1, 1.3 and 2 mm diameter platinum sonotrodes by measuring limiting currents for the one-electron reduction of ferricyanide ions in 0.1 M KCl aqueous solution under insonation has shown that the limiting current is indeed proportional to concentration and electrode area [2]. Under the hydrodynamic conditions of the sonotrode geometry and in aqueous media, δ^* is also found to be proportional to $D^{1/3}$ so that $I_{lim} \propto D^{2/3}$ as is expected for hydrodynamic electrodes [18]. Accordingly, after suitable calibration, δ^*_X can be estimated according to Equation 3.3 for any species of interest provided the relevant diffusion coefficient data is available. During optimisation of the observed diffusion controlled limiting current with insonation intensity by calibration with ferricyanide it was found that diffusion layers of less than 1 μm were accessible. Also, lowering the intensity of the ultrasound from 6.9 W cm^{-2} to 3.5 W cm^{-2} yielded only a ca. 2% increase in δ^* (see Table 3.3). Hence the lower intensity was used in subsequent experiments in order to minimise the ultrasonic erosion of the sonotrode and prolong electrode life. The use of sonotrodes for electroanalysis is the subject of the next chapter.

Ultrasonic Intensity / W cm^{-2}	3.5	6.9
I_{lim} / μA	275	280
δ^* / μm	0.87	0.85

Table 3.3 Limiting sono-currents and diffusion layer thicknesses for the reduction of 4 mM $Fe[(CN)_6]^{3-}$ in 0.1 M KCl(aq) using a 2 mm Pt sonotrode. δ* was calculated from the Nernst model in Equation (3.1).

3.4.3 'SIDE-ON SONOTRODE' GEOMETRY

Like sonotrodes, the 'side-on sonotrodes' were incorporated into the 13 mm diameter titanium horn tips as shown in Figure 3.4. The distance between the centre of the electrode and the end of the horn tip was 2 mm. The mass transport to the 0.8 and 1 mm diameter platinum disc 'side-on sonotrodes' was characterised as follows. The mass transport limited

currents due to oxidation or reduction of various electroactive species in both water and acetonitrile under fixed intensity insonation (3 W cm^{-2}) were measured as a function of concentration and diffusion coefficient for both electrode areas. The diffusion coefficients for decamethyl ferrocene, *p*-chloranil, tetrahexylphenylenediamine and tris(*p*-bromophenyl)amine in acetonitrile / 0.1 M TBAH were measured at a rotating disc electrode according to the procedure outlined in section 2.7. The four values were found to be 1.72, 2.00, 0.49 and 1.67 $\pm 0.10 \times 10^{-5}$ cm^2 s^{-1} respectively. Diffusion coefficients for the aqueous substrates are given in Table 3.1. Typical linear sweep voltammograms (LSVs) for the reduction of $Ru(NH)_6^{3+}$ and the oxidation of ferrocene are shown in Figure 3.11. The variation of sono-limiting current with concentration at fixed ultrasound intensity is seen in Figure 3.12. Next the dependence of the limiting current on diffusion coefficient for different electroactive species was examined by normalising sono-limiting currents to those for a one-electron transfer at a fixed concentration and electrode area. A log-log plot of the resulting currents against the diffusion coefficient shows the power to which D should be raised in the

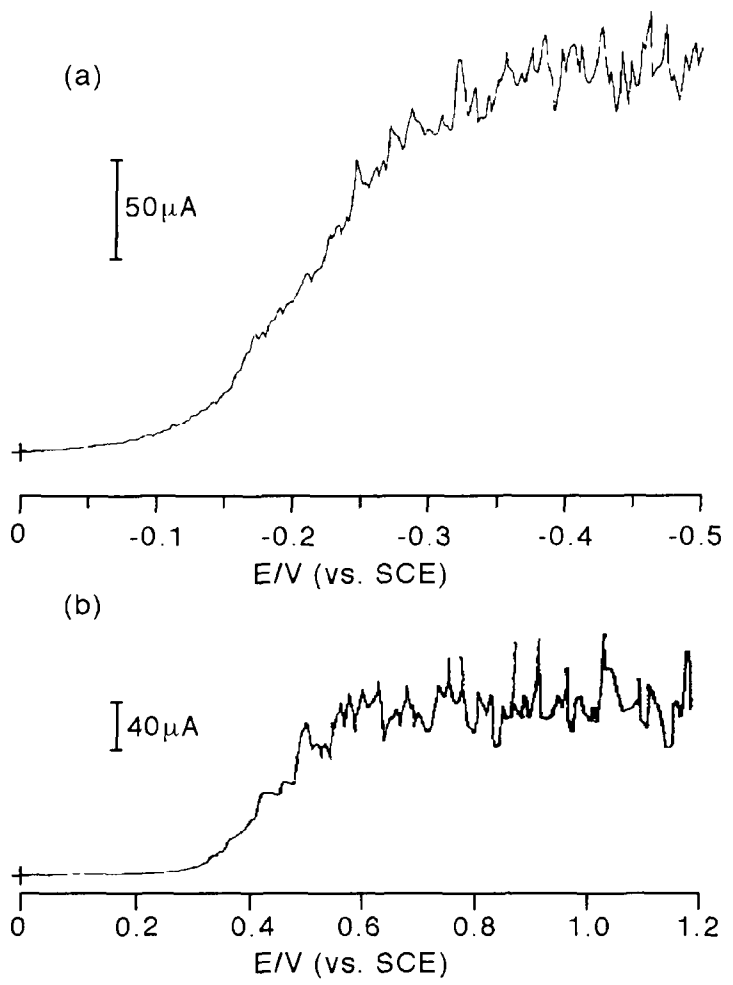

Figure 3.11 'Side-on sonotrode' LSVs at 5 mV s^{-1} at a 1 mm Pt disc for a) the reduction of 10 mM $Ru(NH)_6^{3+}$ in 0.1 M KCl(aq) and b) the oxidation of 5 mM ferrocene in acetonitrile / 0.1 M TBAP.

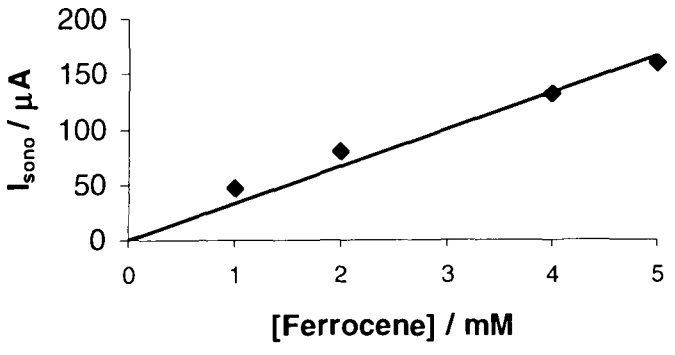

Figure 3.12 Limiting 'side-on sonotrode' current against concentration for a 1 mm Pt disc.

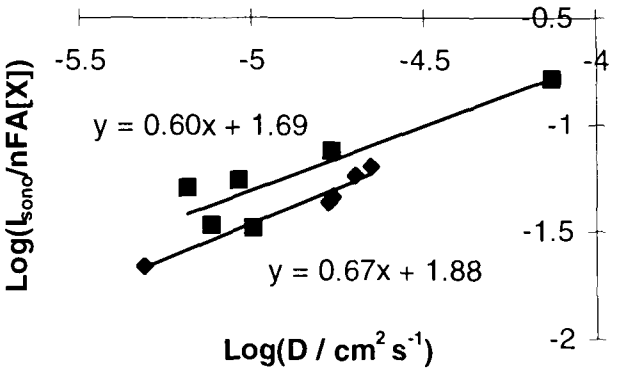

Figure 3.13 Log-log plots of normalised current against diffusion coefficient for water-based (■) and acetonitrile-based (◆) species.

expression for the current. The plots for both water and acetonitrile-based species are seen in Figure 3.13 and have gradients of 0.60 and 0.67 ± 0.10 respectively. Thus under the hydrodynamic conditions of the 'side-on sonotrode' geometry, I_{sono} was also found to be roughly proportional to $D^{2/3}$. In the next section we discuss the origin of such behaviour and employ two different numerical models for predicting the magnitude of the currents under insonation.

3.5 NUMERICAL MODELLING FOR 'SIDE-ON SONOTRODES'

In contrast with the sonotrode geometry, the 'side-on sonotrode' geometry involves movement of solution parallel with the electrode surface. If we consider that acoustic streaming begins around the edge of the horn tip as suggested by Figure 1.14 we can start to estimate the mass transport in terms of a 'flow past a plate' as discussed in section 3.2.2 above. This is performed in the next section and an estimate of the bulk flow velocity is made. Alternatively, the ultrasonic vibration of the tip can be likened to a high speed vibrating electrode. The mathematical description for the mass transport in this case is given in section 3.5.2.

3.5.1 'FLOW PAST A PLATE' MODEL

Adaptation of earlier theory for the 'flow past a plate' model [5] gives the following result for the expected limiting current for a 'side-on sonotrode' (see Appendix 4 for theory):

$$I_{sono} = 0.373nF\pi r^{5/3}[X]h_0^{-1/6}D^{2/3}U^{1/2}\nu^{-1/6} \qquad (3.4)$$

where r is the radius of the electrode, h_0 is the depth of electrode submersion, U is the ultrasonically induced bulk flow and ν is the kinematic viscosity. To gain an estimate of U, we apply the equation to the oxidation of 5 mM ferrocene at a 1 mm diameter electrode in acetonitrile (for which $\nu = 0.00443\ cm^2\ s^{-1}$ [19]) at a horn submersion depth of 2.5 cm. The experimental current of 160 μA would require a bulk flow velocity of ca. 6.2 $m\ s^{-1}$! However, in the locality of the electrode which has an amplitude of ca. 100 μm [4] and a frequency of 20 kHz, the average relative speed (the average relative velocity is of course zero) can be

estimated as 4a/f where a is the amplitude and f is the frequency, assuming the solution is stationary. This equates to an average speed of 8 m s^{-1} suggesting that the above model may well be applicable even under conditions where the electrode itself is the source of insonation.

3.5.2 'VIBRATING ELECTRODE' MODEL

Modification of a previously established equation for predicting the limiting current for vibrating cylinders [20,21] led to the following relationship for the limiting current corresponding to 'side-on sonotrodes' (see Appendix 5 for derivation).

$$I_{sono} = 1.295nF[X]\pi r^2 D^{2/3}\nu^{-1/6}\left(\frac{a}{R}\right)^{2/3} f^{1/2} \qquad (3.5)$$

where R is the diameter of the ultrasonic horn and a, f and r are defined in the previous section. This model predicts currents of ca. 100 μA for the oxidation of 5 mM ferrocene under insonation whereas the experimental observation is 160 μA. Nevertheless the agreement is acceptable considering that the theory is best applied for conditions where there is no turbulence with its related enhancement of mass-transfer coefficient [20].

3.6 CHAPTER 3: REFERENCES

[1] R. G. Compton, J. C. Eklund, S. D. Page, T. J. Mason, D. J. Walton, *J. Appl. Electrochem.* **1996**, *26*, 775.

[2] F. Marken, R. P. Akkermans, R. G. Compton, *J. Electroanal. Chem.* **1996**, *415*, 55.

[3] E. L. Cooper, L. A. Coury Jr., *J. Electrochem. Soc.* **1998**, *145*, 1994.

[4] H. A. O. Hill, Y. Nakagawa, F. Marken, R. G. Compton, *J. Phys. Chem.* **1996**, *100*, 17395.

[5] J. C. Eklund, F. Marken, D. N. Waller, R. G. Compton, *Electrochim. Acta* **1996**, *41*, 1541.

[6] A. Durant, H. Francois, J. Reisse, A. Kirsch-de Mesmaeker, *Electrochim. Acta* **1996**, *41*, 277.

[7] J. Reisse, H. Francois, J. Vandercammen, O. Fabre, A. Kirsch-de Mesmaeker, C. Maerschalk, J.-L. Delplancke, *Electrochim. Acta* **1994**, *39*, 37.

[8] R. G. Compton, J. C. Eklund, F. Marken, D. N. Waller, *Electrochim. Acta* **1996**, *41*, 315.

[9] Dr. E. Cordemans, *Private communication*, Oxford, November, **1996**.

[10] M. Atobe, T. Nonaka, *J. Electroanal. Chem.* **1997**, *425*, 161.
[11] R. G. Compton, J. C. Eklund, S. D. Page, *J. Phys. Chem.* **1995**, *99*, 4211.
[12] T. J. Mason, J. P. Lorimer, D. M. Bates, *Ultrasonics* **1992**, *30*, 140.
[13] M. A. Margulis, A. N. Mal'tsev, *Russ. J. Phys. Chem.* **1969**, *43*, 592.
[14] R. N. Adams, *Electrochemistry at Solid Electrodes*, Marcel Dekker, New York, **1969**, pg. 219.
[15] H. Gunasingham, K. P. Ang, C. C. Ngo, *Anal. Chem.* **1985**, *577*, 505.
[16] F. Marken, J. C. Eklund, R. G. Compton, *J. Electroanal. Chem.* **1995**, *395*, 335.
[17] W. J. Albery, *Electrode Kinetics*, OUP, Oxford, **1975**.
[18] C. M. A. Brett, A. M. O. Brett, *Electrochemistry: Principles, Methods and Applications*, OUP, Oxford, **1993**.
[19] D. R. Lide, (Ed.-in-chief), *CRC Handbook of Chemistry and Physics*, 74^{th} *Ed.*, CRC Press, Boca Raton, Florida, **1993**.
[20] D. E. Williams, K. Ellis, A. Colville, S. J. Dennison, G. Laguillo, J. Larsen, *J. Electroanal. Chem.* **1997**, *432*, 159.
[21] P. Dumargue, P. Humeau, *Electrochim. Acta* **1982**, *27*, 115.

4

SONO-ELECTROANALYSIS: USE OF 'SONOTRODES'

CHAPTER 4: SONO-ELECTROANALYSIS: USE OF 'SONOTRODES'

4.1 CONTENTS

This chapter explores the use of sonotrodes, as introduced in section 1.6.1 and further characterised in the Chapter 3, in the electroanalysis of aqueous metal cations. Some of the work in this chapter is published in a paper in *Electroanalysis* (**1998**, *10*, 26). Sonotrodes were made by implanting a working electrode into the tip of an ultrasonic horn. These were investigated for the use in ultrasound assisted anodic stripping voltammetry (ASV) of Pb^{2+} and Cu^{2+} in aqueous solutions to which Hg^{2+} was added to permit the formation of lead/copper amalgam in a plating step. Insonation not only allows this pre-concentration step to take place under conditions of unusually high mass transport but also causes enrichment of the trace metals in the form of intermetallic compounds leading to sharp stripping responses. The effect of increasing insonation time on the oxidation peak sizes, shapes and positions was studied. Comparison was made with the voltammetry of Pb^{2+} and Cu^{2+} observed at platinum electrodes in the absence of Hg^{2+} where broad signals for both were seen.

The nature of the deposition of mercury on platinum electrodes was studied by both voltammetry and atomic force microscopy (AFM). The growth of mercury droplets with time under 'silent' plating conditions was seen. In anodic stripping experiments using platinum sonotrodes the ratio of Hg^{2+} to Pb^{2+} in the co-deposition was examined along with the total amount of charge deposited for a range of Pb^{2+} concentrations. Sharp anodic stripping responses were obtained down to a Pb^{2+} concentration level of 2 $\mu g\ l^{-1}$ making sono-ASV a potentially valuable technique for the detection of Pb^{2+} in solution.

In contrast glassy carbon sonotrodes were found to be unsatisfactory since the adhesion of mercury under insonation was poor.

4.2 INTRODUCTION

Electrochemical stripping analysis [1,2] is an extremely versatile and sensitive analytical technique which allows the determination of concentrations as low as 10^{-10} M and below [3] in favourable cases whilst utilising relatively inexpensive and simple instrumentation. In almost all cases the first stage in the procedure is the accumulation and hence pre-concentration of the electroactive substance on the surface or in the bulk of the electrode. The second stage is informative and is conducted most often using a potential sweep containing a Faradaic current component directly related to the quantity of material deposited in the accumulation step [3].

Specifically *anodic stripping voltammetry* (ASV) is suited to the detection of trace metals (e.g. Pb, Sn, Fe, Cu, Zn, Cd, Bi, Sb, Co, Au, Cr) [4-12] with many workers performing the stripping analysis using in-situ amalgam deposition on electrodes immersed in the sample solution after addition of a soluble mercury salt. For ASV to be viable this deposition step, as with the pre-concentration of the target species, often has to have its rate enhanced by stirring, rotating the electrode or by using microelectrodes [13]. The use of power ultrasound has been investigated by electrochemists for many years - see [14,15] for reviews. The major feature observed has been the extremely enhanced mass transport, particularly when ultrasonic immersion horn transducers [16,17] are employed. Thus the use of insonation, with its very effective and straightforward increase in the rate of mass transport to the electrode, offers a faster alternative and allows macroelectrodes to have essentially the same transport characteristics as microelectrodes yet with much higher associated currents [18].

Rebbitt *et al.* [19] exploited ultrasound for ASV at glassy carbon electrodes. In these experiments a working electrode was positioned opposite a horn to provide efficient solution agitation. The smaller the horn to electrode separation was made, the higher the mass transport observed. The merits of insonation in analytical electrochemical pre-concentration techniques were discussed [19]. Elsewhere ultrasound was used in sample pre-treatment by Ashley [20]

prior to electroanalysis and also exploited in situ for pre-concentration in ASV using polymer coated mercury / glassy carbon electrodes by Brett *et al.* [21].

An alternative method of coupling ultrasound to electrochemistry is to use the sonic horn tip itself as the electrode as pioneered by Reisse *et al.* [22]. This is then termed a 'sonotrode' [22,23]. More generally sonotrodes can be fashioned by the implantation of a small (~mm) insulated platinum or glassy carbon disc into a titanium horn tip as seen in Figure 4.1 [23]. Furthermore platinum sonotrodes may be mercury plated [24] to extend the cathodic electrochemical window in aqueous solution. Both types of sonotrode enjoy huge rates of mass transport corresponding to diffusion layers which are sub-micron in size [25]. These rates are the result of cavitation in solution [26,27] and acoustic streaming [25]. Moreover the formation of microjets by transient cavitation at the electrode surface provides continuous activation and abrasion [26,28] of the sonotrode surface and its mercury coating. This, depending on the strength of interaction of adsorbed materials, potentially keeps the electrode clean even in "dirty" media and may extend the use of such electrodes to analytical environments where conventional electrodes quickly become fouled.

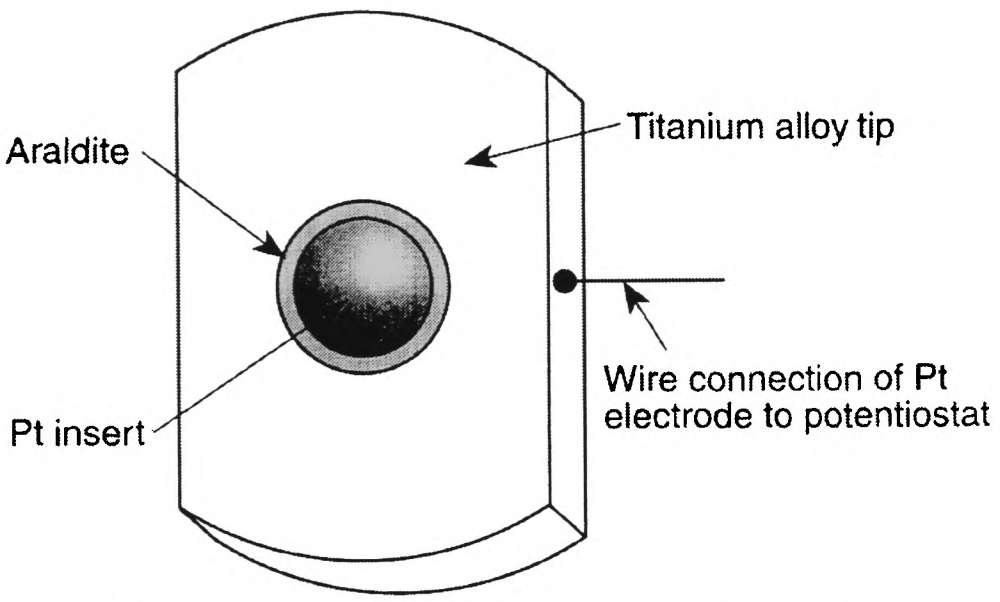

Figure 4.1 Adaptation of the sonic horn tip for the inclusion of a platinum disc insert so as to form a sonotrode.

This chapter seeks to investigate deposition processes on sonotrodes with a view to subsequently using mercury coated sonotrodes in the quantitative trace analysis of lead in aqueous solutions via dc ASV.

4.3 EXPERIMENTAL

The three-electrode electrochemical cell used in this work is shown in Figure 3.5. It was thermostatted at 25 ± 2 °C [19]. The working electrode was embedded into the 13 mm horn tip [29] and secured with non-conducting Araldite™ [23]. The horn employed in this work was as described in section 2.2.1. The sonotrodes used were 1 mm diameter glassy carbon, 1 mm diameter gold, 2 mm diameter platinum and 2 mm diameter copper discs, measured and polished according to the protocols outlined in section 2.1. The level of lead and copper impurity in the background electrolyte was initially found to be a problem in our trace analysis work so pure KNO_3 (Aldrich, 99.99+%) was employed for these investigations. Experiments using aqueous mercury salts were performed at pH 2 (0.01 M HNO_3) in order to prevent precipitation of insoluble mercury hydroxide. Diffusion coefficients for Pb^{2+} and Cu^{2+} were calculated from the rotation speed dependence of the transport limited current [30] for their reduction at rotating disc electrodes as outlined in section 2.7. These experiments used 5 mM solutions of electroactive species ($Cu(NO_3)_2$ and $Pb(NO_3)_2$) in 0.1 M KNO_3 and employed 6 mm platinum and gold electrodes respectively.

Surface imaging of a 4 mm Pt disc electrode before and after mercury plating by AFM was carried out as described in section 2.11. For electrochemical Hg deposition experiments, the 4 mm platinum electrode for AFM studies was plated at 0 V (vs. SCE) for either 2 or 10 minutes in a stirred 5 mM $Hg(NO_3)_2$ (pH 2) solution. After the deposition period, the electrode was quickly removed with the deposition potential still applied in order to prevent loss of mercury due to open circuit conproportionation [31].

4.4 RESULTS AND DISCUSSION

4.4.1 STRIPPING RESPONSES FOR LEAD, COPPER AND MERCURY

Four types of sonotrode (glassy C, Au, Cu and Pt) were all initially employed in deposition and stripping experiments using ca. 50 μM Hg^{2+}, 5 μM Cu^{2+} and 5 μM Pb^{2+} in 0.1 M KNO_3 adjusted to pH 2 with HNO_3. Stripping voltammograms for the glassy carbon

sonotrode consistently revealed no trace of Pb, Cu or Hg suggesting that even at this relatively low ultrasound intensity, mercury cannot adhere to glassy carbon. The copper sonotrode gave a sharp stripping response for Pb (Figure 4.2a) but could not be subjected to potentials more positive than ca. 0 V (vs. SCE) due to oxidation of the electrode material itself. This was also responsible for the signal distortion as seen in Figure 4.2a. Platinum and gold gave very similar responses but the gold sonotrode became rapidly visibly eroded by the ultrasound consistent with its malleable nature. The response for platinum is seen in Figure 4.2b. The stripping potentials of Pb, Cu and Hg were found to be -0.45 V, -0.02 V and +0.46 V (vs. SCE) respectively. These values are in good agreement with literature reports [3]. Thus, mercury was found to adhere to metals more strongly than to glassy carbon and platinum was selected as the best material for further quantitative studies of anodic stripping voltammetry.

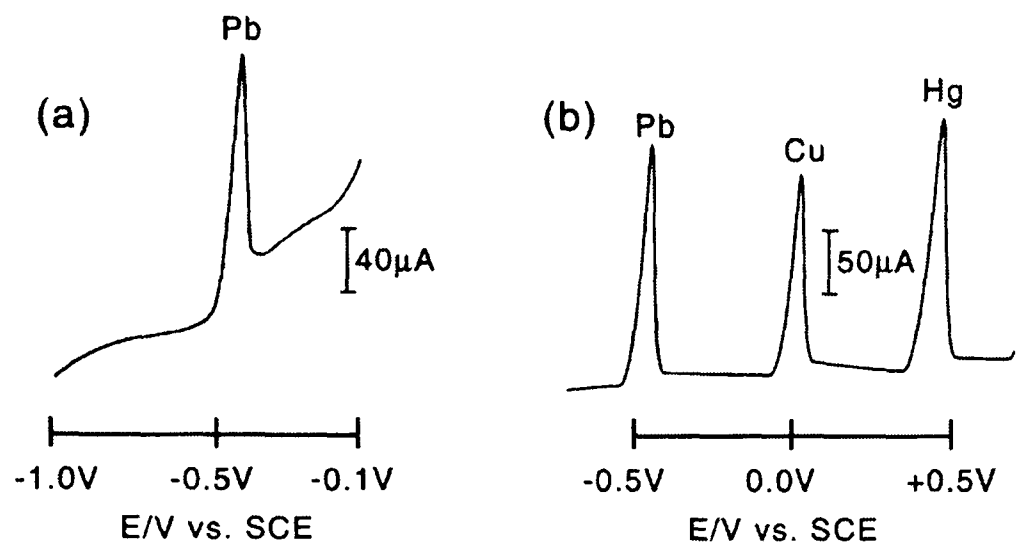

Figure 4.2 Stripping responses obtained at a scan rate of 50 mV s^{-1} for a) 4.8 μM Pb^{2+} on a 2 mm Cu sonotrode and b) 4.8 μM Pb^{2+}, 4.7 μM Cu^{2+} and 50 μM Hg^{2+} on a 2 mm Pt sonotrode both after 2 mins deposition at -1.0 V (vs. SCE) and 3.5 W cm^{-2} ultrasound.

In the absence of mercury, no stripping signal for lead was seen when attempts were made to deposit 50 μM Pb^{2+} in 0.1 M KNO_3 (pH 2) directly onto platinum under insonation at -1.0 V (vs. SCE). However, when 50 μM Cu^{2+} and Pb^{2+} were co-deposited onto platinum under the same conditions, a broad signal was seen for both indicating that Pb will plate in the presence of Cu. The peaks are shown in Figure 4.3 and are

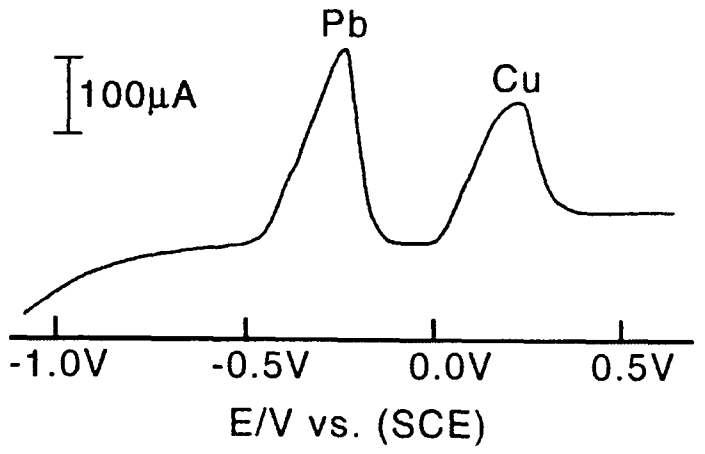

Figure 4.3 Stripping responses for 50 μM Pb^{2+} and 50 μM Cu^{2+} obtained in the absence of mercury at a scan rate of 50 mV s^{-1} on a 2 mm Pt sonotrode after 2 mins deposition at -1.0 V (vs. SCE) and 3.5 W cm^{-2} ultrasound.

shifted to more positive potentials than those obtained in the presence of Hg^{2+}. Before meaningful considerations of the nature of Pb and Cu deposition into Hg amalgams on platinum can be made it is necessary to first investigate the behaviour of mercury plating under ultrasound.

4.4.2 MERCURY DEPOSITION ON PLATINUM

Under silent but mechanically stirred conditions, the growth of mercury droplets on Pt rather than a continuous film can be demonstrated by AFM. There have been corresponding literature reports of mercury deposition of this nature on both platinum [32] and on glassy carbon [33]. Figure 4.4 shows images of a freshly polished 4 mm platinum electrode surface and electrode surfaces after 2 and 10 minutes of mercury deposition under stirring. Deposition was performed using a 5 mM aqueous solution of $Hg(NO_3)_2$ in 0.1 M KNO_3 / 0.01 M HNO_3 (pH 2) at 0 V (vs. SCE). Droplets ranging in size from sub-micron to ca. six microns in diameter can be clearly seen. It is expected that any loss of mercury, which under silent conditions would be caused by coalescence of mercury droplets followed by their gravity induced detachment from the electrode [34], should be drastically affected by the application of power ultrasound. This was seen most dramatically when attempts were made to deposit 50 μM Hg^{2+} onto a 1 mm glassy carbon sonotrode. A reduction current, not less than predicted by Equation (3.1), was seen during 3.5 W cm^{-2}

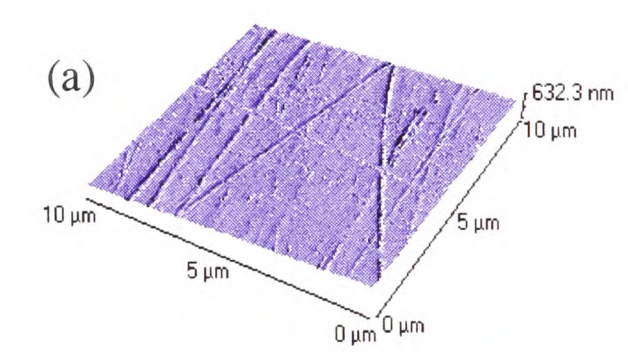

Figure 4.4 AFM images of a) a polished platinum electrode surface, b) and c) a platinum electrode surface after 2 and 10 minute deposition of mercury at 0.0 V (vs. SCE) respectively using an aqueous 5 mM Hg^{2+} solution (0.1 M KNO_3, pH 2).

ultrasound deposition at -1.0 V (vs. SCE) but no mercury stripping signal could be detected at all. Similarly when Cu^{2+} and Pb^{2+} were added to the system, no stripping peaks for these species were observed either. The mercury is simply shaken off and this can be taken as the limiting case for the decrease in Hg signal with decreasing horn to electrode distance in the 'face-on' geometry as reported earlier [19].

The behaviour of mercury plating on platinum sonotrodes as a function of time and concentration was studied in detail. The ranges of these parameters studied were 0 - 180 s and 50 μM - 1 mM Hg^{2+}. Electrodeposition was performed at -1.0 V (vs. SCE) under an ultrasound intensity of 3.5 W cm^{-2}. The stripping peak associated with the oxidation of the mercury deposit occurred at E_p = +0.46 V (vs. SCE) on the positive scan. The charge deposited was calculated by integration of the stripping peak and was found to reach a limiting value as both time and concentration increased. Figure 4.5 shows how the charge stripped varied with time and concentration. The levelling off of these plots corresponds to equal rates of electrodeposition and abrasion which may be considered as a form of steady state, allowing the deposition to proceed to a defined limit with the sonotrode surface covered by microscopically small mercury droplets.

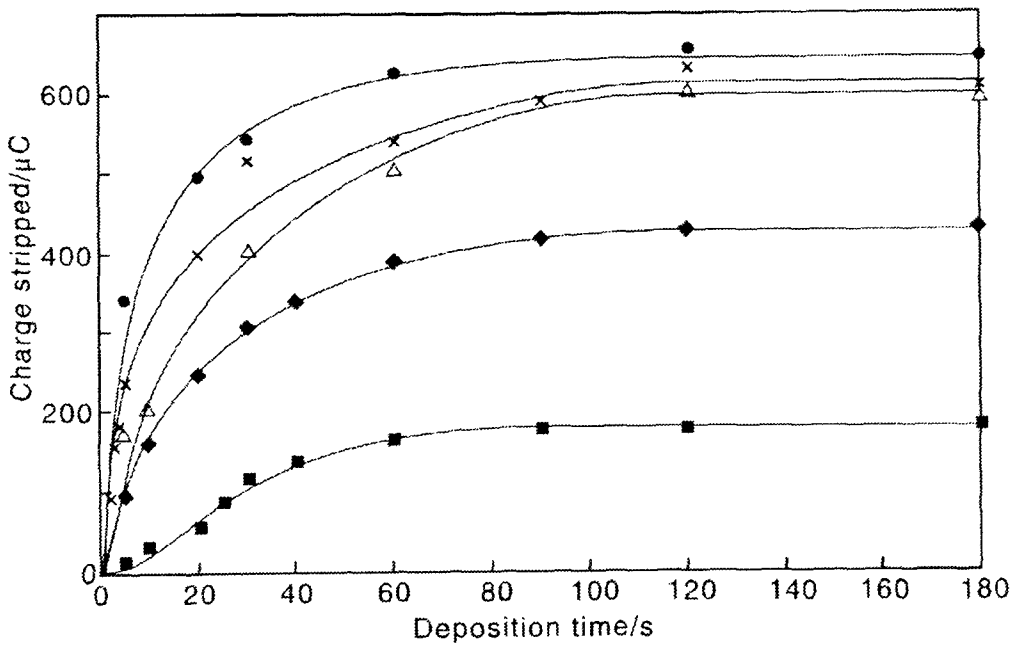

Figure 4.5 Plot of the amount of mercury deposited on a 2 mm Pt sonotrode with time with the potential held at -1.0 V (vs. SCE) and 3.5 W cm^{-2} ultrasound applied. Data for five concentrations of Hg^{2+} (50 μM, 100 μM, 200 μM, 300 μM and 1 mM) in 0.1 M KNO_3 (pH 2) were obtained by integration of the anodic stripping responses obtained under silent conditions using linear sweep voltammetry and a scan rate of 50 mV s^{-1}.

To investigate further the dynamics of the deposition / ablation of the mercury coat experiments were conducted as follows. A 200 μM solution of Hg^{2+} in 0.1 M KNO_3 (adjusted to pH 2 with HNO_3) was plated onto the 2 mm Pt sonotrode for 2 minutes at -1.0 V (vs. SCE)

under 3.5 W cm^{-2} ultrasound. The amount of charge stripped was then calculated by integration of the stripping peak obtained by sweeping in an anodic direction at 50 mV s^{-1}. This was repeated several times and gave a reproducible value of 590 ± 90 μC. The experiment was repeated and this time after the 2 minutes, a further period of ultrasound was applied with no current flowing. After application of ultrasound, the solution was changed to 0.1 M KNO_3 (pH 2) with no Hg^{2+} in solution and the electrode was scanned positive to strip off the mercury. Varying periods of extra ultrasound were examined and a plot of log Q against time, where Q is the amount of charge associated with the mercury stripping, is shown in Figure 4.6.

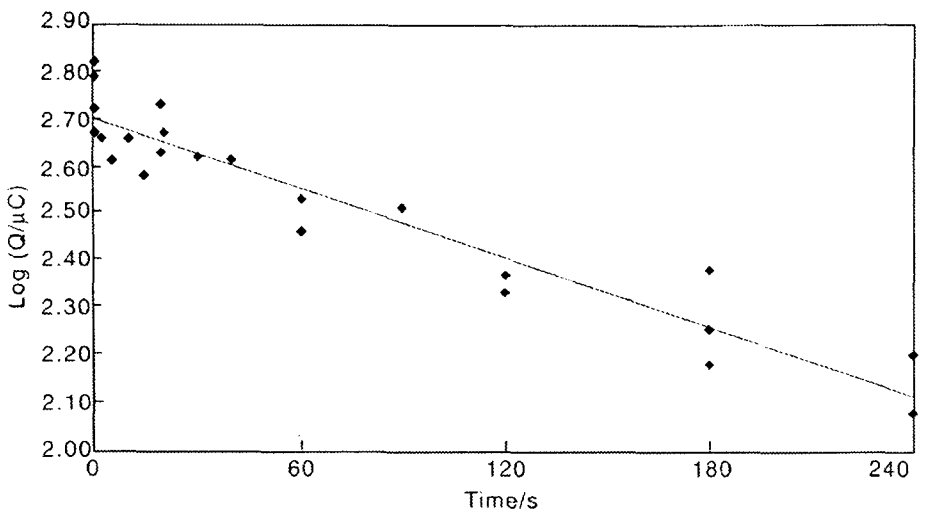

Figure 4.6 Log plot of the amount of mercury (expressed as charge, Q) remaining on the plated 2 mm Pt sonotrode surface after application of further 3.5 W cm^{-2} ultrasound without deposition potential applied.

Assuming a first order decay, the modulus of the gradient of this plot (5.7 ± 1.5 x 10^{-3} s^{-1}) is taken as the ablation rate constant, k_{ab}, for mercury that is already adhered to the platinum surface and is only removed by cavitational cleaning. This is equivalent to a half-life of 120 ± 20 seconds.

To illuminate the nature of the cleaning effect due to ultrasound two naive ablation mechanisms may be considered as follows.

(i) Cavitation in the immediate vicinity of the sonotrode surface generates high velocity liquid jets [26,27] of dimensions of the order of 100 μm which could clean a certain fraction of the amount of mercury present. This type of cleaning may be that studied in the ablation experiments reported above but note that ultrasound is also employed in the deposition stage where other effects may operate. The corresponding differential equation describing the deposition rate (I_{lim}) and the abrasion ($k_{ab}.Q$) processes is given in Equation (4.1) and has a simple solution following an exponential law. This suggests a monotonic increase of deposited charge, Q, converging with time to a limiting value, Q_{lim}.

$$\frac{dQ}{dt} = I_{lim} - k_{ab}.Q \qquad (4.1)$$

In this equation, I_{lim} stands for a constant, transport limited current disregarding any nucleation and growth processes. The solution is as follows.

$$Q = \frac{I_{lim}}{k_{ab}}\left[1 - e^{-k_{ab}t}\right] \qquad (4.2)$$

Hence as $t \rightarrow \infty$ the limit of deposited charge can be related to the current and the rate constant for the ablation abrasion process, k_{ab}, by $Q_{lim} = I_{lim}/ k_{ab}$. Under these conditions the maximum deposited amount of mercury would be expected to scale with bulk concentration, diffusion coefficient and electrode area as given in Equation (3.1). The plots in Figure 4.5 do indeed reach a steady state at sufficiently long times, but also limit with increasing concentration. Moreover the rate at which the plots reach the steady value is faster than predicted by Equation (4.2) on the basis of the measured value of k_{ab}. These observations require other modes of mercury ablation to be considered.

(ii) The loss of mercury might alternatively be considered to be dependent only on the strength of adhesion to the sonotrode surface. This might increase with the area of the droplet, whilst the weight is proportional to the volume so larger droplets will be more affected by the ultrasound and hence more easily shaken off. In this case the limiting value, Q_{lim}, is expected to be independent of the concentration of Hg^{2+} or the limiting current and would only depend on the maximum size threshold of the droplets. However, if this droplet size is only reached at higher concentrations, this would account for the form of Figure 4.5.

Taken together, these two postulated ablation factors may qualitatively explain the form of Figure 4.5.

4.4.3 LEAD AND COPPER DEPOSITION ON MERCURY-PLATED PLATINUM

Having considered the adhesion, ablation and stripping of mercury we next return to a consideration of lead and copper. A solution of 50 μM Hg^{2+}, 5 μM Pb^{2+} and 5 μM Cu^{2+} in 0.1 M KNO_3 / 0.01 M HNO_3 was deposited on a 2 mm Pt sonotrode at -1.0 V (vs. SCE) under 3.5 W cm^{-2} ultrasound for varying lengths of time. The percentage of each metal

stripped was calculated by comparing the experimental stripping results with those expected for deposition according to the limiting current predicted by the Nernst theory in Equation (3.1). These stripping percentages are calculated from:

$$\% \text{ stripped} = \frac{Q_{st}}{Q_{dep}} \times 100 \tag{4.3}$$

where Q_{st} is the charge stripped and Q_{dep} is the amount of charge deposited after a time, t. The latter is calculated from Fick's law as follows.

$$Q_{dep} = \frac{2D_X[X]_0 A.F.t}{\delta_X^*} \tag{4.4}$$

In order to implement Equation (4.4), the diffusion coefficients for Hg^{2+}, Cu^{2+} and Pb^{2+} in 0.1 M KNO_3 are required. Those for Pb^{2+} and Cu^{2+} were determined using a RDE with variable angular frequency ranging from 1 Hz to 25 Hz at 23 °C as described in the experimental section. The values obtained were D = 1.03 ± 0.1 x 10^{-5} cm^2 s^{-1} for Pb^{2+} and D = 1.01 ± 0.1 x 10^{-5} cm^2 s^{-1} for Cu^{2+}. The value of D for Hg^{2+} (8.3 x 10^{-6} cm^2 s^{-1}) is taken from the literature [35].

Values calculated from Equation (4.3) above are given in Table 4.1 along with values calculated for Hg for comparison. The latter give an insight into the large ablating power associated with power ultrasound even at the relatively low intensities of ultrasound employed.

Species	Concentration / μM	Deposition time / s		
		30	60	90
Hg^{2+}	50	14.3	10.0	5.1
	100	18.6	12.0	6.3
	200	14.2	7.5	4.4
	300	10.3	5.5	3.0
	1000	11.0	6.3	3.0
Pb^{2+}, Hg^{2+}	5, 50	81.7	79	84.1
Cu^{2+}, Hg^{2+}	5, 50	77.4	77.8	82.8

Table 4.1. Calculated stripping percentages (see Equation 4.3) for Hg^{2+}, Cu^{2+} and Pb^{2+} reduced on a 2 mm platinum sonotrode with varying deposition times. Deposition potential was -1.0 V (vs. SCE).

The stripping percentages on platinum for both lead and copper in the presence of 50 μM Hg^{2+}, as seen in Table 4.1, consistently worked out to be approximately 80% for both lead and copper for deposition times less than 100 seconds. This contrasted with the high intensity (30 W cm^{-2}), 'face on' glassy carbon experiments [19], where the stripping % varied between 30 and 70, probably due to the more severe mechanical removal of amalgam from the electrode surface. For platinum sonotrodes, the amount of Pb or Cu stripped (measured from the peak areas) varied linearly with time over the first 100 seconds or so although the rate then declined a little. This is seen in Figure 4.7 and contrasts with the plot for mercury deposition (Figure 4.5) where a limiting value is seen within ca. 60 seconds. Thus by far the most significant conclusion to be drawn from Table 4.1 and Figures 4.5 and 4.7 is that while the mercury stripping percentage declines with time and increasing concentration, both lead and copper continue to deposit thus maintaining a roughly constant stripping percentage.

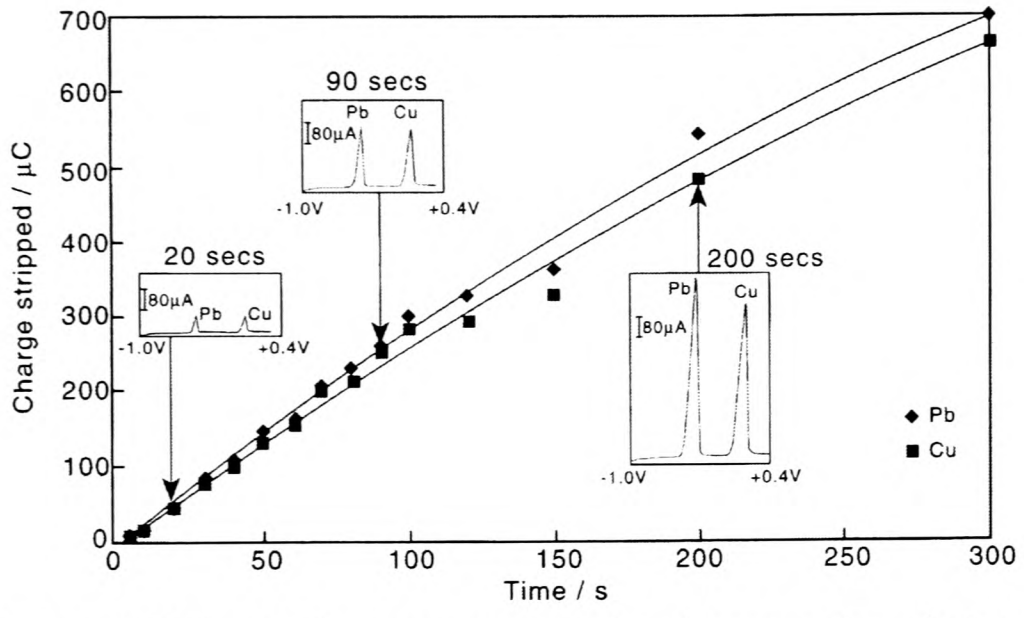

Figure 4.7 Plot of the amount of lead and copper deposited on a 2 mm Pt sonotrode with time with the potential held at -1.0 V (vs. SCE) and 3.5 W cm^{-2} ultrasound applied. Data is for a single solution containing 5 μM Cu^{2+} (■) and Pb^{2+} (◆) in 0.1 M KNO_3 (pH 2) and acquired by integration of the anodic stripping responses (examples are seen in the inserts) obtained under silent conditions using linear sweep voltammetry and a scan rate of 50 mV s^{-1}.

It is evident that the ablation of Cu and Pb is much less than that of Hg and that it is possible to deposit substantially greater amounts of Cu and Pb than Hg. Moreover the inserts in Figure 4.7 show that as the deposition proceeds the current / voltage characteristics of the stripping peaks change gradually from those of a Pb / Cu amalgam to those seen from the deposition of Pb and Cu in the absence of Hg (Figure 4.3). This is emphasised by the data in Table 4.2.

E_{peak} / ± 0.01 V (vs. SCE)		Peak width at half height / ± 5 mV		Deposition time / s
Pb	Cu	Pb	Cu	
-0.45	0.02	30	40	20
-0.42	0.06	45	55	90
-0.37	0.11	80	80	200
-0.32	0.15	105	110	600
-0.26	0.22	160	180	120 (No Hg^{2+} present)

Table 4.2 Typical values for the peak potential and half-height widths for 5 μM Cu^{2+} and Pb^{2+} stripping voltammograms obtained in the presence of 50 μM Hg^{2+} at different deposition times under 3.5 W cm^{-2} US and a scan rate of 50 mV s^{-1}.

Further insight into the nature of the Pb deposits is understandable in the light of experiments investigating deposition from variable concentrations of Pb^{2+} in the context of calibration of the sono-ASV experiment for the analysis of Pb^{2+}. It is this work to which we next turn. We consider first varying the lead concentration (from 0.4 nM to 10 μM) for a fixed mercury concentration (50 μM) and then second varying the mercury concentration (from 10 μM to 1 mM) for a fixed lead concentration (5 μM). In both cases the charge stripped under the lead oxidation peak was examined. All experiments were performed with 3.5 W cm^{-2} ultrasound and plating was carried out at -1.0 V (vs. SCE). The anodic stripping scan rate was 50 mV s^{-1}. Figure 4.8 shows a plot of charge stripped against lead concentration. Figure 4.9 shows the low concentration data expanded for clarity. Figures 4.10 and 4.11 show the corresponding peak height against concentration plots.

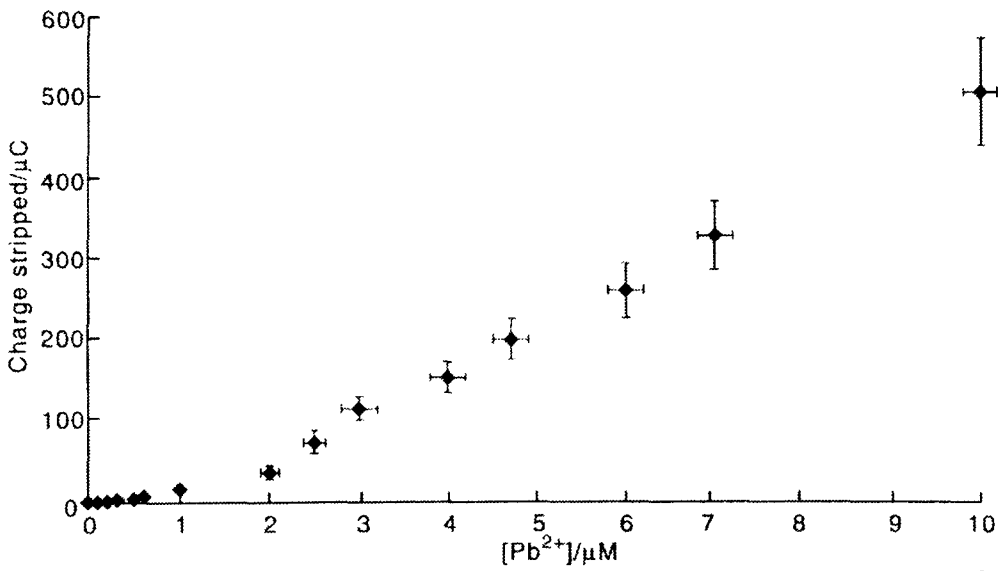

Figure 4.8 Plot of the amount of charge stripped against $[Pb^{2+}]$ for 2 minutes of 3.5 W cm^{-2} ultrasound at -1.0 V (vs. SCE) on a 2 mm Pt sonotrode. Solution contained 50 μM Hg^{2+} in 0.1 M KNO_3 (pH 2) and the scan rate was 50 mV s^{-1}.

At low concentrations of lead a linear dependence is seen both in respect of the charge stripped and the height of the stripping peak. At higher lead concentrations there are

inflexions in both types of plots and these may, tentatively, be attributed to phase changes. For example that in Figure 4.11 at $[Pb^{2+}] \approx 200$ nM corresponds approximately to the deposition of Pb and Hg in the ratio 1:63 which in turn corresponds to the known solubility [36] of Pb in Hg of 1.6% at 298 K. The other inflexions may correspond to the formation of intermetallic compounds of Pb and Hg [36,37].

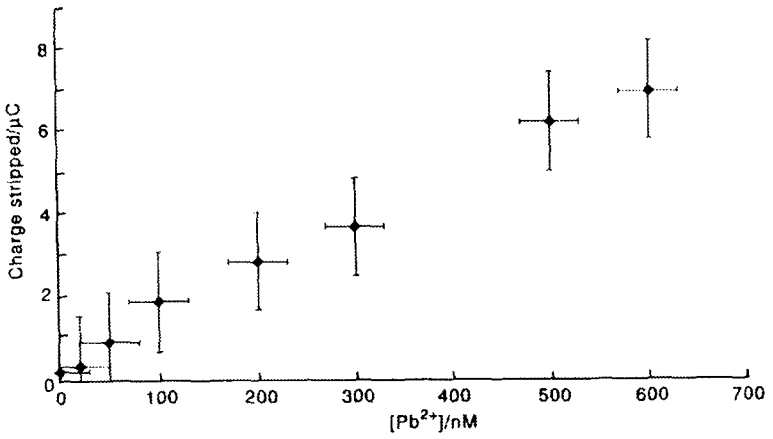

Figure 4.9 Low $[Pb^{2+}]$ plot of the amount of charge stripped against $[Pb^{2+}]$.

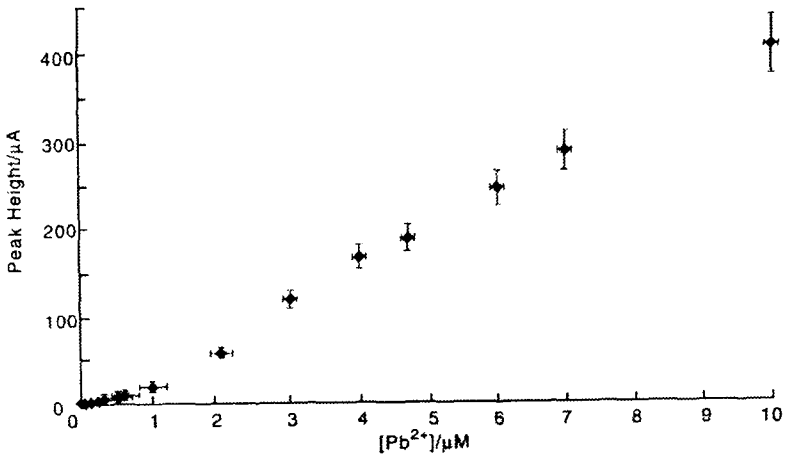

Figure 4.10 Plot of the Pb stripping peak height against $[Pb^{2+}]$.

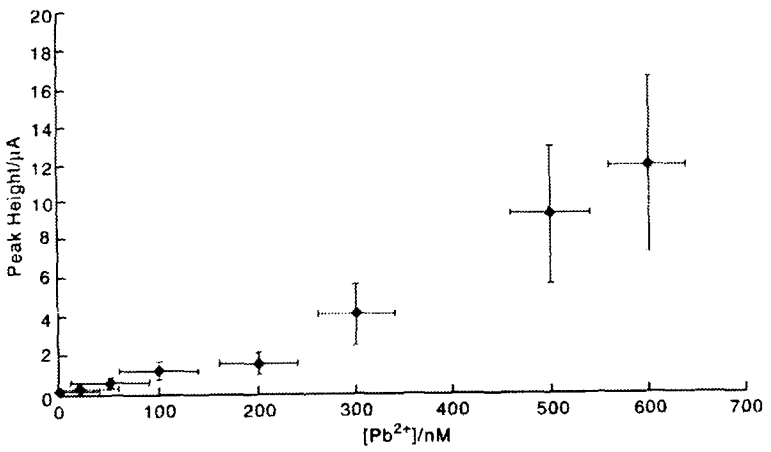

Figure 4.11 Low $[Pb^{2+}]$ plot of the Pb stripping peak height against $[Pb^{2+}]$.

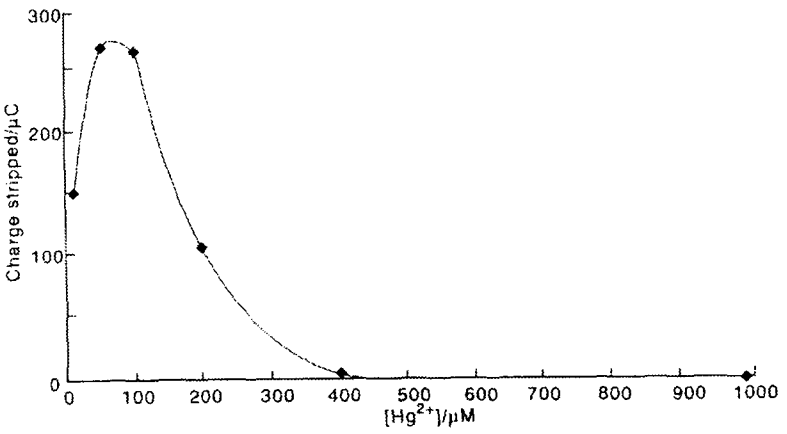

Figure 4.12 Plot of the amount of charge stripped for lead against $[Hg^{2+}]$.

Deposition for all four plots was 2 minutes of 3.5 W cm^{-2} US at -1.0 V (vs. SCE) on a 2 mm Pt sonotrode. Solution contained 50 μM Hg^{2+} in 0.1 M KNO_3 (pH 2) and the scan rate was 50 mV s^{-1}.

Figure 4.12 shows how the charge stripped in the lead oxidation peaks varies with the concentration of Hg^{2+} added to the solution. For 5 μM Pb^{2+}, the charge stripped goes through a maximum at ~70 μM Hg^{2+}. On the low concentration side the Pb is possibly deposited as an intermetallic compound of fixed stoichiometry so that increasing the amount of mercury increases the total amount of material (Pb and Hg) on the sonotrode surface (cf. Figure 4.7). For higher mercury concentrations where the charge falls off the probable explanation lies in the dynamic nature of the steady-state case where the maximum and limiting amount of mercury has been deposited (Figure 4.5) so that there is increasing dilution of the Pb in the

film. It is thus possible to optimise the conditions for the most sensitive detection by using only small quantities of Hg^{2+} added into the sample solution and by choosing the deposition time to yield a high enrichment of Pb in the mercury film.

Using a 2 mm platinum sonotrode and 50 μM Hg^{2+} in solution, down to 4 x 10^{-10} M Pb^{2+} can be detected with a 2 minute accumulation time. However, this was superimposed on a large background mercury plating current so that the useful detection limit for simple dc ASV is probably approximately one order of magnitude higher than this.

4.5 CONCLUSIONS

The deposition of mercury onto a platinum sonotrode is subject to a considerable amount of ablation through both cavitation at the electrode surface and mechanical shear forces affecting larger droplets. Nevertheless sufficient mercury adheres to allow formation of an amalgam when copper and lead are co-deposited. Similar results have been reported previously for glassy carbon electrode substrates [38], though not under insonation. On mercury-plated platinum, stripping signals can be seen for both copper and lead, even at very low concentrations. In this respect sonotrodes provide an attractive complementary approach to the use of microelectrodes [39] for ASV. This is due to efficient sono-preconcentration of ions as a result of the extremely high mass transport enjoyed by sonotrodes. The useful working range of the technique (5 nM to 10 μM Pb^{2+}) is thus well suited to analysis of lead levels in common liquid samples such as river water, drinks and blood where conventional electrochemical experiments may experience problems of electrode fouling which might be alleviated by the cleaning action of insonation. This last aspect is investigated in the next chapter where preliminary results concerning the sono-ASV of metals in white wine are reported.

4.6 CHAPTER 4: REFERENCES

[1] A. M. Bond, *Modern Polarographic Methods in Analytical Chemistry*, Marcel Dekker, New York, **1980**.

[2] W. R. Heineman, H. B. Mark, Jr., J. A. Wise, D. A. Roston, *Laboratory Techniques in Electroanalytical Chemistry* (Eds. P. T. Kissinger, W. R. Heineman), Marcel Dekker, New York, **1984**.

[3] Kh. Z. Brainina, E. Neyman, *Electroanalytical Stripping Methods*, John Wiley, New York, **1993**.

[4] I. Turyan, D. Mandler, *Anal. Chem.* **1993**, *65*, 2089.

[5] B. J. Feldman, J. D. Osterloh, B. H. Hata, A. Dalessandro, *Anal. Chem.* **1994**, *66*, 1983.

[6] H. Ping Wu, *Anal. Chem.* **1996**, *68*, 1639.

[7] Kh. Z. Brainina, A. M. Bond, *Anal. Chem.* **1995**, *67*, 2586.

[8] Z. Q. Gao, K. S. Siow, *Talanta* **1996**, *43*, 727.

[9] Z. Q. Gao, K. S. Siow, *Talanta* **1996,** *43*, 255.

[10] G. Henze, S. Sander, F. Heppeler, *Anal. Chim. Acta* **1996**, *319*, 19.

[11] Z. Q. Gao, K. S. Siow, *Electroanalysis* **1996**, *8*, 602.

[12] C. Locatelli, E. Vasca, C. Bighi, F. Fagioli, T. Garai, *Electroanalysis* **1996**, *8*, 165.

[13] A. M. Bond, *Analyst* **1994**, *119*, R1.

[14] D. J. Walton, S. S. Phull, *Adv. Sonochem.* (Ed. T. J. Mason) **1996**, *4*, 205.

[15] R. G. Compton, J. C. Eklund, F. Marken, *Electroanalysis* **1997**, *7*, 509.

[16] T. J. Mason, J. P. Lorimer, *Sonochemistry: Theory, Applications and Uses of Ultrasound in Chemistry*, Ellis Horwood, Chichester, **1988**.

[17] K. S. Suslick, *Ultrasound: Its Chemical, Physical and Biological Effects*, VCH, Weinheim, **1988**.

[18] F. Marken, T. O. Rebbitt, R. G. Compton, *J. Chem. Soc. Chem. Comm.* **1996**, *9*, 1017.

[19] F. Marken, T. O. Rebbitt, J. Booth, R. G. Compton, *Electroanalysis* **1997**, *9*, 19.

[20] K. Ashley, *Electroanalysis* **1995,** *7*, 1189.

[21] F-M. Matysik, S. Matysik, A. M. O. Brett, C. M. A. Brett, *Anal. Chem.* **1997**, *69*, 1651.

[22] J. Reisse, H. Francois, J. Vandercammen, O. Fabre, A. Kirsch-de Mesmaeker, C. Maerschalk, J-L. Delplancke, *Electrochim. Acta* **1994**, *39*, 37.

[23] J. C. Eklund, F. Marken, D. N. Waller, R. G. Compton, *Electrochim. Acta* **1996**, *41*, 315.

[24] C.-W. Lee, R. G. Compton, J. C. Eklund, D. N. Waller, *Ultrasonics Sonochemistry* **1995**, *1*, S59.

[25] F. Marken, R. P. Akkermans, R. G. Compton, *J. Electroanal. Chem.* **1996**, *415*, 55.

[26] J. Klima, C. Bernard, C. Degrand, *J. Electroanal. Chem.* **1995**, *399*, 147.

[27] R. G. Compton, J. C. Eklund, S. D. Page, T. J. Mason, D. J. Walton, *J. App. Electrochem.* **1996**, *8*, 775.

[28] R. G. Compton, J. C. Eklund, S. D. Page, G. H. W. Sanders, J. Booth, *J. Phys. Chem.* **1994**, *98*, 12410.

[29] R. G. Compton, J. C. Eklund, *Electrochim. Acta* **1996**, *41*, 315 & 1541.

[30] W. J. Albery, *Electrode Kinetics*, OUP, Oxford, **1975**.

[31] C. D. Evans, I. Nicic, J. Q. Chambers, *Electrochim. Acta* **1995**, *40*, 2611.

[32] W. S. Kruijt, M. Sluyters-Rehbach, J. H. Sluyters, A. Milchev, *J. Electroanal. Chem.* **1994**, *371*, 13.

[33] H. Ping Wu, *Anal. Chem.* **1994**, *66*, 3151 and references sited therein.

[34] C. L. Colyer, K. B. Oldham, S. Fletcher, *J. Electroanal. Chem.* **1990**, *290*, 33.

[35] H. Gunasingham, K. P. Ang, C. C. Ngo, *Anal. Chem.* **1985**, *577*, 505.

[36] C. Guminski, Z. Galus, *IUPAC Solubility Data Series Vol. 25: Metals in Hg*, Pergamon, New York, **1992**.

[37] M. Hansen. *Constitution of Binary Alloys* (2nd Ed.), McGraw Hill, New York, **1958**.

[38] H. Gunasingham, R. R. Dalangin, *Anal. Chim. Acta* **1991**, *246*, 309.

[39] S. Nomura, K. Nozaki, S. Okazaki, *Electroanalysis* **1991**, *3*, 617.

5

SONO-ELECTROANALYSIS: DETECTION OF LEAD IN WINE

CHAPTER 5: SONO-ELECTROANALYSIS: DETECTION OF LEAD IN WINE

5.1 CONTENTS

This chapter explores the use of anodic stripping voltammetry, as introduced in section 1.3.1, in the sono-electroanalysis of aqueous lead cations in a sample of wine. Some of the work in this chapter is published in a paper in *Electrochimica Acta* (**1998**, *43*, 3443). The quantitative detection of lead in wine is shown to be possible by anodic stripping voltammetry under conditions of insonation. An immersion horn probe is introduced into a thermostatted conventional three-electrode cell opposite a mercury plated platinum disc working electrode. This geometry is used since the high level of ablation of the mercury layer seen in the previous chapter renders analysis by 'sonotrodes' difficult to reproduce during multiple scans. Following acidification of the wine sample lead ions can be reduced at the Hg/Pt electrode surface at -1.0 V (vs. SCE). The large mass transport associated with power ultrasound yields efficient pre-concentration of the lead before it is stripped by an anodic linear sweep of the potential. Insonation further offers the crucial benefits of first surface activation and cleaning, helping to prevent electrode fouling by the organic components in wine and second fully equilibrating "free" and "bound" Pb^{2+} ions in the complex matrix. By use of standard microaddition of lead to the solution the system can be calibrated to give the *total* amount of lead present. Experiments using samples of a white Italian Chardonnay give a total lead content of 22 ± 6 μg l^{-1}. This value is compared with those obtained by independent atomic absorption spectroscopy (AAS) measurements performed by two different laboratories. Quantitative agreement is found and the key benefit of insonation is shown to be the requirement of minimal sample pre-treatment when compared with the literature approaches described in the next section.

5.2 INTRODUCTION

The use of anodic stripping voltammetry (ASV) in the measurement of trace metals in foodstuffs has been widely attempted [1,2]. The attraction is the sensitivity of the technique resulting from the effective *in situ* pre-concentration of the target metal into a mercury film electrode or, recently, microelectrode [3] combined with the relative simplicity and low cost of the necessary equipment. However despite these merits problems have arisen. For example the organic matrix may interfere with the electrochemical process [1]. Alternatively sample pre-treatments of varying complexity [4-9] may be required if reliable results consistent with independent methods are to be obtained. In addition issues arise as to whether the electrochemical methods probe the total metal content or merely reflect some fraction of the free ions present. In this chapter we consider the potential use of ultrasound to alleviate these problems.

The synergy between ultrasound and electrochemistry has been the subject of detailed study for many years [10,11]. The two main features have been :

(i) the extremely enhanced mass transport to the electrode particularly as induced, at least in part, by *acoustic streaming* [12] when ultrasonic immersion horn transducers [13] are employed and

(ii) the effective cleaning and activation of electrode surfaces through cavitational collapse at the solid - liquid interface [14,15].

These features are thus well suited to an electroanalytical technique that requires both efficient pre-concentration of a target species in solution and prevention of electrode fouling.

The use of insonation in analytical electrochemical experiments in ASV in aqueous solutions has already been initiated in the previous chapter and elsewhere [16,17]. Both of the sets of experiments reported in the literature used similar experimental arrangements with a working electrode positioned opposite an ultrasonic horn to provide efficient solution agitation. The work described in this chapter builds on these experiments and attempts to realise their potential in a 'real' system, namely the ASV detection of lead in wine.

The attractions of ASV for the analysis of metals in wine and related foodstuffs have been noted [18] but problems arise due to the adsorption of organic material on the electrode surface [1]. Pre-treatment procedures have been devised [4-9] the most successful of which reduce the levels of surface active material and / or release the metal ions bound in inorganic and organic complexes. In the following we will show that insonation permits quantitative measurements in white wine *without* problems of electrode fouling. Moreover the use of ultrasound to promote equilibration between 'free' and 'bound' metal cations allows reliable measurements *without* the need for elaborate sample pre-treatment. The *total* lead content as determined by sono-ASV will be seen to agree quantitatively with that established via atomic absorption spectroscopy (AAS) measurements.

5.3 MICROADDITION THEORY

In this section, relevant theory is developed concerning the use of microadditions of standard lead for the calibration of the *total* lead content of the wine via sono-ASV.

5.3.1 ASV RESPONSE RESULTING FROM STANDARD MICROADDITION

The lead present in wine will comprise Pb^{2+} in either a state "bound" to the wine matrix or "free" in solution. The lead detected by ASV may not be the total amount of lead in the sample but merely reflect the unbound Pb^{2+}. The following equilibrium can be considered

$$Pb^{2+}_{(free)} \rightleftharpoons Pb^{2+}_{(bound)} \tag{5.1}$$

The equilibrium constant, K_{eq}, for the above reaction is given by

$$K_{eq} = \frac{[Pb^{2+}_{(bound)}]}{[Pb^{2+}_{(free)}]} \tag{5.2}$$

and the total concentration of lead, $[Pb^{2+}_{(tot)}]$, is given by the equation

$$[Pb^{2+}_{(tot)}] = [Pb^{2+}_{(free)}] + [Pb^{2+}_{(bound)}] \tag{5.3}$$

If a small volume of aqueous lead standard solution (experimentally typically of the order of 10 to 100 µl) is added to the sample (a "standard microaddition") then the total composition can be described by

$$[Pb^{2+}_{(tot)}] = [Pb^{2+}_{(wine)}] + [Pb^{2+}_{(\mu a)}] \tag{5.4}$$

where $[Pb^{2+}_{(wine)}]$ is the initial total concentration in the wine and $[Pb^{2+}_{(\mu a)}]$ is the additional total concentration due to the microaddition. Assuming only $Pb^{2+}_{(free)}$ is detected by the ASV then to proceed, Equation (5.3) is substituted into (5.2) to give

$$K_{eq} = \frac{[Pb^{2+}_{(tot)}] - [Pb^{2+}_{(free)}]}{[Pb^{2+}_{(free)}]} \tag{5.5}$$

Substituting (5.4) into (5.5) gives

$$K_{eq} = \{[Pb^{2+}_{(wine)}] + [Pb^{2+}_{(\mu a)}]\}\left(\frac{1}{[Pb^{2+}_{(free)}]}\right) - 1 \tag{5.6}$$

If Equation (5.6) is rearranged into the following form

$$[Pb^{2+}_{(free)}] = \frac{1}{K_{eq}+1}[Pb^{2+}_{(\mu a)}] + \frac{1}{K_{eq}+1}[Pb^{2+}_{(wine)}] \tag{5.7}$$

it suggests that if $[Pb^{2+}_{(free)}]$ is plotted against $[Pb^{2+}_{(\mu a)}]$ then the concentration in the wine is given by

$$[Pb^{2+}_{(wine)}] = \frac{\text{intercept}}{\text{gradient}} \tag{5.8}$$

The value of $[Pb^{2+}_{(free)}]$ is directly proportional to a stripping peak area, A_{peak} (C), and the ASV results can therefore be analysed by plotting a graph of A_{peak} vs. $[Pb^{2+}_{(\mu a)}]$ where $[Pb^{2+}_{(wine)}]$ is again given by Equation (5.8).

5.4 EXPERIMENTAL

The well characterised [19] and thermostatted (25 ± 2°C) sono-electrochemical cell employed in this work is shown in Figure 2.1. The cell volume was ca. 250 cm^3. For the sono-ASV experiments the ultrasonic intensity was set to 26.0 ± 0.5 W cm^{-2}. This intensity was chosen as a good balance between providing high mass transport whilst causing minimal ablation of the mercury film.

The wine used was a dry white Italian Chardonnay (Stowells of Chelsea, London). This was supplied in a wine box thus avoiding any variable sample contamination through lead salts deposited on the necks of corked bottles protected by lead foils. Samples were prepared by adding 88 cm^3 0.0968 N nitric acid to 162 cm^3 wine. All other standard experimental procedures were as outlined in Chapter 2.

The working electrode was placed opposite a sonic horn at a horn-electrode separation of 10 mm for the sono-ASV experiments. The mercury film for sono-ASV experiments was prepared ex-situ in a mechanically stirred solution of 5 mM $Hg(NO_3)_2$ at pH 2 by holding the potential of a 4 mm diameter platinum disc at 0 V (vs. SCE) for 10 minutes. The resulting electrodes were characterised by atomic force microscopy in the previous chapter. The effect of ultrasound on the mercury coats was also reported.

For comparison of total lead content experiments were conducted using atomic absorption spectroscopy (AAS) according to standard protocols known to give the *total* lead content [20-23]. The analyses were conducted 'blind' using Perkin Elmer A-Analyst™100 Atomic Absorption Spectrometers operated by the Prof. Andrew Smith group in the Plant Sciences Department of Oxford University and also independently by Warwick Analytical Services (Coventry).

5.5 RESULTS AND DISCUSSION

Once the sono-electrochemical cell was calibrated as described in Chapter 3 it was possible to make reliable and meaningful measurements in sono-ASV experiments. Specifically for 26 W cm^{-2} ultrasound intensity a 10 mm horn-electrode separation corresponded to a

diffusion layer thickness of 3.2 μm for Pb^{2+} at a 4 mm diameter Hg/Pt disc working electrode, using a value of D for Pb^{2+} of $1.03 \pm 0.05\ cm^2\ s^{-1}$ (see Chapter 4). The experiments for detecting lead in wine were subsequently performed at this intensity and separation.

The ultrasonic pre-concentration time for formation of the lead amalgam from Pb^{2+} ions in the sample at the plated 4 mm diameter Hg/Pt electrode was 4 minutes at -1.0 V (vs. SCE). The ultrasound was then switched off. The potential was swept anodically at a scan rate of 50 mV s^{-1} and the area of the lead stripping peak calculated. A typical voltammogram is seen in Figure 5.1. Integration of the peak yielded the amount of charge deposited onto the electrode. To deduce the concentration of lead in the wine sample a series of

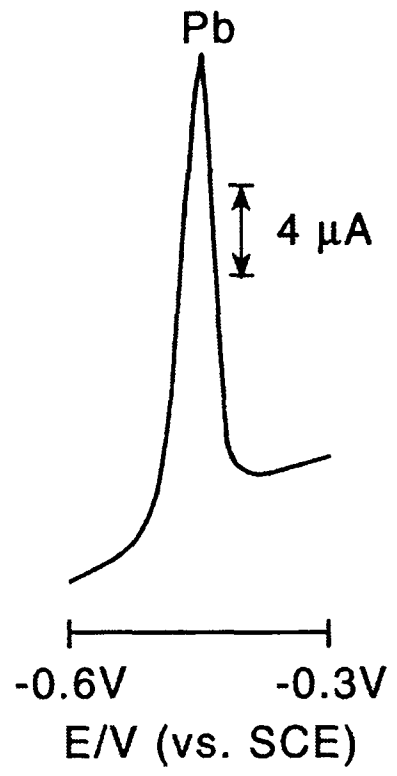

Figure 5.1 Stripping response for wine after the addition of 128 μg l^{-1} Pb^{2+} obtained at a scan rate of 50 mV s^{-1} on a 4 mm Hg/Pt electrode after 4 minutes deposition at -1.0 V (vs. SCE) under 26 W cm^{-2} ultrasound.

microadditions of 100 μl of lead analytical standard (Aldrich, 1 ml = 0.1 mg of Pb) were made to the test solution. Each addition was sonicated for 10 minutes to allow equilibration and complete mixing to occur before peak areas were recorded as before. The results of a typical experimental run are shown in Table 5.1.

Total amount of Pb^{2+} standard added (±10%) / μl	Stripping Peak Area (± 30%) / μC
0	3.4
10	3.7
20	5.0
120	9.4
220	15.1
320	20.8
420	29.6
520	40.3

Table 5.1 Typical results obtained for sono-ASV analysis of a white Chardonnay wine as detailed in the text.

After conversion of the amount of standard Pb^{2+} solution added to a concentration (μg l^{-1}) the results in Table 5.1 were then analysed as suggested by Equation (5.7). The resulting plot is shown in Figure 5.2 which shows a least squares regression analysis of the data. The value for $[\,Pb^{2+}_{(wine)}\,]$ yielded by sono-ASV after being scaled up for dilution effects was, for pure wine, 22 (± 6) μg l^{-1}. Returning to Figure 5.2 some curvature of the plot is

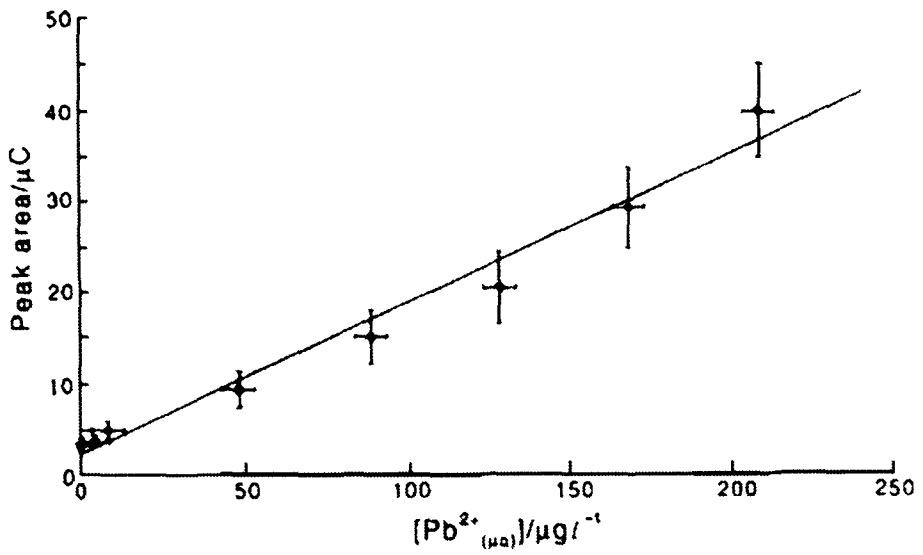

Figure 5.2 A graph showing the variation in peak area with addition of Pb^{2+}. The best-fit equation of the unsaturated situation is $A_{peak} = 0.166[Pb^{2+}_{(\mu a)}] + 2.35$ where A_{peak} is measured in μC and $[Pb^{2+}_{(\mu a)}]$ in μg l^{-1}.

evident: this may be attributable to a range of binding sites becoming saturated thus altering slightly the pertinent values of K_{eq}.

Last for comparison the total lead content in the wine was obtained by AAS which is the current standard method [21] for total lead detection in wine samples. Two independent values for $[Pb^{2+}_{(wine)}]$ were obtained by separate laboratories and found to be 24 and 27 (± 4) μg l^{-1}. The agreement between the two techniques is excellent confirming that the sono-ASV method can be reliably used to give *total* lead content data.

5.6 CONCLUSIONS

The level of agreement between the AAS and ASV results reported in the preceding section is highly satisfactory suggesting that ASV can be reliably used as an alternative to the presently accepted procedures [20-23] with corresponding benefits of speed, cost and simplicity of approach. In addition the possibility of portable electrochemical equipment for reliable heavy metal analysis appears viable.

It is noted that previous attempts to employ ASV for lead detection have been unsuccessful in that typically only ~50% of the lead levels detected by AAS were recorded [18]. The benefits of insonation may likely be first the maintenance of a clean, active electrode surface to ensure the uptake of metal from the range of complex lead cation species grouped under the label "free" lead in the above treatment and second, the maintenance of equilibration between 'free' and 'bound' ions as described by the equilibrium constant K_{eq}. A particular merit of the procedure described is that the wine is analysed directly without the need for the removal or destruction of organic matter via elaborate and lengthy pre-treatment strategies [18,20].

5.7 OUTLOOK

The work in this and the previous chapter along with previous literature reports [16,17] suggests that 'sono-electroanalysis' is an excellent tool for quantitative analysis especially in complex and / or 'dirty' media. In the next chapter, the possibility of electroanalysis in a mixed phase system is investigated. Chapters 8 and 9 will further employ the use of sonovoltammetry for the determination of aqueous ascorbic acid.

5.8 CHAPTER 5: REFERENCES

[1] S. Mannino, J. Wang, *Electroanalysis* **1992**, *4*, 835.

[2] J. Wang, *Stripping Analysis*, VCH, Deerfield Beach, FL, **1985**.

[3] S. Daniele, M. A. Baldo, P. Ugo, G. A. Mazzocchin, *Anal. Chim. Acta* **1989**, *219*, 9.

[4] H. W. Nurnberg, *Electrochemistry in Research and Development* (Eds. R. Kalvoda, R. Parsons), Plenum Press, NY, **1985**, pgs. 121-149.

[5] S. K. C. Chang, E. Holm, J. Schwarz, P. Rayas-Duarte, *Anal. Chem.* **1979**, *168*, 353.

[6] L. Sipos, J. Golimoski, P. Valenta, H. W. Nurnberg, *Frensius' Z. Anal. Chem.* 1979, *298*, 1.

[7] J. Golimoski, K. Golimoski, *Anal. Chim. Acta* **1996**, *325*, 111.

[8] S. Mannino, *Riv. Vitic. Enol. Conegiano* **1982**, *6*, 297.

[9] D. Jagner, S. Westerlund, *Anal. Chim. Acta.* **1980**, *117*, 159.

[10] D. J. Walton, S. S. Phull, *Adv. Sonochem.* (Ed. T. J. Mason) **1996**, *4*, 205.

[11] R. G. Compton, J. C. Eklund, F. Marken, *Electroanalysis* **1997**, *7*, 509.

[12] F. Marken, R. P. Akkermans, R. G. Compton, *J. Electroanal. Chem.* **1996**, *415*, 55.

[13] T. J. Mason, J. P. Lorimer, *Sonochemistry: Theory, Applications and Uses of Ultrasound in Chemistry,* Ellis Horwood, Chichester, **1988**.

[14] J. Klima, C. Bernard, C. Degrand, *J. Electroanal. Chem.* **1995**, *399*, 147.

[15] R. G. Compton, J. C. Eklund, S. D. Page, T. J. Mason, D. J. Walton, *J. App. Electrochem.* **1996**, *8*, 775.

[16] F. Marken, T. O. Rebbitt, J. Booth, R. G. Compton, *Electroanalysis* **1997**, *9*, 19.

[17] F-M. Matysik, S. Matysik, A. M. O. Brett, C. M. A. Brett, *Anal. Chem.* **1997**, *69*, 1651.

[18] M. A. Baldo, C. Bragato, S. Daniele, *Analyst* **1997**, *122*, 1.

[19] R. G. Compton, J. C. Eklund, S. D. Page, *J. Phys. Chem.* **1995**, *99*, 4211.

[20] P. B. Zeeman, L. R. P. Butler, *Appl. Spectrosc.* **1962**, *16*, 120.

[21] P. M. Bersier, J. Howell, C. Bruntlett, *Analyst* **1994**, *119*, 219.

[22] *Perkin Elmer A-Analyst™100 Instruction Manual*, PE, USA, **1996**.

[23] Office International de la Vigne et du Vin, *Recueil des Méthodes Internationales d'Analyse des Vins et des Mouts*, OIVV, Paris, **1990**.

6

SONO-ELECTROANALYSIS: DETECTION OF LEAD IN PETROL

CHAPTER 6: SONO-ELECTROANALYSIS: DETECTION OF LEAD IN PETROL

6.1 CONTENTS

In this chapter we build on the anodic stripping voltammetric methodologies employed in Chapters 4 and 5 and extend them to electroanalysis in aqueous/organic phase emulsions. Some of the work in this chapter is reproduced in a paper accepted for publication in *Electroanalysis* in May 1999. The quantitative detection of lead in petrol is shown to be possible by anodic stripping voltammetry in aqueous media under conditions of insonation-induced emulsification. An immersion horn probe is introduced into a thermostatted conventional three-electrode cell opposite a mercury-plated platinum disc working electrode. Under ultrasonic emulsification of the sample, lead is pre-concentrated as an amalgam on the Hg/Pt electrode surface via reduction at -1.0 V (vs. SCE). The large mass transport associated with power ultrasound makes this step highly efficient. Subsequently the lead is quantified by applying an anodic linear sweep of the potential from -1.0 V to -0.15 V (vs. SCE) so as to oxidise the Pb(0) to Pb (II). The area under the stripping peak gives a measure of the lead formed during the initial step. By use of standard microaddition of lead to the solution the system can be calibrated to give the *total* amount of lead present in the petrol sample. Experiments using samples of 4 star leaded petrol gave a total lead content of 380 ± 40 mg l^{-1}. This value was in quantitative agreement with that obtained 'blind' by an independent laboratory using atomic absorption spectroscopy (AAS).

In addition to the high mass transport and emulsification insonation offers the crucial benefits of first surface activation and cleaning, helping to prevent electrode fouling by the organic components of petrol and second the complete extraction of lead from the water-insoluble target phase.

6.2 INTRODUCTION - CURRENT METHODS FOR LEAD DETECTION

Many methods of varying complexity have been reported for the detection of lead in petrol. The most widely used methods are based on atomic absorption spectroscopy (AAS) [1] and involve stabilisation of the petrol prior to analysis. Several authors first attempted analysis during the 1960s using iso-octane or butanone as a sample diluent [2-5] but difficulties were encountered as different alkyl lead compounds gave different responses. Subsequently, the use of petrol pre-treatment with iodine or bromine at elevated temperatures prior to flame AAS was employed to counter this [6-8] Other reported methods for lead analysis in petroleum include inductively coupled plasma mass spectrometry (ICP-MS) [9] and differential pulse anodic stripping voltammetry after decomposition of the organolead compounds with concentrated nitric acid then ashing at 300°C [10]. A method involving stripping potentiometry was reported by Jagner *et al.* [11] with a sample pre-treatment to dilute the petrol sample in a matrix containing ethanol, nitric acid, mercury ions and detergent. Polarography after treatment with iodine monochloride was investigated [12] whilst the extraction of lead and other heavy metals from waste oils using ultrasound and acid digestion has also been reported [13]. None of these methods is both fast and straightforward, whilst at the same time avoiding the use of high temperatures or flames that are hazardous in a refinery environment. Owing to the continuing focus on total lead concentrations in petrol [14,15], there is increasing demand for simple and rapid methods of determination.

6.3 ANODIC STRIPPING VOLTAMMETRY OF LEAD IN PETROL

6.3.1 PRELIMINARY ATTEMPTS

The possibility of detecting lead in petrol without the need for elaborate sample pre-treatments or emulsification agents was investigated. Anodic stripping voltammetry was chosen as a simple yet sensitive technique for the detection of lead in solution as documented in Chapters 4 and 5. Ultrasound was deployed to emulsify the immiscible phases of organic

petrol and dilute aqueous acid. Furthermore ultrasound was then applied during the pre-concentration step of a routine, aqueous, ASV experiment in order to reduce any Pb^{2+} in solution into an amalgam.

Prior to the work undertaken it was not known whether the transfer of lead from the organic phase into the mercury droplets could be achieved. Furthermore there was no precedent to suggest a mode of transfer should this be possible. A background electrolyte of 0.1 M nitric acid was used to allow the breakdown of the lead tetraethyl in the aqueous phase should this be necessary.

Initial experiments were conducted in the trial sono-electrochemical cell shown in Figure 2.2 with a 12 ml solution of 0.1 M nitric acid and a 4 mm platinum working electrode, mercury-plated in accordance with the procedure outlined in section 2.1. Small quantities of petrol were added to the solution of 0.1 M nitric acid. The two phase system was emulsified using 52 W cm^{-2} of 20 kHz ultrasound, delivered from a 3 mm stepped horn transducer, using a horn to electrode separation of 7 ± 0.5 mm.

Under these conditions it was found that it *was* possible to obtain lead anodic stripping voltammetric signals by the following procedure. First the potential at the electrode was held at 0 V (vs. SCE) to strip out any residual target metal from the electrode surface. Second the electrode potential was switched to -1.0 V (vs. SCE) for a period of 240 seconds under 52 W cm^{-2} ultrasound. The system was only sonicated during the electrolysis and was 'silent' at all other times. Third the electrode was subjected to a linear potential sweep from -1.0 V to –0.15 V (vs. SCE). This three step procedure is summarised in Figure 6.1.

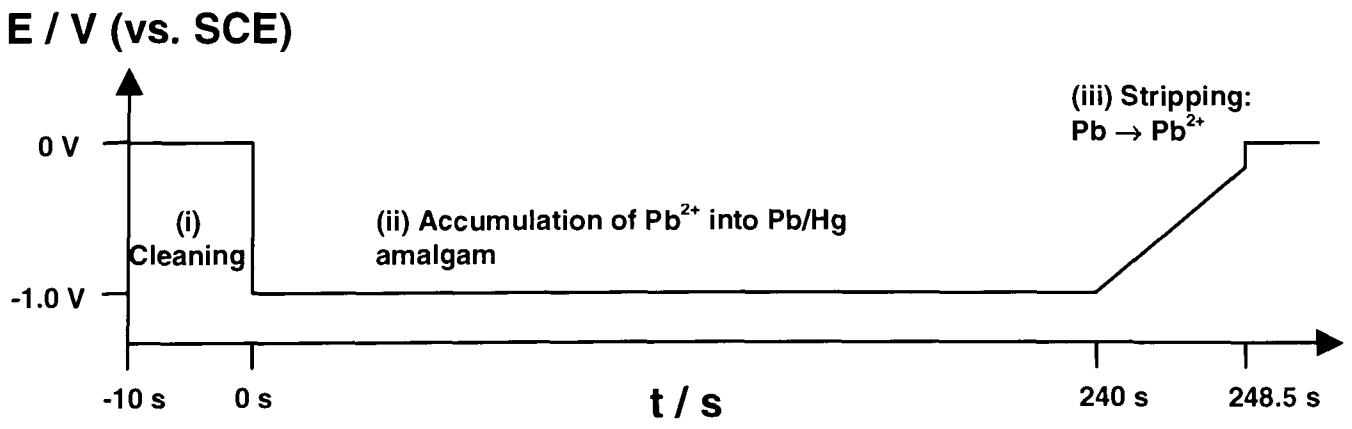

Figure 6.1 The schematic potential sweep profile for the detection of lead in petrol with i) 10 s at 0 V (vs. SCE) to clean any residual target metal from the electrode surface, ii) an accumulation at -1.0 V (vs. SCE) for 4 minutes under 52 W cm^{-2} of ultrasound and iii) a linear stripping scan from -1.0 V to -0.15 V (vs. SCE) at 100 mV s^{-1}.

The linear potential sweep stripped the lead out of the Hg/Pb amalgam and into solution as Pb^{2+}. Repetition of the three step procedure of (i) cleaning, (ii) accumulation and (iii) stripping caused the anodic stripping peak to grow in size and then start levelling off. This was consistent with the notion of accumulating lead from two sources in step (ii), namely the petrol, in which there remained lead to be extracted and/or the aqueous solution, which now contained Pb^{2+} from previous stripping experiments. Initially only the former source was important but the latter source came to dominate when much of the lead had been extracted from the organic petrol phase.

The anodic stripping peaks shown in Figure 6.2 were attributed to the oxidation of Pb(0) to Pb(II) first as evidenced by comparison to data in Chapters 4 and 5 and second in the light of the observation that addition of Pb(II) to the aqueous phase increased the size of the observed peak.

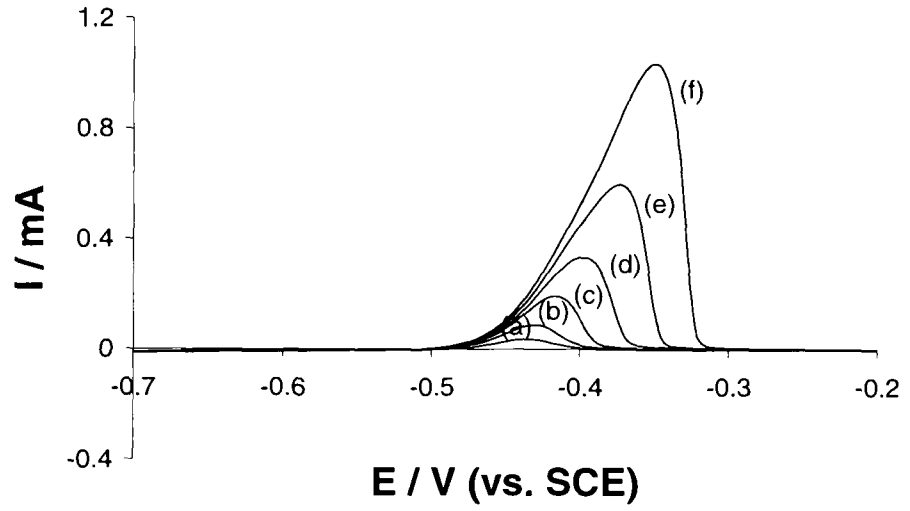

Figure 6.2 Anodic LSVs at 100 mV s^{-1} at a 4 mm Pt/Hg disc for 120 µl of petrol added to 12 ml of 0.1 M nitric acid. The accumulation times at –1.0 V (vs. SCE) under 52 W cm^{-2} ultrasound power were a) 7s, b) 15 s, c) 30 s, d) 60 s, e) 120 s and f) 240 s.

Figure 6.2 shows typical linear sweep voltammograms (LSVs) obtained using 120 µl of petrol detected on a 4 mm mercury-plated platinum electrode. LSVs (a) to (f) correspond to different accumulation times in the range 7 – 240 s at –1.0 V (vs. SCE) under 52 W cm^{-2} of ultrasound (i.e. for step (ii) in Figure 6.1). The peak heights and areas increase with accumulation time. This is simply because with more time for lead to accumulate in the amalgam there is more lead to be subsequently stripped out. The peak position is also observed to shift, from –0.43 V to –0.35 V (vs. SCE) as the accumulation time is increased from 7 s to 240 s, because of diffusion-limited transport within the mercury droplets.

Integration of the peaks in Figure 6.2 showed that the total stripping charge scaled in a linear fashion with the accumulation time. This is shown in Figure 6.3. The discovery that

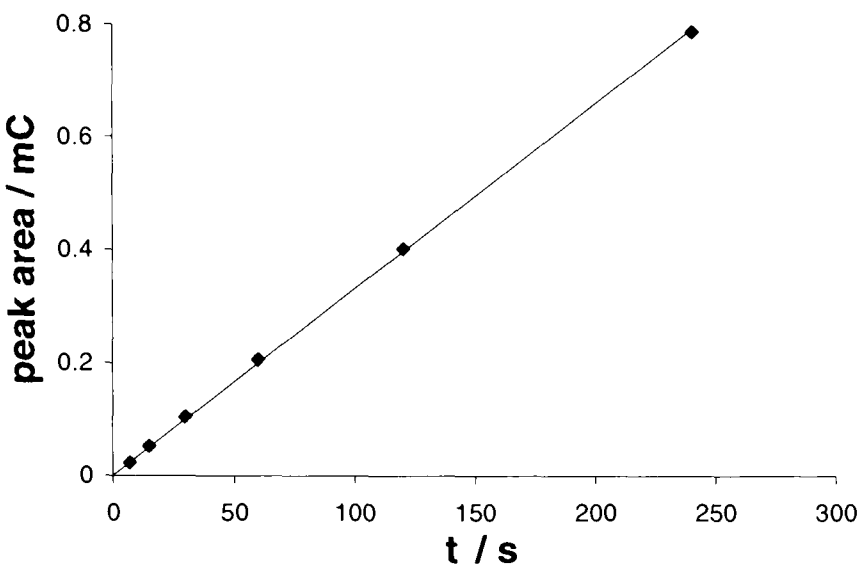

Figure 6.3 Plot of charge against accumulation time for the lead stripping peaks at a 4mm Pt/Hg disc for 120 µl of petrol added to 12 ml of 0.1 M nitric acid.

the mercury-plated platinum electrode so reliably gave peak areas proportional to accumulation time indicated that the system should in principle be sufficiently sensitive and reliable to give peak areas which scale with the concentration of lead in solution.

6.3.2 USE OF SONICATION AND NEGATIVE ACCUMULATION POTENTIAL

Experiments were conducted in the initial sono-electrochemical trial cell (as shown in Figure 2.2) with 80 µl petrol added to 12 ml 0.1 M nitric acid solution. The horn was fixed at a separation of 7 mm over the 4 mm mercury-plated platinum electrode. The aim was to ascertain which elements of the accumulation period at –1.0 V (vs. SCE) were essential for the extraction of lead from the organic petrol phase into the electrode surface mercury droplets. The three experiments described below were conducted sequentially using the set-up described above.

(a) Electrolysis at –1.0 V (vs. SCE) for ca. 10 mins in the *absence of ultrasound* was attempted but as expected failed absolutely to detect any lead because the petrol phase simply floated above the aqueous phase. This is an example of a situation in which a key advantage of ultrasound, namely emulsification, is essential for electroanalysis.

(b) In the same apparatus sonication was conducted for 1 hour in the *absence of any electrolysis* (the wires to all electrodes being disconnected). This also led to no release of any detectable lead, this time after 1 hour. The accumulation step (ii) at –1.0 V (vs. SCE) is, therefore, essential for the extraction of lead from the organic petrol phase into the electrode surface amalgam.

(c) Using the same set-up, it was found that LSVs similar to those shown in Figure 6.2

could be obtained when electrolysis and ultrasound were used simultaneously once again.

6.4 PHASE TRANSFER OF LEAD

The lead tetraalkyl is initially dissolved in the organic petrol phase. It is accumulated on the electrode surface in the liquid mercury phase under simultaneous electrolysis and ultrasound. But does the lead transfer directly from the organic petrol phase into the liquid mercury phase or through an intermediate stage of dissolution in aqueous solution? The two possible mechanisms are represented in Figure 6.4.

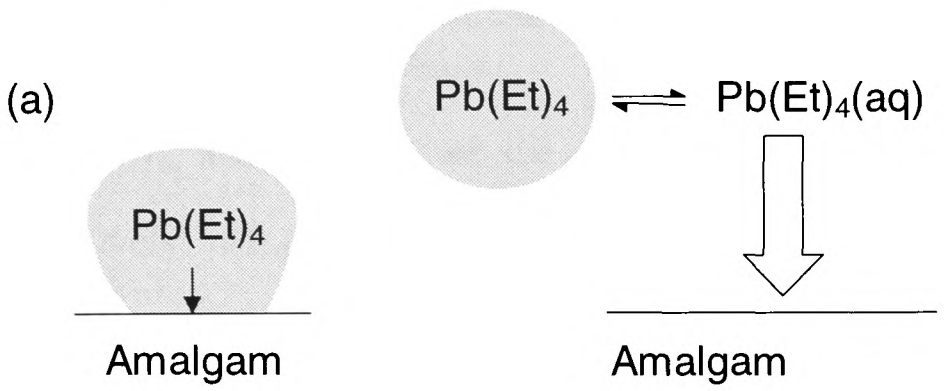

Figure 6.4 Models for the transfer of lead from the organic petrol phase into the mercury amalgam phase (a) directly and (b) via the intermediary stage of dissolution in aqueous solution.

In order to test this, two model systems were required: one in which the solute would partition appreciably into the aqueous phase and one in which the solute was essentially insoluble in aqueous solution. The simplest method for determining partition coefficients is by UV-visible spectroscopy. This requires solutes with strong chromophores to be found. Iodine (with a measured absorption peak at 522 nm) and ferrocene (with measured absorption peaks at 324 nm and 441 nm) were chosen. Petrol is mostly made up of octane so this was chosen as the organic phase.

Peak absorbances in octane - all of which were below the limit of reasonable applicability of Beer's Law at ca. 2.0 absorbance units - were measured at the respective peak positions over a range of known concentrations (0 – 11.4 mM ferrrocene in octane and 0 – 3.4 mM iodine in octane). Calibration lines were fitted to the data by the method of least squares giving R^2 values in excess of 0.998.

Solutions of 9.68 mM ferrocene and 4.02 mM iodine in octane were prepared and combined in various proportions with 0.1 M nitric acid. Following vigorous shaking for one

minute and separation of the octane and aqueous phases, the organic phase was removed. UV-visible spectroscopy was then utilised to measure the absorbances of any iodine or ferrocene which had partitioned into the organic phase. No peaks were observed for ferrocene indicating that negligible partitioning took place.

The partition coefficient of iodine between water and octane is defined as:

$$K = \frac{[I_2]_{aq}}{[I_2]_{organic}} = \frac{\left\{ n(I_2, aq) \Big/ V_{aq} \right\}}{[I_2]_{organic}} \qquad (6.1)$$

where $[I_2]_{aq}$ and $[I_2]_{organic}$ are the concentrations of iodine in the water and octane phases respectively, $n(I_2,aq)$ is the number of moles of iodine in the aqueous phase and V_{aq} is the volume of the aqueous phase. The equation is recast as $y = KV_{aq}$ where $y = \left(n(I_2, aq)/[I_2]_{organic}\right)$. A plot of y against V_{aq} furnished a straight line ($R^2 = 0.996$) with a gradient of dimensionless K. The partition coefficient for iodine between water and octane (Equation 6.1) was thereby found to be $K = 0.030 \pm 0.002$, indicating appreciable partitioning of iodine into the aqueous phase. Assuming a minimum detectable peak height of 0.005 absorbance units and similar extinction coefficients for iodine and ferrocene, the absence of a detectable peak for ferrocene in the octane partition indicates a partition coefficient of $K \leq 0.003$ for ferrocene.

The electroactive species iodine and ferrocene were dissolved in octane, added to 12 ml 0.1 M potassium nitrate solution and emulsified via insonation in the cell shown in Figure 2.2. UV-visible spectroscopy showed that whilst appreciable partitioning of iodine into water occurred, negligible ferrocene was detected. Voltammetrically measurable currents were seen for the former but not the latter, suggesting that partitioning of lead tetraalkyl into the aqueous phase is a key step in the mechanism (Figure 6.4b) for the detection of lead in petrol.

6.5 PROPOSED MECHANISM FOR LEAD DETECTION IN PETROL

Longer electrolysis times gave proportionately more accumulation of lead from the petrol into the electrode surface amalgam phase (section 6.3.1). Simultaneous ultrasound and electrolysis at –1.0 V (vs. SCE) was found to be essential for the accumulation of lead (section 6.3.2). UV-visible spectroscopy and LSV experiments on ferrocene and iodine suggest that partitioning of lead tetraalkyl into the aqueous phase is also a key step in the process (section 6.4). A mechanism consistent with these observations is as follows:

$$(1) \qquad PbR_4(org) \overset{)))}{\rightleftharpoons} PbR_4(aq)$$

$$(2) \qquad PbR_4(aq) + 4e^- + 4H^+ \xrightarrow{-1.0\ V} Pb(amalgam) + 4RH$$

$$(3) \qquad Pb(amalgam) - 2e^- \xrightarrow{ca.\ -0.3\ V} Pb^{2+}(aq).$$

The first step involves the ultrasound assisted extraction of the tetraalkyl lead from the petrol phase. The possibility of homogeneous chemical transformation of the aqueous PbR_4 is not excluded [16-18]. However the extracted lead clearly undergoes reduction at the electrode surface whilst the latter is held at a potential of –1.0 V (step 2). Following accumulation the stripping step produces aqueous Pb^{2+} (step 3) and if the analytical procedure is repeated the latter builds up in solution. The observations thus far clearly indicate the potential suitability of sono-ASV for the quantitative detection of lead in petrol. This is explored in the remainder of the chapter.

6.6 TIME PROFILES FOR DETECTION PROCEDURE REPETITIONS

In section 6.3.1 it was shown that LSV could usefully be applied to the detection of lead in an organic petrol phase (Figure 6.2). Further experiments led to the conclusion that extraction of the lead into aqueous solution and then into the liquid amalgam phase were key steps (section 6.5). The next important question was whether complete extraction of the lead from the organic petrol phase into the aqueous solution phase could be achieved by means of ultrasound and electrolysis alone. Could this aqueous lead then be reliably sampled by

accumulation into the liquid amalgam phase? If so, a limiting lead stripping peak area would be expected, which would yield the charge passed and, by comparison with a calibration experiment, a value for the *total* lead content of petrol.

Further experiments were conducted in the sono-electrochemical trial cell shown in Figure 2.2 with 120 µl petrol added to 12 ml 0.1 M nitric acid solution and a separation of 7 mm between the horn and the 4 mm mercury-plated platinum electrode. The three step analytical procedure of (i) cleaning, (ii) insonated accumulation and (iii) stripping (as shown in Figure 6.1) was repeated many times in succession in an attempt to extract all the lead from the organic petrol phase into the aqueous solution phase. All initial attempts failed to achieve limiting peak areas for two main reasons. First, it took far too long to reach a maximum lead stripping peak area; around 40 repetitions of the three step procedure (including the 4 minute insonated accumulation) were required. This meant that each experiment took well over four hours to complete (see Figure 6.5). Second, the lead stripping peak areas did not limit but reached a maximum and then started decreasing again (also shown in Figure 6.5). It was thought that this may be due to ablation of the mercury droplets from the platinum surface by four hours of power ultrasound, as was observed in Chapter 4.

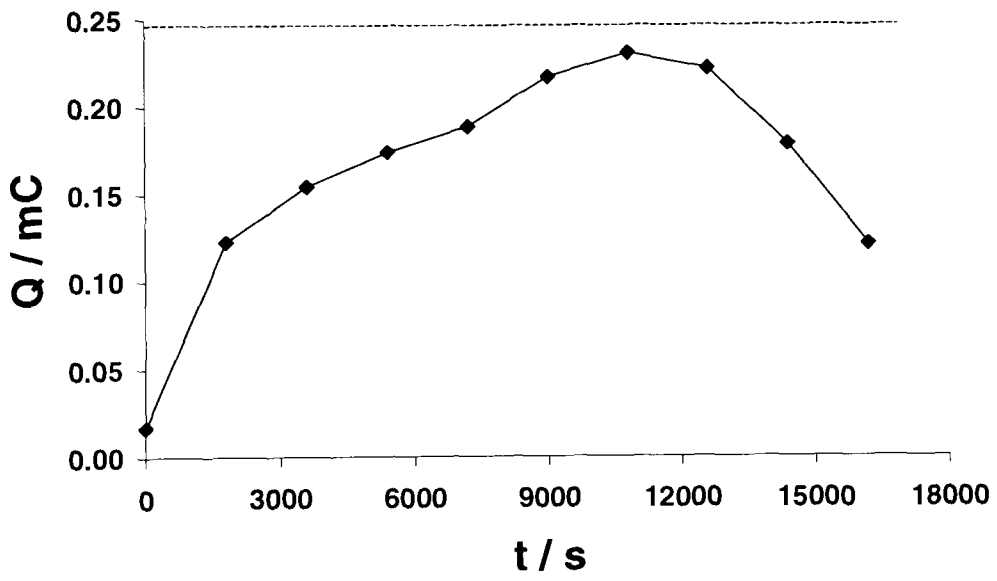

Figure 6.5 Plot of charge against cumulative accumulation time for the lead stripping peaks at a 4 mm Pt/Hg disc for 120 µl petrol added to 12 ml of 0.1 M nitric acid. Q_∞ has an estimated value of 0.24 mC.

Figure 6.5 shows the lead stripping peak areas as a function of the total cumulative accumulation time. The latter is the sum of all the times at which the working electrode was held at a potential of –1.0 V (vs. SCE) under 52 W cm^{-2} ultrasound.

It was realised that the apparatus employed thus far was much too slow for extracting the lead from the organic petrol phase into the aqueous solution phase and that it was necessary to find a quicker method of analysis both for accuracy and eventual viability as an analytical technique. The possibility that a chemical degradation step limited the full extraction and accumulation of the lead was investigated by using more concentrated nitric acid. Repetition of the experiment in section 6.6 with 1.0 M nitric acid as the background electrolyte instead of 0.1 M nitric acid did not accelerate the extraction of lead from solution. It did however cause the peak areas to decay prematurely, possibly as a consequence of enhanced mercury oxidation. Accordingly attention turned to the dynamics of the cell instead.

6.7 LEAD EXTRACTION AS A FIRST ORDER PROCESS

It was proposed that the extraction of lead from the petrol emulsion into the Pb/Hg amalgam electrode coating was transport limited. In order to verify this, a comparison was made between the half-lives for

(i) the sono-electrochemical extraction of lead tetraalkyl from the petrol emulsion and

(ii) the simple quantitative reduction of hexaammineruthenium (III) chloride.

It was assumed that for a fully dissolved substrate (X) in a solution volume, V, at an electrode area, A, the rate of depletion is given by:

$$V\frac{d[X]}{dt} = -\frac{D[X]A}{\delta} \qquad (6.2)$$

for transport limited conditions where δ is the thickness of the diffusion layer. The half-life for the removal of X is therefore:

$$t_{1/2} = \frac{\delta V \ln 2}{DA} = \frac{\ln 2}{k} \qquad (6.3)$$

where k, in s^{-1}, is the effective rate constant.

6.7.1 HALF-LIFE FOR THE FULL SONO-ELECTROCHEMICAL EXTRACTION OF LEAD FROM THE PETROL EMULSION

The amount of lead remaining to be extracted is proportional to $Q_\infty - Q$ where Q, in mC, is the area under the lead stripping peak and Q_∞ is the area under the lead stripping peak once all the lead has been extracted from the organic petrol phase into the aqueous solution. The total cumulative accumulation time is t. Assuming a first order process for extraction means:

$$(Q_\infty - Q) = Q_\infty e^{-kt} \tag{6.4}$$

For the full sono-electrochemical extraction of lead from the petrol emulsion in 12 ml of 0.1 M nitric acid, the time profile in Figure 6.5 gives an approximate half life as:

$$t_{1/2} = \frac{\ln 2}{k} = \frac{\ln 2}{0.000156\ s^{-1}} = 4440\ s \tag{6.5}$$

which corresponds to 74 minutes (see Figure 6.6).

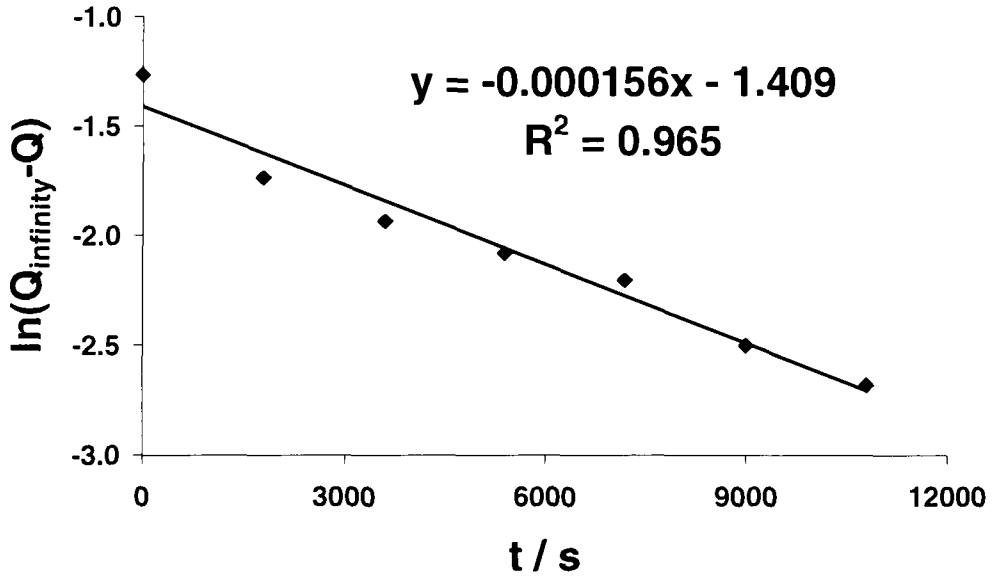

Figure 6.6 Plot of the log of the difference between the limiting charge and the charge against cumulative accumulation time for the lead stripping peaks at a 4 mm Pt/Hg disc for 120 µl of petrol added to 12 ml of 0.1 M nitric acid.

6.7.2 HALF-LIFE FOR THE ELECTROLYSIS OF HEXAAMMINERUTHENIUM (III)

A solution of $Ru(NH_3)_6^{3+}$ was exhaustively electrolysed at a reducing potential of -0.3 V (vs. SCE). The current was measured at frequent time intervals (see Figure 6.7). For the exhaustive electrolysis of $Ru(NH_3)_6^{3+}$ the current, I, for reduction is proportional to the concentration of $Ru(NH_3)_6^{3+}$, [Ru(III)], in solution:

$$\frac{d[Ru(III)]}{dt} \propto \frac{dI}{dt} = -kI \tag{6.6}$$

and using the gradient from Figure 6.8 gives:

$$t_{½} = \frac{\ln 2}{k} = \frac{\ln 2}{0.000130\ s^{-1}} = 5330\ s \tag{6.7}$$

which corresponds to 89 minutes.

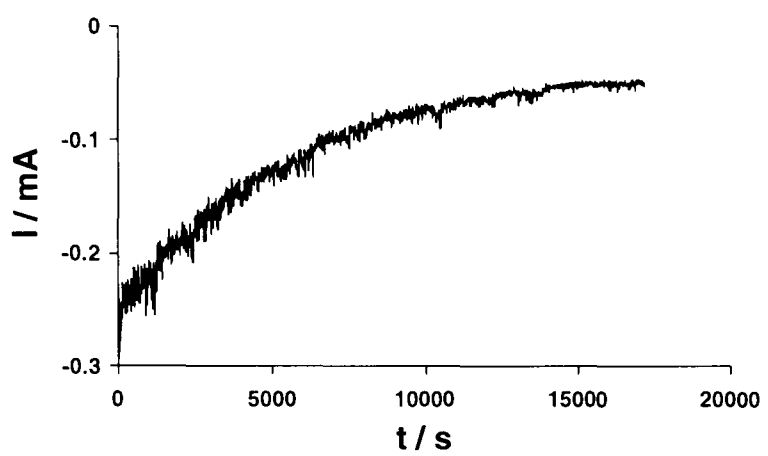

Figure 6.7 Plot of current against time for the quantitative reduction of $Ru(NH_3)_6Cl_3$ in 14 ml of 0.1 M KCl at a 4 mm Pt disc.

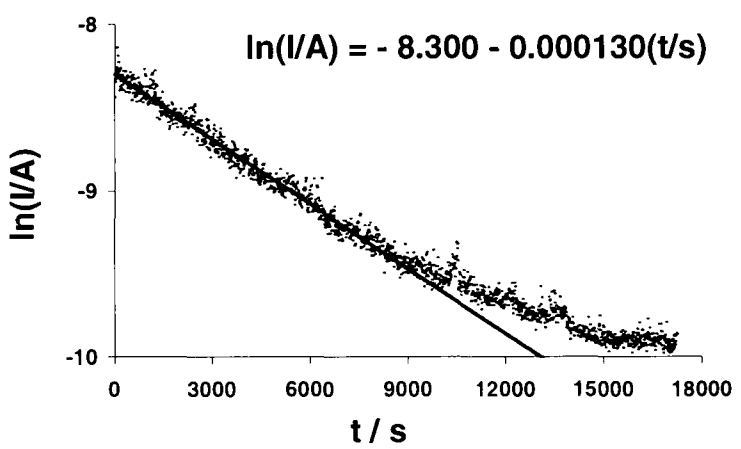

Figure 6.8 Plot of log (current) against time for the quantitative reduction of $Ru(NH_3)_6Cl_3$ in 14 ml of 0.1 M KCl at a 4 mm Pt disc.

6.7.3 TRANSPORT LIMITED CONDITIONS

The effective rate constants for the full sono-electrochemical extraction of lead from the petrol emulsion and the exhaustive electrolysis of $Ru(NH_3)_6^{3+}$ from aqueous solution can be compared using Equation (6.3) assuming that the diffusion layer thickness is the same in each case. For the former case [19]:

$$k_{Pb} = \frac{DA}{\delta V} = \frac{\left(1\times10^{-5}\ cm^2 s^{-1}\right)[\pi(0.2\ cm)^2]}{\delta(12\ cm^3)} = \frac{1.05\times10^{-7}\ cm\ s^{-1}}{\delta} \tag{6.8}$$

and for the latter case:

$$k_{Ru} = \frac{DA}{\delta V} = \frac{\left(9.1\times10^{-6}\ cm^2 s^{-1}\right)[\pi(0.2\ cm)^2]}{\delta(14\ cm^3)} = \frac{8.2\times10^{-8}\ cm\ s^{-1}}{\delta} \tag{6.9}$$

The effective rate constants for the full sono electrochemical extraction of lead from the petrol emulsion and the exhaustive electrolysis of $Ru(NH_3)_6^{3+}$ are similar to within 23% of one another. There is no chemical step in the reduction of $Ru(NH_3)_6^{3+}$. This implies that the full sono-electrochemical extraction of lead from the petrol emulsion is probably limited

by transport to the electrode surface amalgam, and not by a chemical degradation step. It was therefore decided that the sonoelectrochemical cell should be optimised so as to give the fastest possible extraction of lead from the petrol.

6.8 OPTIMISATION OF THE SONO-ELECTROCHEMICAL CELL

It was necessary to speed up – i.e. reduce the half-life for - the sono-electrochemical extraction of the lead from the petrol emulsion in order to overcome the problems outlined in section 6.6. Consideration of Equation (6.3), which is appropriate under transport limited conditions, indicated how this could be achieved. Desirable modifications to the cell were a larger electrode area, A, and a smaller cell volume, V. A larger diffusion layer thickness, δ, would also have been desirable. However, this could only have been achieved with a greater intensity of ultrasound and would unfortunately have increased the risk of damaging the mercury droplets on the platinum working electrode.

A new platinum electrode of 12 mm diameter was custom made by the mechanical workshops in the PTCL, Oxford University to give a 9-fold increase over the previous electrode area. The cell volume was additionally reduced to ca. 9 ml. No further reduction could be achieved whilst maintaining the horn at a suitably large immersion depth. The optimised cell is shown in Figure 6.9.

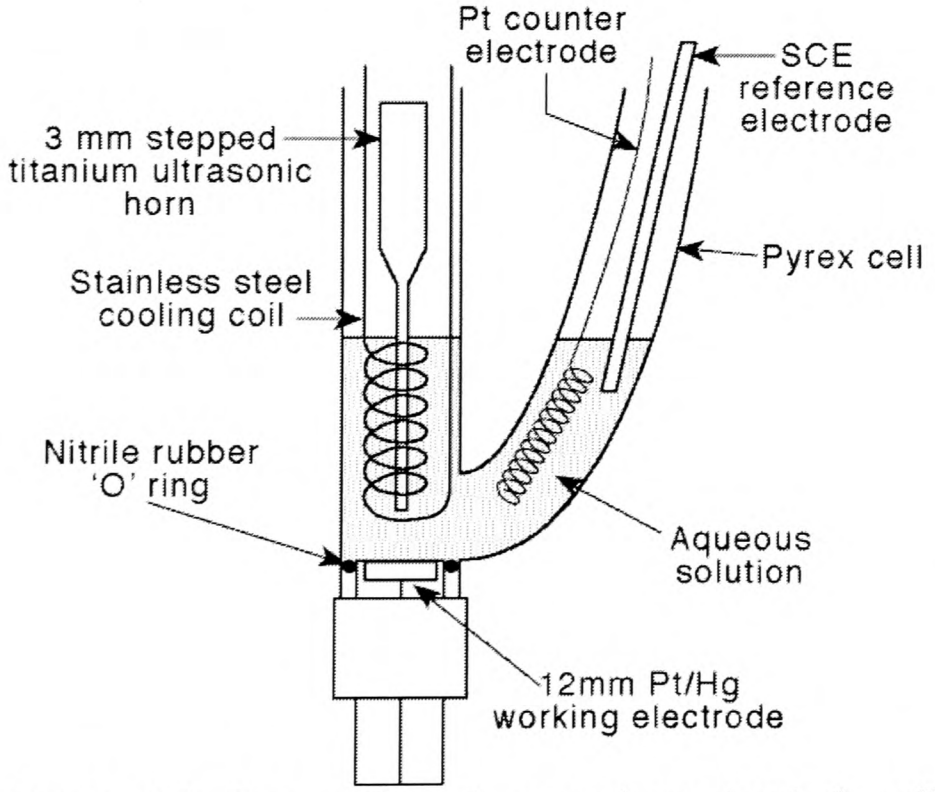

Figure 6.9 The optimised sono-electrochemical cell incorporating a 12 mm diameter Pt/Hg disc working electrode and the avoidance of 'dead volumes' in the cell.

6.9 A QUANTITATIVE PROCEDURE USING THE OPTIMISED CELL

Attention could now be focused on the development of a quantitative procedure based on the above observations and using the new sono-electrochemical cell shown in Figure 6.9. Accordingly experiments were conducted in which three additions of 5 µl of petrol were made stepwise to 0.1 M nitric acid at the start of the first insonated accumulation. The measured stripping signals using a pre-plated 12 mm platinum electrode are shown in Figure 6.10 and as a function of time in Figure 6.11. It can be seen that after ca. 2000 seconds the response has increased to a steady plateau which is not inconsistent with the complete extraction of organic lead into the aqueous phase. Figures 6.11 and 6.12(●) show that further additions lead to equivalent responses consistent with this notion.

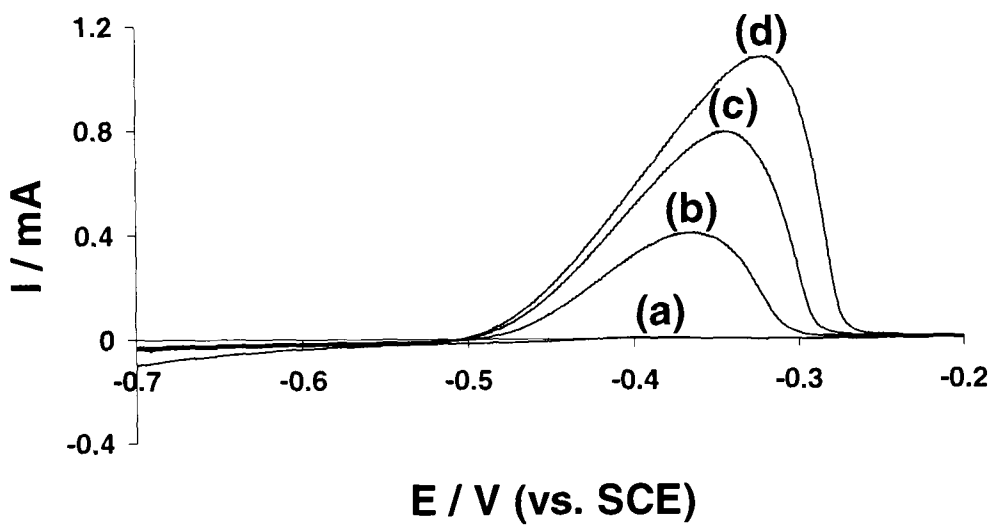

Figure 6.10 ASVs at 100 mV s^{-1} at a 12 mm Pt/Hg disc. Sweeps were performed after 4 minutes of accumulation at –1.0 V (vs. SCE) under 52 W cm^{-2} ultrasound for a) no petrol added, b) 5 µl, c) 10 µl and d) 15 µl of petrol added to 9 ml of 0.1 M nitric acid.

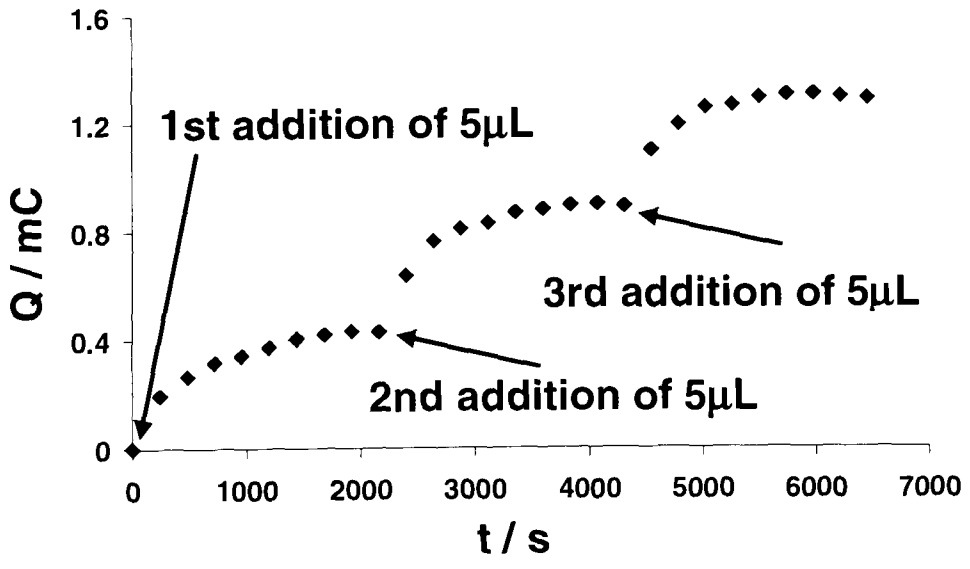

Figure 6.11 Plot of charge under the lead stripping peaks with time for consecutive additions of 5 µl of petrol to 9 ml of 0.1 M nitric acid. A 12 mm Pt/Hg disc electrode was used. Each point corresponds to an accumulation period of 4 minutes under 52 W cm^{-2} ultrasound at a horn-to-electrode distance of 7 mm.

Comparison of the data in Figures 6.5 and 6.11 clearly shows the improved speed and accuracy of lead determination achieved by optimising the sono-electrochemical cell.

The new sono-electrochemical cell was calibrated by making four additions of 0.1 mg/ml of aqueous Pb^{2+} lead standard stepwise to 0.1 M nitric acid at the start of the first insonated accumulation. The measured stripping signals using a pre-plated 12 mm platinum electrode are shown as a function of time in Figure 6.12(▲).

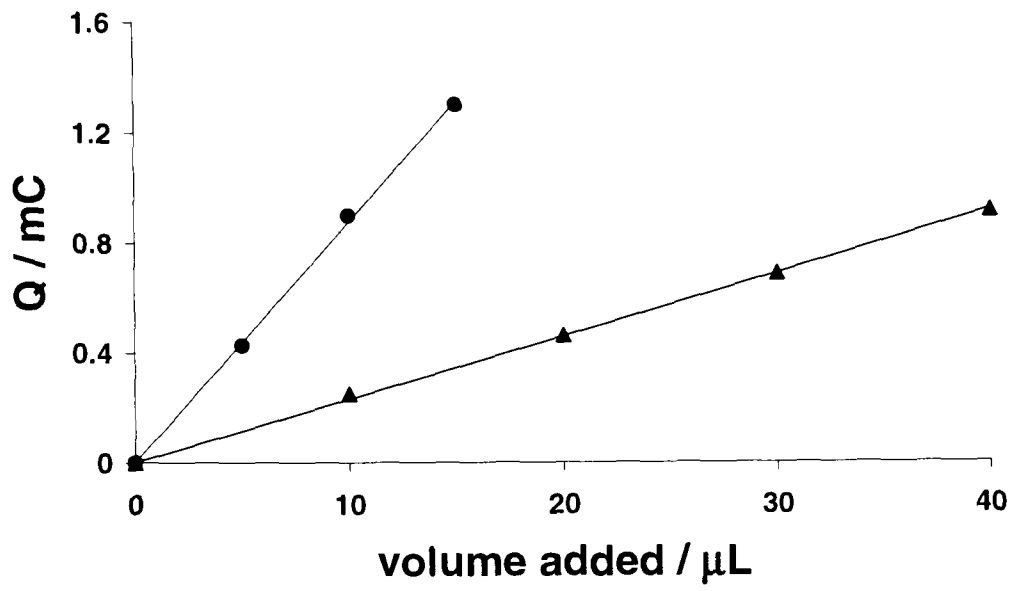

Figure 6.12 Plot of charge under the lead stripping peaks as a function of solution volume added for lead standard (▲) and petrol (●) microadditions to 9 ml of 0.1 M nitric acid. A 12 mm Pt/Hg disc electrode was used for 4 minute accumulation periods under 52 W cm^{-2} ultrasound at a horn-to-electrode distance of 7 mm.

The mean value of the three limiting values for each petrol addition was taken and plotted in Figure 6.12 against volume of petrol added. The gradients in Figure 6.12 allow a determination of the total lead content of petrol expressed in g/l:

$$[Pb]_{petrol} = \frac{0.087\ mC/\mu l}{0.023\ mC/\mu l} \times 0.1 g/l = 0.38 g/l \qquad (6.10)$$

This gives value of $380 \pm 40\ mg\ l^{-1}$ for the concentration of lead in petrol detected by sono-ASV.

For comparison of the total lead content a petrol sample was sent to Rooney Laboratories Ltd. (Basingstoke, UK) for independent analysis using atomic absorption spectroscopy (AAS) according to the Institute of Petroleum method no. 362/93 [20]. The lead concentration was found by this method to be $400 \pm 20\ mg\ l^{-1}$ which is in excellent quantitative agreement with the sono-ASV result.

6.10 CONCLUSIONS

6.10.1 SUCCESSFUL OPTIMISATION BY HALF-LIFE COMPARISON

The sono-electrochemical procedure outlined above permits a quantitative and absolute determination of the total lead content in petrol in a total time of ca. 2 hours *without* any sample pre-treatment. The rapidity of the procedure relies crucially on the optimisation of the cell to incorporate a large area (1.13 cm^2) electrode together with the minimisation of the total cell contents (9.0 ml) and the avoidance of 'dead volumes'. Quantitative two-electron reduction of 1.02 mM $CuSO_4$ at –0.6 V (vs. SCE) at a 12 mm Pt disc in 9.0 ml of 0.1 M Na_2SO_4 (Figure 6.13) allowed the half-life for reduction in the optimised cell to be determined (Figure 6.14):

$$t_{1/2} = \frac{\ln 2}{k} = \frac{\ln 2}{0.001865\ s^{-1}} = 372\ s \qquad (6.11)$$

which is equivalent to 6.2 ± 0.3 minutes.

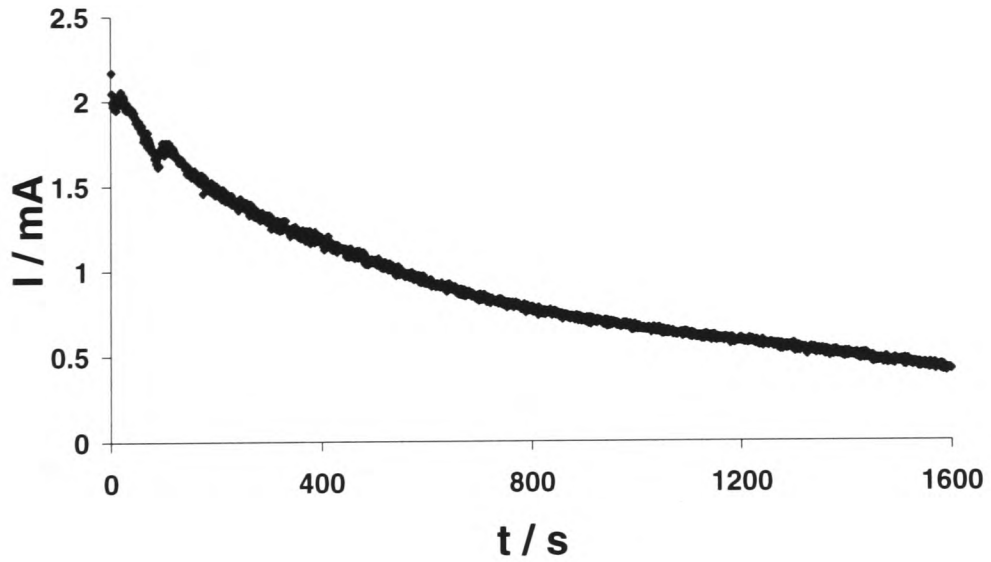

Figure 6.13 Variation of current as a function of time for the quantitative reduction of 1.02 mM copper (II) sulphate at -0.6 V (vs. SCE) at a 12 mm Pt disc in 9.0 ml of 0.1 M sodium sulphate.

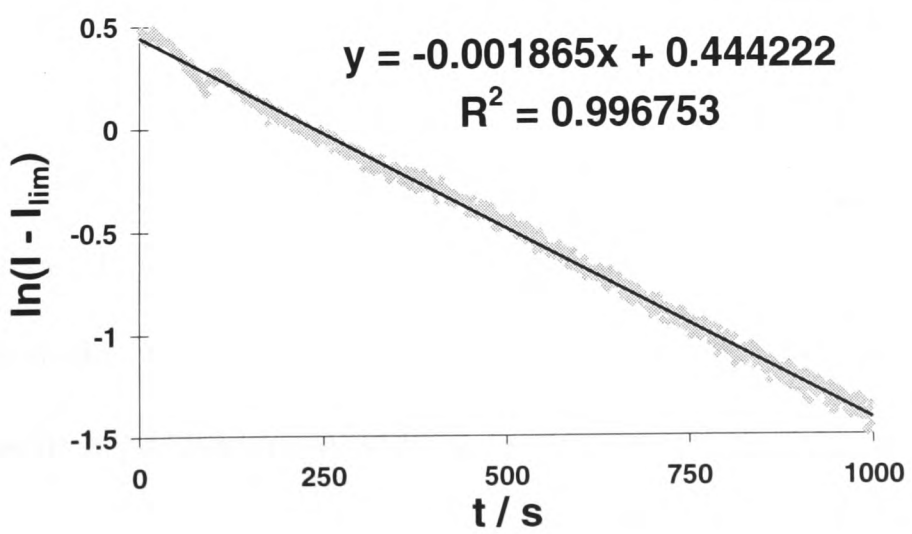

Figure 6.14 Plot of log of current against time for the quantitative reduction of 1.02 mM copper (II) sulphate at -0.6 V (vs. SCE) at a 12 mm Pt disc in 9.0 ml of 0.1 M sodium sulphate

Using Equation (6.3) gives:

$$\delta = \frac{DAt_{1/2}}{V \ln 2} = \frac{(8\times10^{-6}\,cm^2s^{-1})[\pi(0.6\,cm)^2](372\,s)}{(9\,cm^3)\ln 2} = 5.40\times10^{-4}\,cm \qquad (6.12)$$

A value of ca. 5.4 μm for δ is consistent with values measured under similar conditions [21].

Quantitative comparison of Figures 6.11 and 6.13 shows that the half-life for the full sono-electrochemical extraction of lead from the petrol emulsion is of the same order of magnitude as measured for the fully dissolved copper sulphate. This suggests that if the extraction from the organic phase provides a kinetic barrier then the rate of mass transport must be augmented in the case of the electrolysis of the emulsion by virtue of electroactive material leaving the organic droplets inside the diffusion layer so enhancing the rate of transport. Similar effects have been reported for electroactive solids dissolved in water / organic solvent emulsions [22].

6.10.2 SUITABILITY FOR DEPLOYMENT AS AN ANALYTICAL TECHNIQUE

The technique described above shows currents as large as 1 mA corresponding to the stripping of lead present at levels of ca. 400 mg l^{-1}. It is evident that useful measurable signals could be obtained with significantly lower lead levels, possibly of as much as two orders of magnitude, which would be consistent with detection of the increasingly lower lead levels being required by legislation. For many years tetraethyl lead was routinely added to petrol as an antiknock agent but its use has now been curbed due to its incompatibility with catalytic converters and environmental concerns.

Indeed unleaded petrol only is now available in, for example, the Netherlands and Germany, and the use of leaded petrol will be phased out in the EU from 2000 [15].

The level of agreement between the AAS and ASV results reported in section 6.9 is highly satisfactory suggesting that ASV can be reliably used as an alternative to the presently accepted procedures [1-13] with corresponding benefits of speed, cost and simplicity of approach; a particular advantage being the absence of *any* necessary sample pre-treatment.

The key to the whole technique is the rapid emulsification and mass transport afforded by the introduction of power ultrasound. In the next chapter we explore the utilisation of ultrasonically induced emulsions in the discipline of electrosynthesis.

6.11 CHAPTER 6: REFERENCES

[1] *IP Standards for Petroleum and its Products*, Part 1. Vol. 1. Institute of Petroleum, London, **1985**.

[2] J. W. Robinson, *Anal. Chim. Acta* **1961**, *24*, 451.

[3] R. M. Dagnall, T. S. West, *Talanta* **1964**, *11*, 1553.

[4] D. J. Trent, *Perkin-Elmer At. Abs. Newsletter* **1965**, *4 (9)*, 348.

[5] R. A. Mostyn, A. F. Cunningham, *J. Inst. Petrol.* **1967**, *53*, 101.

[6] M. Kashiki, S. Yamazoe, S. Oshima, *Anal. Chim. Acta* **1971**, *53*, 95.

[7] E. Cardelli, M. Cifani, M. Mecozzi, G. Sechi, *Talanta* **1986**, *33*, 279.

[8] C. G. Taylor, J. M. Trevaskis, *Anal. Chim. Acta* **1986**, *179*, 491.

[9] *Varian Instrument Applications* **1991**, *20*, 7.

[10] M. H. Pournaghi-Azar, A. H. Ansary-Fard, *Talanta* **1998**, *46*, 607.

[11] D. Jagner, L. Renman, Y. Wang, *Anal. Chim. Acta* **1992**, *267*, 165.

[12] J. L. Guinón, R. Grima, *Analyst* **1988**, *113*, 613.

[13] A. Fontana, C. Braekman-Danheux, C. G. Jung, *Fuel Process. Tech.* **1996**, *48*, 107.

[14] *Eurostat*: *Statistics in Focus*, Environment, no. 1/98 – see website at http://europa.eu.int/en/comm/eurostat/servern/home.htm.

[15] Directive 98/70/EC of the European Parliament.

[16] M. Morris, *J. Electroanal. Chem.* **1969**, *20*, 263.

[17] B. Fleet, N. B. Fouzder, *J. Electroanal. Chem.* **1979**, *99*, 215.

[18] *Encyclopaedia of the Electrochemistry of the Elements*, (Ed. A. J. Bard) Vol. 8, Marcel Dekker, New York, **1976**, pgs. 60-62.

[19] J. C. Eklund, S. D. Page, R. G. Compton, *J. Phys. Chem.* **1995**, *99*, 4211.

[20] Institute of Petroleum (Great Britain), *Standard Methods for Analysis and Testing of Petroleum and Related Products*, John Wiley, Chichester, UK, **1995**.

[21] H. A. O. Hill, Y. Nakagawa, F. Marken, R. G. Compton, *J. Phys. Chem.* **1996**, *100*, 17395.

[22] F. Marken, R. G. Compton, S. D. Bull, S. G. Davies, *J. Chem. Soc. Chem. Comm.* **1997**, 995.

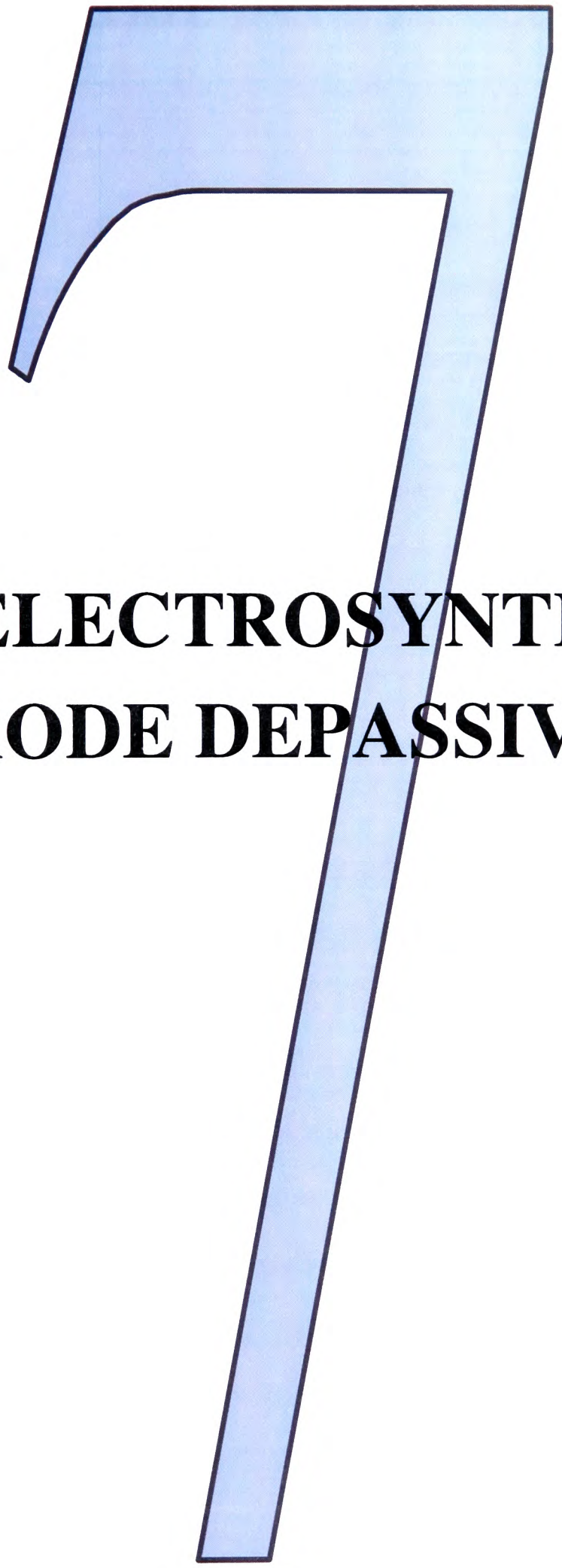

SONO-ELECTROSYNTHESIS: ELECTRODE DEPASSIVATION

CHAPTER 7: SONO-ELECTROSYNTHESIS: ELECTRODE DEPASSIVATION

7.1 CONTENTS

This chapter explores a new method of synthesis where ultrasound is employed for the promotion of emulsification of aqueous and organic phases. The electrosynthesis of water-insoluble products such as *leuco*-methylene green from soluble precursors can be accomplished using such an emulsion formed via insonation so that the organic phase constantly extracts the product and simultaneously prevents the electrode passivation which would occur in aqueous solution alone. Some of the work presented in this chapter is reproduced in a paper published in the *Journal of the Chemical Society, Chemical Communications* (**1999**, *12*, 115).

7.2 INTRODUCTION

The introduction of power ultrasound into electrochemical systems has many benefits [1,2] as discussed in Chapter 1. In the previous chapters the crucial factors were the extremely enhanced mass transport resulting from acoustic streaming [3] or microjetting [4] and electrode activation arising from cavitational erosion [5]. However, in addition ultrasound has been used to permit the electrochemical study of essentially water-insoluble organic species in aqueous solution [6,7, Chapter 6]. Sonication can therefore be seen as a convenient and effective alternative to the use of high-speed stirring and/or detergents for the promotion of emulsions for electrochemistry [8]. In this chapter a new and general use of ultrasound in electrosynthesis is reported, involving a novel emulsification technique. The presence of an organic phase which emulsifies under insonation is shown to lead to (i) 'clean' useful voltammetry, (ii) the extraction of reduction products and (iii) the preservation of electrode activity where in aqueous solution alone passivation would preclude useful electrosynthesis.

Many potentially viable electrode processes are inhibited if not entirely passivated by the adsorption, precipitation or polymerisation of reaction products or intermediates on the electrode surface. Two such reactions in aqueous solution are discussed here, the two-electron reduction of methylene green to *leuco*-methylene green [9-11] (shown in Figure 7.1) and the oxidation of iodide to solid iodine [12-14], both at platinum electrodes.

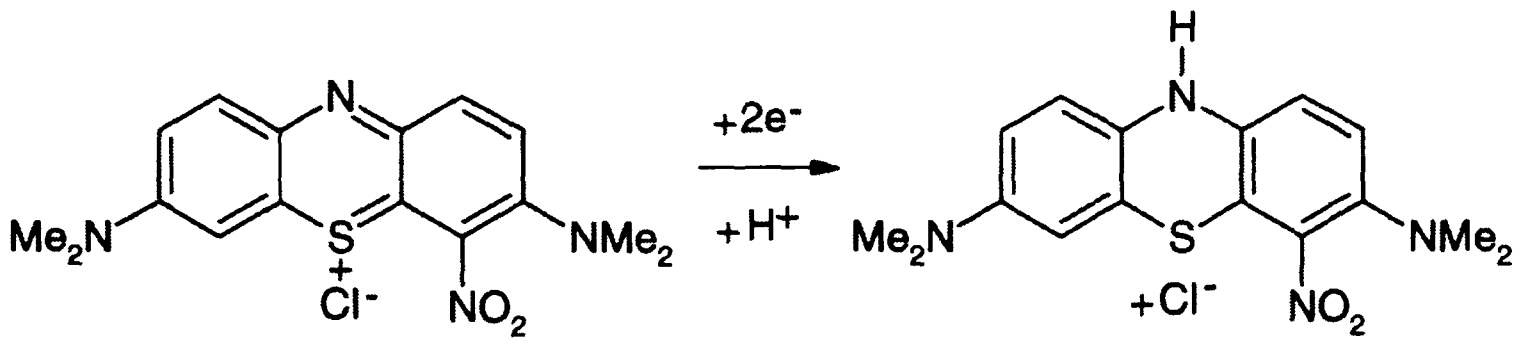

Figure 7.1 The two-electron reduction of methylene green (MG) to *leuco*-methylene green (*l*-MG).

7.3 ELECTROSYNTHESIS OF *LEUCO*-METHYLENE GREEN

Experiments were conducted using the 250 ml sonovoltammetric cell shown in Figure 2.1. It was thermostatted at 20°C and incorporated the 13 mm diameter titanium tipped ultrasonic horn probe. Full descriptions of the sono-electrochemical and sonovoltammetric procedures are given in Chapter 2. Cyclic voltammograms for 0.2 and 2 mM aqueous solutions of methylene green in 0.1 M KCl, buffered at pH 6.5 ± 0.1 with 0.2 M KH_2PO_4 were recorded in quiescent solution. A typical 'silent' voltammogram for the 0.2 mM solution is shown in Figure 7.2. The two peaks can be attributed to the following processes which will be examined in further detail in Chapter 12:

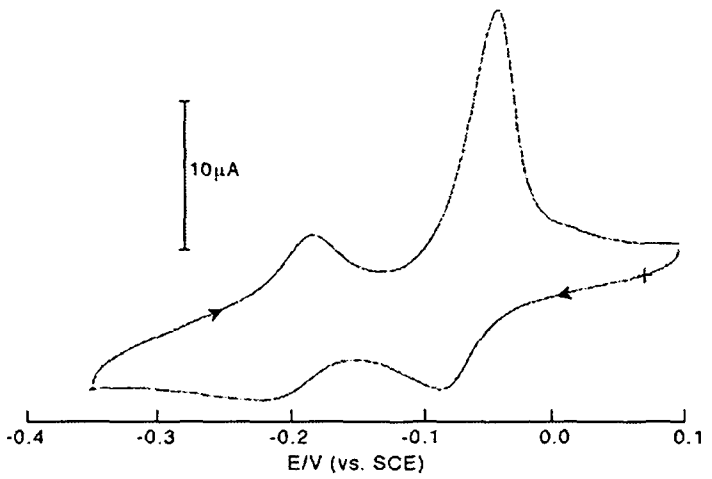

Figure 7.2 'Silent' CV of 0.2 mM MG in 0.1 M KCl / 0.2 M KH_2PO_4(aq) at pH 6.5. The scan rate was 10 mV s^{-1} and the working electrode was a 6 mm diameter Pt disc.

$$MG(aq) + H^+ + 2e^- \rightleftharpoons l\text{-}MG(s) \qquad E^{red}_{peak} = -0.09\ (vs.\ SCE) \qquad (7.1)$$

$$MG(aq) + H^+ + 2e^- \rightleftharpoons l\text{-}MG(aq) \qquad E^{red}_{peak} = -0.22\ (vs.\ SCE) \qquad (7.2)$$

The two-electron character of each wave was evidenced first by Tafel analysis [15] and second by the observation that the reduction potentials shifted by ca. 30 mV per pH unit in the pH range 6 to 8 consistent with a two electron, one proton reduction. Notice the large 'stripping' peak corresponding to the re-oxidation of the insoluble surface-bound *leuco*-methylene green.

In the case of the 2 mM solution only one clear forward peak and one reverse peak are seen in the 'silent' voltammogram shown in Figure 7.3. The reason for this is that the higher concentration of methylene green in solution leads to a greater quantity of surface bound *l*-MG as a result of the first two-electron process. This leads to passivation of the electrode which prevents the occurrence of the second solution process; thus the current drops off at more negative potentials.

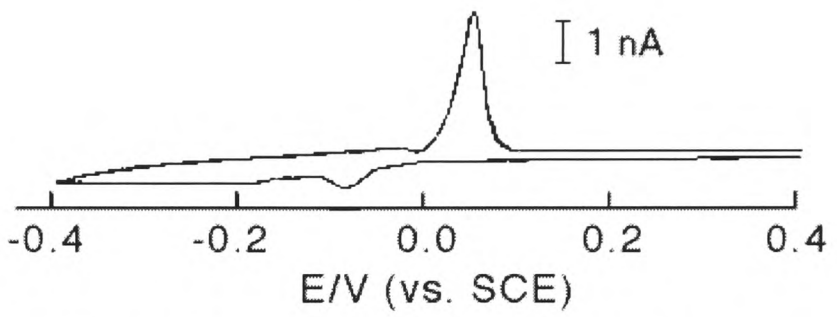

Figure 7.3 'Silent' CV of 2 mM MG in 0.1 M KCl / 0.2 M KH_2PO_4(aq) at pH 6.5. The scan rate was 10 mV s^{-1} and the working electrode was a 30 µm diameter Pt disc.

When 25 W cm^{-2} of power ultrasound was introduced into the cell the voltammetry changed markedly due to the significantly enhanced mass transport as is shown in Figure 7.4. Notice first that a much larger stripping peak is seen corresponding to the greater deposition resulting from the enhanced currents flowing due to the increased mass transport. Second whilst there is a mass-transport limited current analogous to a polarogram relating to the two-electron processes, reflecting the constant flux of material due to steady-state convection/diffusion, the wave at more negative potential shows a progressive decrease of

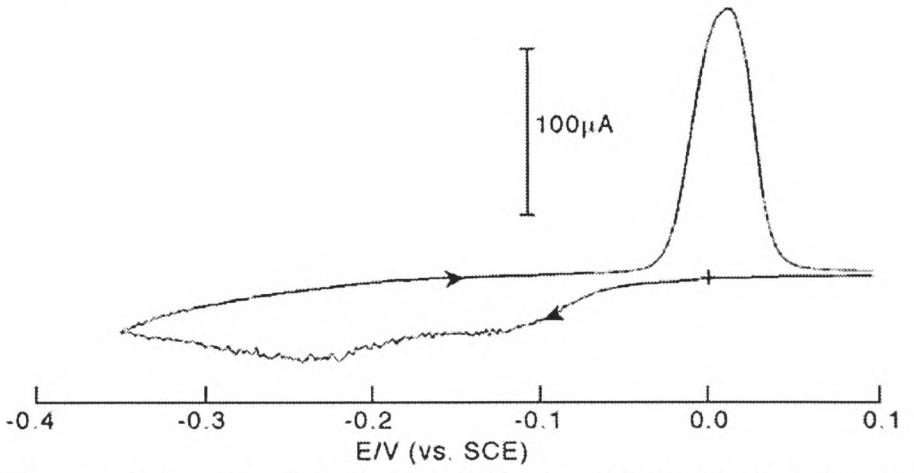

Figure 7.4 CV of 0.2 mM MG in 0.1 M KCl / 0.2 M KH_2PO_4(aq) at pH 6.5. 25 W cm^{-2} ultrasound was employed at a horn-to-electrode distance of 22 mm. The scan rate was 10 mV s^{-1} and the working electrode was a 6 mm diameter Pt disc.

signal at potentials negative of ca. -0.23 V (vs. SCE). The effect of increasing ultrasonic intensity on the amount of passivation is shown in Figure 7.5.

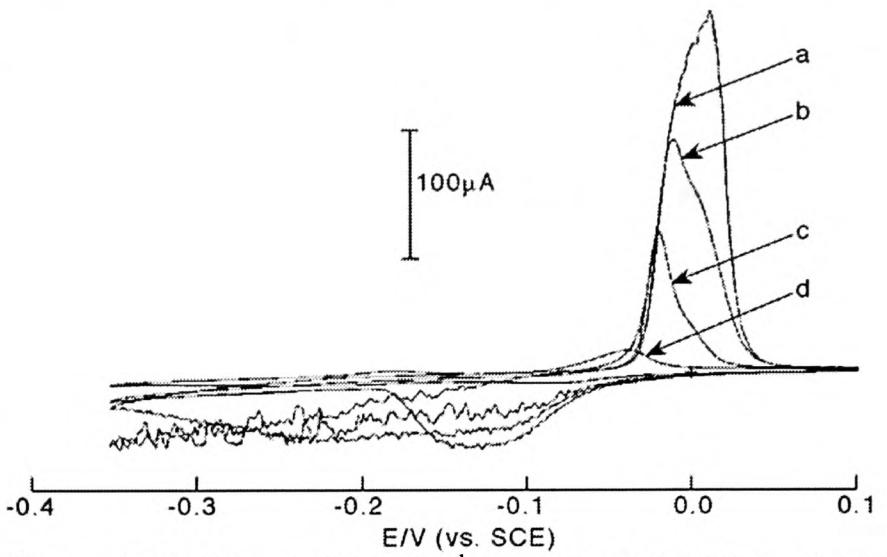

Figure 7.5 CVs at 10 mV s^{-1} for 0.2 mM MG in 0.1 M KCl / 0.2 M KH_2PO_4(aq) at pH 6.5 under a) 25 W cm^{-2}, b) 13 W cm^{-2} and c) 50 W cm^{-2} ultrasound at a horn-to-electrode distance of 22 mm. Trace d) is in the absence of ultrasound. The working electrode was a 6 mm Pt disc.

At lower ultrasonic intensities, lower mass transport results in reduction of a smaller quantity of methylene green and hence a smaller stripping peak upon re-oxidation (Figure 7.5b). At higher levels of ultrasound an even smaller stripping peak is seen (Figure 7.5c) and we attribute this to the rapid blocking of the electrode under faster mass transport conditions which inhibits further deposition at more negative potentials. This electrode passivation was also seen (i) under silent conditions at higher concentrations and (ii) during hydrodynamic voltammetry (for example at a channel electrode) and effectively precludes the electrosynthetic generation of useful quantities of *leuco*-methylene green. However when voltammetry was conducted using a 20% (v/v) solution of toluene in water and 18 W cm^{-2} ultrasound was utilised to form an emulsion, the sonovoltammetry was very different as shown in Figure 7.6. Now, two apparently steady-state sigmoidal reduction waves are observed with no evidence of a stripping peak on sweeps to positive potentials. We attribute this to the solubility of the reduction product in the emulsified organic phase that bathes the electrode surface. Similar effects were seen using n-octane instead of toluene, though sustained emulsification was found to be more difficult.

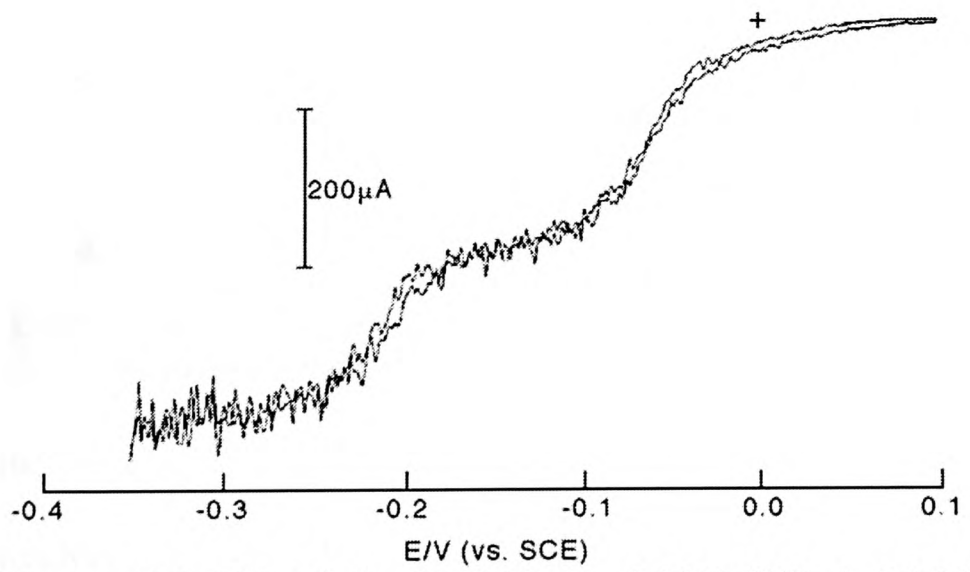

Figure 7.6 CV of 2 mM MG in 0.1 M KCl / 0.2 M KH_2PO_4(aq) at pH 6.5 and 20% (v/v) toluene (emulsified). 18 Wcm^{-2} ultrasound was employed at a horn-to-electrode distance of 19 mm. The scan rate was 10 mV s^{-1} and the working electrode was a 6 mm diameter Pt disc.

A typical voltammogram is shown in Figure 7.7 and although two mass transport limited waves are evident on reduction, upon re-oxidation a stripping peak is clearly evident suggesting incomplete removal of the *l*-MG by the octane which is not seen for toluene. The presence of the reduction product in the organic phase was confirmed by conducting a 30 minute sono-electrolysis experiment during which the potential of the solution (200 ml of 2 mM MG in 0.1 M KCl / 0.2 M KH_2PO_4 at pH 6.5 and 50 ml of toluene) was maintained at -0.35 V vs. SCE under ultrasound. The toluene reaction mixture was then isolated under argon, evaporated to dryness and the product dissolved in octane for UV-visible characterisation of the *leuco* base via the peak at 263 nm [16] shown in Figure 7.8.

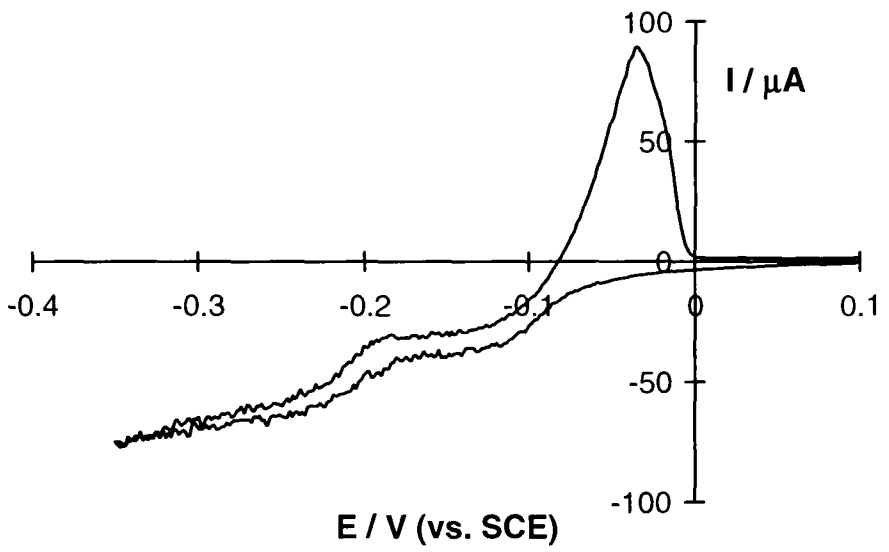

Figure 7.7 CV at 10 mV s^{-1} of 2 mM MG in 0.1 M KCl / 0.2 M KH_2PO_4(aq) at pH 6.5 and 10% (v/v) n-octane (emulsified). 18 W cm^{-2} ultrasound was employed at a 6 mm Pt disc at a horn-to-electrode distance of 21 mm.

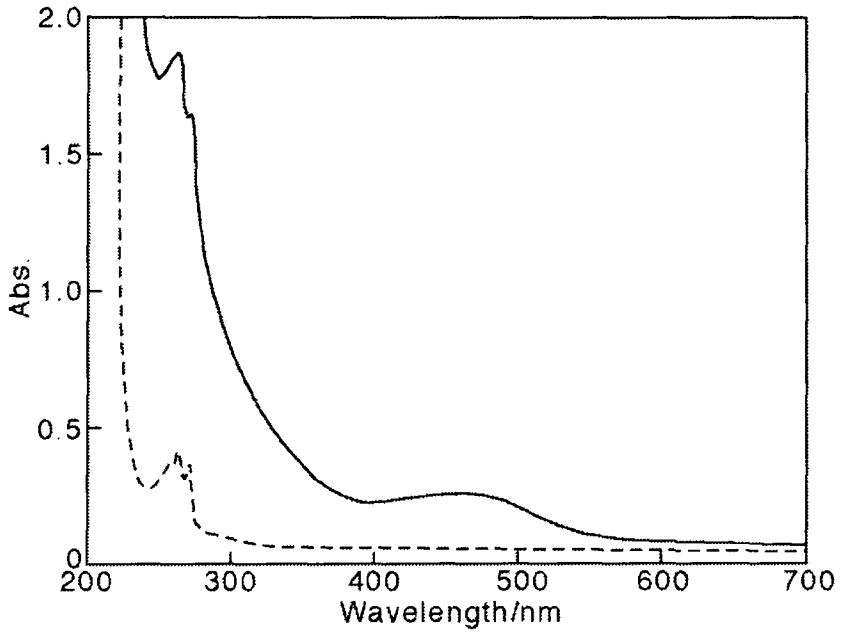

Figure 7.8 UV-visible spectra of n-octane (- - -) and the experimental product dissolved in n-octane (—).

Examination of Figure. 7.6 shows two roughly equal waves corresponding to the two electron reduction of methylene green giving respectively solid *l*-MG and aqueous phase *l*-MG. The former, of course, is rapidly removed by the emulsion. The relative sizes of the two waves reflect the amount of material that can nucleate and adsorb or precipitate in the case of the first wave and the fact that the overall magnitude of the two waves taken together reflects the rate of mass transport of MG to the electrode surface. The mechanism of the reduction along with that for related dyes will be the subject of further investigation in later chapters but the scope for 'clean' voltammetric measurements in otherwise passivating systems in the presence of ultrasound is evident.

7.4 ELECTRODE DEPASSIVATION DURING IODIDE OXIDATION

The oxidation of iodide at platinum electrodes is complicated by the formation of solid iodine at higher concentrations when the solubility of iodine is exceeded (1.1 mM in water at 25°C [17]). Cyclic voltammetry of 1 and 10 mM aqueous solutions of potassium iodide in 0.125 M H_2SO_4 was performed under 19 W cm^{-2} ultrasound at a horn-to-electrode distance of 12 mm. This is shown in Figure 7.9. At the higher concentration the voltammetry deviates from the expected steady-state behaviour and heavy electrode passivation leads to current fall-off.

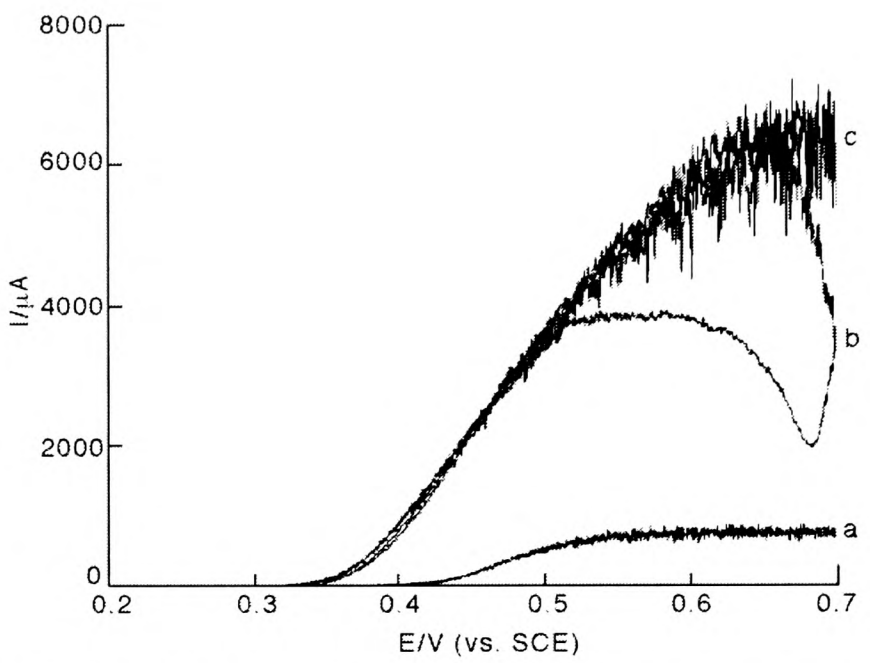

Figure 7.9 CVs on a 6 mm Pt disc electrode at 10 mV s^{-1} for a) 1 mM and b) 10 mM KI in 0.125 M H_2SO_4. 18 W cm^{-2} ultrasound was employed at a horn-to-electrode distance of 12 mm. Trace c) is as for b) except that 10% (v/v) of the aqueous solution was replaced with dichloromethane and emulsified.

When 10% (25 ml) of the aqueous solution was replaced with dichloromethane and the mixture was emulsified, steady-state behaviour was achieved and is seen in Figure 7.9c. This was confirmed spectroscopically to be due to the dissolution of iodine from the platinum electrode. UV-visible spectra were taken of the dichloromethane phase and are shown in Figure 7.10. By comparison with control experiments, one of the peaks observed was identified as iodine. A more in-depth study of the mechanism of oxidation of iodide at platinum electrodes is presented in Chapter 11.

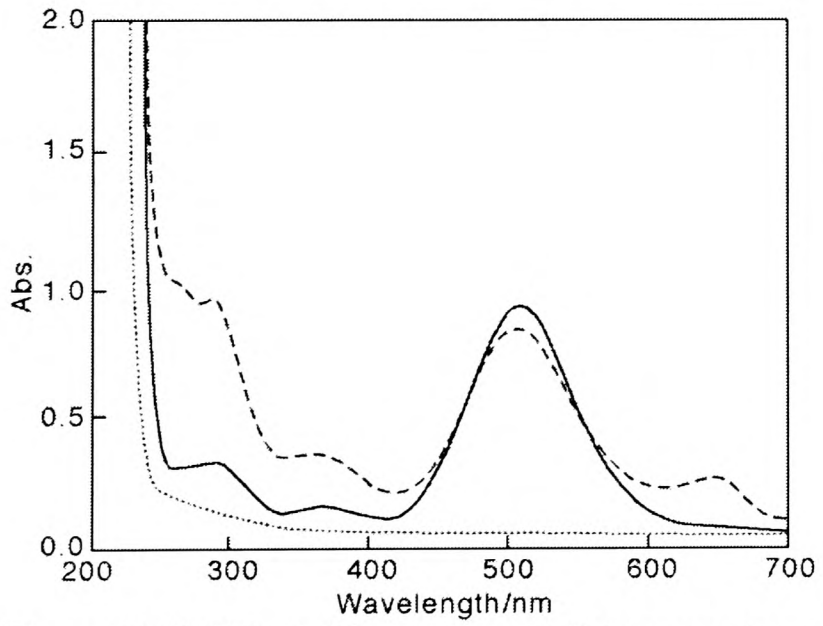

Figure 7.10 UV-visible spectra of dichloromethane (···), iodine dissolved in dichloromethane (—) and the dichloromethane phase of the emulsion experiment (- - -).

7.5 CONCLUSIONS

Sonication is found to be a convenient and effective alternative to the use of high-speed stirring and/or detergents for the promotion of emulsions for electrochemistry [8] although the possibility of a small amount of parallel chemistry resulting from sono-decomposition of the solvents (water, toluene and dichloromethane) should be noted.

The use of the sono-emulsion technique to depassivate electrochemical systems promises much for synthetic, mechanistic and analytical studies and can be expected to considerably broaden the range of chemical systems amenable to electrochemical study. In the next chapter we turn our attention to a parallel methodology for maintaining clean electrodes, namely laser activation and compare it directly with sonovoltammetry for the electroanalysis of ascorbic acid.

7.6 CHAPTER 7: REFERENCES

[1] D. J. Walton, S. S. Phull, *Adv. Sonochem.* **1996**, *4*, 205.
[2] R. G. Compton, J. C. Eklund, F. Marken, *Electroanalysis* **1997**, *7*, 509.
[3] F. Marken, R. P. Akkermans, R. G. Compton, *J. Electroanal. Chem.* **1996**, *415*, 55.
[4] J. Klima, C. Bernard, C. Degrand, *J. Electroanal. Chem.* **1995**, *399*, 147.
[5] R. G. Compton, J. C. Eklund, S. D. Page, G. H. W. Sanders, J. Booth, *J. Phys. Chem.* **1994**, *98*, 12410.
[6] F. Marken, R. G. Compton, S. D. Bull, S. G. Davies, *J. Chem. Soc. Chem. Comm.* **1997**, 995.
[7] F. Marken, R. G. Compton, *Electrochim. Acta* **1998**, *43*, 2157.
[8] S. Schweizer, J. F. Rusling, Q. Huang, *Chemosphere* **1994**, *28*, 961.
[9] Q. Chi, S. Dong, *Anal. Chim. Acta* **1994**, *285*, 125.
[10] Y. Zhu, S. Dong, *Electrochim. Acta* **1990**, *35*, 1139.
[11] D.-M. Zhou, H.-Q. Fang, H.-Y. Chen, H.-X. Ju, Y. Wang, *Anal. Chim. Acta* **1996**, *329*, 41.
[12] L. M. Dané, L. J. J. Janssen, J. G. Hoogland, *Electrochim. Acta* **1968**, *13*, 507.
[13] Y. A. Yaraliyev, *Electrochim. Acta* **1984**, *29*, 1213.
[14] Y. Chen, H. Zhang, B. Wu, *J. Electroanal. Chem.* **1992**, *335*, 321.
[15] A. C. Fisher, *Electrode Dynamics*, OUP, Oxford, **1996**, pgs. 8-9.
[16] A. T. Vartanyan, *Optika i Spektroskopia* **1956**, *1*, 478.
[17] S. Swathirajan, S. Bruckenstein, *J. Electroanal. Chem.* **1980**, *112*, 25.

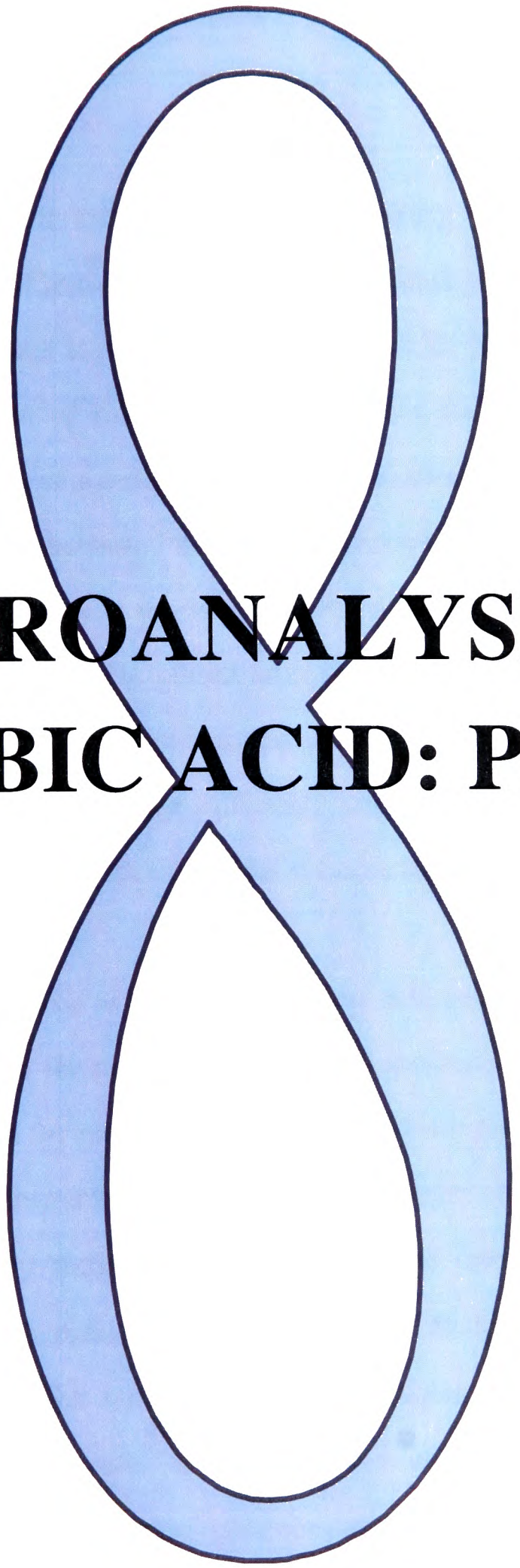

ELECTROANALYSIS OF ASCORBIC ACID: PART I

CHAPTER 8: ELECTROANALYSIS OF ASCORBIC ACID: PART I

8.1 CONTENTS

This chapter explores the use of sono-electrochemistry and electrochemistry under laser ablation in the analysis of aqueous solutions of L-ascorbic acid at platinum electrodes. Some of the work in this chapter is published in a paper in *Electroanalysis* (**1998**, *10*, 613). The electroanalytical detection of L-ascorbic acid (AA) via its two-electron oxidation in aqueous solution is the subject of a comparison of two voltammetric methodologies both of which rely in part on electrode abrasion. First in *sonovoltammetry* cavitational collapse at the electrode - solution interface can lead to electrode erosion and activation. Second in *laser ablation voltammetry* (LAbV) a 10 Hz pulsed laser (532 nm, 0.7 mJ per pulse) is used to abrade the electrode. In both cases the concomitant agitation of the solution leads to regular refreshment of the diffusion layer so that at sufficiently extreme potentials sustained transport limited currents are observed which scale with the concentration of ascorbic acid present and permit quantitative electroanalysis.

Comparison of the methods as applied to ascorbic acid shows that for LAbV the laser light intensity can be adjusted for maximum ablation of surface adsorbed blocking species but with minimum damage to the platinum surface itself. This is then termed *laser activated voltammetry* (LAV) and is desirable as it maintains a constant, clean electrode surface. In contrast the sonovoltammetry technique does not facilitate selective erosion of surface adsorbed species. Instead the mass transport, amount of cavitation and damage to the electrode are all interlinked with the intensity of ultrasound employed. Thus while the amount of cavitation at the electrode surface can be controlled the relative adsorbate / electrode abrasion cannot. The limiting currents under insonation were found to be substantially (ca. 15 times) larger than for LAV suggesting that the major benefit of sonovoltammetry is in terms of enhanced mass transport whereas LAV shows more selective

surface cleaning. The development of a novel sono-LAV experiment where the cleaning potential of LAV is coupled with the mass transport enhancement of ultrasound is reported with application to the quantitative electroanalysis of ascorbic acid.

8.2 INTRODUCTION

The technique of applying power ultrasound during electrochemical measurements and reactions is known as *sono-electrochemistry* and is introduced in section 1.6. It is a field that has grown rapidly world-wide in recent years [1,2]. Applications of this dual stimulation have been found in electroplating [3], reaction mechanism and kinetic analysis [4,5], synthesis [6-16, Chapter 7] and most recently electroanalysis [17-20, Chapters 4-6]. The dominant ultrasonic effects in all of these uses are those of greatly enhanced mass transport of electroactive substrate to the electrode and the activation of the electrode surface through cavitational cleaning action. In addition the *sonolysis* of water [21] to produce hydroxyl radicals occurs and can be exploited to initiate radical reactions in aqueous solution coupled to electrode processes [15].

A separate example of *dual activation* employs the synergistic use of electrochemical and photochemical stimuli. However, unlike the field of *photoelectrochemistry* [22] where photons participate directly in an electrode process via electronic excitation of electroactive solution phase species, in *laser ablation voltammetry* (LAbV) illumination does not provide direct chemical effects. Instead a pulsed laser light source is used, as elegantly introduced by Watanabe *et al.* [23], to provide ablation of an electrode surface and so under favourable conditions allow it to retain its electrochemical reactivity in the presence of species that may otherwise passivate solid electrodes through the adsorption of reactants, intermediates or products in the ascorbic acid electrode process [24].

In this chapter we seek to compare and contrast the two techniques in several respects. First their mass transport characteristics are examined. The limiting currents obtained for both voltammetries are compared in terms of size and origin. Second the effectiveness for the purposes of electrode cleaning and activation is evaluated. Third new

electroanalytical applications are tested culminating in the development of a novel *triple activation* experiment, "sono-laser activated voltammetry" (sono-LAV), where electrochemistry, ultrasound and laser activation are all employed simultaneously in the successful electroanalysis of L-ascorbic acid. The accurate determination of ascorbic acid content is particularly important in the food industry where it is used extensively as an anti-oxidant [25-27]. A reliable electroanalytical method might offer greater selectivity, time efficiency and reproducibility than current chemical or spectroscopic methods such as titration with 2,6-dichloroindophenol [28,29] and UV-visible detection [30,31].

8.3 EXPERIMENTAL

All experiments were conducted in one of two cells shown in Figures 2.1 and 2.4. The working platinum electrode in the sonovoltammetry experiments was a 3 mm disc positioned directly opposite the ultrasonic horn tip and close to the bottom of the cell. A 2 mm x 2 mm platinum square electrode was used in the LAV and sono-LAV experiments. Other experimental details are given in full in Chapter 2.

Typical laser voltammetry experiments were performed at 7.0 ± 0.3 mW and hence due to the pulse frequency of 10 Hz, the average energy per pulse was ca. 0.7 mJ. High power ablation experiments employed powers of up to 100 mW.

Sono-LAV experiments utilised the ultrasonic horn introduced from the top of the cell in a 'side-on' arrangement [32] as discussed in section 1.6.1 and shown in Figure 2.7. The distance, d, from the horn tip to the centre of the electrode was 16 ± 1 mm.

Potassium dihydrogen orthophosphate (KH_2PO_4) served as both a buffer and the supporting electrolyte. The pH of solutions was adjusted using a solution of 0.1 M potassium hydroxide to form a phosphate buffer solution (PBS).

Atomic force microscopy (AFM) surface imaging of a platinum disc before and after surface laser ablation was carried out as outlined in section 2.11 for comparison with work reported previously on the ultrasonic ablation of platinum [33].

8.4 RESULTS AND DISCUSSION

8.4.1 'SILENT' VOLTAMMETRY OF ASCORBIC ACID

The electrochemical oxidation of L-ascorbic acid (AA) has been reviewed by Dryhurst *et al.* [34] and studied extensively at platinum [24,35], gold [36] and glassy carbon [37] electrodes. While the glassy carbon electrodes yield low levels of surface passivation the kinetics of electron transfer are slow unless the surface is chemically modified [37]. In contrast the electron transfer kinetics at metallic electrodes are much higher but surface fouling occurs due to the slow desorption of the oxidised products from the metal inhibiting the uptake of fresh substrate for oxidation [24]. A reaction scheme for the two-electron oxidation of ascorbic acid in acidic solution at platinum electrodes is shown in Figure 8.1.

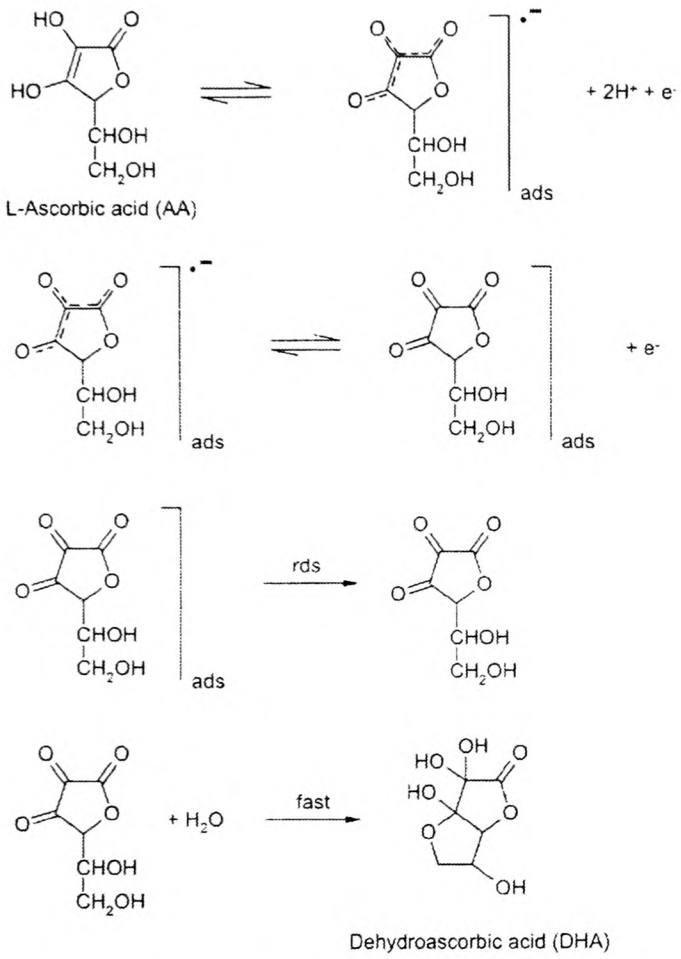

Figure 8.1 Reaction scheme for the two-electron oxidation of L-ascorbic acid on platinum in aqueous solution.

It is believed that the decreasing peak current in the cyclic voltammetry of AA as seen in Figure 8.2 is a consequence of the rate-limiting desorption of dehydroascorbic acid (DHAA) from the platinum surface before its hydration [24]. The lack of reduction wave on the reverse scan is indicative of a chemically irreversible oxidation. In neutral solutions, the electroactive species is the ascorbate mono-anion (HA^-) according to the reported pK values

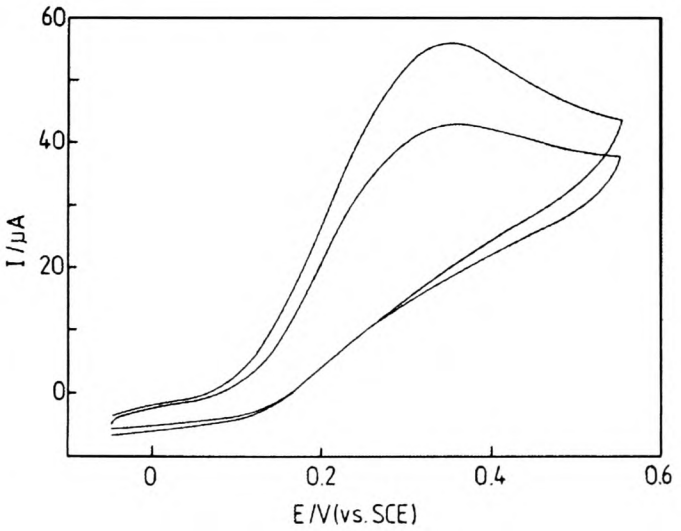

Figure 8.2 Consecutive CVs at 50 mV s^{-1} for the oxidation of 4 mM AA in 0.15 M PBS on a 3 mm diameter Pt disc electrode showing the decrease in peak current between the first and second scans due to passivation.

of $pK_1 = 4.17$ and $pK_2 = 11.57$ at 25°C [38] but the oxidation is still a two-electron process [39].

8.4.2 ELECTRODE EROSION AND MASS TRANSPORT OF SOLUTION

The work in this chapter seeks to explore the use of ultrasound and laser ablation in the activation of solid electrodes in the context of the electroanalysis of ascorbic acid. We report surface activation effects and a comparison of the mass transport associated with each of the dual activation techniques.

Before we examine the electrochemical effects of both techniques it is desirable to look into the physical processes behind the electrode erosion. The phenomenon of acoustic cavitation due to power ultrasound and its effect on platinum electrodes is well known and has been reported previously [33]. Ultrasonic erosion increases as a function of sonic intensity, exposure time and decreasing source to target distance. While the use of high powered lasers for metal cutting and welding has been commonplace for many years [40], no work to the authors' knowledge has been reported on the study of laser ablation of platinum by atomic force microscopy. When sufficient power is applied the laser pulses cause damage to the electrode surface with concomitant acoustic and thermal emission [23]. AFM pictures of a polished platinum surface before and after subjection to 30 seconds of 35 mW laser irradiation are seen in Figure 8.3. Surface damage is clearly evident and again increases as a function of laser intensity (as does the acoustic emission [23]) and time of exposure. However unlike ultrasound, due to the coherent nature of laser illumination, the

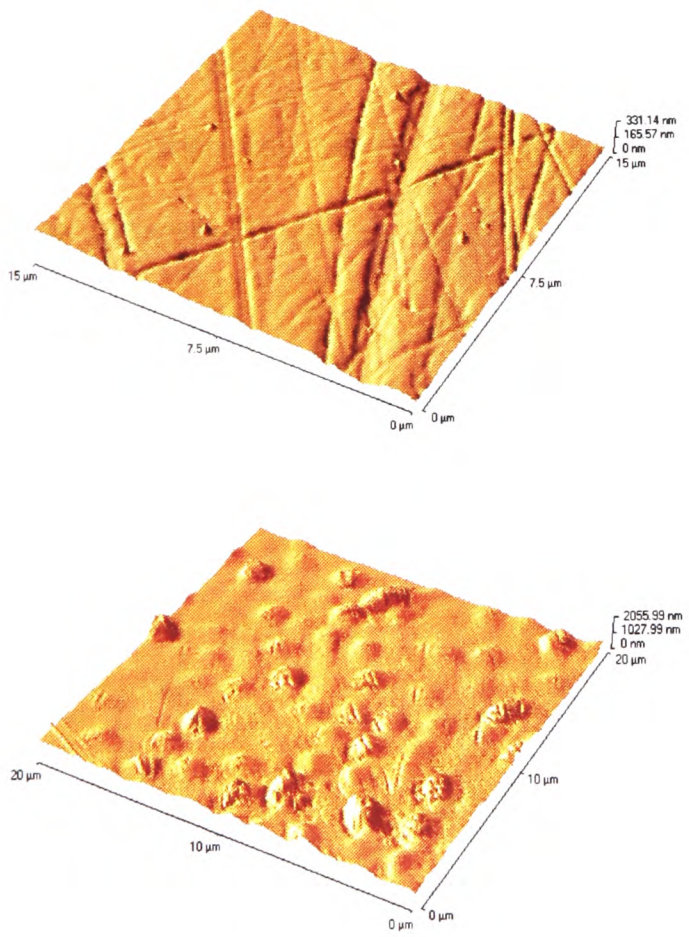

Figure 8.3 AFM pictures of a platinum electrode: top) polished and unablated and bottom) after subjection to 35 mW laser ablation for 30 seconds.

source to target distance has little bearing on the level of ablation unless the medium of transmission absorbs light at the wavelength of propagation.

8.4.3 VOLTAMMETRY DURING ULTRASONIC OR LASER ACTIVATION

For successful sonovoltammetry, optimisation of the parameters of insonation intensity, temperature, horn-to-electrode distance and exposure time has led to a methodology that yields maximum mass transport and surface activation but minimum electrode wear. A typical sono-voltammogram for the oxidation of 4 mM AA buffered at pH 4 is seen in Figure 8.4 and shows a well defined mass transport limited oxidation wave with very little noise due to cavitational damage. The limiting current is approximately 15 times the peak current observed under 'silent' conditions. The effects of increasing the intensity and duration of the ultrasound during sonovoltammetric measurements are well known for many systems [15]. The 'face-on' sono-limiting current at a scan rate of 10 mV s^{-1} was measured for solutions of ascorbic acid buffered at pH 4 in the concentration range 0.5 – 5 mM. The data plotted in Figure 8.5 clearly illustrate a proportional relationship.

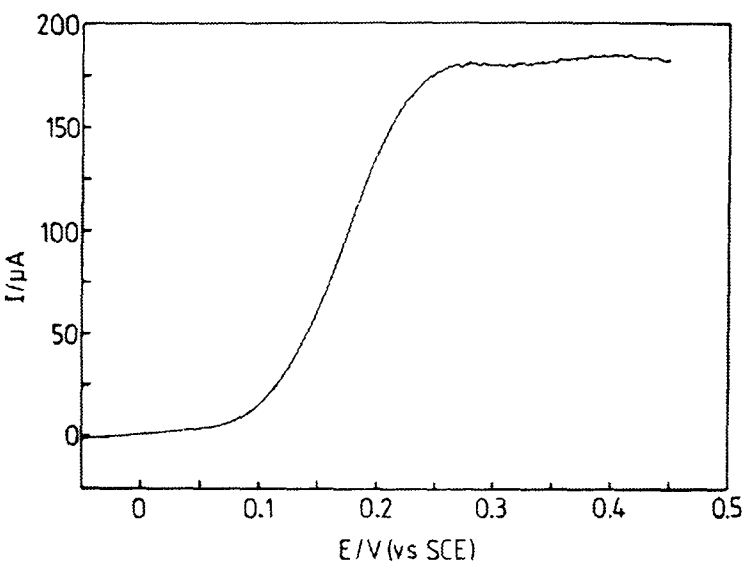

Figure 8.4 Sono-voltammogram for the oxidation of 4 mM AA in 0.15 M PBS at pH 4.0 on a 3 mm Pt disc electrode and a scan rate of 10 mV s^{-1}. US intensity was 25 W cm^{-2} and the 'face-on' horn-to-electrode distance was 4 mm.

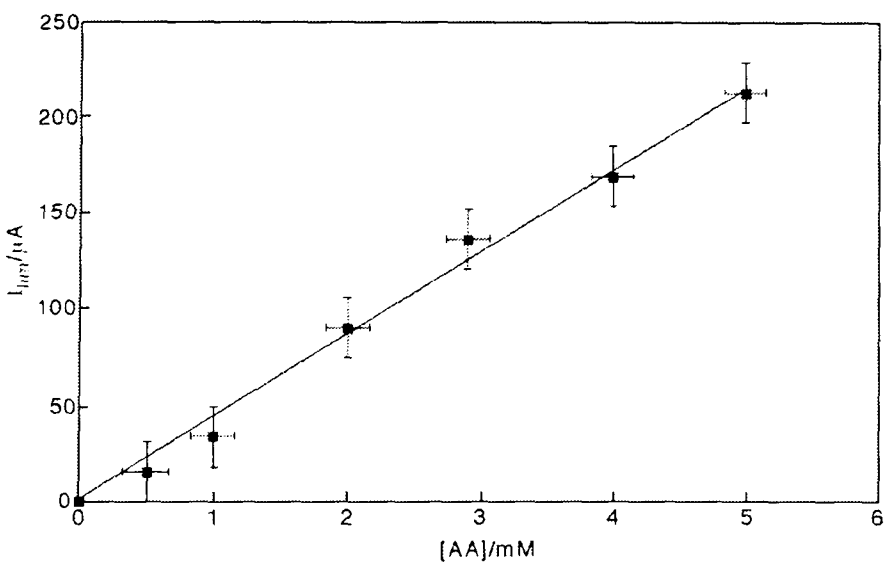

Figure 8.5 Sono-limiting current against AA concentration plots for solutions in 0.15 M PBS at pH 4.0 for a 3 mm Pt disc electrode and a scan rate of 10 mV s^{-1}. The US intensity was 25 W cm^{-2} and the 'face-on' horn-to-electrode distance was 4 mm.

Next the effect of laser intensity on the anodic linear sweep voltammetry of ascorbic acid was studied. Linear sweep voltammetry for AA oxidation at four increasing laser powers

ranging from 7 mW to 100 mW is seen in Figure 8.6. The first interesting point is the apparent modulation in the current spikes at medium powers which may be a consequence of undulating power output from the laser or may indicate cumulative effects occurring at the electrode surface. At high powers wildly fluctuating current spikes are produced possibly as a consequence of the large temperature jumps associated with electrode damage events [41]. At relatively low levels of illumination, little visible electrode ablation occurs and a sustained mass transport limiting current is seen. We attribute this behaviour to a threshold laser power setting where only the molecules adsorbed to the surface are ablated hence revitalising the electrode for the uptake of fresh ascorbic acid from solution. In the case of the colourless AA solutions described, the externally measured power threshold that yielded renewed voltammetry was 7.0 ± 0.3 mW. Powers below this value produced voltammetry similar to that seen 'in the dark' - see Figure 8.2. We estimate a ca. 5% drop in power actually reaching the electrode due to reflectance losses from the quartz window. We believe that the critical factor in laser ablation, at the low powers we employed, is the energy per unit area per pulse. This threshold energy density value is ca. 10 mJ cm^{-2} $pulse^{-1}$ for the threshold power quoted above. A schematic of this 'surface selective' laser ablation is shown in Figure 8.7.

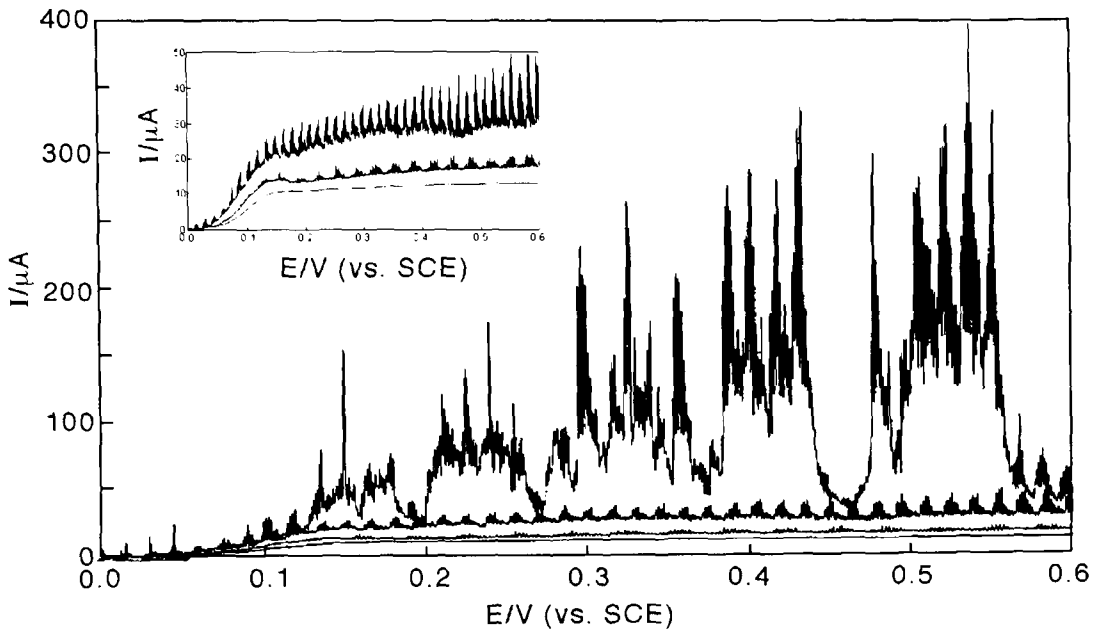

Figure 8.6 Current vs. potential plots for the oxidation of 4 mM AA in 0.15 M PBS on a 2 mm x 2 mm Pt electrode at a scan rate of 5 mV s^{-1} subject to increasing power of laser ablation ranging from 7 mW to 100 mW. The lower 3 traces are enlarged in the top left insert.

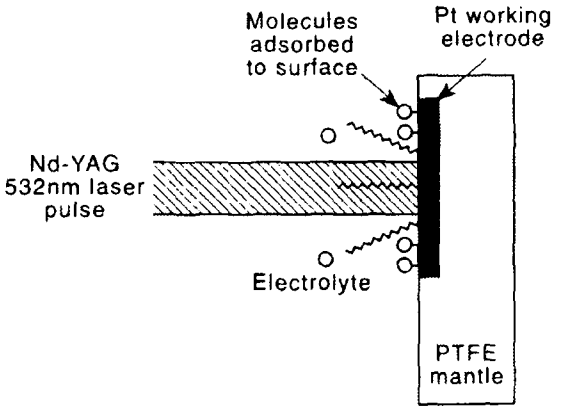

Figure 8.7 A schematic of the mechanism of electrode activation and surface substrate erosion through laser-photon local heating.

To observe the contrast between illuminated and 'dark' oxidation scans, experiments were conducted on various concentrations of AA buffered at pH 6.9. Figure 8.8 shows the effect of 7 mW illumination on the voltammetry of a 3 mM ascorbic acid solution at a 2 mm x 2 mm square platinum electrode. The first illuminated scan is followed by two in the dark during which electrode fouling occurs and the current drops off. The fourth scan, with the laser ablation re-applied, retraces the original scan with good reproducibility. By 'tuning' the laser pulses to the minimum power described above, we observed renewed voltammetry with each successive scan replicating the first scan on a nominally 'virgin' electrode. However, although the electrode remains activated, with LAV alone there is little significant increase in mass transport to the electrode in contrast to the insonated case. The limiting oxidation currents were measured for a concentration range of 0 - 6 mM AA at pH 6.9 and are plotted in Figure 8.9. A proportional relationship is evident.

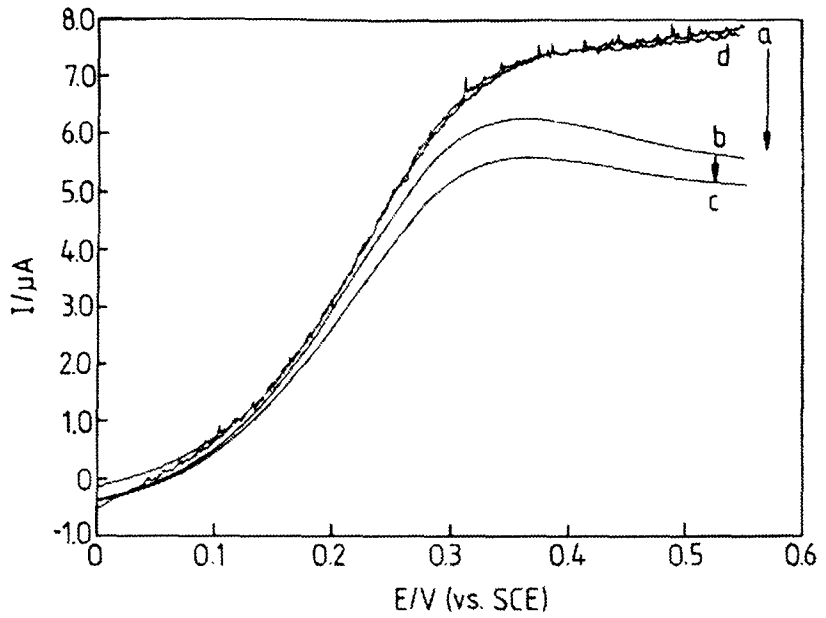

Figure 8.8 Voltammograms for the oxidation of 3 mM AA in 0.15 M PBS at pH 6.9 on a 2 mm x 2 mm square Pt electrode and a scan rate of 5 mV s^{-1}. a) initial scan - laser on; b) second scan - 'dark'; c) third scan - 'dark' and d) fourth scan - laser on, yielding renewed activity.

In contrast to insonation, laser ablation delivers power directly to the electrode with minimal disturbance of the surrounding electrolyte. The key difference in the two forms of stimuli is that ultrasound provides gradual surface erosion but greatly enhanced mass

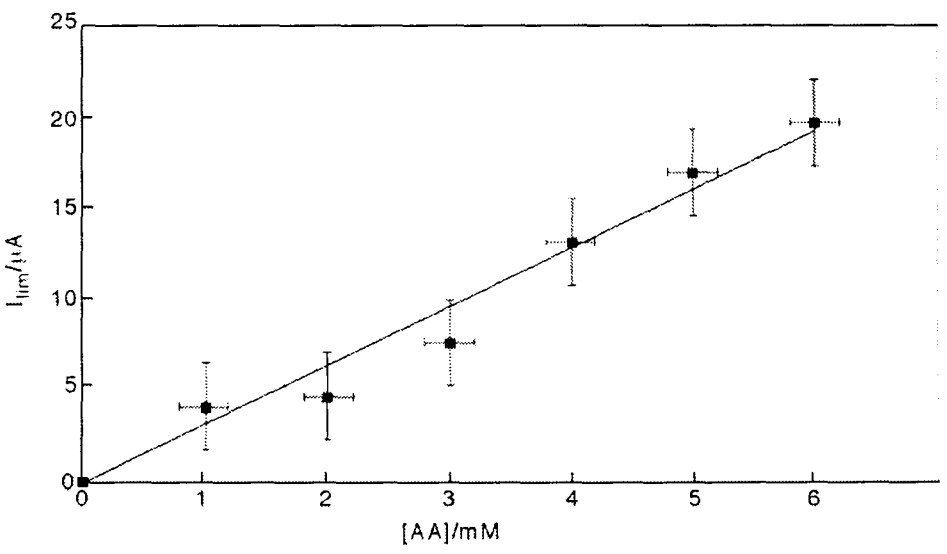

Figure 8.9 Limiting current against AA concentration plots for solutions in 0.15 M PBS at pH 6.9 subject to laser ablation. The electrode used was a 2 mm x 2 mm square Pt electrode at a scan rate of 5 mV s^{-1}. The laser power was 7.0 ± 0.3 mW and the beam diameter was ca. 3 mm.

transport of electroactive species to the electrode whereas laser bombardment yields focused surface activation but next to no bulk solution agitation.

To apply ultrasound in tandem with laser illumination the 'side-on' geometry shown in Figure 2.7 was used since a 'face on' geometry would have involved a different cell design. Initially the effect of 'side-on' insonation alone on the voltammetry of a range of AA concentrations (0 - 7 mM) was studied. Mass transport enhanced, steady-state voltammograms were produced and are shown for three sample concentrations in Figure 8.10. At potentials beyond ca. 0.35 V (vs. SCE) transport-limited behaviour is developed although a completely potential-independent plateau is not seen, partly as a result of a sloping baseline and partly through potential-dependent cavitationally induced 'noise'. A plot of current in the transport-limited region as determined by subtraction of baseline current from the average current in the range 0.45 - 0.5 V (vs. SCE) against AA concentration is shown in Figure 8.11 and shows a linear relationship within error limits. The least squares best-fit line shown has a gradient of 47.8 μA/mM. The high noise levels are attributable to the poorly defined hydrodynamic flow and significant acoustic reflections within the asymmetric cell design.

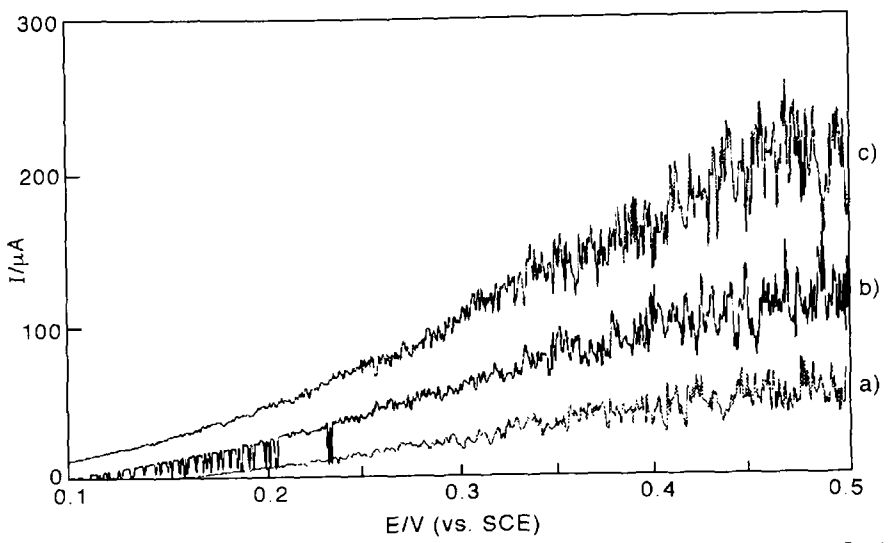

Figure 8.10 Sample voltammograms for oxidation of a) 1 mM AA, b) 2 mM AA and c) 4 mM AA for solutions in 0.15 M PBS at pH 6.9 subject to 'side-on' insonation with 25 W cm^{-2} US at a horn-to-electrode distance of 16 mm. The electrode used was a 2 mm x 2 mm square Pt electrode at a scan rate of 5 mV s^{-1}.

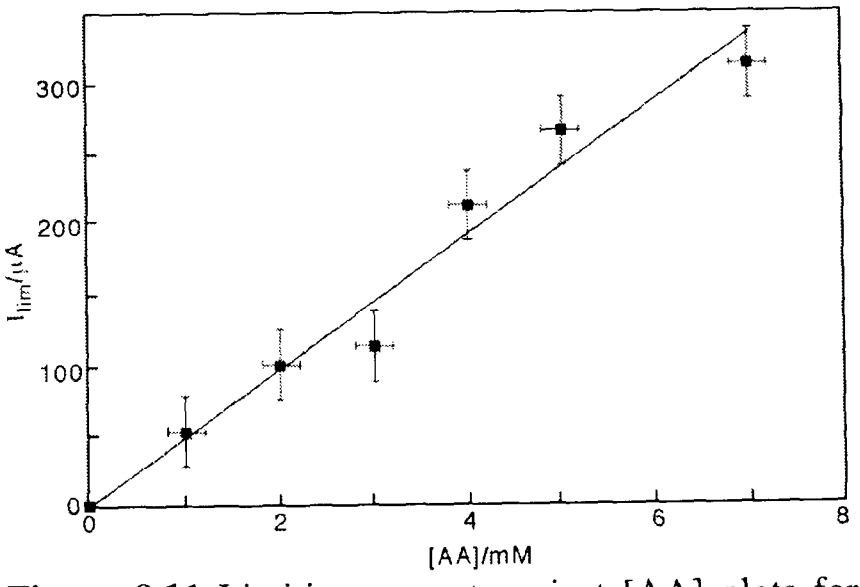

Figure 8.11 Limiting current against [AA] plots for solutions in 0.15 M PBS at pH 6.9 subject to 'side-on' insonation with 25 W cm^{-2} US at a horn-to-electrode distance of 16 mm. The electrode used was a 2 mm x 2 mm square Pt electrode at a scan rate of 5 mV s^{-1}.

8.4.4 SONO-LASER ACTIVATED VOLTAMMETRY (SONO-LAV)

The above 'side-on' sonovoltammetric experiments were repeated under illumination with 7 mW laser power to assess the usefulness of using the two techniques in tandem to form a novel sono-LAV methodology. Two sample voltammograms are shown in Figure 8.12. The corresponding limiting currents, as determined by the average current between 0.5 and 0.55 V (vs. SCE) are plotted against AA concentration in the range 0 - 9 mM and shown in Figure 8.13. The gradient of the least squares best fit line for the sono-LAV plot is 48.8 μA/mM illustrating the relatively small benefit of applying laser ablation over and above the use of power ultrasound alone in the case of ascorbic acid. There are many well-known systems however where the use of ultrasound alone is inadequate at activating electrodes exposed to strongly adsorbing substrates [42] and it is here where LAV may have the necessary surface cleaning power to provide reproducible voltammetry.

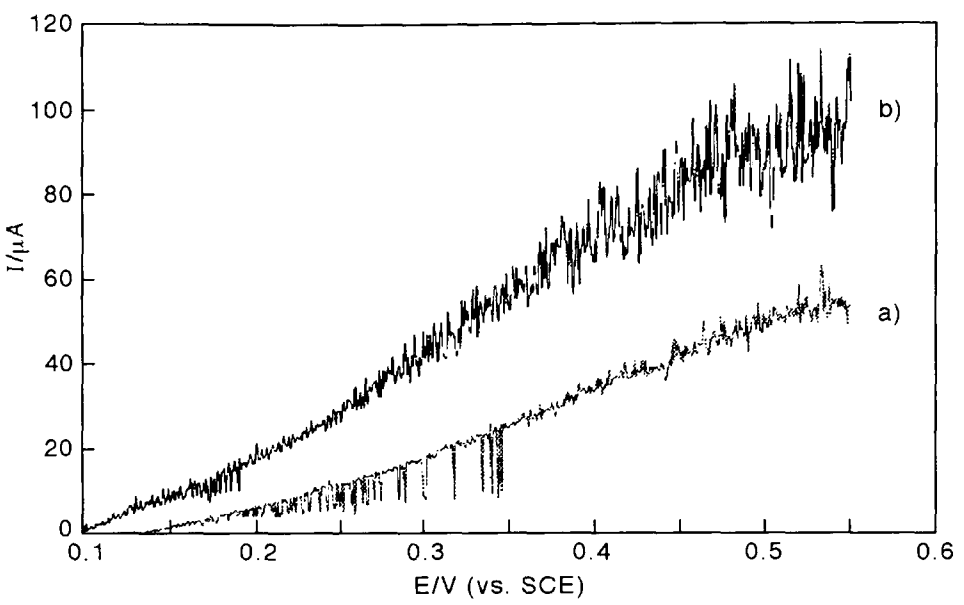

Figure 8.12 Sample voltammograms for oxidation of a) 1 mM AA and b) 2 mM AA for solutions in 0.15 M PBS at pH 6.9 subject to 'side-on' insonation with 25 W cm^{-2} US at a horn-to-electrode distance of 16 mm *and* laser activation. The electrode used was a 2 mm x 2 mm square Pt electrode at a scan rate of 5 mV s^{-1}. A laser power of 7.0 ± 0.3 mW was used. The laser beam diameter was ca. 3 mm.

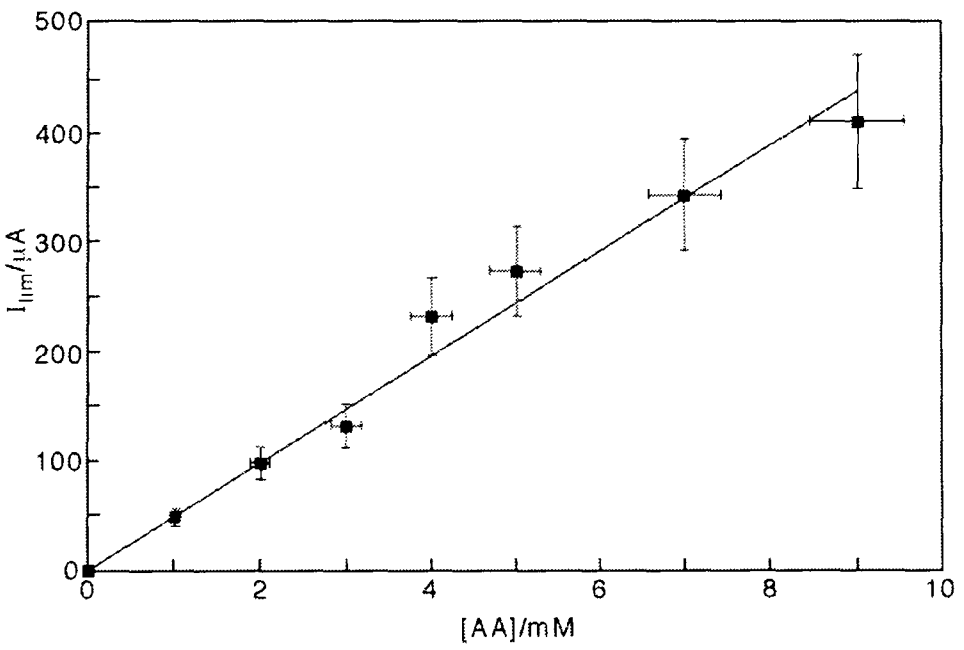

Figure 8.13 Limiting current against AA concentration plots for the voltammetry illustrated in Figure 8.12.

8.5 CONCLUSIONS

In the specific case of ascorbic acid oxidation the use of laser ablation voltammetry provides a complementary approach to the utilisation of power ultrasound. Both yield limiting currents that are proportional to the concentration of ascorbic acid present and are reproducible provided care is taken in the case of LAV with the laser alignment and power setting. As a consequence both techniques offer the prospect of quantitative electroanalysis of AA which is laborious by non-electrochemical methods and irreproducible by conventional electrochemistry. The combination of the two techniques to form the sono-LAV method showed only a small additional benefit in the case of ascorbic acid. Voltammetry can be performed that is not subject to electrode fouling and may have particular application in systems that strongly passivate electrodes such as fruit juices or phenothiazine dye substrates. In the next chapter we apply sonovoltammetry and laser activated voltammetry to the analysis of ascorbic acid in a 'real' system – Ribena (!) before taking a more in-depth look at the phenomenon of laser activation and its versatility in Chapter 10.

8.6 CHAPTER 8: REFERENCES

[1] D. J. Walton, S. S. Phull, *Adv. Sonochem.* (Ed. T. J. Mason) **1996,** *4*, 205.

[2] R. G. Compton, J. C. Eklund, F. Marken, *Electroanalysis* **1997,** *7*, 509.

[3] R. Walker, *Chem. Britain.* **1990,** *26*, 251.

[4] R. G. Compton, J. C. Eklund, S. D. Page, *J. Phys. Chem.* **1995,** *99*, 4211.

[5] R. G. Compton, J. C. Eklund, S. D. Page, T. O. Rebbitt, *J. Chem. Soc. Dalton Trans.* **1995,** *3*, 389.

[6] T. J. Mason, *Chem. Soc. Rev.* **1997,** *26*, 443.

[7] F. Marken, R. G. Compton, S. G. Davies, S. D. Bull, T. Thiemann, M. L. S. E. Melo, A. C. Neves, J. Castillo, C. G. Jung, A. Fontana, *J. Chem. Soc. Perkin Trans. 2* **1997,** *10*, 2055.

[8] M. Atobe, S. Fuma, N. Sato, T. Nonaka, *Denki Kagaku* **1997,** *65*, 495.

[9] M. Atobe, T. Nonaka, *Chem. Letters* **1997,** *4*, 323.

[10] M. Atobe, T. Nonaka, *Ultrasonics Sonochemistry* **1997,** *4*, 17.

[11] F. Marken, R. G. Compton, S. D. Bull, S. G. Davies, *J. Chem. Soc. Chem. Comm.* **1997,** *11*, 995.

[12] T. J. Mason, J. P. Lorimer, D. J. Walton, *Ultrasonics* **1990,** *28*, 333.

[13] M. Atobe, T. Nonaka, *J. Electroanal. Chem.* **1997,** *425*, 161.

[14] A. Chyla, J. P. Lorimer, G. Smith, D. J. Walton, *J. Chem. Soc. Chem. Comm.* **1989,** *9*, 603.
[15] J. C. Eklund, D. N. Waller, T. O. Rebbitt, F. Marken, R. G. Compton, *J. Chem. Soc. Perkin Trans. 2* **1995,** *11*, 1981.
[16] A. Durant, H. Francois, J. Reisse, A. Kirsch de Mesmaeker, *Electrochim. Acta* **1996,** *41*, 277.
[17] F. Marken, T. O. Rebbitt, J. Booth, R. G. Compton, *Electroanalysis* **1997,** *9*, 19.
[18] N. A. Madigan, T. J. Murphy, J. M. Fortune, C. R. S. Hagan, L. A. Coury Jr., *Anal. Chem.* **1995,** *67*, 2781.
[19] F-M. Matysik, S. Matysik, A. M. O. Brett, C. M. A. Brett, *Anal. Chem.* **1997,** *69*, 1651.
[20] C. Agra-Gutiérrez, R. G. Compton, *Electroanalysis* **1998**, *10*, 603.
[21] C. Petrier, A. Jeunet, J. L. Luche, G. Reverdy, *J. Am. Chem. Soc.* **1992,** *114*, 3148.
[22] R. G. Compton, R. A. W. Dryfe, *Prog. Reaction Kinetics* **1995,** *20*, 245.
[23] T. Hinoue, I. Watanabe, H. Watarai, *Chem. Letters* **1996,** *5*, 329.
[24] P. Karabinas, D. Jannakoudakis, *J. Electroanal. Chem.* **1984,** *160*, 159.
[25] E. Graf, *J. Agri. Food Chem.* **1994,** *42*, 1616.
[26] D. M. Schaeffer, Q. P. Liu, C. Faustman, M. C. Yin, *J. Nutrition* **1995,** *125*, S1792.
[27] E. N. Frankel, *Food Chem.* **1996,** *57*, 51.
[28] *Pearson's Composition and Analysis of Food* (9th Ed.) (Eds. R. Kirk, R. Sawyer), Longman Scientific & Technical, Harlow, UK, **1991.**
[29] *Official Methods of Analysis of AOAC International* (16th Ed., Vol. II) (Ed. P Cunniff), AOAC International, Gaithersburg, Maryland, USA, **1995,** Chapter 45, pgs.16-17.
[30] E. S. Wagner, B. Lindley, R. D. Coffin, *J. Chromatogr.* **1979,** *163*, 225.
[31] J. W. Finley, E. Duang, *J. Chromatogr.* **1981,** *207*, 449.
[32] J. C. Eklund, F. Marken, D. N. Waller, R. G. Compton, *Electrochim. Acta* **1996,** *41*, 1541.
[33] R. G. Compton, J. C. Eklund, S. D. Page, G. H. W. Sanders, J. Booth, *J. Phys. Chem.* **1994**, *98*, 12410.
[34] G. Dryhurst, K. Kadish, F. Scheller, R. Renneberg, *Biological Electrochemistry*, Academic Press, New York, **1982,** *1*, 256.
[35] M. Brezina, J. Koryta, T. Loucka, D. Marsikova, J. Pradac, *J. Electroanal. Chem.* **1972,** *40*, 13.
[36] M. Rueda, A. Aldaz, F. Sanchez-Burgos, *Electrochim. Acta* **1978,** *23*, 419.
[37] I. G. Casella, M. R. Guascito, *Electroanalysis* **1997,** *9*, 1381.
[38] *Merck Index* (11th Ed.), Rahway, NJ, USA, **1989,** pg. 858.
[39] R. G. Compton, F-M. Matysik, *Electroanalysis* **1996,** *8*, 213.
[40] J. Wilson, J. F. B. Hawkes, *Lasers: Principles and Applications*, Prentice-Hall, London, **1987.**
[41] J. F. Smalley, C. V. Krishnan, M. Goldman, S. W. Feldberg, I. Ruzic, *J. Electroanal. Chem.* **1988,** *248*, 255.
[42] H. A. O. Hill, Y. Nakagawa, F. Marken, R. G. Compton, *J. Phys. Chem.* **1996,** *100*, 17395.

ELECTROANALYSIS OF ASCORBIC ACID: PART II

CHAPTER 9: ELECTROANALYSIS OF ASCORBIC ACID: PART II

9.1 CONTENTS

This chapter develops the use of sonovoltammetry and laser activated voltammetry for the analysis of aqueous solutions of L-ascorbic acid at platinum electrodes which was introduced in Chapter 8. The goal is the determination of ascorbic acid in a 'real' system. Some of the work in this chapter is published in a paper in *Electroanalysis* (**1998**, *10*, 814). In this chapter a comparison is again made between two 'dual activation' electroanalytical techniques, this time for the detection and measurement of vitamin C (L-ascorbic acid) in a commercially available fruit drink via its two-electron oxidation at platinum electrodes. Glucose is found not to interfere with the analytical response. First in *sonovoltammetry* pulses of 25 W cm^{-2} ultrasound are applied and the current response characterised in the 'pulse off' period where a current plateau is attained. Second in *laser activated voltammetry* a 10 Hz pulsed laser (532 nm, ca. 240 mW cm^{-2} average intensity) is used to 'burn' surface adsorbed passivating species off the electrode. Both methods cause agitation of the solution in the bulk phase or at the electrode-solution interface and lead to regular renewal of the diffusion layer. The mass transport limited oxidation currents so obtained are found to scale with ascorbic acid concentration in media where electroanalysis without simultaneous ultrasonic or laser stimulation may be precluded due to electrode passivation.

Application to the quantitative electroanalysis of ascorbic acid in the fruit drinks Ribena® and 'No added sugar' Ribena® is reported. The results obtained are in excellent agreement with those yielded by independent chemical and electrochemical methods.

9.2 INTRODUCTION

The coupling of ultrasonic stimulation with electrochemistry is an example of *dual activation* which is the centre of focus of this thesis and is currently revitalising the field of electroanalysis [1-5, Chapters 4-6, 8]. The technique employed is generally known as *sonovoltammetry* and in recent years a detailed picture of the processes and effects involved has been developed [6,7]. The key advantages of voltammetry in the presence of ultrasound have been alluded to in the previous chapters though sono-electrochemical procedures have also been exploited for reaction mechanism analysis [8,9], electroplating [10] and very importantly for efficient and novel synthetic applications [11-27, Chapter 7].

Dual activation can also be achieved by the simultaneous use of light and voltammetry. In *photoelectrochemistry* [28] photons participate directly in an electrode process via the electronic excitation of electroactive species in solution. As yet surprisingly limited use has been made of this methodology for electroanalysis [29-34]. However light can be used not only to excite electroactive species in solution but also to activate the electrode surface itself. In early work pulsed lasers were used to depassivate iron surfaces in corrosion studies [35] and prepare silicon surfaces for surface analysis [36]. Subsequently electrochemistry at laser-depassivated iron [37,38] and glassy carbon [39,40] electrodes has been reported. In *laser ablation voltammetry* (LAbV) [41] a relatively high power pulsed laser light source is used to produce ablation of an electrode surface. Constant renewal of fresh electrode surface allows LAbV under favourable conditions to study electrochemistry in the presence of species that otherwise passivate solid electrodes [41]. The work in Chapter 8 on the electroanalysis of ascorbic acid in aqueous solution sought to use lower levels of laser power in order to activate the electrode surface without ablating it. At these low power levels the temperature jumps associated with laser pulses [42] are too small to cause any change in state in the platinum surface. Instead elastic stresses build up in the metal as a

consequence of bulk thermal expansion. This is known as the *thermoelastic effect* [37,43]. It is only at higher powers that energy absorbed from the laser pulse by the metal is sufficient to give rise to melting or even vaporisation of a small amount of surface material. This is the *ablation effect* [41,43]. It is accompanied by acoustic emission and visible surface scarring which was studied in air by atomic force microscopy in Chapter 8 and will be further characterised in aqueous solution in Chapter 10.

In this chapter we seek to compare the electroanalytical performances of pulsed sonovoltammetry and low power LAV in the measurement of vitamin C in a commercially available fruit drink. Vitamin C (L-ascorbic acid) is used extensively as an anti-oxidant in the food and drink industry [44-46] and the accurate determination of its concentration is of considerable commercial importance.

A new and reliable electroanalytical method might offer greater selectivity, time efficiency and reproducibility than current chemical or spectroscopic methods such as titration with 2,6-dichloroindophenol (DCIP) [47,48] and UV-visible detection [49,50], whilst conventional electroanalysis is precluded by surface adsorption of ascorbic acid oxidation intermediates and products giving rise to passivation of platinum electrodes [51].

9.3 EXPERIMENTAL

In pulsed sonovoltammetry experiments the three-electrode electrochemical cell shown in Figure 2.1 was used. The working platinum 3 mm disc electrode was positioned directly opposite the 13 mm diameter ultrasonic horn tip at a distance of 4 mm. Ultrasound (US) power levels up to 25 W cm^{-2} were employed in pulsed mode, whilst the temperature was maintained at 25 $\pm$ 2°C. The three-electrode electrochemical cell used in the laser ablation voltammetry (LAV) experiments is shown in Figure 2.5. This was modified from the cell used in the previous chapter by including a Teflon cylinder with a quartz window in the end to allow the path length of the laser light through the solution to the electrode to be adjusted. Typically the quartz

window was set to a distance of 1 mm away from the electrode. The working electrode was a 2 mm x 2 mm platinum square. The light source employed was the GCR 130 Q-switched Nd-YAG laser detailed in Chapter 2. Typical experiments were performed at 17.0 ± 0.6 mW and hence the average energy per pulse was ca. 1.7 mJ. These values correspond to power levels recorded *outside the electrochemical cell*. No visible scarring of the electrode was observed after experimental runs suggesting that this power (once slightly diminished by reflections and absorption through the cell) is below the threshold value for ablation of platinum as evidenced by atomic force microscopy (AFM).

Blackcurrant Ribena® and 'No added sugar' Ribena® (SmithKline Beecham) were bought in 250 ml 'ready to drink' cartons. UV/visible spectra of neat and buffered Ribena® solutions were recorded in a quartz cuvette of path length 1 cm as outlined in section 2.12. Extinction coefficients were calculated by measuring absorbances as a function of concentration so as to permit estimates of power lost when the laser beam passed through a certain path length of purple Ribena® solution.

All other chemicals, apparatus and procedures employed are fully detailed in Chapter 2.

9.4 RESULTS AND DISCUSSION

9.4.1 VOLTAMMETRY OF L-ASCORBIC ACID IN NEUTRAL SOLUTION IN THE ABSENCE OF ULTRASOUND OR LASER ACTIVATION

The electrochemical oxidation of L-ascorbic acid has been reported previously at mercury drop [52], gold [53], glassy carbon [54] and platinum [51,55] electrodes and reviewed by Dryhurst et al. [56]. The electrochemical oxidation scheme given below for ascorbic acid (H_2A) in neutral solution at platinum electrodes (Equations 9.1 to 9.4) has been suggested [51,55-56]. It involves deprotonation, two single-electron transfers and the formation of an ascorbate radical ($A^{\bullet -}$) which has been detected by electron spin resonance

[56]. The end product is the hydrated form of dehydroascorbic acid (DHAA) once the adsorbed oxidation product has desorbed into solution.

$$HA^- - e^- \rightleftharpoons A^{\bullet -} + H^+ \quad (9.1)$$

$$A^{\bullet -} - e^- \rightleftharpoons DHAA_{ads} \quad (9.2)$$

$$DHAA_{ads} \rightarrow DHAA_{(aq)} \text{ (rds)} \quad (9.3)$$

$$DHAA_{(aq)} + H_2O \rightarrow \text{Hydrate (rapid)} \quad (9.4)$$

In the above scheme HA^- is the ascorbate mono-anion which is the predominant species in neutral solution according to the reported pK values of $pK_1 = 4.17$ and $pK_2 = 11.57$ at 25°C [57]. The structures of the molecules in the scheme are shown in Figure 9.1.

While at glassy carbon electrodes relatively little surface passivation is observed, the kinetics of electron transfer are slow unless the surface is chemically modified [54] or laser activated [39]. Much faster electron transfer kinetics are observed at platinum electrodes but surface fouling due to the slow desorption of the oxidised products from the metal which inhibits the uptake of fresh substrate for oxidation [51] must be overcome. In order to observe this effect cyclic voltammetry (CV) of the AA in Ribena® solutions was performed. A solution of Ribena® was made up by diluting 100 ml of the drink as received with 150 ml 0.15 M PBS to form a solution at pH 6.5. The potential of a 3 mm platinum disc electrode was raised from 0 V to 0.55 V (vs. SCE) and back again at 50 mV s^{-1}. It is believed that the decreasing peak current in the consecutive scans seen in Figure 9.2 is a consequence of the rate-limiting desorption of dehydroascorbic acid (DHAA)

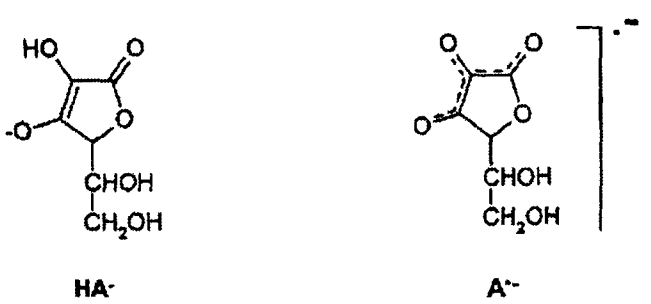

Figure 9.1 Structures of the species involved in the two-electron oxidation of ascorbate anions at platinum in neutral aqueous solution.

from the platinum surface before its hydration [51]. The lack of reduction wave on the reverse scan is indicative of a chemically irreversible oxidation.

In the next two sections we examine the possible use of sono-voltammetry or laser activated voltammetry for maintaining electrode activity during the oxidation of ascorbic acid in Ribena® at platinum electrodes.

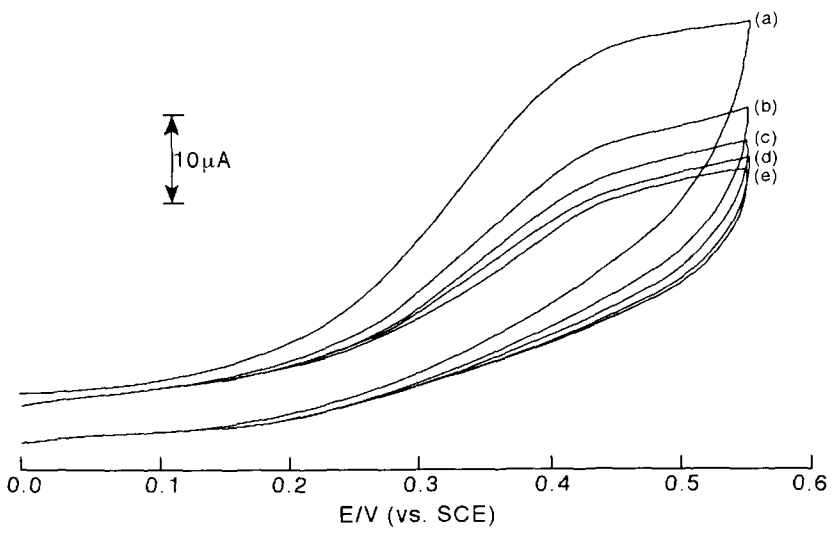

Figure 9.2. Consecutive CVs for the oxidation of AA in 100 ml Ribena® / 150 ml 0.15M PBS (pH 6.5) at a 3 mm disc Pt electrode and a scan rate of 50 mV s^{-1} showing the decrease in peak current due to passivation between a) the first scan and b) to e) subsequent scans.

9.4.2 VOLTAMMETRY IN THE PRESENCE OF ULTRASOUND

We consider first analysis of Ribena® using sono-voltammetric methodology. In the presence of power ultrasound linear sweep voltammograms for the oxidation of ascorbic acid in the buffered Ribena® solution described in the previous section at a 3 mm platinum disc working electrode were obtained as illustrated in Figure 9.3. These experiments employed the 'face-on' geometry, 25 W cm^{-2} continuous ultrasound at a horn-to-electrode distance of 4 mm and a scan rate of 10 mV s^{-1}. The current was over one order of magnitude larger than that obtained in quiescent solution. However no limiting current was observed. To test if glucose interfered with the voltammetry, a similarly buffered solution of 'no added sugar' Ribena® was analysed and gave an identical response in terms of waveshape and limiting current. As a further check ca. 5 g of glucose was added to both

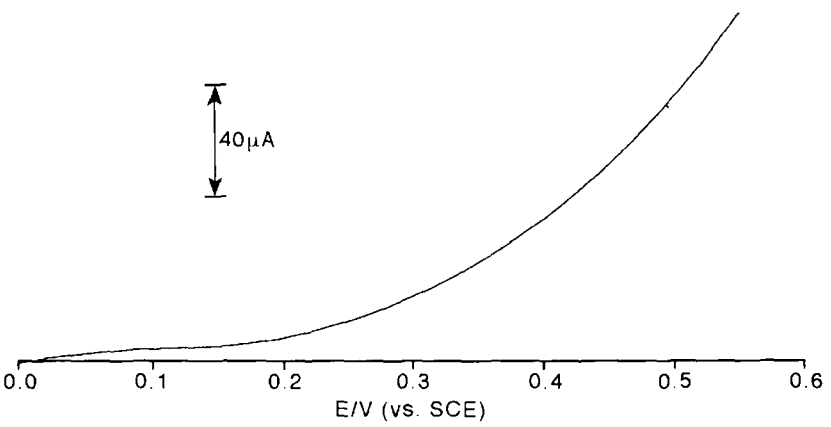

Figure 9.3 Sono-voltammogram for the oxidation of AA in 100 ml Ribena® / 150 ml 0.15M PBS (pH 6.5) on a 3 mm Pt disc electrode and a scan rate of 5 mV s^{-1}. US intensity was 25 W cm^{-2} and the horn-to-electrode distance was 4 mm.

solutions again with no change in the voltammetry in the range 0 - 0.7 V (vs. SCE). Moreover the manufacturers quote the 'sugar' content to be 14.7 g / 100 ml in blackcurrant Ribena® and 0.3 g / 100 ml in 'no added sugar' Ribena® and so interference from sugar can be discounted in the ascorbic acid analysis.

In order to circumvent the problems associated with the use of continuous ultrasound, a previously reported 'pulsed ultrasound' analytical technique [2] was employed to obtain voltammograms with a well-defined current plateau as seen in Figure 9.4. This voltammetry was performed under the same conditions as the continuous ultrasound experiments above except that the ultrasound was pulsed at 0.5 s on, 0.8 s off.

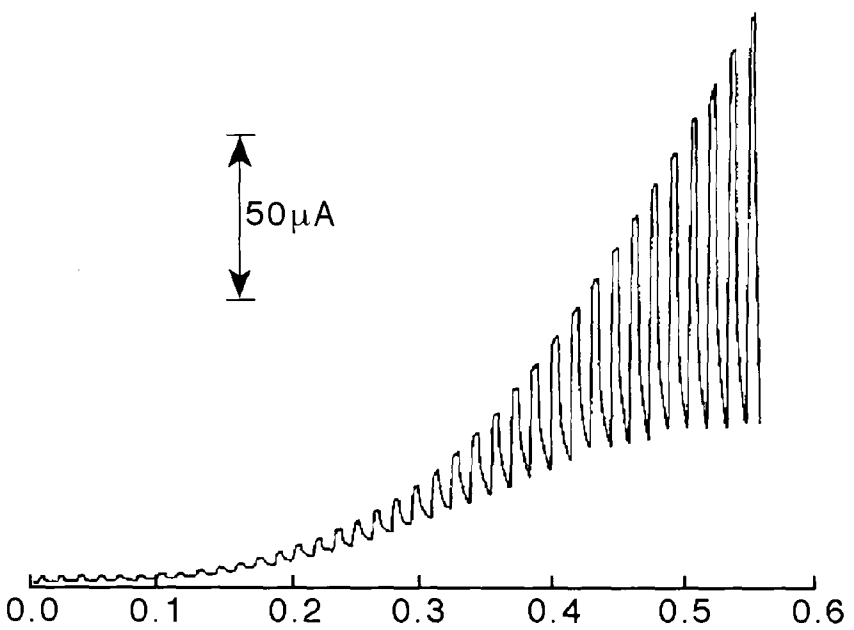

Figure 9.4 Pulsed sono-voltammogram for the oxidation of AA in 100 ml Ribena® / 150 ml 0.15M PBS (pH 6.5) on a 3 mm Pt disc electrode and a scan rate of 10 mV s^{-1}. US intensity was 25 W cm^{-2} during the 'pulse on' stage and the horn-to-electrode distance was 4 mm. Pulse on time: 0.5 s, pulse off time: 0.8 s.

To analyse the fruit drink for ascorbic acid, solutions of 100 ml Ribena® or 100 ml 'no added sugar' Ribena® were made up to 250 ml with 0.15 M PBS to form buffered solutions (0.09 M PBS) at pH 6.5. They were subjected to pulsed ultrasound operated at 0.5 s on, 0.8 s off during linear sweep voltammetry in the anodic direction at a scan rate of 5 mV s^{-1}. The current traces associated with the oxidation of AA in the 'pulse off' mode were evaluated and the limiting currents relative to the background scan of buffer alone were measured. The next stage was the standard addition of ascorbic acid (RMM = 176.13 g) in 44.03 mg amounts to increase the concentration of AA in the 250 ml solutions in 1 mM steps. This calibrates the procedure and allows the concentration of ascorbic acid in 100 ml of the drink to be calculated from a linear plot of

limiting current against concentration of added ascorbic acid by dividing the intercept by the gradient. Such plots for Ribena® and 'no added sugar' Ribena® are seen in Figures 9.5 and 9.6. Good linearity is observed and the value yielded for both solutions was 31 ± 3 mg/100 ml ascorbic acid respectively. The error represents the maximum deviation seen over repetitions of the experiment. The values are compared with those obtained by other methods below.

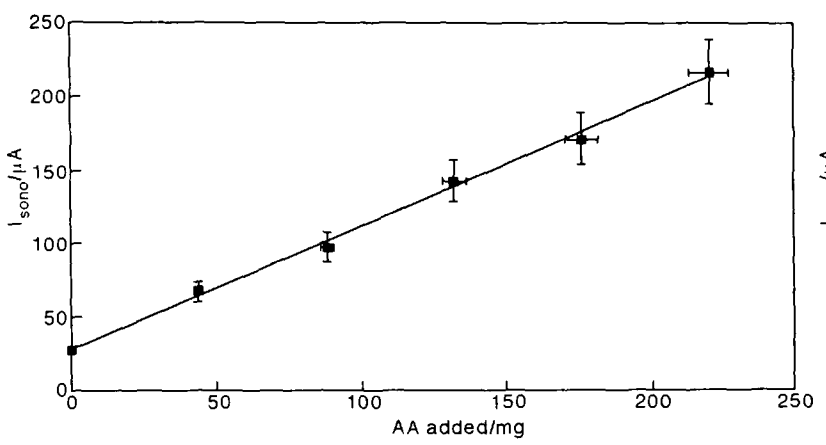

Figure 9.5 Plot of limiting current against AA added to 100 ml Ribena® / 150 ml 0.15M PBS (pH 6.5) for linear sweep pulsed sonovoltammetry on a 3 mm Pt disc electrode at a scan rate of 5 mV s^{-1}. The gradient is 0.852 μA/mg and the intercept is 26.8 μA.

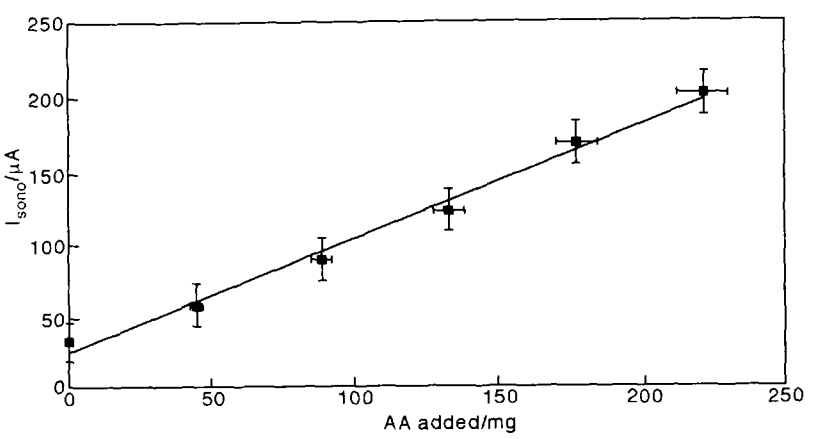

Figure 9.6 Plot of limiting current against AA added to 100 ml 'No added sugar' Ribena® / 150 ml 0.15M PBS (pH 6.5) for linear sweep pulsed sonovoltammetry on a 3 mm Pt disc electrode at a scan rate of 5 mV s^{-1}. The gradient is 0.798 μA/mg and the intercept is 25.0 μA.

9.4.3 VOLTAMMETRY IN THE PRESENCE OF LASER ACTIVATION

Before laser activated experiments were performed consideration was given to the optical characteristics of the solution in respect of the green light (532 nm) used for laser activation voltammetry. A UV/visible spectrum of Ribena® is shown in Figure 9.7. In order to estimate the amount of energy getting to the electrode, extinction coefficients for buffered and unbuffered Ribena® and 'no added sugar' Ribena® were calculated from absorbance against concentration plots. Values are tabulated in

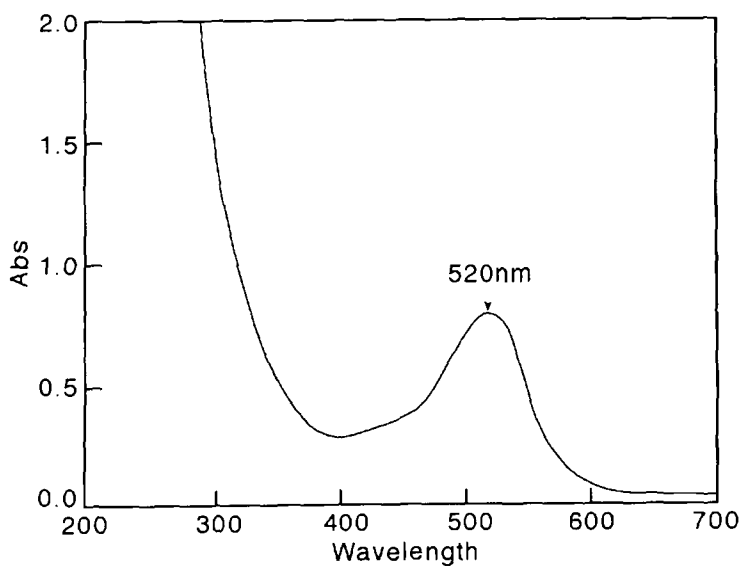

Figure 9.7 UV/Visible spectrum of a buffered solution of Ribena® at pH 6.5.

Table 9.1 for absorption at both 520 nm (the absorption maximum) and 532 nm (the wavelength used in experiments). By using buffered Ribena® solutions and the modified electrochemical cell pictured in Figure 2.5 the attenuation of the laser in typical experiments could be reduced to ca. 6%. In addition it was observed that after a few hours of experimentation there was some photo-bleaching of the solutions leading to paler colour and a slight decrease in the absorption; accordingly for quantitative work measurements were completed within 30 minutes.

Solution composition \ wavelength	520 nm	532 nm
Pure Ribena®	2.51	2.21
Pure 'No added sugar' Ribena®	2.76	2.31
Ratio Ribena® : 0.15 M PBS = 2 : 3 (pH 6.5)	0.94	0.82
Ratio 'No added sugar' Ribena® : 0.15 M PBS = 2 : 3 (pH 6.5)	1.31	1.23

Table 9.1 Extinction coefficients in $cm^2\ g^{-1}$ for Ribena® solutions at two different wavelengths.

Anodic linear sweep voltammetry from 0 to 0.6 V (vs. SCE) at 5 mV s^{-1} was performed on Ribena® solutions as described in the previous section. The electrochemical cell shown in Figure 2.5 was used and the working electrode was a 2 mm x 2 mm platinum square. Initially the laser power was set at a low setting and then gradually turned up until the voltammetry was affected in respect of increased oxidative currents. The lowest power to yield reproducible voltammograms was measured as 17.0 ± 0.6 mW. This average power, taken with a beam diameter of ca. 3 mm corresponds to a 'fluence' or average energy per unit area of ca. 24 mJ cm^{-2}. The corresponding average laser intensity was then 240 mW cm^{-2}, due to the pulse frequency being 10 Hz.

The effect of the laser illumination on the voltammetry is clearly illustrated in Figure 9.8. Traces with the laser on show a mass-transport limited current and retain good repeatability whilst in the 'dark' the peak current quickly diminishes with successive scans. As soon as the laser is re-applied the electrode is immediately refreshed and the trace returns to its original height. It is the repeatable voltammetry facilitated by laser illumination that forms the basis of this electroanalytical technique. We attribute the effect to the cleaning action of the laser pulses which cause thermoelastic stresses [37,43] in the platinum and lead to adsorbed passivating ascorbic acid oxidation products being removed whilst leaving the bulk electrode unscathed. At the same time the diffusion layer is continually refreshed leading to mass transport that is slightly enhanced when compared with voltammetry 'in the dark'.

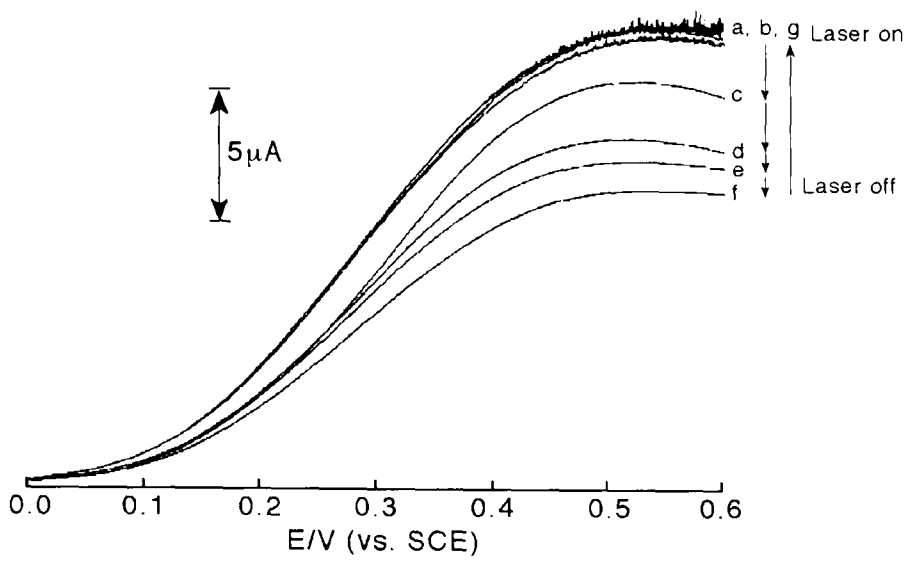

Figure 9.8 LAVs for the oxidation of 100 ml 'No added sugar' Ribena® / 150 ml 0.15M PBS (pH 6.5) with 10 mM AA added on a 2 mm x 2 mm square Pt electrode and a scan rate of 5 mV s^{-1}. The laser power was 17.0 ± 0.6 mW and the beam diameter was ca. 3 mm. a) & b) initial scans: laser on; c), d), e) & f) third, fourth, fifth and sixth scans: 'dark'; g) seventh scan: laser on, giving renewed activity.

Before experiments were conducted to determine the ascorbic acid content it was important to again discount the effect of sugar in solution on the voltammetry. Successive scans recorded with increasing amounts of glucose added to the Ribena® solution (up to the solution being saturated) showed no change in the range 0 - 0.7 V (vs. SCE). The background current of the buffer solution alone was also recorded under the laser conditions above. The next stage was the standard addition of ascorbic acid to increase the concentration of AA in the 250 ml buffered solutions of Ribena® and 'no added sugar' Ribena® in the same manner

as described in section 9.4.2. Multiple steady-state scans at each concentration were taken and the average value of limiting current recorded.

Further independent investigations were carried out a different energy density setting. The beam diameter was increased to ca. 5mm and the power to 23.0 ± 0.7 mW. This ensured that the entire electrode surface was illuminated with a more even though slightly lower energy density of fluence ca. 12 mJ cm^{-2}. The experiment was then repeated for Ribena® and the voltammetry is seen in Figure 9.9. As before the concentration of ascorbic acid in each drink can be calculated from a linear plot of limiting current against concentration of added ascorbic acid by dividing the intercept by the gradient. Such plots for Ribena® (under two different laser conditions) and 'no added sugar' Ribena® for ranges of added AA of 1 - 10 mM (44.03 - 440.3 mg) yielded good linearity and the values of ascorbic acid concentrations calculated from the data in Table 9.2 are 28.7 ± 1.0, 28.5 ± 0.5 and 28.3 ± 0.4 mg/100 ml respectively. These values are discussed in the next section.

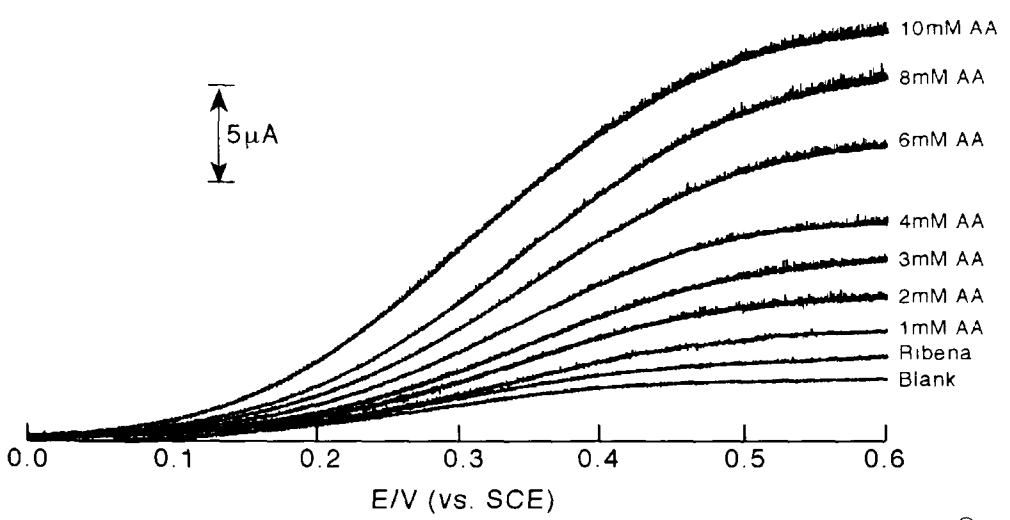

Figure 9.9 Sample LAVs for oxidation of 100 ml Ribena® / 150 ml 0.15M PBS (pH 6.5) with added AA on a 2 mm x 2 mm square Pt electrode at a scan rate of 5 mV s^{-1}. The laser power was 23.0 ± 0.7 mW and the beam diameter was ca. 5 mm ensuring total electrode coverage.

Sample (power / mW)	Ready to drink Blackcurrant Ribena® (17)	Ready to drink Blackcurrant Ribena® (23)	Ready to drink 'No added sugar' Ribena® (17)
Fluence / mJ cm^{-2}	~24	~12	~24
Slope / μA mg^{-1}	0.0296	0.0377	0.0295
Intercept / μA	0.850	1.065	0.838
R^2	0.9950	0.9976	0.9968

Table 9.2 Data from plots of limiting current against ascorbic acid added to 100 ml Ribena® / 150 ml 0.15M PBS (pH 6.5) for linear sweep laser ablation voltammetry on a 2 mm x 2 mm Pt square electrode at a scan rate of 5 mV s^{-1}.

9.4.4 RELATIVE ANALYTICAL PERFORMANCES

The ascorbic acid concentrations obtained by the electroanalytical procedures described in previous sections are summarised in Table 9.3 along with values obtained by other independent methods. All the values agree within error limits and the laser technique gives accuracy levels which are comparable to those obtained by wet chemical methods requiring elaborate pre-treatment.

AA detection method \ sample	Ready to drink Blackcurrant Ribena®	Ready to drink 'No added sugar' Ribena®
SmithKline Beecham manufacturing process: checked by HPLC[a] and DCIP[b] titration [58]	> 24	> 24
Warwick Analytical Service DCIP titration	28.6 ± 0.4	28.5 ± 0.2
Photoelectroanalysis with toluidine blue [34]	28.7 ± 1.0	28.2 ± 1.0
Pulsed sono-electroanalysis[c]	31 ± 3	31 ± 3
Laser activated electroanalysis [c] ~3 mm[d], 17 mW	28.7 ± 1.0	28.4 ± 0.5
Laser activated electroanalysis [c] ~5 mm[d], 23 mW	28.3 ± 0.4	-

Table 9.3 Concentrations of ascorbic acid in mg/100 ml determined by various methods. [a] High performance liquid chromatography, [b] dichloroindophenol, [c] this work and [d] laser beam diameter.

One interesting possibility that may explain the very slightly higher values of the sono-analysis is that ultrasound can interfere with the electrochemistry via the formation of radicals. It is possible that some of the electrogenerated dehydroascorbic acid can be reduced by atomic hydrogen [59] known to be formed by the ultrasonic splitting (sonolysis) of water [60]. The small amount of radical thus formed ($A^{\bullet-}$ in Figure 9.1) could then be re-oxidised electrochemically, generating extra current. In contrast to the application of pulsed ultrasound, laser activation delivers power directly to the electrode with minimal disturbance of the surrounding electrolyte and no photochemical interaction with ascorbic acid. Thus the key difference in the two forms of stimuli is that ultrasound provides gradual surface erosion but greatly enhanced mass transport of electroactive species to the electrode whereas laser irradiation yields focused surface activation but relatively little bulk solution agitation.

9.5 CONCLUSIONS

It has been shown that both pulsed sonovoltammetry and low power laser ablation voltammetry can be reliably used for the electroanalysis of vitamin C at platinum electrodes in media where 'unaided' electrochemistry is precluded by passivation and specifically in a commercially available fruit drink. This analysis is laborious by non-electrochemical methods and irreproducible by conventional electrochemistry. Both methods reported yield limiting currents that are proportional to the concentration of ascorbic acid present and are reproducible provided care is taken in the case of LAV with the laser alignment and power setting. While the pulsed ultrasound technique offers higher mass transport and limiting currents the LAV technique gave better repeatability and surface cleaning provided the whole electrode was subject to continuous refreshment.

As a consequence both techniques offer the prospect of quick and simple quantitative electroanalysis of ascorbic acid in Ribena®. Agreement with independent values obtained by various other methods is excellent. In the next chapter we take a more detailed view of the phenomenon of laser activation and seek to characterise and expand on the mass transport, surface effects and analytical applications of this novel technique.

9.6 CHAPTER 9: REFERENCES

[1] N. A. Madigan, T. J. Murphy, J. M. Fortune, C. R. S. Hagan, L. A. Coury Jr., *Anal. Chem.* **1995**, *67*, 2781.
[2] R. G. Compton, F-M. Matysik, *Electroanalysis* **1996**, *8*, 213.
[3] F. Marken, T. O. Rebbitt, J. Booth, R. G. Compton, *Electroanalysis* **1997**, *9*, 19.
[4] F-M. Matysik, S. Matysik, A. M. O. Brett, C. M. A. Brett, *Anal. Chem.* **1997**, *69*, 1651.
[5] C. Agra-Gutiérrez, R. G. Compton, *Electroanalysis* **1998**, *10*, 204.
[6] D. J. Walton, S. S. Phull, *Adv. Sonochem.* (Ed. T. J. Mason) **1996**, *4*, 205.
[7] R. G. Compton, J. C. Eklund, F. Marken, *Electroanalysis* **1997**, *7*, 509.
[8] R. G. Compton, J. C. Eklund, S. D. Page, *J. Phys. Chem.* **1995**, *99*, 4211.

[9] R. G. Compton, J. C. Eklund, S. D. Page, T. O. Rebbitt, *J. Chem. Soc. Dalton Trans.* **1995**, *3*, 389.
[10] R. Walker, *Chem. Britain* **1990**, *26*, 251.
[11] H. Fujiwara, M. Atobe, H. Kanetsuna, T. Nonaka, *J. Chinese Chem. Soc.* **1998**, *45*, 175.
[12] T. J. Mason, *Chem. Soc. Rev.* **1997**, *26*, 443.
[13] M. Atobe, T. Nonaka, *Bull. Chem. Soc. Jpn.* **1998**, *71*, 397.
[14] F. Marken, R. G. Compton, S. G. Davies, S. D. Bull, T. Thiemann, M. L. S. E. Melo, A. C. Neves, J. Castillo, C. G. Jung, A. Fontana, *J. Chem. Soc. Perkin Trans. 2* **1997**, *10*, 2055.
[15] M. Atobe, S. Fuma, N. Sato, T. Nonaka, *Denki Kagaku* **1997**, *65*, 495.
[16] M. Atobe, T. Nonaka, *Chem. Letters* **1997**, *4*, 323.
[17] M. Atobe, T. Nonaka, *Ultrasonics Sonochemistry* **1997**, *4*, 17.
[18] F. Marken, R. G. Compton, S. D. Bull, S. G. Davies, *J. Chem. Soc. Chem. Comm.* **1997**, *11*, 995.
[19] M. Atobe, K. Matsuda, T. Nonaka, *Electroanalysis* **1996**, *8*, 784.
[20] T. J. Mason, J. P. Lorimer, D. J. Walton, *Ultrasonics* **1990**, *28*, 333.
[21] M. Atobe, T. Nonaka, *J. Electroanal. Chem.* **1997**, *425*, 161.
[22] A. Chyla, J. P. Lorimer, G. Smith,, D. J. Walton, *J. Chem. Soc. Chem. Comm.* **1989**, *9*, 603.
[23] M. Atobe, T. Nonaka, *Chem. Letters* **1995**, 669.
[24] M. Atobe, K. Matsuda, T. Nonaka, *Denki Kagaku* **1994**, *62*, 1298.
[25] K. Matsuda, M. Atobe, T. Nonaka, *Chem. Letters* **1994**, 1619.
[26] J. C. Eklund, D. N. Waller, T. O. Rebbitt, F. Marken, R. G. Compton, *J. Chem. Soc. Perkin Trans. 2* **1995**, *11*, 1981.
[27] A. Durant, H. Francois, J. Reisse, A. Kirsch-de Mesmaeker, *Electrochim. Acta* **1996**, *41*, 277.
[28] R. G. Compton, R. A. W. Dryfe, *Prog. Reaction Kinetics* **1995**, *20*, 245.
[29] W. LaCourse, I. S. Krull, K. Bratin, *Anal. Chem.* **1985**, *57*, 1810.
[30] W. LaCourse, I. S. Krull, *Anal. Chem.* **1986**, *58*, 49.
[31] W. LaCourse, I. S. Krull, *Anal. Chim.* Acta **1988**, *215*, 45.
[32] S. G. Weber, C. G. Cohen, *Anal. Chem.* **1993**, *65*, 169.
[33] J. C. Eklund, A. Hallick, S. Kumbhat, R. G. Compton, *Electroanalysis* **1996**, *8*, 702.
[34] J. A. Cooper, M. Wu, R. G. Compton, *Anal. Chem.* **1998**, *70*, 2922.
[35] R. K. Ulrich, R. C. Alkire, *J. Electrochem. Soc.* **1981**, *128*, 1169.
[36] P. L. Cowan, J. A. Golovchenko, *Vacuum Sc. Tech.* **1980**, *17*, 5.
[37] R. Oltra, G. M. Indrianjafy, J. P. Boquillon, *J. Phys. IV, Colloque C7, 769, Suppl. J. Phys. III* **1991**, 12.
[38] R. Oltra, G. M. Indrianjafy, M. Keddam, H. Takenouti, *Corrosion Sci.* **1993**, *35*, 827.
[39] M. Poon, R. L. McCreery, *Anal. Chem.* **1986**, *58*, 2745.

[40] R. K. Jaworski, R. L. McCreery, *J. Electroanal. Chem.* **1994**, *369*, 175.
[41] T. Hinoue, I. Watanabe, H. Watarai, *Chem. Letters* **1996**, *5*, 329.
[42] J. F. Smalley, C. V. Krishnan, M. Goldman, S. W. Feldberg, I. Ruzic, *J. Electroanal. Chem.* **1988**, *248*, 255.
[43] J. D. Aussel, A. Le Brun, J. C. Baboux, *Ultrasonics* **1988**, *26*, 245.
[44] E. Graf, *J. Agri. Food Chem.* **1994**, *42*, 1616.
[45] D. M. Schaeffer, Q. P. Liu, C. Faustman, M. C. Yin, *J. Nutrition* **1995**, *125*, S1792.
[46] E. N. Frankel, *Food Chem.* **1996**, *57*, 51.
[47] *Pearson's Composition and Analysis of Food* (9th Ed.) (Eds. R. Kirk, R. Sawyer), Longman Scientific & Technical, Harlow, UK, **1991.**
[48] *Official Methods of Analysis of AOAC International* (16th Ed., Vol. II) (Ed. P Cunniff), AOAC International, Gaithersburg, Maryland, USA, **1995**, Chapter 45, pgs.16-17.
[49] E. S. Wagner, B. Lindley, R. D. Coffin, *J. Chromatogr.* **1979**, *163*, 225.
[50] J. W. Finley, E. Duang, *J. Chromatogr.* **1981**, *207*, 449.
[51] P. Karabinas, D. Jannakoudakis, *J. Electroanal. Chem.* **1984**, *160*, 159.
[52] J. J. Ruiz, A. Aldaz, M. Domínguez, *Can. J. Chem.* **1977**, *55*, 2799.
[53] M. Rueda, A. Aldaz, F. Sanchez-Burgos, *Electrochim. Acta* **1978**, *23*, 419.
[54] I. G. Casella, M. R. Guascito, *Electroanalysis* **1997**, *9*, 1381.
[55] M. Brezina, J. Koryta, T. Loucka, D. Marsikova, J. Pradac, *J. Electroanal. Chem.* **1972**, *40*, 13.
[56] G. Dryhurst, K. Kadish, F. Scheller, R. Renneberg, *Biological Electrochemistry*, Academic Press, New York, **1982**, *1*, 256.
[57] *Merck Index* (11th Ed.), Rahway, NJ, USA, **1989**, pg. 858.
[58] J. Francis, Nutrition Dept., SmithKline Beecham, Brentford, UK, *private communication,* **1998.**
[59] B. H. J. Bielski, D. A. Comstock, R. A. Bowen, *J. Am. Chem. Soc.* **1971**, *93*, 5624.
[60] T. J. Mason, *Practical Sonochemistry,* Ellis Horwood, Chichester, **1991**, pg. 26.

10

CHARACTERISATION OF LASER ACTIVATED VOLTAMMETRY (LAV)

CHAPTER 10: CHARACTERISATION OF LASER ACTIVATED VOLTAMMETRY (LAV)

10.1 CONTENTS

The work described in this chapter explores the use of electrochemistry under laser activation and seeks to characterise the mass transport and surface effects encountered. Additionally, the analytical applications introduced in the previous two chapters are further investigated. Some of the work in this chapter was accepted for publication in May 1999 in *Electroanalysis*.

The voltammetry of various well-characterised aqueous and non-aqueous electrochemical systems is studied at platinum and gold disc electrodes under illumination from a 10 Hz pulsed Nd:YAG laser frequency doubled to operate at 532 nm. A simple Nernst diffusion layer model is established to quantify the mass transport observed as a function of laser intensity in the thermoelastic region where light energy absorbed by the metal is insufficient to cause localised melting or vaporisation but does lead to a thinning of the diffusion layer thickness through surface heating/vibration. This leads to sigmoidal shaped voltammograms whilst maintaining a clean, reproducible electrode surface. Above the ablation threshold, the minimum laser intensity required to cause electrode damage, atomic force microscopy (AFM) is used to probe the nature of the surface damage and its relationship to the laser intensity. The Nernst-diffusion model is verified by means of potential step chronoamperometric measurements in water and acetonitrile where good agreement with theory is seen for transport across a diffusion layer of a thickness corresponding to that inferred from the steady-state voltammetry.

Applications of the laser activation technique are illustrated by three systems found to be passivating in aqueous media; the two-electron reduction of toluidine blue dye, iodide oxidation and the oxidation of ferrocyanide in the presence of the blood protein, fibrinogen.

In all cases clean, reproducible and quantitative voltammetry is seen in contrast to that observed in the absence of laser activation.

10.2 INTRODUCTION

The maintenance of a clean, reproducible electrode surface is of critical importance in making meaningful electroanalytical measurements. Indeed the limited use of such methodology in real-world analytical usage likely derives substantially from the fact that in many non-model systems typically encountered outside of the research laboratory the inevitable presence of surface active materials can lead to significant interference and electrode passivation problems. Moreover since as little as *monolayer* coverage is often sufficient to perturb the path of electrode processes it follows that only trace amounts of the adsorbing interferent may be significant.

Classically potential passivation problems were alleviated through the use of a dropping mercury electrode (DME) but this device is less suitable than those based on solid electrodes for many (such as on-line) analytical purposes and entirely inapplicable if significant oxidising potentials are required. In addition mercury is environmentally compromising and its use is in decline due to increasing legislation world-wide. Accordingly the development of methods to facilitate the wider and more general use of solid electrodes without the need for mercury would be timely. Hitherto electrode cleaning has been achieved most simply through ex-situ mechanical polishing, though both scratching [1-6] and cleaving [7,8] can have activating effects. The use of power ultrasound for electrode depassivation via cavitational cleaning has also been successfully utilised [9] and is discussed in section 1.5.2, though damage to the electrode surface is evident when high intensities are employed [10]. This chapter concentrates on the illumination of electrodes with lasers and recently Watanabe and co-workers [11] used a relatively high power infra-red laser source to maintain fresh platinum and gold electrode surfaces by physically removing the top layer of electrode surface every few seconds via the phenomenon of 'laser ablation' [11]. This followed work by McCreery and colleagues who used high intensity, in-situ infra-red laser pulses to activate

the surface and increase heterogeneous electron-transfer kinetics at glassy carbon and platinum electrodes [12-19] It is important to note that these [11-19] experiments use laser illumination solely to activate or refresh the electrode surface but not to provide direct chemical effects and a contrast can be drawn with situations where either solution phase species absorb laser light to form electronically excited species which then lead to electrochemical processes [20] or where irradiation of a semiconducting electrode is used to generate charge carriers [21].

The present chapter seeks to explore and quantify the laser activation of a platinum electrode in the context of illuminated linear sweep and potential step voltammetry. The term *activation* is again used to distinguish the depassivation and current enhancement effects obtained while maintaining an essentially undamaged electrode from the drastic current fluctuations and major electrode damage associated with the *ablation* technique as employed by Watanabe *et al.* [11] and discussed in section 1.7 and Chapter 9. Under ablating conditions large fluctuating current spikes and pulses are produced possibly as a consequence of the large temperature jumps associated with electrode damage events [22]. This electrode damage occurs when the laser pulses have sufficient energy to cause localised surface melting or even vaporisation [23,24]. In the following, the nature of the electrode damage at the electrode/solution interface caused by the laser in the ablation mode is probed by ex-situ atomic force microscopy (AFM) as a function of intensity above a critical threshold value.

Laser activated voltammetry (LAV) using a 10 Hz pulsed Nd:YAG laser at 532 nm is performed on several redox systems to establish a quantitative model for the rate of mass transport to the illuminated electrode. Gold and platinum are used as the electrode substrates and voltammetry in both water and acetonitrile is examined. Variation of experimental parameters including electrode area, concentration, diffusion coefficient and laser intensity is investigated and potential-step chronoamperometry is used to verify a simple Nernst diffusion model.

Finally, applications of the laser activation technique are illustrated with reference to several aqueous based systems. These are the oxidation of iodide, the oxidation of

ferrocyanide in the presence of two electrode passivating blood proteins, bovine albumin and fibrinogen, and the two-electron reduction of toluidine blue dye as a function of pH.

10.3 EXPERIMENTAL

Laser activated voltammetry in nominally stationary solution was conducted in the three-electrode cells shown in Figures 2.5 and 2.6. For most experiments a 1 mm diameter platinum disc working electrode was used having been embedded in a Perspex window set in a Teflon mount. Other experiments employed a 1 mm diameter gold disc or 2, 3 or, 4 mm square platinum electrodes. When acetonitrile was used as the solvent, a 1 mm platinum disc embedded in soda glass was utilised. Voltammetry under flow conditions utilised optically transparent channel flow cells as detailed in section 2.6. All other experimental procedures were performed as outlined in Chapter 2.

10.4 RESULTS AND DISCUSSION

10.4.1 THERMAL EFFECTS

We first investigate the effects of increasing solution temperature on the half-wave potentials for three simple electrochemically reversible systems. The temperature dependence of the ferrocene / ferrocenium, ferri/ocyanide and $Ru(NH_3)_6^{3+}$ / $Ru(NH_3)_6^{2+}$ redox couples was determined as detailed in section 2.3 in the apparatus shown in Figure 2.8. The values are tabulated in Table 10.1 and in the case of $[Fe(CN)_6]^{4/3-}$ are in excellent agreement with the literature [25]. Use of these measurements will be made for comparison with laser-induced electrode heating encountered in the next section.

Redox couple	Solvent / Electrolyte	Temperature dependence of $E_{1/2}$ / ± 0.01 mV K^{-1}
$[Fe(CN)_6]^{4/3-}$	Water / 0.1 M KCl	-1.53
$Ru(NH_3)_6^{3/2+}$	Water / 0.1 M KCl	+0.46
ferrocene / ferrocenium	MeCN / 0.1 M TBAH	+0.71

Table 10.1 Half-wave potential shifts with temperature for three simple redox systems.

10.4.2 LASER INTENSITY EFFECTS

We next describe linear sweep voltammetry experiments conducted on simple well-characterised redox systems in order to identify the effects of increasing levels of laser illumination. Two electrode materials (platinum and gold) and two solvents (acetonitrile and water) were examined. In aqueous media the one-electron oxidation of a 10 mM solution of potassium ferrocyanide and the one-electron reduction of a 10 mM solution of ruthenium hexaamine trichloride, both in 0.1 M KCl, were studied. In acetonitrile the one electron oxidation of a 10 mM solution of ferrocene in 0.1 M TBAH was examined. Under 'dark' conditions, linear sweep voltammetry showed peak potentials in good agreement with those reported in the literature [26-28]. Scans at increasing laser intensities were then recorded and typical examples are shown in Figure 10.1.

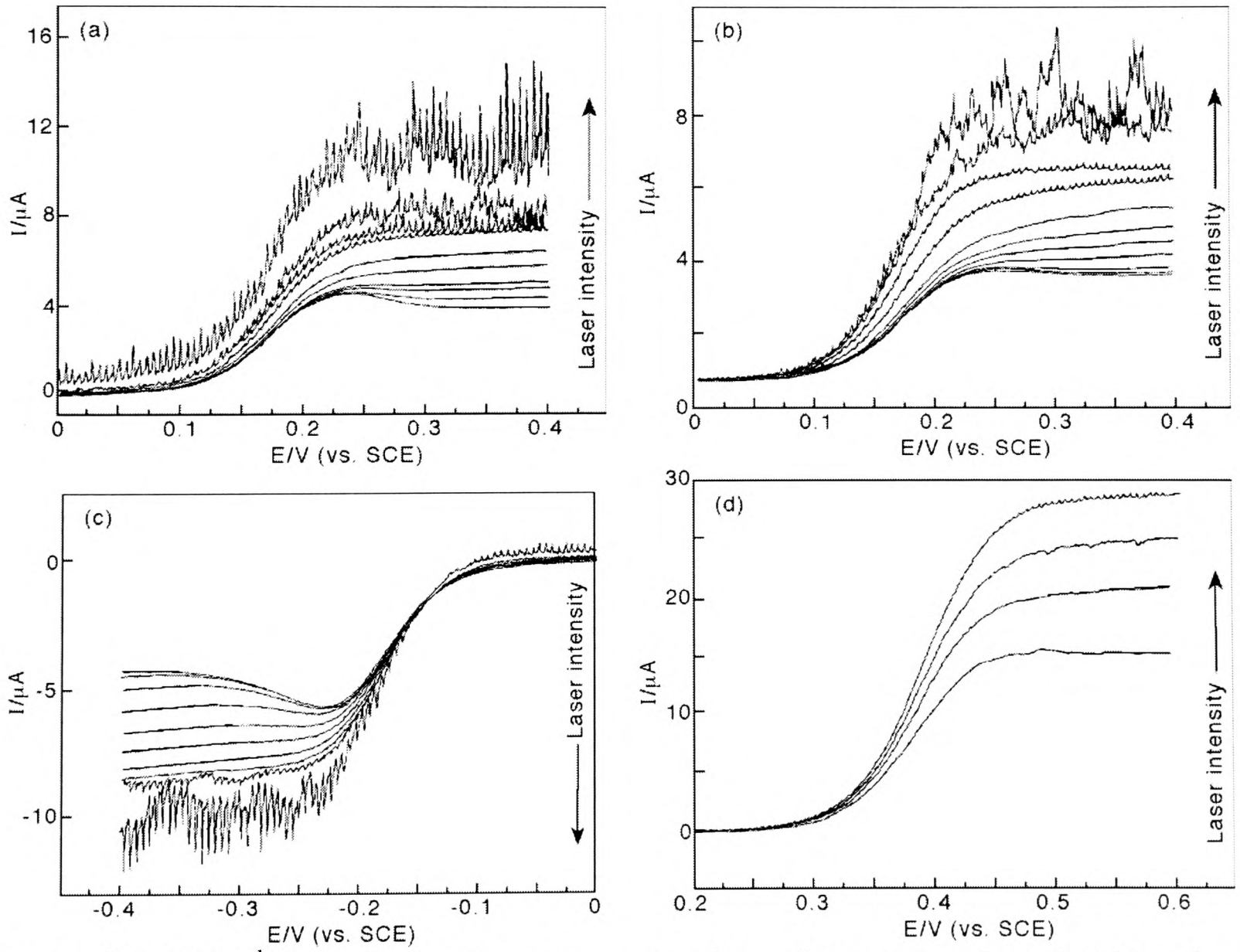

Figure 10.1 5 mV s^{-1} linear sweep voltammograms at a 1 mm diameter disc electrode subjected to increasing laser intensities for a) 10 mM ferrocyanide in 0.1 M KCl(aq) on platinum, b) 10 mM ferrocyanide in 0.1 M KCl(aq) on gold, c) 10 mM $Ru(NH_3)_6Cl_3$ in 0.1 M KCl(aq) on platinum and d) 10 mM ferrocene in acetonitrile / 0.1 M TBAH on platinum. For (a)-(c) intensities from zero up to 1.3 W cm^{-2} were employed; for (d) zero up to 0.8 W cm^{-2}.

At average light intensities below ca. 100 mW cm^{-2} essentially 'dark' linear sweep voltammetric behaviour was seen with peak currents that were only slightly higher (ca. 10%) than the dark scans. Above this laser intensity effectively *steady-state* voltammograms were achieved with limiting currents that became larger with increasing intensity. Measured half-wave potentials were found to be in good agreement with previously reported values in the absence of light [27,29,30] except where noted; these potentials are given in Table 10.2 along with measured or literature values for diffusion coefficients.

Redox Species	Solvent / Electrolyte	Redox process	$E_{1/2} \pm 0.02$ / V (vs. SCE)[a]	D / $cm^2 s^{-1}$ (298 K)[b]	Ref.
$[Fe(CN)_6]^{3-}$	Water / 0.1 M KCl	1 e^- red^n.	+0.20	7.6×10^{-6}	[31]
$[Fe(CN)_6]^{4-}$	Water / 0.1 M KCl	1 e^- oxid^n.	+0.18	6.5×10^{-6}	[31]
$Ru(NH_3)_6^{3+}$	Water / 0.1 M KCl	1 e^- red^n.	-0.18	9.1×10^{-6}	[27]
I^-	Water / 0.125 M H_2SO_4	1 e^- oxid^n.	+0.42	1.99×10^{-5}	[31]
H^+	Water / 0.1 M KCl	1 e^- red^n.	-0.40	7.42×10^{-5}	[31]
Ascorbate[c]	Water / 0.1 M PBS, pH 7.0	2 e^- oxid^n.	+0.31	4.7×10^{-6}	[32]
Toluidine Blue[d]	Water / 0.1 M PBS, pH 2.7	2 e^- red^n.	+0.03	4.6×10^{-6}	[33]
Ferrocene	MeCN / 0.1 M TBAH	1 e^- oxid^n.	+0.40	2.3×10^{-5}	[28]
Decamethyl ferrocene	MeCN / 0.1 M TBAH	1 e^- oxid^n.	-0.12	1.72×10^{-5}	this work
$(p\text{-}BrC_6H_4)_3N$[e]	MeCN / 0.1 M TBAH	1 e^- oxid^n.	+1.06	1.63×10^{-5}	this work
p-Chloranil[f]	MeCN / 0.1 M TBAH	1 e^- red^n.	+0.02	1.84×10^{-5}	this work
p-BNB[g]	MeCN / 0.1 M TBAH	1 e^- red^n.	-1.05	2.0×10^{-5}	[34]

Table 10.2 Redox species employed in laser activated voltammetry experiments. [a] Experimentally measured at Pt electrodes. [b] Literature values except where stated. [c] Mono-anion of ascorbic acid. [d] Toluidine blue dye used as $ZnCl_4^{2-}$ salt. [e] Tris-4-bromophenylamine. [f] Tetrachloro-*p*-benzoquinone. [g] *p*-Bromonitrobenzene.

At these relatively low levels of illumination (ca. 100 - 700 mW cm^{-2}), no visible electrode ablation was apparent to the naked eye and this was confirmed by a negligible increase in surface roughness as defined by the ratio of surface area to projected area measured by AFM. Specifically the sustained mass transport limiting currents seen can be

attributed to a system-dependent threshold laser power setting where convection caused by local heating is responsible for the increased mass transport described in the next section. Half-wave potentials for the ferrocyanide, ruthenium hexaammine trichloride and ferrocene systems described above were measured as a function of laser intensity and are tabulated in Table 10.3. The direction of the shifts is consistent with the data reported in Table 10.1 for ferri/ocyanide (ca. -1.53 mV K^{-1}), ruthenium hexaammine trichloride (ca. +0.46 mV K^{-1}) and ferrocene (ca. +0.71 mV K^{-1}).

Species / solution / electrode	Laser Intensity / ± 20 mW cm^{-2}	$E_{1/2}$ / ± 2 mV	δ / ± 3 μm[a]
$[Fe(CN)_6]^{4-}$ / 0.1 M KCl in water / Pt.	110	175	107
	190	175	95
	290	176	85
	490	175	78
	800	170	68
	1240	168	57
$[Fe(CN)_6]^{4-}$ / 0.1 M KCl in water / Au.	130	179	125
	210	179	112
	360	180	97
	550	178	84
	720	169	76
	960	168	62
	1320	167	59
$Ru(NH_3)_6^{3+}$ / 0.1 M KCl in water / Pt.	170	-172	115
	270	-170	102
	390	-171	94
	600	-173	90
	840	-175	85
	1120	-175	73
Toluidine Blue / 0.1 M KCl, 0.1 M PBS, pH 4.0 in water / Pt.	200	-110	118
	400	-109	92
Ferrocene / 0.1 M TBAH in MeCN / Pt.	170	387	91
	340	389	79
	800	392	67

Table 10.3 Half-wave potential data for linear sweep voltammetry at different laser intensities.
[a] Calculated from steady state current using Equation 10.1.

Since the half-wave shift with temperature for ferrocyanide is reported [25] as -1.53 mVK^{-1} we can estimate the ca. 7 and 12 mV negative shifts in half-wave potential for

platinum and gold respectively to be a consequence of increases in time-averaged electrode temperature of ca. 4 and 8 K each for changes in intensity from 200 to 1300 mW cm^{-2}. The relative values for gold and platinum likely depend on an interplay between the relative heat capacities, absorption coefficients for visible (532 nm) radiation and thermal conductivities [35] Within experimental error, a ca. 4 K increase in average temperature for the platinum electrode over the above intensity range is also consistent with the half-wave shifts for [$Ru(NH_3)_6^{3+}$] and ferrocene recorded in Table 10.3. Since the electrode was illuminated for only approximately 100 ns every second the bulk heating of the electrode was small at these intensities and led to negligible heating of the bulk solution.

As the intensity was increased further above ca. 700 mW cm^{-2} both regular electrical noise and irregular current spikes due to temperature-jump induced surface events occurred and can be seen in the upper traces in Figure 10.1. The irregular current fluctuations are caused by the onset of *laser ablation* which is known to occur when laser pulses of sufficient power damage the platinum surface with concomitant acoustic and thermal emission [11]. This damage caused at higher intensities was investigated using AFM.

AFM pictures of a polished platinum surface before and after subjection to 60 seconds of increasing laser irradiation intensity in 0.1 M PBS at pH 7.5 are seen in Figure 10.2 and compared with a micrograph of platinum that had been irradiated in air at ca. 0.5 W cm^{-2} for 35 seconds. For the latter a more undulating surface is observed with a greater roughness at lower power whereas for the former, below ca. 1.5 W cm^{-2} there is no visible scarring of the platinum seen by eye and negligible difference seen in the surface roughness as imaged by AFM. Surface roughness was measured both in terms of maximum surface peak height and as a ratio of surface area to the projected surface area of the 15×15 μm micrographs. The average values are given in Table 10.4. As the intensity is increased above 1.5 W cm^{-2} surface damage becomes clearly evident and increases as a function of laser intensity (as does the acoustic emission [11]) and time of exposure.

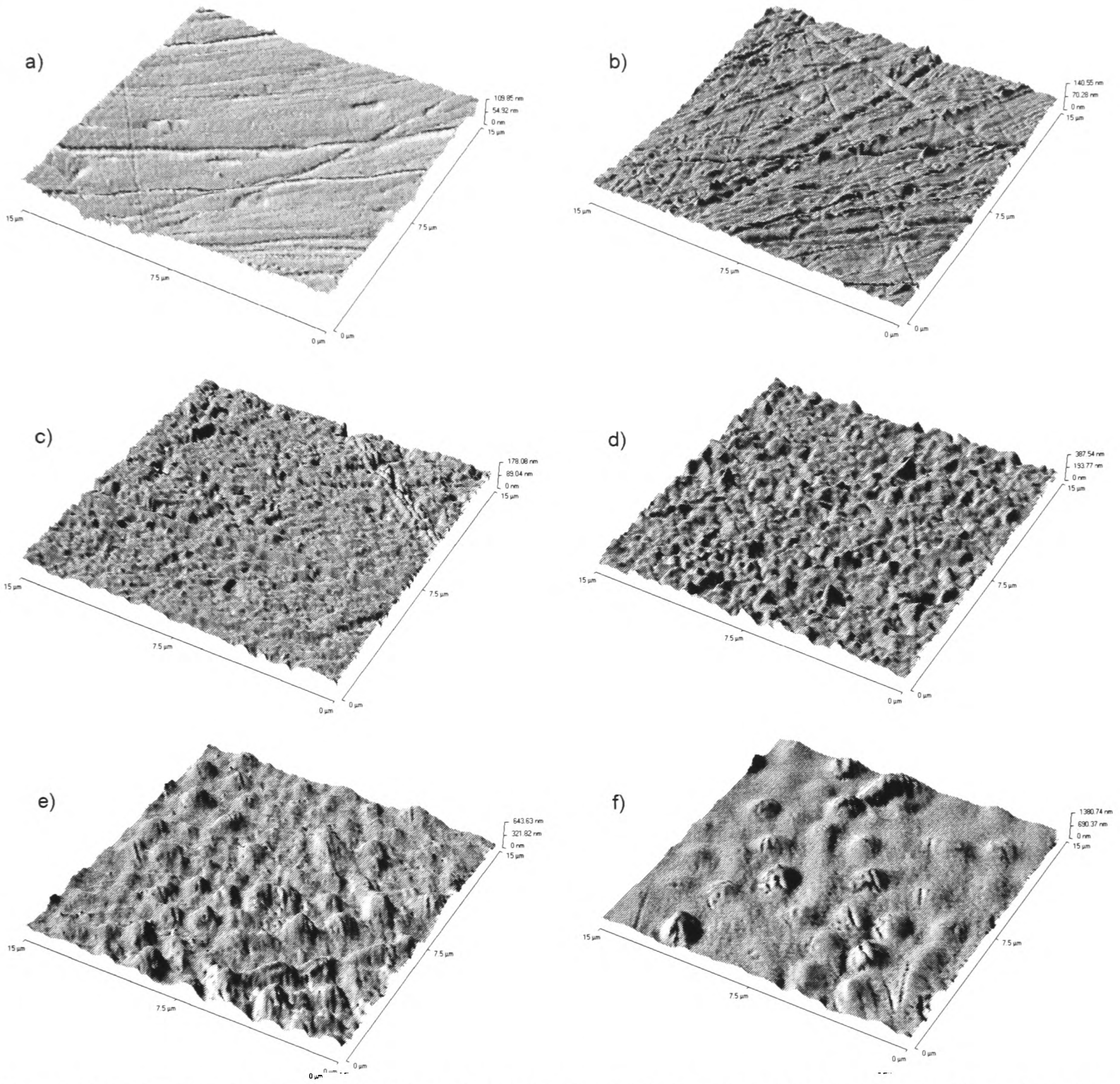

Figure 10.2 AFM pictures of a platinum electrode: a) polished and unablated b) to e) after subjection to laser ablation of increasing laser intensity (1.56, 1.80, 1.98 and 2.12 W cm^{-2}) for 60 seconds in buffered aqueous solution and f) after subjection to 0.50 W cm^{-2} laser intensity for 35 seconds in air.

Conditions	Laser Intensity / ± 20 mW cm^{-2}	Max. Surface Height / nm	Surface Roughness[a]
Polished Pt	No laser	110	1.011
Pt:buffer(aq)	1560	141	1.016
Pt:buffer(aq)	1800	178	1.021
Pt:buffer(aq)	1980	388	1.051
Pt:buffer(aq)	2120	644	1.095
Pt:air[b]	500	1381	1.184

Table 10.4 AFM data for a polished platinum surface subjected to 60 seconds of laser ablation. [a] (Surface area / projected surface area, as described in section 2.11). [b] 35 seconds of irradiation.

10.4.3 MASS TRANSPORT MODEL

Having established the effect of increasing laser intensity on simple electrochemical systems, the variation of electrode area size, concentration and diffusion coefficient of the electroactive substrate was studied at fixed light intensities. Again, effectively steady-state linear sweep voltammetry was performed on solutions of potassium ferricyanide and ferrocene in water and acetonitrile respectively. For area experiments, a laser intensity of ca. 150 mW cm^{-2} was employed in tandem with solution concentrations of 10 mM. A plot of limiting current against electrode area for both systems is shown in Figure 10.3 and the good linearity of both sets of data confirms the direct relationship of current to electrode area. By using a constant laser intensity of ca. 100 mW cm^{-2} and a 1 mm platinum disc electrode, linear sweep scans of 2, 4, 6, 8 and 10 mM solutions of the two systems above were then performed. Plots of the limiting currents against concentration are shown in Figure 10.4 for both systems and again indicate proportional

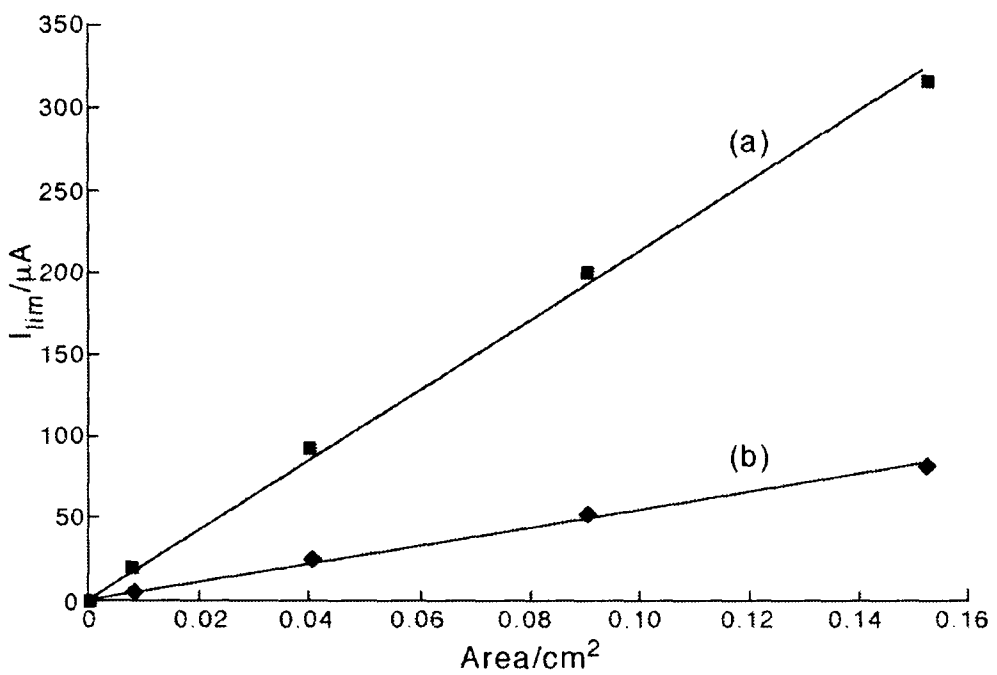

Figure 10.3 Plots of limiting current against electrode area for 5 mV s^{-1} LSVs at a 1 mm diameter disc, 2, 3 and 4 mm square platinum electrode subject to ca. 150 mW cm^{-2} laser intensity for a) 10 mM ferrocene in acetonitrile / 0.1 M TBAH (■) and b) 10 mM ferrocyanide in 0.1 M KCl(aq) (◆).

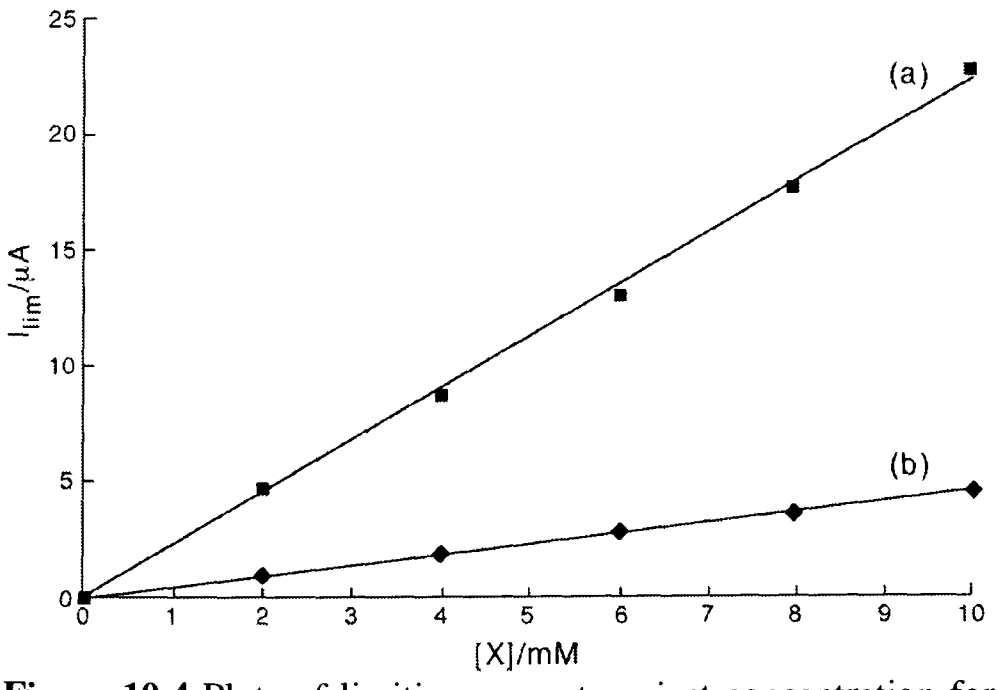

Figure 10.4 Plots of limiting current against concentration for 5 mV s^{-1} LSVs at a 1 mm diameter platinum disc, subject to 100 mW cm^{-2} laser intensity for a) ferrocene / 0.1 M TBAH in acetonitrile (■) and b) ferrocyanide in 0.1 M KCl(aq) (◆).

relationships.

Next, the voltammetry of all the systems in Table 10.2 was studied in order to assess the effect of varying the diffusion coefficient. Steady-state limiting currents for a fixed laser intensity were measured for each system using a 1 mm platinum electrode. Even conventionally passivating systems like toluidine blue [33], ascorbate [36] and *p*-bromonitrobenzene [34] gave time-reproducible steady-state voltammograms under laser illumination, as discussed further below, allowing quantitative analysis. Log-log plots of current against diffusion coefficient for both water and acetonitrile are shown in Figure 10.5.

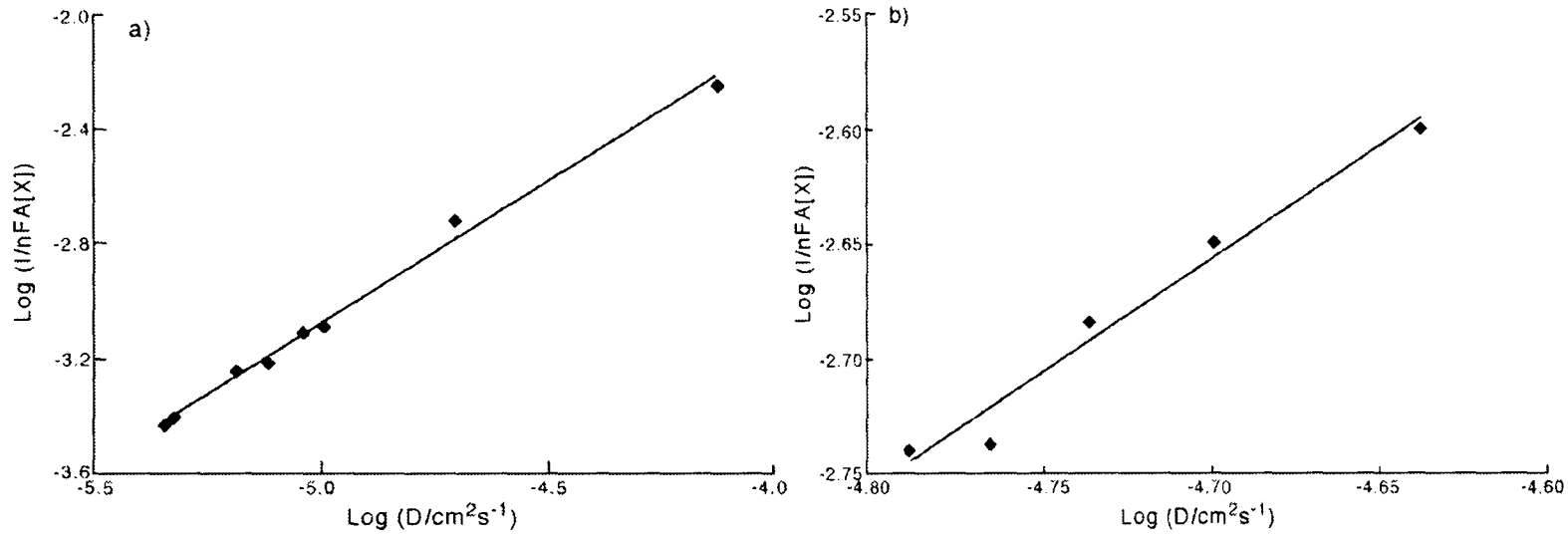

Figure 10.5 Log-log plots of limiting current against diffusion coefficient for linear sweep voltammetry of redox species in a) water and b) acetonitrile. The gradients of the straight 'least squares best fit' lines are 1.007 and 1.006 respectively.

The least squares best fit straight lines through the data reveal the gradient which corresponds to the exponent to which D appears in the expression for determining the current. The two gradients for water and acetonitrile are both 1.01 ± 0.01 suggesting a closely linear dependence of the limiting current on the diffusion coefficient of the redox active molecule or ion. Taking the linear dependence of the limiting current on concentration, electrode area and diffusion coefficient we suggest a naïve model for mass-transport of electroactive species to the electrode based on a uniform Nernst diffusion layer thickness that is light intensity dependent and gives rise to a mass transport limited current (I_{LAV}) given by the simple expression:

$$I_{LAV} = \frac{nAFD[X]_0}{\delta} \qquad (10.1)$$

where n is the number of electrons transferred in the redox process, A is the area of the electrode, F is 96485 C mol^{-1}, D is the diffusion coefficient of the electroactive species, X, of bulk concentration $[X]_0$ and δ is the diffusion layer thickness. We propose that *thermoelastic stresses* [24,37] are induced in the platinum electrode by absorption of laser energy together with localised heating and solution convection currents which in turn maintain a diffusion layer at the electrode surface and facilitate a steady mass-transport limited current. Values of δ as a function of laser intensity are given in Table 10.3 and can be seen to decrease as the laser-induced thermal convection increases.

10.4.4 LASER ACTIVATED POTENTIAL STEP CHRONOAMPEROMETRY

To confirm the suggested mass transport under laser activation, potential step chronoamperometry was employed at a 1 mm platinum disc for a 10 mM solution of ferrocene in acetonitrile / 0.1 M TBAH. For two constant laser intensities, (340 and 800 ± 20 mW cm^{-2}) experiments were performed in which after 10 seconds of equilibration at a pre-oxidation wave potential (0.2 V vs. SCE), the potential was jumped in 0.1 seconds to a post-wave potential (0.6 V vs. SCE) and the chronoamperometric response recorded. Typical experimental responses are shown in Figure 10.6.

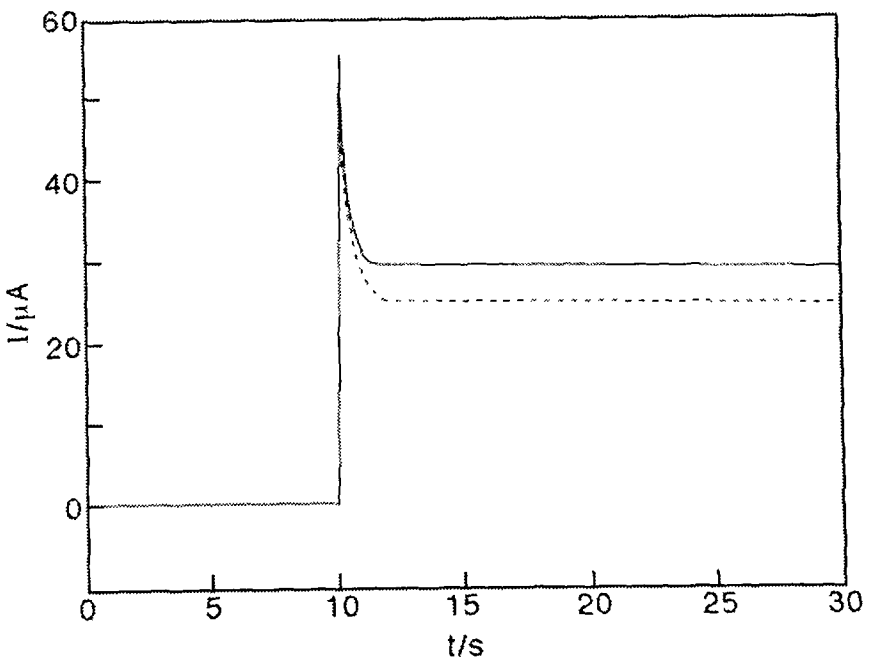

Figure 10.6 Transient current responses for 10 mM ferrocene / 0.1 M TBAH in acetonitrile when the potential is stepped from 0.2 V to 0.6 V (vs. SCE) after 10 seconds at 340 (- - - -) and 800 (——) mW cm^{-2}.

In order to model the potential step chronoamperometric transients recorded in the presence of a diffusion layer of finite thickness, δ, numerical simulations were conducted to solve Fick's second law for one dimensional diffusion,

$$\frac{\partial[X]}{\partial t} = D_x \frac{\partial^2[X]}{\partial x^2} \qquad (10.2)$$

where [X] is the concentration of the electroactive species, D_X is its diffusion coefficient, t is time after the potential step and x the direction of diffusion perpendicular to the electrode. The equation is solved subject to the following boundary conditions.

$$t \leq 0; \quad \text{all } x; \quad [X] = [X]_0 \tag{10.3}$$

$$t > 0; \quad x = 0; \quad [X] = 0 \tag{10.4}$$

$$t > 0; \quad x = \delta; \quad [X] = [X]_0 \tag{10.5}$$

The backwards implicit method [38] was used for these calculations which gave [X] as a function of x and t. The corresponding currents, I(t), were evaluated from

$$I(t) = nFAD_X \left.\frac{\partial[X]}{\partial x}\right|_{x=0} \tag{10.6}$$

where symbols are as above. Results were summarised in the form of a working curve showing the dimensionless current, $\frac{I(t)}{I(t \to \infty)}$ as a function of the dimensionless time, $\tau = \frac{Dt}{\delta^2}$. The relationship is shown in Figure 10.7.

Using the working curve, values of τ can be obtained for experimental values of the normalised transient currents. These in turn can be plotted against real time, t, in order to calculate values for the diffusion layer thickness, δ, from the above expression for τ, given that D is known.

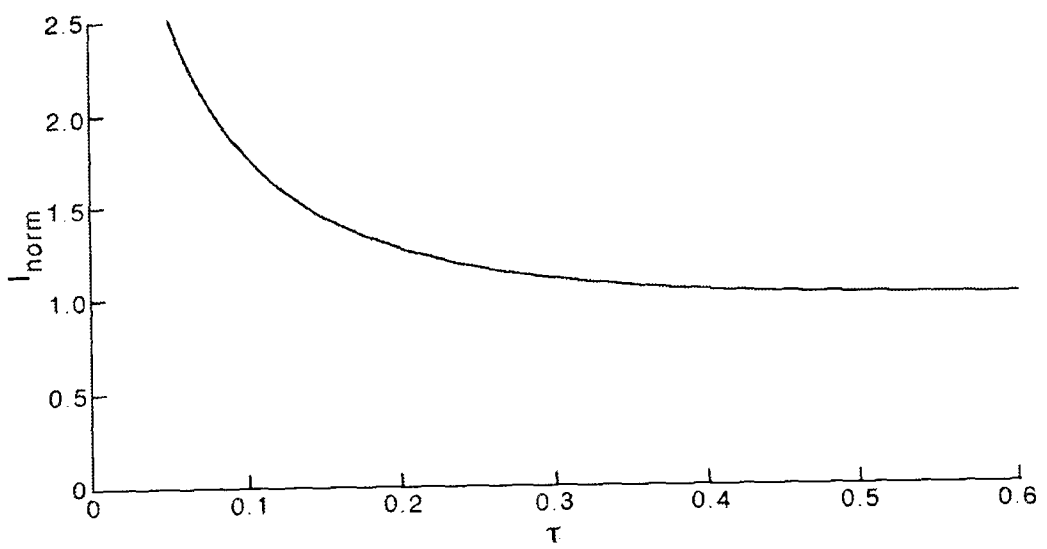

Figure 10.7 Plot of normalised current against normalised time for a backward implicit, fixed diffusion layer, one-dimensional diffusion model simulation.

Experimental transients and τ against t data for ferrocene in acetonitrile at two different laser intensities are plotted in Figures 10.8 and 10.9. The gradients of the straight lines allow calculation of the theoretical diffusion layer thickness given that the diffusion coefficient is

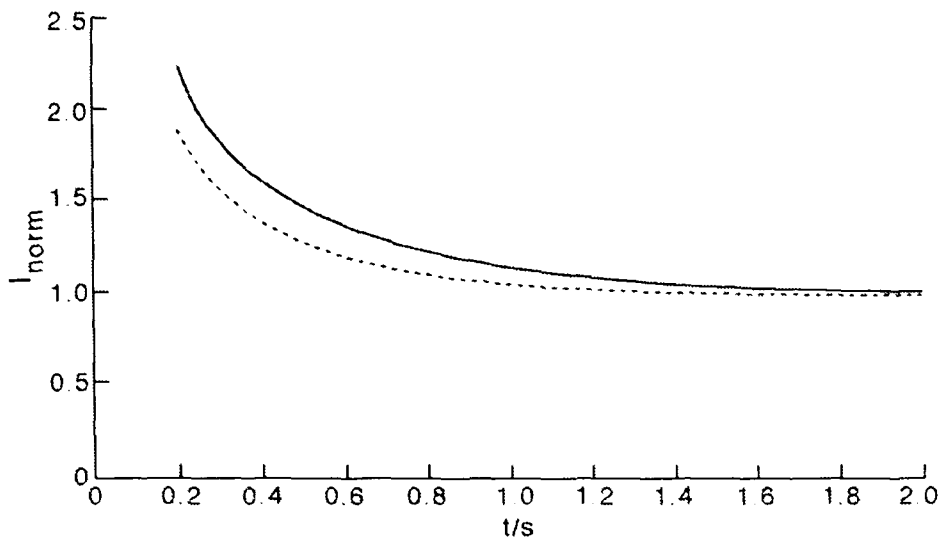

Figure 10.8 Potential step normalised transient current responses for 10 mM ferrocene in acetonitrile / 0.1 M TBAH at 340 (—) and 800 (---) mW cm^{-2}.

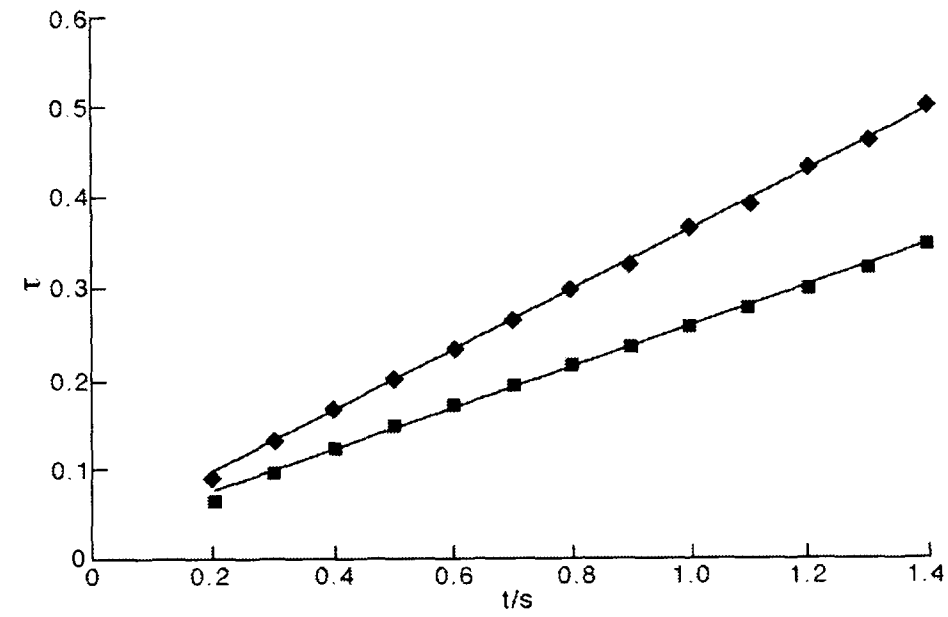

Figure 10.9 τ against t plots for 10 mM ferrocene in acetonitrile / 0.1 M TBAH at 340 (■) and 800 (◆) mW cm^{-2}. The gradients are 0.229 and 0.339 s^{-1} respectively.

known. For laser intensities of 340 and 800 ± 20 mW cm^{-2}, the values calculated for δ were 100 and 82 ± 2 μm respectively which are in approximate agreement with the experimentally determined values in Table 10.3. This provides support to the simple theoretical diffusion model for the convective mass transport at laser illuminated electrodes. Similar evidence is reported below for the aqueous, conventionally passivating toluidine blue dye two electron reduction [33] at platinum electrodes.

10.4.5 DEPASSIVATION AND ANALYTICAL APPLICATIONS

The effects of laser illumination of platinum electrodes were next investigated for three electrochemically passivating systems; toluidine blue dye, iodide and ferrocyanide in the presence of the blood protein fibrinogen. In the first of these laser activated voltammetry of 0.2 mM aqueous solutions of toluidine blue (as its $(C_{15}H_{16}N_3S)_2^+.ZnCl_4^{2-}$ salt shown in Figure 10.10) were

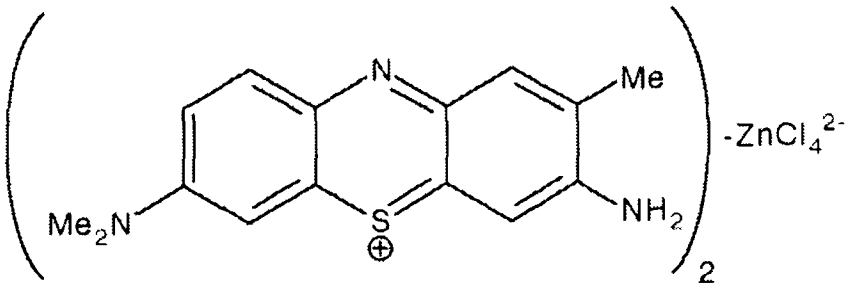

Figure 10.10 Structure of Toluidine Blue (TB).

performed at 0.5 mV s^{-1} to study the steady-state voltammetry of the dye as a function of pH in the range 1.2 to 9.5. The two-electron reduction of toluidine blue [33] (TB) can be represented as follows.

$$TB + 2e^- + mH^+ \rightleftharpoons H_mTB^{(m-2)+} \tag{10.7}$$

From the Nernst equation,

$$E = E^{0'} - \frac{RT}{2F} \ln \frac{[H_mTB^{(m-2)+}]}{[TB][H^+]^m} \tag{10.8}$$

where $E^{0'}$ is the formal potential of the TB redox couple, the half-wave potential seen for hydrodynamic voltammetry is given by [39]

$$E_{1/2} = \text{const.} - \frac{RT}{2F} \ln[H^+]^m \tag{10.9}$$

Since

$$pH = -\log[H^+] \tag{10.10}$$

then

$$E_{1/2} = \text{another const.} - 2.303m\frac{RT}{2F}(pH) \tag{10.11}$$

This gives a value for the pH dependence of the half-wave potential at 20 ± 2°C of -(29.1 ± 0.2)m mV $decade^{-1}$ where m is the number of protons taken up on reduction of the dye.

Successive 'dark' voltammograms of the solutions at all pHs revealed progressive deterioration of the reduction wave due to electrode fouling. Under 200 mW cm^{-2} laser illumination however, a reproducible steady-state wave was achieved with a half-wave potential that shifted with pH. A typical dark and laser activated response at a pH of 2.7 are shown in Figure 10.11 and give good evidence for the

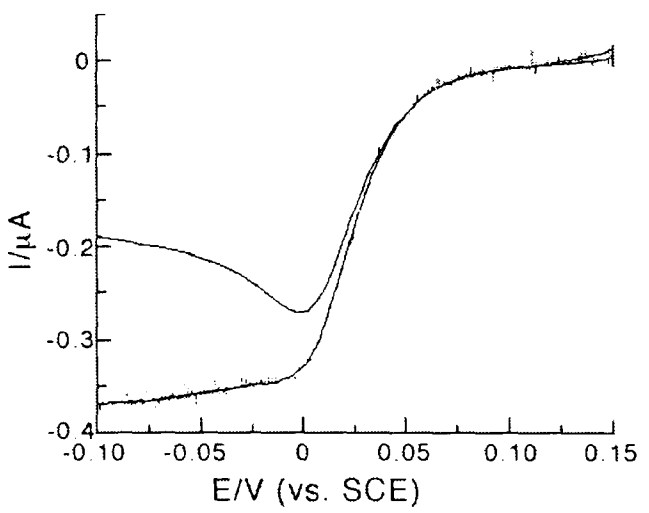

Figure 10.11 5 mVs^{-1} LSVs at a 1 mm diameter platinum disc electrode in the dark (upper trace) and subjected to 200 mW cm^{-2} laser illumination (lower trace) for a 0.2 mM solution of TB in 0.1 M KCl / PBS(aq) at pH 2.7.

surface cleaning effect of laser illumination. The half-wave potentials of the laser-activated steady-state waves were measured over the pH range above and are plotted in Figure 10.12. Three linear regions can clearly be seen with gradients of -87.1, -58.8 and -28.8 ± 0.4 mV decade^{-1} and these are interpreted below. As an additional check that steady-state was indeed being reached, potential step transient, point-by-point, chronoamperometric experiments were also performed at all pHs under 200 mW cm^{-2} laser illumination. These experiments recorded the transient currents seen after 0.02 V potential steps before, during and after the toluidine blue reduction wave. A typical response at pH 5.0 is shown in Figure 10.13. The steady limiting currents after each potential step were measured and plotted as a function of potential to construct a point-by-point voltammogram from which a value of the half-wave potential could be measured. A typical plot is compared with a corresponding linear sweep voltammogram in Figure 10.14. Good agreement between the two can be seen and an equivalent plot of half-wave

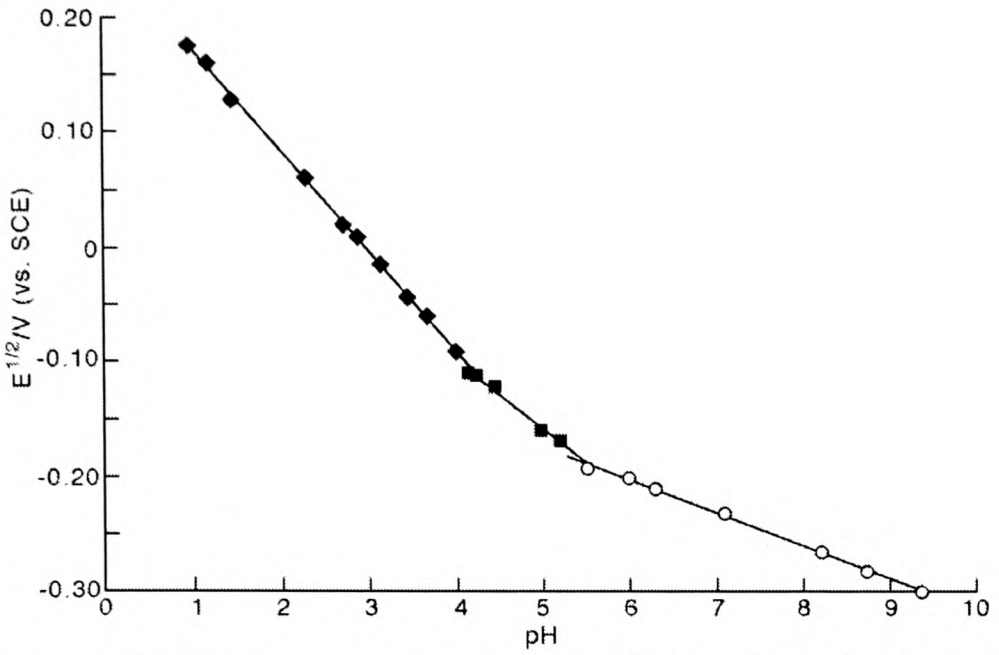

Figure 10.12 $E_{1/2}$ as a function of pH for the reduction of toluidine blue as measured by linear sweep voltammetry at 0.5 mVs^{-1} on a 1 mm platinum disc electrode.

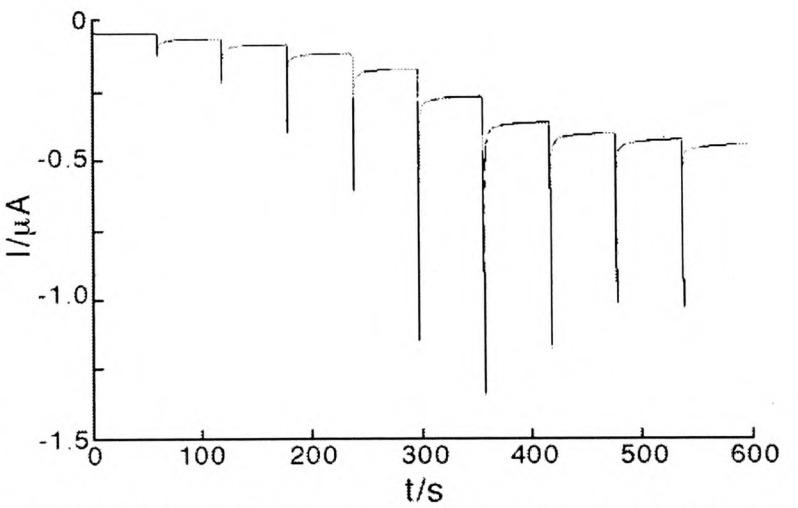

Figure 10.13 Chronoamperometric response for the reduction of 0.2 mM TB in 0.1 M KCl / PBS(aq) at pH 5.0 in 0.02 V steps from -0.06 to -0.24 V (vs. SCE).

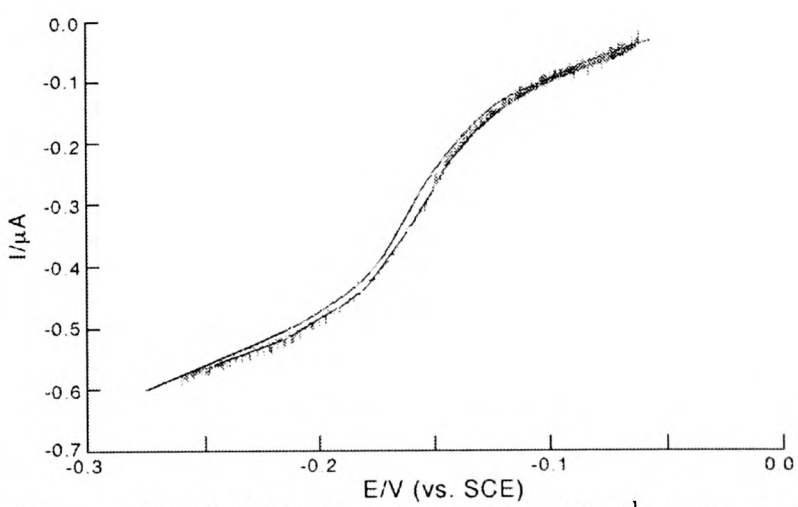

Figure 10.14 LSV (noisy) at 0.5 mV s^{-1} compared with a point-by-point voltammogram for the reduction of 0.2 mM TB in 0.1 M KCl at pH 5.0.

potential against pH using values obtained from the potential step data is shown in Figure 10.15. Again this has three well-defined linear regions with gradients this time of -88.2, -59.4 and -29.6 ± 0.4 mV decade^{-1}. From Equation 10.11 it can be shown that these three gradients represent three, two and then one net protonation(s) as the pH increases. This is in good agreement with previously reported work [33,40] on the toluidine blue system and illustrates the use of laser activation to maintain electrode activity across a whole range of pH.

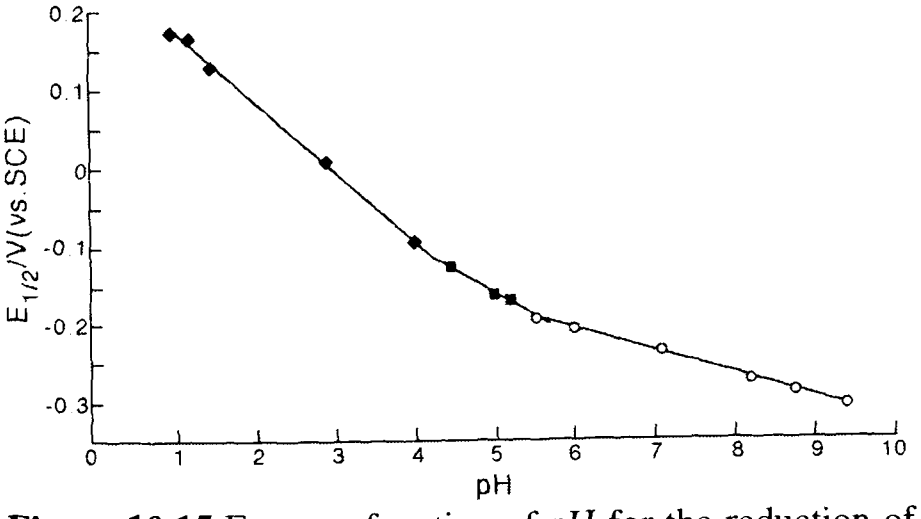

Figure 10.15 $E_{1/2}$ as a function of pH for the reduction of toluidine blue as measured by potential step chronoamperometry on a 1 mm platinum disc electrode.

Once it had been demonstrated that electrode fouling was removed via laser activation it was possible to use the system for further verification of the diffusion layer model via large jump potential step voltammetry as was described above for the ferrocene system. Potentials were stepped from those corresponding to zero current flow to those corresponding to transport-limited current flow (from 0.1 to -0.3 V vs. SCE). Experimental and normalised potential step current transients performed on a 5 mM aqueous solution of TB buffered at pH 4.0 under three conditions of laser illumination (200, 400 and 1060 mW cm^{-2}) are shown in Figure 10.16. Again by using the

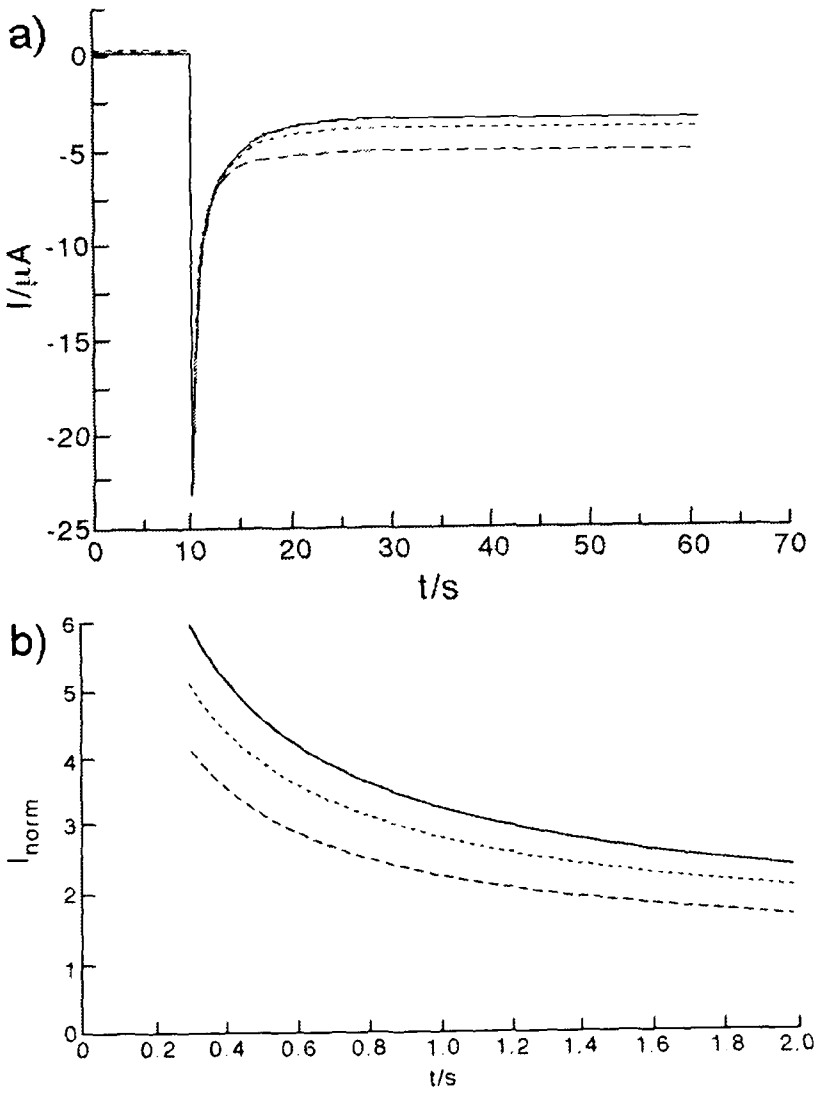

Figure 10.16 a) Experimental and b) normalised potential step transient current responses for 5 mM toluidine blue in 0.1 M KCl / PBS(aq) at pH 4.0 under 200 (—), 400 (- - -) and 1060 (– –) mW cm^{-2}.

simulated working curve given in Figure 10.7 it is possible to plot normalised time, τ, against real time, t, in order to obtain an estimate of the diffusion layer thickness as a function of illumination intensity. This is done in Figure 10.17. The three gradients of 0.0568, 0.0371 and 0.0277 s^{-1} correspond to δ values of 90, 111 and 129 μm for intensities of 1060, 400 and 200 mW cm^{-2} respectively. These values compare favourably with the other aqueous estimates seen in Table 10.3. It was estimated that absorption of light by the strongly coloured toluidine blue dye solution was < 10 % over the relatively small path length of approximately 1 mm.

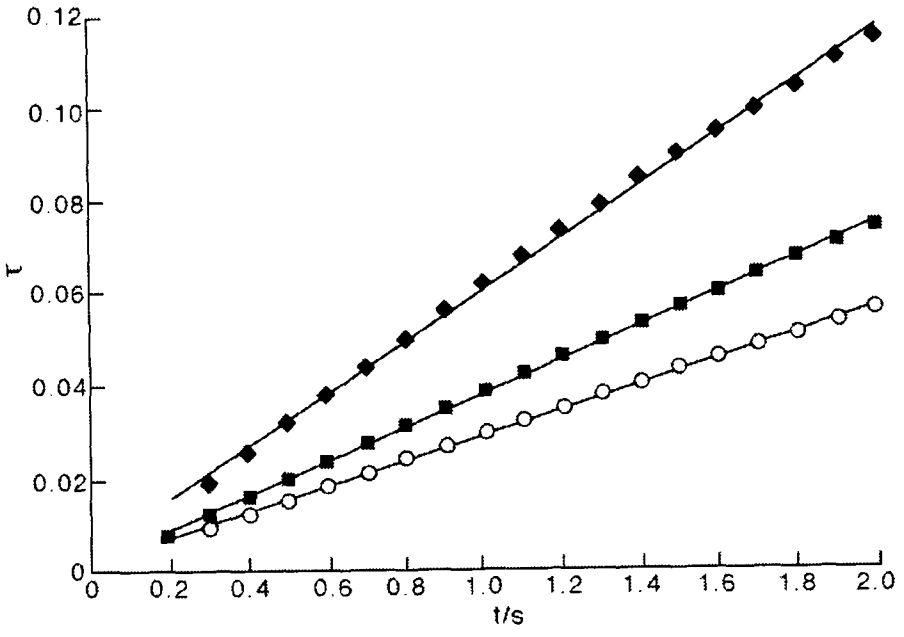

Figure 10.17 τ against t plots for 5 mM toluidine blue in 0.1 M KCl / PBS(aq) at pH 4.0 under 200 (◯), 400 (■) and 1060 (◆) mW cm^{-2} laser illumination.

Having successfully used laser activation to measure half-wave potentials and limiting currents for a passivating redox system, attention was then turned to the electrochemistry of the reversible oxidation of ferrocyanide in the presence of surface passivating species that are electro-inactive in this potential region. The blood proteins fibrinogen and bovine albumin (BA) were used for this purpose. An aqueous solution of 10 mM $K_4[Fe(CN)_6]$ in 0.1 M PBS along with 10 g l^{-1} BA and 1 g l^{-1} fibrinogen was adjusted to pH 6.81. Dissolution of the mixture was aided by 20 minutes of mechanical stirring to form a pale yellow, viscous solution.

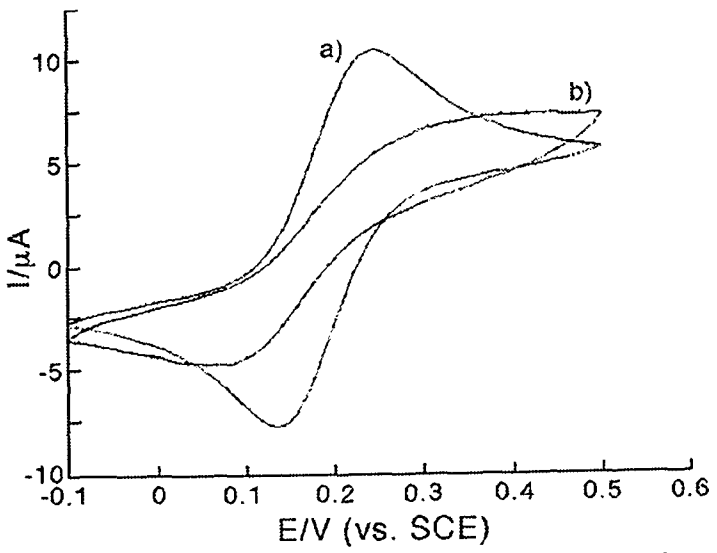

Figure 10.18 CVs for 10 mM potassium ferrocyanide in 0.1 M KCl at 50 mVs^{-1} on a 1 mm diameter Pt disc electrode a) in the absence of protein and b) buffered at pH 6.81 with 10 g l^{-1} BA and 1 g l^{-1} fibrinogen added.

Cyclic voltammetry at 50 mV s^{-1} was performed on the solution to investigate the effects of the added proteins. A typical scan in the presence of protein is shown in Figure 10.18 along with a comparison scan in the absence of bovine albumin and fibrinogen. The

waveshape and peak currents rapidly deteriorate with successive scans (the scan shown is the fifth in a series of ten) and we attribute this to the surface adsorption of electro-inactive protein molecules which gradually block the electron transfer from the ferrocyanide ion and reduce its reversibility. To investigate the effects of laser activation on this passivating layer, linear sweep voltammetry at 20 mV s^{-1} was performed both in the dark and subject to 500 mW cm^{-2} laser irradiation. Figure 10.19 shows six consecutive scans, the first and last of which are subject to illumination by the laser and retrace the same path after the four diminishing dark scans. However after many scans the wave essentially disappears and even laser illumination at 500 mW cm^{-2} is insufficient to regain clean electrode behaviour! This suggests that the irreversibility of passivation via protein absorption becomes greater with repeated potential scans. Under 1200 mW cm^{-2} irradiation the wave is partially recovered but a mass transport limited current is not observed. This is illustrated in Figure 10.20.

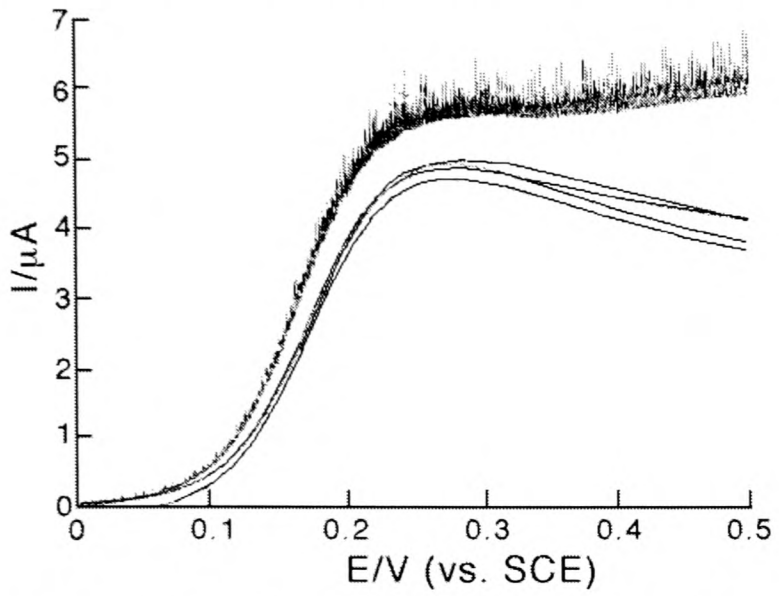

Figure 10.19 LSVs at 20 mVs^{-1} for the oxidation of 10 mM $K_4[Fe(CN)_6]$ in 0.1 M PBS at pH 6.81 in the presence of 10 g l^{-1} BA and 1 g l^{-1} fibrinogen on a 1 mm diameter Pt disc electrode. The top two traces are subject to 500 mW cm^{-2} laser illumination and the four lower traces diminish gradually in the dark.

Experiments were extended to apply laser activated voltammetry for the interrogation of ferrocyanide in whole equine blood. In these experiments 10 or 20 mM ferrocyanide was added to both haemolysed (laked) and oxalated horse blood and used without the addition of any further electrolyte.

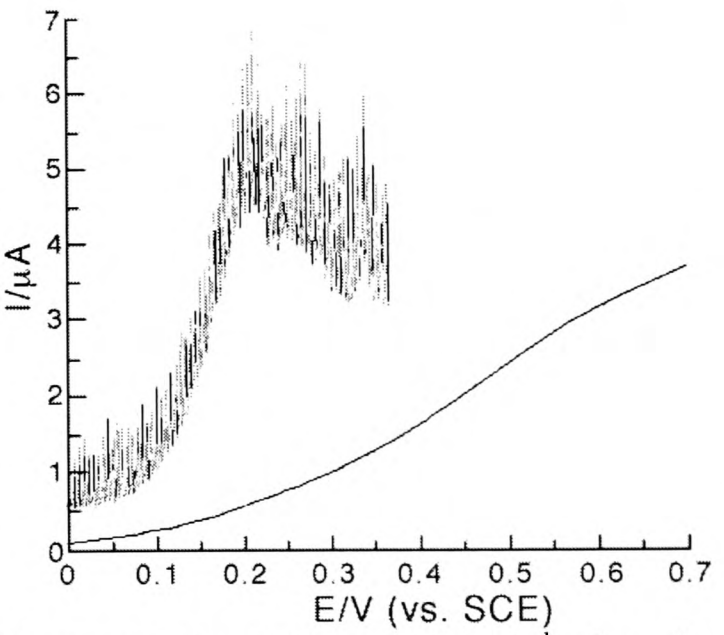

Figure 10.20 LSVs at 5 mVs^{-1} for the oxidation of 10 mM $K_4[Fe(CN)_6]$ in 0.1 M PBS at pH 6.81 in the presence of 10 g l^{-1} BA and 1 g l^{-1} fibrinogen on a 1 mm diameter Pt disc electrode. The lower trace is a typical result obtained after ca. 50 scans. The upper (noisy) trace was obtained after subjection to 1200 mW cm^{-2} laser illumination.

Similar results to those reported above were discovered suggesting the value of LAV for analysis in neat blood samples. The electroanalytical applications of laser activation in conventional aqueous media have been documented in Chapters 8 and 9.

Last we consider the oxidation of iodide in aqueous sulphuric acid. This has been demonstrated to lead to the production of solid iodine when adequately high concentrations (> ca. 3 mM) of iodide are employed [41-46]. Figure 10.21 shows a linear sweep voltammogram for the oxidation of 10 mM potassium iodide in 0.125 M H_2SO_4. Under dark conditions the formation of iodine appears as the current peak at ca. 0.48 V vs. SCE [44]. This leads to partial passivation of the electrode making quantitative interpretation a challenging exercise [45]. Under 300 mW cm^{-2} illumination a sustained transport-limited current is observed. The removal of solid iodine from the electrode surface is illustrated by Figure 10.22 which shows corresponding cyclic voltammograms measured under flow conditions (1×10^{-3} $cm^3 s^{-1}$ through a flow cell of cross-sectional area 0.6 cm × 0.04 cm). The upper trace (a) shows an appreciable stripping peak for the reduction of surface iodine to iodide. This was recorded under dark conditions. In contrast (b) shows the effect of 1200 mW cm^{-2} illumination on the same experiment. The reverse cyclic

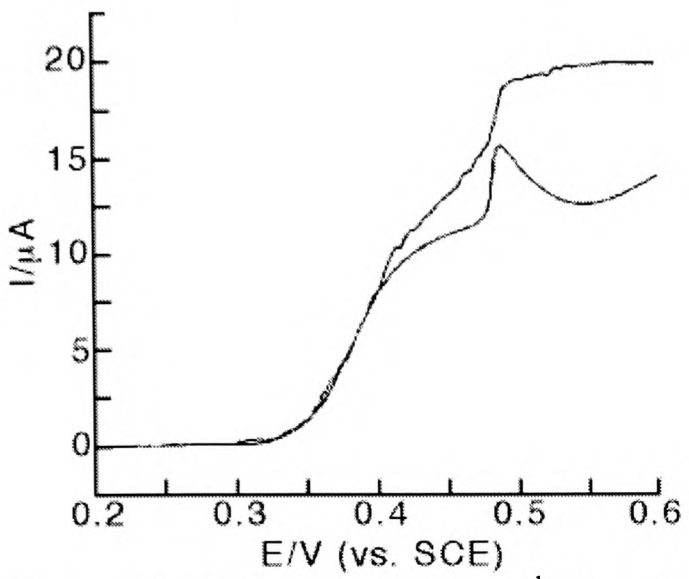

Figure 10.21 LSVs at 5 mVs^{-1} for the oxidation of 10 mM KI in 0.125 M H_2SO_4 on a 1 mm diameter Pt disc electrode under dark (lower trace) and 300 mW cm^{-2} laser illuminated (upper trace) conditions.

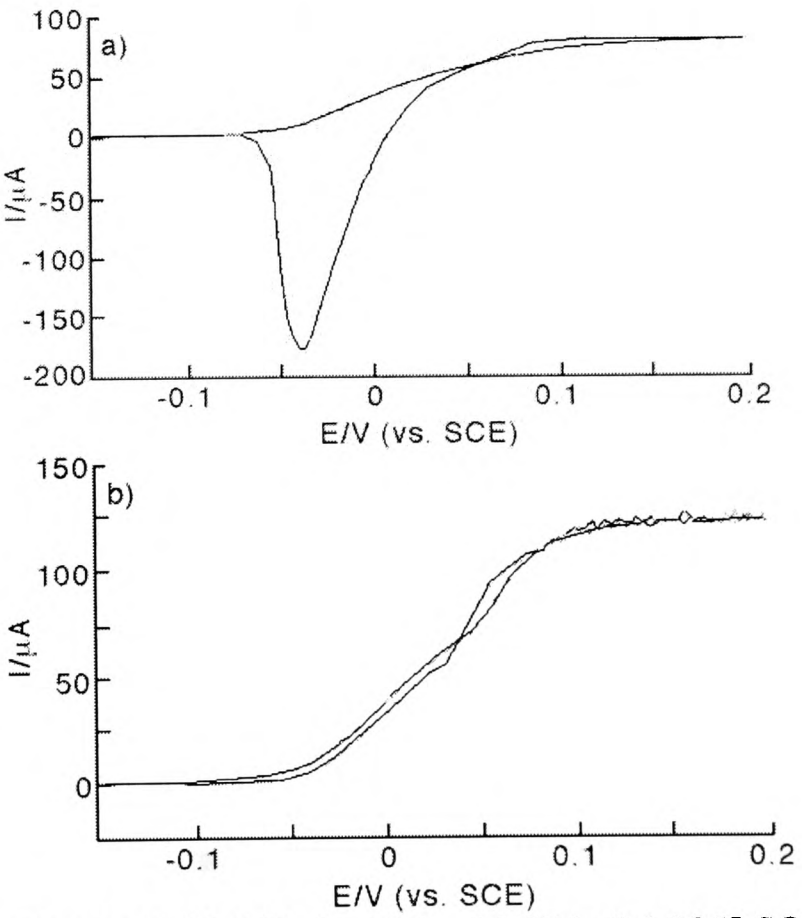

Figure 10.22 CVs for 10.2 mM KI in 0.1 M H_2SO_4 at 5 mVs^{-1} on a 2 mm square Pt electrode under flow conditions. a) Dark. b) Under 1200 mW cm^{-2} laser illumination (smoothed trace).

voltammetry scan essentially retraces the anodic sweep and a well-defined hydrodynamic is seen with no hysteresis. The oxidation of iodide will be studied further and quantitatively in the next chapter but the ability of LAV to maintain an active electrode surface especially under convective conditions again offers considerable analytical value.

10.5 CONCLUSIONS

The nature of laser activated voltammetry has been addressed through identification of mass transport and surface effects. The considerable potential for laser activation in electroanalytical methodology is illustrated with reference to the demonstrable revitalisation of electrode activity for three separate conventionally passivating systems namely toluidine blue dye reduction, ferrocyanide oxidation in the presence of bovine albumin / fibrinogen and iodide oxidation. In the next chapter we seek to apply further use of laser illumination to scrutinise the oxidation of iodide at platinum electrodes and postulate a mechanism through comparison with theoretical computer simulation.

10.6 CHAPTER 10: REFERENCES

[1] C. A. Odegard, A. Bronson, *Corrosion* **1997**, *53*, 800.

[2] G. T. Burstein, *J. Electroanal. Chem.* **1983**, *130*, 2133.

[3] G. T. Burstein, R. D. K. Misra, *Electrochim. Acta* **1983**, *28*, 363.

[4] R. C. Newman, G. T. Burstein, *J. Electroanal. Chem.* **1981**, *129*, 343.

[5] G. T. Burstein, R. C. Newman, *J. Electroanal. Chem.* **1981**, *128*, 2270.

[6] G. T. Burstein, D. H. Davies, *J. Electrochem. Soc.* **1981**, *128*, 33.

[7] K. R. Kneten, R. L. McCreery, *Anal. Chem.* **1992**, *64*, 2518.

[8] G. T. Burstein, R. J. Cinderey, *Corrosion Sci.* **1991**, *32*, 1195.

[9] R. G. Compton, J. C. Eklund, F. Marken, T. O. Rebbitt, R. P. Akkermans, D. N. Waller, *Electrochim. Acta* **1997**, *42*, 2919.

[10] R. G. Compton, J. C. Eklund, S. D. Page, G. H. W. Sanders, J. Booth, *J. Phys. Chem.* **1994**, *98*, 12410.

[11] T. Hinoue, I. Watanabe, H. Watarai, *Chem. Letters* **1996**, *5*, 329.

[12] P. H. Chen, R. L. McCreery, *Anal. Chem.* **1996**, *68*, 3958.

[13] P. H. Chen, M. A. Frylung, R. L. McCreery, *Anal. Chem.* **1995**, *67*, 3115.

[14] R. K. Jaworski, R. L. McCreery, *J. Electrochem. Soc.* **1993**, *140*, 1360.

[15] R. L. McCreery, R. Bowling, R. Packard, M. Poon, *Abs. Pap. Am. Chem. Soc.* **1988**, *196*, 185.
[16] M. Poon, R. L. McCreery, R. Engstrom, *Anal. Chem.* **1988**, *60*, 1725.
[17] M. Poon, R. L. McCreery, *Anal. Chem.* **1987**, *59*, 1615.
[18] M. Poon, R. L. McCreery, *Anal. Chem.* **1986**, *58*, 2256.
[19] E. Hershenhart, R. L. McCreery, R. D. Knight, *Anal. Chem.* **1984**, *56*, 2745
[20] R. G. Compton, R. A. W. Dryfe, *Prog. Reaction Kinetics* **1995**, *20*, 245.
[21] S. R. Morrison, *Electrochemistry at Semiconductor and Oxidised Metal Electrodes*, Plenum Press, New York, **1980**.
[22] J. F. Smalley, C. V. Krishnan, M. Goldman, S. W. Feldberg, I. Ruzic, *J. Electroanal. Chem.* **1988,** 248, 255.
[23] J. H. Bechtel, *J. Appl. Phys.* **1975**, *46*, 1585.
[24] J. D. Aussel, A. Le Brun, J. C. Baboux, *Ultrasonics* **1988**, *26*, 245.
[25] R. G. Compton, B. A. Coles, F. Marken, *J. Chem. Soc. Chem. Comm.* **1998**, 2595.
[26] M. L. Von Stackelberg, M. Pilgram, V. Toome, *Z. Elektrochem.* **1953**, *57*, 342.
[27] F. Marken, J. C. Eklund, R. G. Compton, *J. Electroanal. Chem.* **1995**, *395*, 335.
[28] P. Sharp, *Electrochim. Acta* **1983**, *28*, 301.
[29] R. G. Compton, J. C. Eklund, S. D. Page, *J. Phys. Chem.* **1995**, *99*, 4211.
[30] R. G. Compton, J. C. Eklund, S. D. Page, T. J. Mason, D. J. Walton, *J. Appl. Electrochem.* **1996**, *26*, 775.
[31] R. N. Adams, *Electrochemistry at Solid Electrodes*, Marcel Dekker, New York, **1969**.
[32] R. G. Compton, F-M. Matysik, *Electroanalysis* **1996**, *8*, 213.
[33] J. A. Cooper, M. Wu, R. G. Compton, *Anal. Chem.* **1998**, *70*, 2922.
[34] R. G. Compton, R. A. W. Dryfe, A. C. Fisher, *J. Electroanal. Chem.* **1993**, *361*, 275.
[35] D. R. Lide, (Ed.-in-chief), *CRC Handbook of Chemistry and Physics*, *74th Ed.*, CRC Press, Boca Raton, Florida, **1993**.
[36] P. Karabinas, D. Jannakoudakis, *J. Electroanal. Chem.* **1984**, *160*, 159.
[37] R. Oltra, G. M. Indrianjafy, J. P. Boquillon, *J. Phys. IV*, Colloque C7, 769, Suppl. *J. Phys. III* **1991**, *12*.
[38] A. C. Fisher, R. G. Compton, *J. Phys. Chem.* **1991**, *95*, 7538.
[39] P. Zuman, *The Elucidation of Organic Electrode Processes,* Academic Press, New York, **1969**.
[40] H. Ju, L. Dong, H. Chen, *Anal. Lett.* **1996**, *29*, 587.
[41] C-Y. Liu, S. R. Snyder, A. J. Bard, *J. Phys. Chem. B* **1997**, *101*, 1180.
[42] H. Tang, A. Kitani, M. Shiotani, *J. Appl. Electrochem.* **1996**, *26*, 36.
[43] Y. Chen, H. Zhang, B. Wu, *J. Electroanal. Chem.* **1992**, *335*, 321.
[44] Y. A. Yaraliyev, *Electrochim. Acta.* **1984**, *29*, 1213.
[45] P. Beran, S. Bruckenstein, *Anal. Chem.* **1968**, *40*, 1044.
[46] L. M. Dané, L. J. J. Janssen, J. G. Hoogland, *Electrochim. Acta* **1968**, *13*, 507.

11

LAV: MECHANISTIC DETERMINATION OF IODIDE OXIDATION

CHAPTER 11: LAV: MECHANISTIC DETERMINATION OF IODIDE OXIDATION

11.1 CONTENTS

This chapter builds on the characterisation of laser activated voltammetry which was the subject of the previous chapter and looks at the possibility of mechanistic discrimination by a combination of maintaining a clean electrode and theoretical modelling. Some of the work in this chapter was accepted for publication in the *Journal of Physical Chemistry* in July 1999. The mechanism of iodide oxidation on platinum electrodes is investigated using laser activated voltammetry under both channel flow and no flow conditions together with independent *in situ* atomic force microscopy (AFM) measurements. Laser activation using a 10 Hz pulsed Nd:YAG 532 nm laser is shown to remove bulk iodine from the electrode surface so that under sustained pulsed irradiation a steady-state surface evolves at which the iodide oxidation can be reproducibly studied. By modelling the concentration and flow rate dependence of the voltammetric waveshape the mechanism is shown to be

$$2I^- (aq) - 2e^- \rightleftharpoons I_2 (aq) \qquad \text{(i)}$$

$$I_2 (aq) + I^- (aq) \rightleftharpoons I_3^- (aq) \qquad \text{(ii)}$$

$$I_2 (aq) \rightleftharpoons I_2 (s) \qquad \text{(iii)}$$

$$I^- (aq) + I_2 (s) \rightarrow I_3^- (aq) \qquad \text{(iv)}$$

where the formal redox potential for reaction (i) is 0.358 V vs. SCE in 0.1 M H_2SO_4, the equilibrium constant for reaction (ii) is 580 M^{-1} with a forward rate constant of 1 x 10^5 mol^{-1} cm^3 s^{-1}, the solubility of I_2 (reaction (iii)) is 1.85 x 10^{-3} M, and the heterogeneous rate constant for reaction (iv) is 1.6 x 10^{-3} cm s^{-1}.

11.2 INTRODUCTION

The surface modification of both single-crystal and polycrystalline platinum with iodine has been the subject of considerable structural and electrochemical study [1-7]. It has

been reported that aqueous iodide undergoes spontaneous oxidation upon chemisorption to form a layer of zerovalent atomic iodine on platinum electrodes [8] at potentials between 0 V and +0.4 V vs. SCE. At higher potentials, further deposition of atomic iodine leads to the formation of molecular iodine which can either form a solid deposit of iodine [9,10] or dissolve into the solution phase. The exact mechanism of how molecular iodine is formed from atomic iodine is not yet fully understood [11]. Moreover, iodine formed electrochemically on the platinum electrode surface by the oxidation of aqueous iodide changes the conductivity and kinetic properties of the electrode in a complicated fashion [11]. Electrochemical iodine growth has been studied by optical microscopy [12], surface reflectance measurements [13], surface-enhanced Raman spectroscopy [14], atomic force microscopy [15] and scanning tunnelling microscopy [16]. Various electrochemical mechanisms of iodine formation have been summarised by Dané *et al.* [17] however the formation of bulk iodine necessarily complicates the interpretation of voltammetric data not least due to the constantly changing electrode condition as voltammetry proceeds.

Recently the use of lasers to keep electrode surfaces clean and activated has become increasingly common. Watanabe and co-workers [18] used a relatively high power infra-red laser source to maintain fresh platinum and gold electrode surfaces by physically removing the top layer of electrode surface every few seconds via the phenomenon of 'laser ablation' [18]. This followed work by McCreery and colleagues who used high intensity, in-situ infra-red laser pulses to activate the surface and increase heterogeneous electron-transfer kinetics at glassy carbon and platinum electrodes [19-26]. Oltra *et al.* have additionally used laser pulses to depassivate an iron electrode under the hydrodynamic conditions of a channel flow cell [27] whilst Hinoue *et al.* used an argon-ion laser to examine the effect of heating on the electron transfer process of Fe (II/III) aqueous species in a flow system [28]. Characterisation of the effects of laser illumination on electrochemical measurements was the subject of the previous chapter.

In this chapter laser activated voltammetry (LAV) using a 10 Hz pulsed Nd:YAG laser at 532 nm is employed to control the build up of solid iodine formed by aqueous iodide

oxidation and to investigate the mechanism of oxidation at platinum electrodes, both under stationary and hydrodynamic channel flow conditions. Under the latter conditions numerical modelling of the channel flow voltammetry gives qualitative mechanistic inferences together with quantitative kinetic data. Furthermore, atomic force microscopy (AFM) is utilised to visualise the growth of bulk iodine deposits on the electrode surface.

11.3 THEORY

11.3.1 THE OXIDATION OF AQUEOUS IODIDE IN A CHANNEL FLOW CELL

We consider first the voltammetric behaviour of the aqueous I^-/I_2 system in the limit of low concentrations [7] where iodine is formed at concentrations below its solubility and at levels such that the formation of I_3^- can be neglected. The electrochemically reversible oxidation process is as follows:

$$I^-(aq) - e^- \rightleftharpoons \tfrac{1}{2} I_2(aq) \qquad (11.1)$$

Application of the Nernst equation to Equation (11.1) gives the following expression:

$$\left\{\left(\frac{[I_2]_0}{[I_2]^*}\right)^{1/2} \Big/ \left(\frac{[I^-]_0}{[I^-]^*}\right)\right\} = \exp(\theta) \qquad (11.2)$$

where $\theta = (F/RT)(E - E^{0'})$, $[I^-]_0$ and $[I_2]_0$ are the surface concentrations and $[I^-]^*$ and $[I_2]^*$ the thermodynamic standard states of iodide and iodine respectively, F is the Faraday constant, E is the electrode potential and $E^{0'}$ is the formal potential of the I_2/I^- redox couple. For the case of voltammetry conducted at a hydrodynamic electrode this leads to the following result for the current (I) – voltage (θ) behaviour [29-31]:

$$\ln\left\{\left(\frac{I_{Lim}}{I}\right)^{1/2} - \left(\frac{I}{I_{Lim}}\right)^{1/2}\right\} = -\theta - \frac{1}{2}\ln\left\{\frac{2D_{12}}{D_{I^-}}[I^-]_{bulk}\right\} \qquad (11.3)$$

where I_{Lim} is the mass transport limited current, D is the relevant diffusion coefficient and $[I^-]_{bulk}$ is the bulk concentration of iodide. Equation (11.3) implies that the half-wave potential, $E_{1/2}$, where $I = I_{Lim}/2$ for the iodide oxidation intrinsically varies with both the ratio

$\frac{D_{I_2}}{D_{I^-}}$ and the bulk concentration of iodide, even in the absence of any following homogeneous (or other) kinetics. Quantitatively,

$$-\frac{1}{2}\ln\left\{\frac{D_{I2}}{D_{I^-}}[I^-]_{bulk}\right\} = \left(\frac{F}{RT}\right)\left(E_{1/2} - E^{0'}\right) = \theta_{1/2} \tag{11.4}$$

so that increasing the concentration of I^- in solution shifts the half-wave potential of the oxidation wave to less positive potentials.

In the low concentration limit, the steady-state convection–diffusion equations describing the electrochemical process at a channel electrode are as follows.

$$D_{I^-}\frac{\partial^2[I^-]}{\partial y^2} - v_x\frac{\partial[I^-]}{\partial x} = 0 \tag{11.5}$$

$$D_{I_2}\frac{\partial^2[I_2]}{\partial y^2} - v_x\frac{\partial[I_2]}{\partial x} = 0 \tag{11.6}$$

where x and y are defined in Figure 1.10. Under parabolic laminar flow conditions, v_x is defined quantitatively by

$$v_x = v_0\left(1 - \frac{(h-y)^2}{h^2}\right) \tag{11.7}$$

where v_0 is central velocity in the channel and 2h is the cell height.

The boundary conditions relevant to the calculation of the current-voltage curve in the low concentration limit are:

$$x < 0: \quad [I^-] = [I^-]_{bulk} \tag{11.8}$$

$$0 < x < x_e,\ y = 0:\ [I_2]/[I^-]^2 = \exp(\theta);\ [I_2] \le [I_2]_{sat} \tag{11.9}$$

$$0 < x < x_e,\ y = 0:\ 2D_{I_2}\left.\frac{\partial[I_2]}{\partial y}\right|_{y=0} = -D_{I^-}\left.\frac{\partial[I^-]}{\partial y}\right|_{y=0} \tag{11.10}$$

$$y = 2h: \quad \frac{\partial[I^-]}{\partial y} = \frac{\partial[I_2]}{\partial y} = 0 \tag{11.11}$$

The coupled transport equations are solved using the backwards implicit (BI) method [32] with back-to-back grids [33] to relate the species in the electrode reaction couple. These methods were used exactly as previously described [32,33] with the exception that as Equation (11.9) is non-linear, it cannot be used directly to define the electrode surface concentrations of I^- and I_2. A linearisation procedure [34,35] is employed to calculate the concentration of I^- and I_2 at the electrode surface. It is:

$$[I_2]_{K+1} / (2[I^-]_K [I^-]_{K+1} - [I^-]_K^2) = \exp(\theta) \qquad (11.12)$$

where K is the grid number in the x direction. The electrode current, I, is then evaluated from the following expression

$$I = wF \int_0^{x_e} D_{I^-} \left[\frac{\partial [I^-]}{\partial y} \right]_{y=0} dx \qquad (11.13)$$

where w is the width of the electrode as defined in Figure 1.10.

Figure 11.1 shows computed waves for iodide oxidation at two different concentrations (0.2 and 2 mM) and for three different typical flow rates (0.02, 0.04 and 0.07 $cm^3\ s^{-1}$) for a channel electrode of typical dimensions (electrode length 0.18 cm, electrode width 0.18 cm, cell depth 0.04 cm and cell width 0.6 cm). Notice that the simulations predict the variation of $E_{1/2}$ with concentration anticipated by Equation (11.4). Simulations over the concentration range $0.1 < [I^-]_{bulk} / mM < 2$ gave quantitative agreement with this equation. In addition Tafel analysis of the simulated waveshapes conducted on the basis of Equation (11.3) showed excellent agreement with the predictions of analytical theory. Figure 11.2 shows typical Tafel plots for 0.2 and

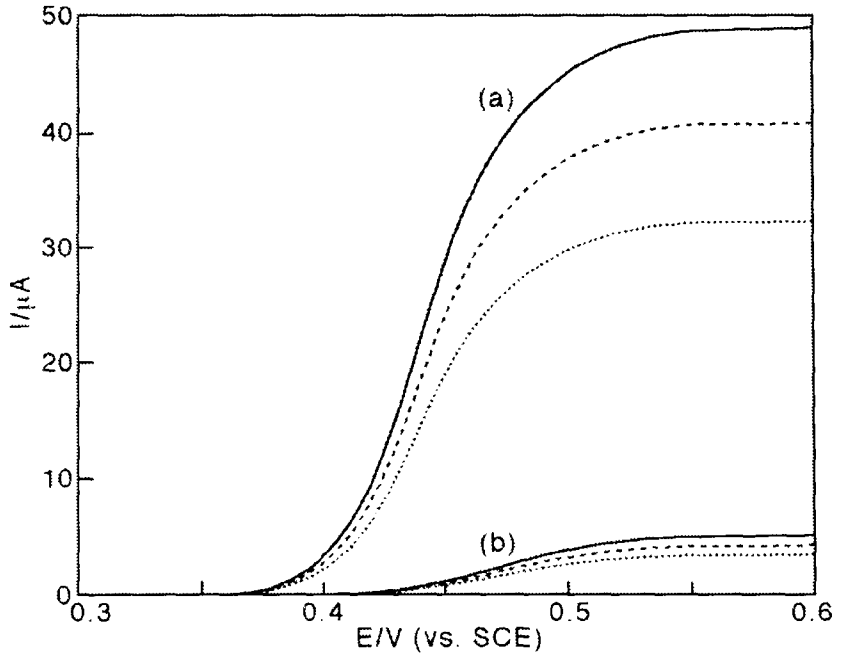

Figure 11.1 Simulated voltammograms at flow rates of 0.02 (···), 0.04 (- - -) and 0.07 (—) $cm^3\ s^{-1}$ for a) 2.0 mM KI and b) 0.2 mM KI. $K_2 = k_{het} = 0$ and $[I_2]_{sat} = 10$ mM ensuring saturation is not reached.

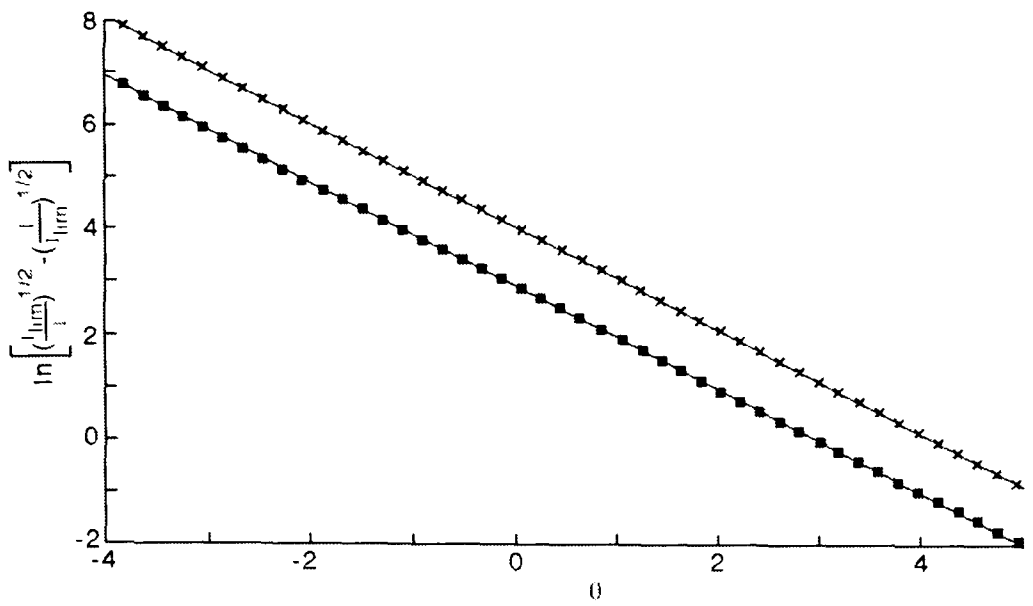

Figure 11.2 Tafel analysis plots for the 0.04 $cm^3 s^{-1}$ waves in Figure 11.1 (X = 0.2 mM, ■ = 2 mM).

2 mM iodide concentrations; the observed slopes of -1.000 and -1.001 respectively are in quantitative agreement with Equation (11.3).

We next consider the well-established formation of tri-iodide (I_3^-) from the reaction between *aqueous* iodide and iodine [17]. The reaction mechanism now becomes:

$$2I^-(aq) - 2e^- \rightleftharpoons I_2(aq) \tag{11.14}$$

$$I^-(aq) + I_2(aq) \underset{k_b}{\overset{k_f}{\rightleftharpoons}} I_3^-(aq) \tag{11.15}$$

where k_f and k_b are forward and backward rate constants respectively for the generation of the tri-iodide. The modified steady-state convection-diffusion equations include the new species as follows.

$$D_{I^-}\frac{\partial^2[I^-]}{\partial y^2} - v_x\frac{\partial[I^-]}{\partial x} - k_f[I^-][I_2] + k_b[I_3^-] = 0 \tag{11.16}$$

$$D_{I_2}\frac{\partial^2[I_2]}{\partial y^2} - v_x\frac{\partial[I_2]}{\partial x} - k_f[I^-][I_2] + k_b[I_3^-] = 0 \tag{11.17}$$

$$D_{I_3^-}\frac{\partial^2[I_3^-]}{\partial y^2} - v_x\frac{\partial[I_3^-]}{\partial x} + k_f[I^-][I_2] - k_b[I_3^-] = 0 \tag{11.18}$$

Further boundary conditions are now applicable to tri-iodide,

$$0 < x < x_e,\ y = 0:\ D_{I_3^-}\frac{\partial[I_3^-]}{\partial y} = 0 \tag{11.19}$$

$$y = 2h:\ \frac{\partial[I_3^-]}{\partial y} = 0 \tag{11.20}$$

It is readily shown using analytical arguments [36] that the dimensionless shift in half-wave potential, $\theta_{1/2}$, must be a unique function of two normalised parameters. First the normalised second order rate constant is defined as

$$K_2 = k_f [I^-]_{bulk} (4h^4 x_e^2 d^2 / 9 v_f^2 D_{I^-})^{1/3} \quad (11.21)$$

where v_f is the volume flow rate and d is the cell width. Second a dimensionless equilibrium constant, K, for the chemical reaction is defined as

$$K = 1/(K_{eq} [I^-]_{bulk}) \quad (11.22)$$

where K_{eq} (= k_f/k_b) is the equilibrium constant for the chemical reaction given in Equation (11.15). Figure 11.3 shows the simulated behaviour in terms of a working surface relating $\theta_{1/2}$ to K_2 and K. In addition consideration of Equations (11.14) and (11.15) lead one to expect that as K_{eq} and K_2 are increased then the effective number of electrons transferred per iodide ion (N_{eff}) will fall below one since iodine released into solution will 'trap' incoming iodide as tri-iodide before it can react at the electrode. Figure 11.4 shows a working surface relating N_{eff} to K and K_2. It can be seen that N_{eff} does indeed decrease when tri-iodide formation is favoured both kinetically and thermodynamically.

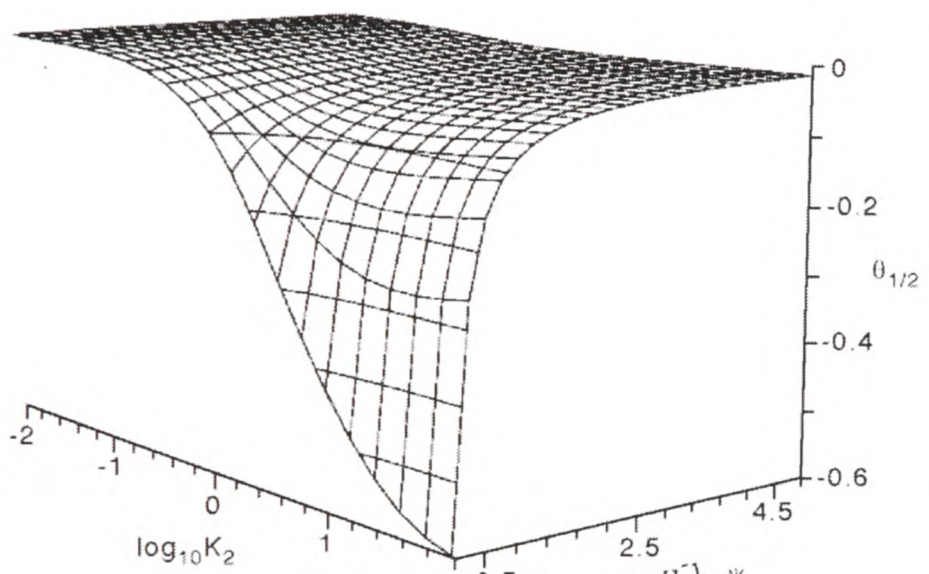

Figure 11.3 Working surface for the effect of K_2 and K on $\theta_{1/2}$. $[I_2]_{sat}$ = 1.2 mM and k_{het} = 0 cm s^{-1}.

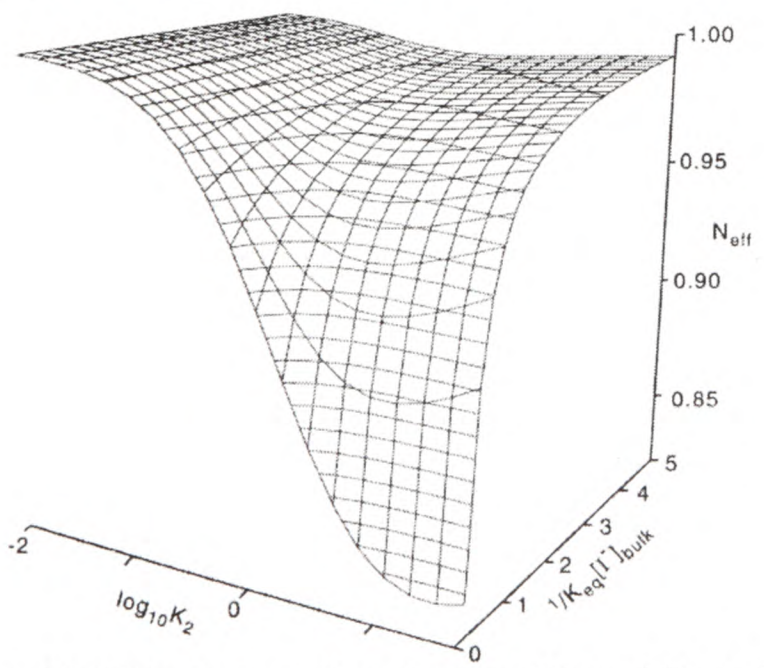

Figure 11.4 Working surface for the effect of K_2 and K on N_{eff}. $[I_2]_{sat}$ = 1.2 mM and k_{het} = 0 cm s^{-1}.

We consider next the equilibrium between aqueous iodine and solid iodine on the electrode surface. At higher concentrations of iodide (> ca. 3 mM) the iodine formed at the electrode forms a locally saturated solution within the diffusion layer. As the concentration of iodine increases such that it exceeds its solubility, i.e. $[I_2] > [I_2]_{sat}$, crystallisation can occur on the platinum surface and the following boundary condition applies

$$0 < x < x_e,\ y = 0:\ [I_2]_{sat} / [I^-]^2 = \exp(\theta)\ ;\ [I_2] \geq [I_2]_{sat} \qquad (11.23)$$

Equation (11.10) may be used approximately under these new conditions provided the net precipitation rate is small compared with the overall fluxes at the electrode surface.

Figure 11.5 shows simulated voltammetry for a 6 mM iodide solution for varying hypothetical values of iodine saturation, $[I_2]_{sat}$. The significant effect of the iodine solubility on both the waveshape and the total magnitude of the voltammetric wave is evident. Interestingly N_{eff} is controlled by the solubility because of the influence of that parameter on the tri-iodide levels in the diffusion layer. The distinctive voltammetric waveshape in the presence of solid iodine at the interface is characteristic of precipitation but might for example be, in this system, easily mistaken for the following reactions as separate electrode processes:

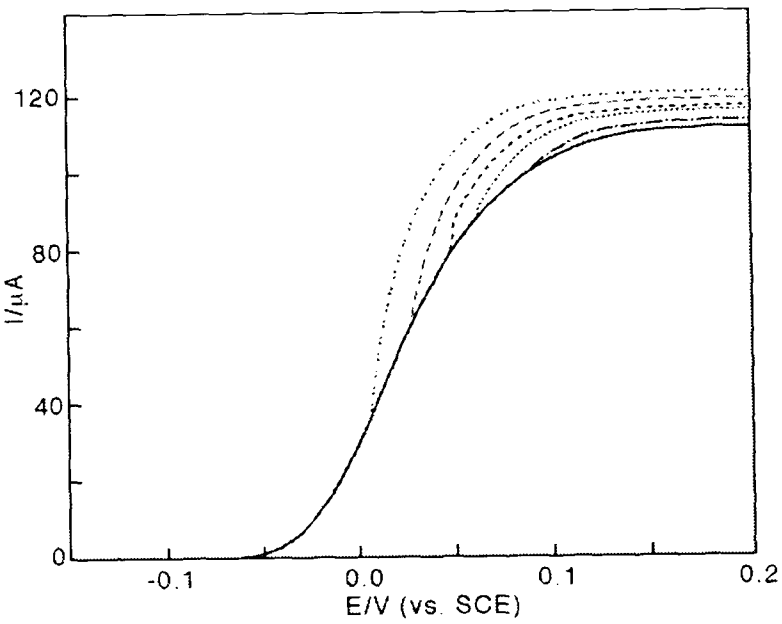

Figure 11.5 Simulated voltammograms for 6 mM KI at a flow rate of 0.04 $cm^3\ s^{-1}$ for hypothetical iodine saturation concentrations of 0.5 (-- --), 1 (——), 1.5 (- - -), 2 (···), 3 (— ·) and 4 (—) mM. $k_f = 1 \times 10^5\ mol^{-1}\ cm^3\ s^{-1}$ and $k_{het} = 0\ cm\ s^{-1}$

$$I^- - 2/3\ e^- \rightarrow 1/3\ I_3^- \qquad (11.24)$$

and

$$I^- - e^- \rightarrow 1/2\ I_2 \qquad (11.25)$$

Last we consider a final possible complication: once iodine is present on the electrode surface there is the possibility of dissolution into iodide solution [11] to form aqueous

tri-iodide ions according to the following heterogeneous reaction which is in competition with the charge transfer in Equation (11.1)

$$I^- (aq) + I_2 (s) \xrightarrow{k_{het}} I_3^- (aq) \tag{11.26}$$

where k_{het} is the heterogeneous rate constant (cm s^{-1}) for the reaction. Simulation of this requires a change of the electrode surface boundary condition for tri-iodide diffusion in Equation (11.19) to

$$0 < x < x_e,\ y = 0:\ D_{I_3^-} \frac{\partial [I_3^-]}{\partial y} = -k_{het}[I^-] \tag{11.27}$$

and correspondingly changes the expression for the current from Equation (11.13) to

$$I = wF\int_0^{x_e} \left\{ D_{I^-} \left[\frac{\partial [I^-]}{\partial y} \right]_{y=0} - k_{het}[I^-] \right\} dx \tag{11.28}$$

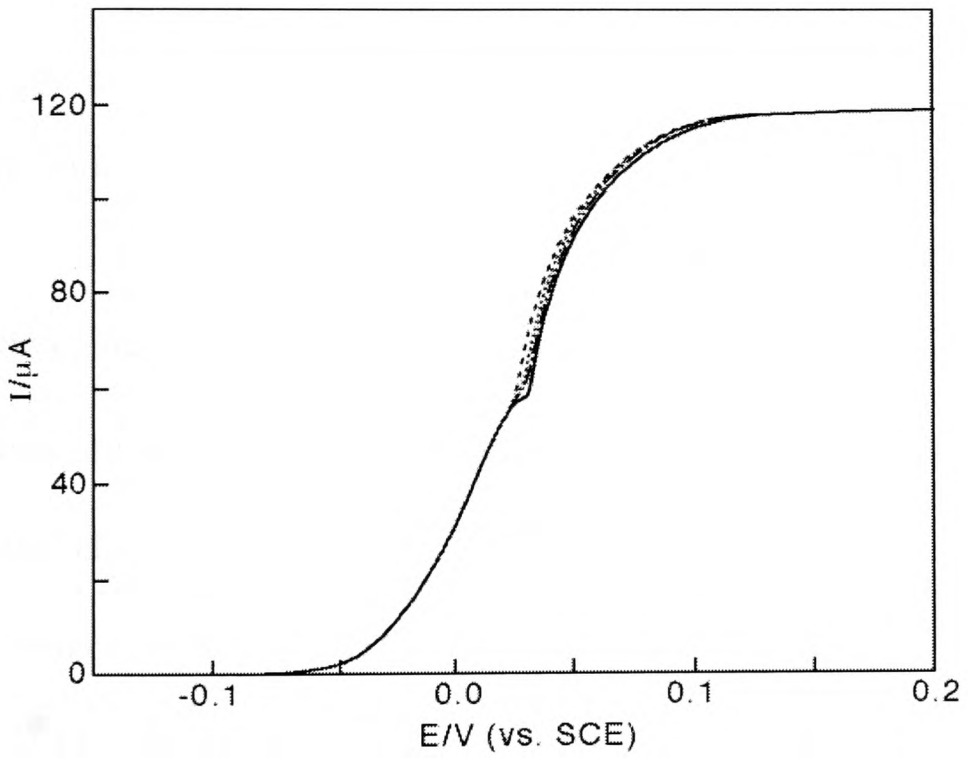

Figure 11.6 Simulated voltammograms for 6 mM KI at a flow rate of 0.04 $cm^3 s^{-1}$, $k_f = 1 \times 10^5$ $mol^{-1} cm^3 s^{-1}$ and $[I_2]_{sat}$ = 1 mM for hypothetical values of k_{het} of 0 (- - -), 0.5 (···), 1 (— ·) and 1.5 (—) x 10^{-3} cm s^{-1}.

Figure 11.6 shows simulated voltammograms for varying k_{het} and clearly shows the change in waveshape as k_{het} increases. This reflects the competition between Equations (11.1) and (11.26) alluded to above and the added injection of tri-iodide into the diffusion layer.

11.4 EXPERIMENTAL

Laser activated voltammetry and chronoamperometry in nominally stationary solution was conducted in the three-electrode cell shown in Figure 2.6. For most experiments this utilised a 1 mm diameter platinum disc working electrode embedded in a Perspex window set in a Teflon mount. Voltammetry under gravity flow conditions was performed using the

apparatus shown in Figure 2.10. It utilised optically transparent channel flow cells as detailed in section 2.6 and either a platinum 2 mm diameter disc or 2 mm square electrode maintained in a fixed position relative to the incident laser beam. The theory for the transport limited current expected at a circular channel flow electrode is given in Appendix 6. All other experimental procedures were as detailed in Chapter 2.

11.5 RESULTS AND DISCUSSION

11.5.1 FORMAL POTENTIAL AND EQUILIBRIUM CONSTANT MEASUREMENT

We consider first the measurement of the formal potential of the electrode process given in Equation (11.1). Chronopotentiometric experiments were performed with a platinum electrode immersed in a 50 ml solution of 0.2506 mM iodine with 6 small additions of 0.5 ml aqueous 1.07 mM iodide every 60 seconds to measure the change in cell potential relative to the SCE as a function of concentration. Analysis of the results using the Nernst equation revealed a value of 0.358 ± 0.004 V (vs. SCE) for the formal cell potential.

We then obtained a value for the equilibrium constant, K_{eq}, of Equation (11.15) by UV/visible spectroscopy. Stock solutions of 0.109 M KI and 0.752 mM I_2 in 0.1 M H_2SO_4 were mixed in various proportions and the absorption due to tri-iodide recorded. Once calibrated by comparison with a standard solution of potassium tri-iodide, the equilibrium constant at 18°C was calculated as 580 ± 20 M^{-1}. This compares favourably with the value of 620 M^{-1} (25°C, 0.5 M H_2SO_4) reported in the literature [17].

11.5.2 AFM OF SURFACE IODINE

We next consider the oxidation of iodide in aqueous sulphuric acid. This has been demonstrated to lead to the production of solid iodine when adequately high concentrations (> ca. 3 mM) of iodide are employed [1,2,17,37-39]. This formation of solid iodine occurs when the solubility of iodine is exceeded (1.1 mM in water at 25°C) [40]. The growth of electrochemically generated iodine on the platinum electrode surface was investigated by *in situ* AFM. Whilst maintaining a potential of +0.56 V (vs. SCE) at a platinum electrode

immersed in aqueous potassium iodide solution, scans were taken at approximately minute intervals to probe the build up of surface deposits. Figure 11.7 shows six AFM images which illustrate the increasing deposition. The growth of crystals on the electrode surface is evident.

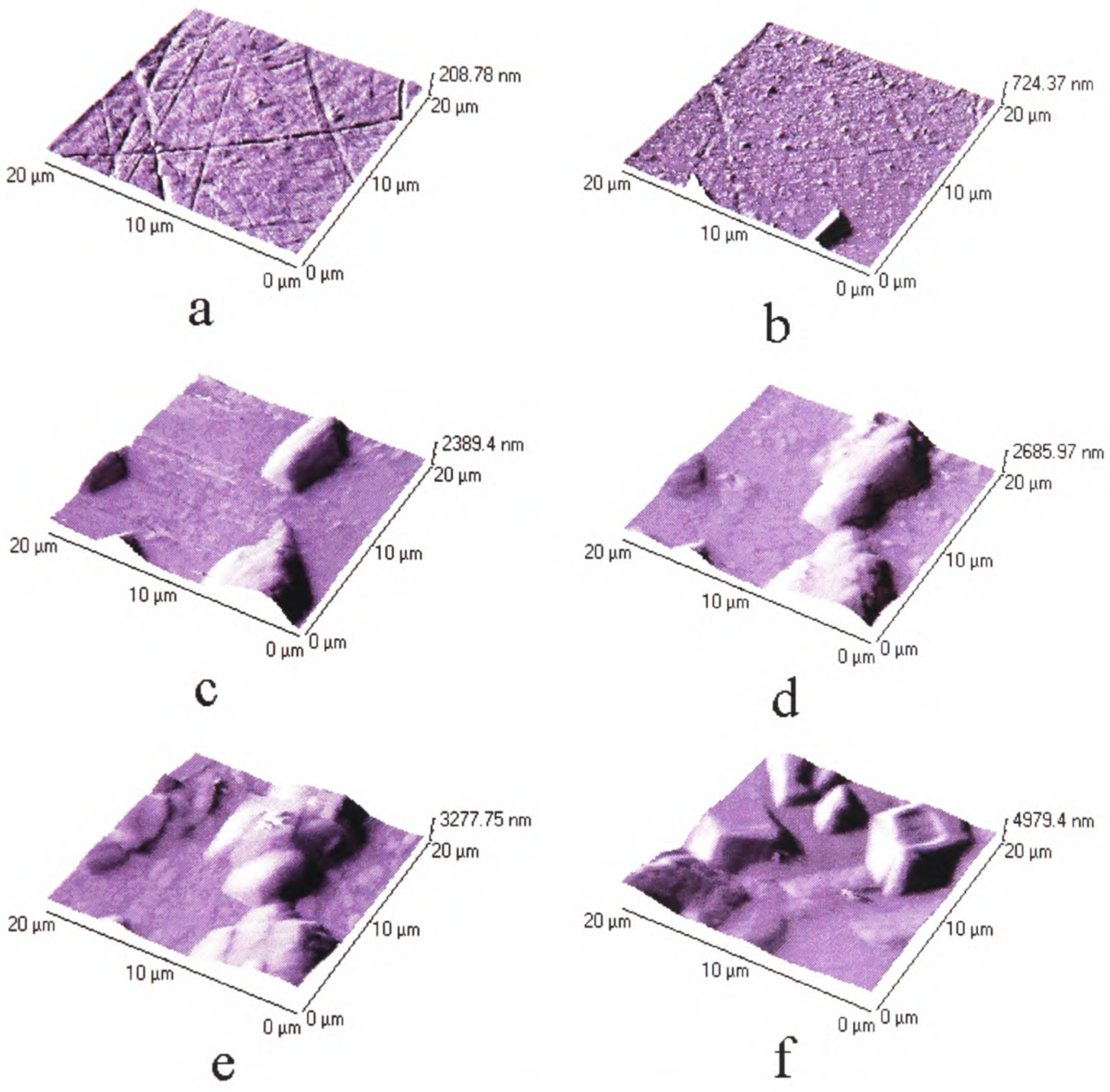

Figure 11.7 AFM pictures of a platinum electrode: a) polished, b) after 208 s, c) after 416 s, d) after 571 s, e) after 728 s all at 0.56 V in 3 mM KI, 0.01 M H_2SO_4 and f) after 420 s at 0.56 V in 5 mM KI, 0.01 M H_2SO_4.

11.5.3 LINEAR SWEEP VOLTAMMETRY

Introduction of laser irradiation to the electrode surface can be expected to interfere with the surface deposition processes studied in the previous section. Linear sweep voltammetry in nominally stationary solution was performed at a variety of scan rates, iodide concentrations and laser intensities to probe the surface cleaning properties of laser activation. Figure 11.8 shows a typical linear sweep voltammogram for the oxidation of 10 mM potassium iodide in 0.125 M H_2SO_4. In the absence of laser illumination (Figure

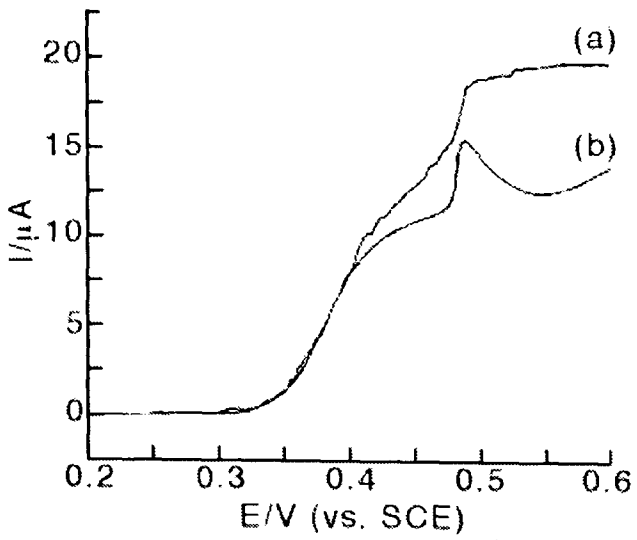

Figure 11.8 LSVs at 5 mVs^{-1} for the oxidation of 10 mM KI in 0.125 M H_2SO_4 on a 1 mm diameter Pt disc electrode under a) dark and b) 0.3 W cm^{-2} laser illuminated conditions.

During 300 mW cm^{-2} illumination a sustained transport-limited current is observed (Figure 11.8a) due to a small amount of thermal convection at the electrode surface. This intensity is insufficient to cause ablation of the platinum surface immersed in aqueous solution, as shown in Chapter 10.

The removal of solid iodine from the electrode surface is illustrated by Figure 11.9 which shows corresponding cyclic and linear sweep voltammograms measured under flow conditions of 1.0×10^{-3} $cm^3 s^{-1}$ (a & b) and 6.9×10^{-3} $cm^3 s^{-1}$ (c) through a flow cell of cross-sectional area 0.6 cm × 0.04 cm using the apparatus shown in Figure 2.10. Trace (a) shows an appreciable stripping peak for the reduction of surface iodine to iodide. This was recorded under dark conditions. In contrast 11.8b) the formation of iodine appears as the current peak at ca. 0.48 V vs. SCE [2]. This leads to partial passivation of the electrode making quantitative interpretation a challenging exercise [39].

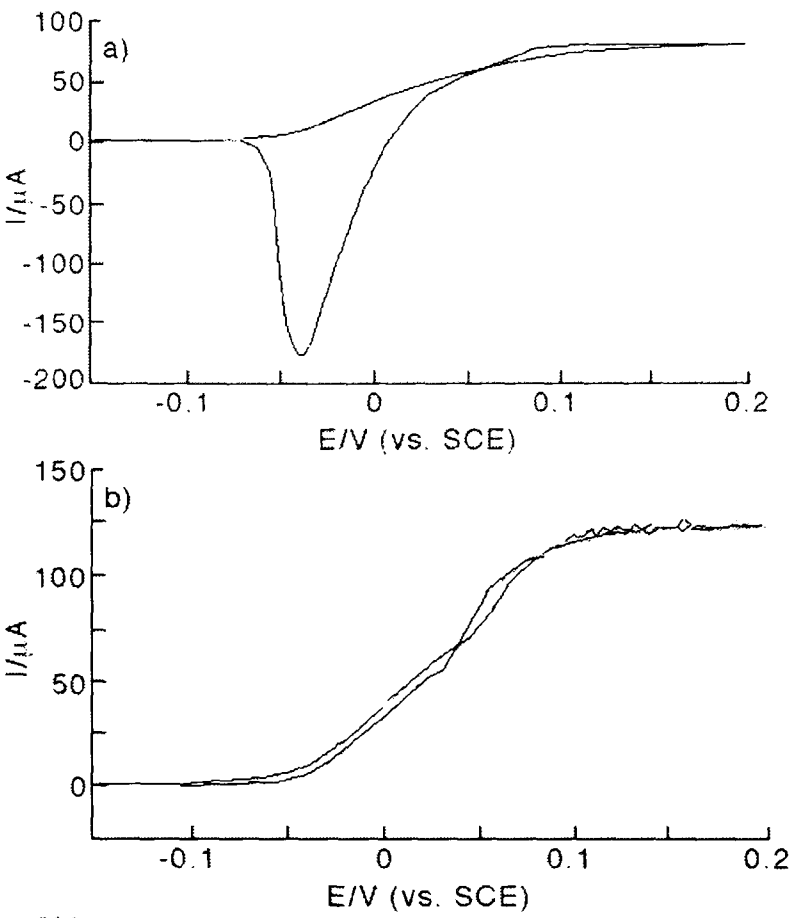

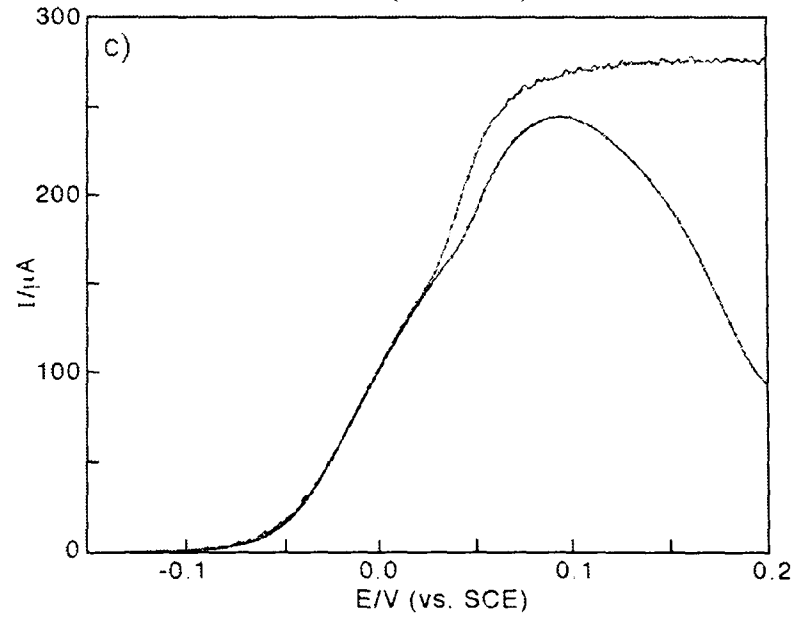

Figure 11.9 Voltammograms for 10.2 mM KI in 0.1 M H_2SO_4 at 5 mVs^{-1} on a 2 mm square Pt electrode under flow conditions: a) CV with no laser with $v_f = 1 \times 10^{-3}$ $cm^3 s^{-1}$, b) CV under 1200 mW cm^{-2} laser illumination with $v_f = 1 \times 10^{-3}$ $cm^3 s^{-1}$ (smoothed trace) and c) LSV at $v_f = 6.9 \times 10^{-3}$ $cm^3 s^{-1}$ in the dark (lower trace) and under 1200 mW cm^{-2} laser illumination (upper, smoothed trace).

(b) shows the effect of 1200 mW cm^{-2} illumination on the same experiment. The reverse cyclic voltammetry scan essentially retraces the anodic sweep and a well-defined hydrodynamic wave is seen. Figure 11.9(c) shows the current-fall off in the dark (lower trace) due to enhanced iodine deposition under faster flow conditions and the corresponding laser activated (upper) trace with its mass-transport limited current plateau suggesting the removal of the insulating surface iodine layer.

11.5.4 CHANNEL FLOW LASER ACTIVATED VOLTAMMETRY

Next further laser activated linear sweep voltammetry under gravity flow conditions was performed for comparison with simulated voltammetry. It is important to note that the mass transport limited waves are now controlled by the channel flow hydrodynamics and laser intensities can be used such that no current enhancement due to electrode heating effects are seen. This was readily confirmed by performing linear sweep voltammetry on separate 5 mM solutions of ruthenium hexaammine trichloride and potassium ferrocyanide in 0.1 M KCl. At laser intensities below 1200 mW cm^{-2} and flow rates above 1.0×10^{-3} cm^3 s^{-1}, the laser and dark voltammograms coincided, except for some current spiking and noise on the laser traces. The same was observed for solutions of iodide below ca. 3 mM suggesting that for these simple reversible systems, the mass transport is dominated by the channel flow and not by laser-induced electrode heating. However, at high concentrations of iodide, the ability of the laser to keep the surface clean as mentioned above does result in a larger current being seen under illumination at a given flow rate as shown in Figure 11.9c. This was evidenced by Levich analysis of waves both in the presence and absence of laser activation.

Figure 11.10 shows 5 mV s^{-1} laser activated linear sweep experimental waves for three different concentrations of aqueous iodide (2.1, 8.7 and 10.4 mM) at different flow rates and 1200 mW cm^{-2} laser intensity. This data was then simulated using the full theory outlined earlier. The measured values of v_f, K_{eq}, $E^{0\prime}$, $[I^-]_{bulk}$, electrode area, temperature and cell parameters were employed along with optimised values for $[I_2]_{sat}$, K_2 and k_{het} to produce the best fit for wave position, shape and limiting current. The last parameter was necessary to

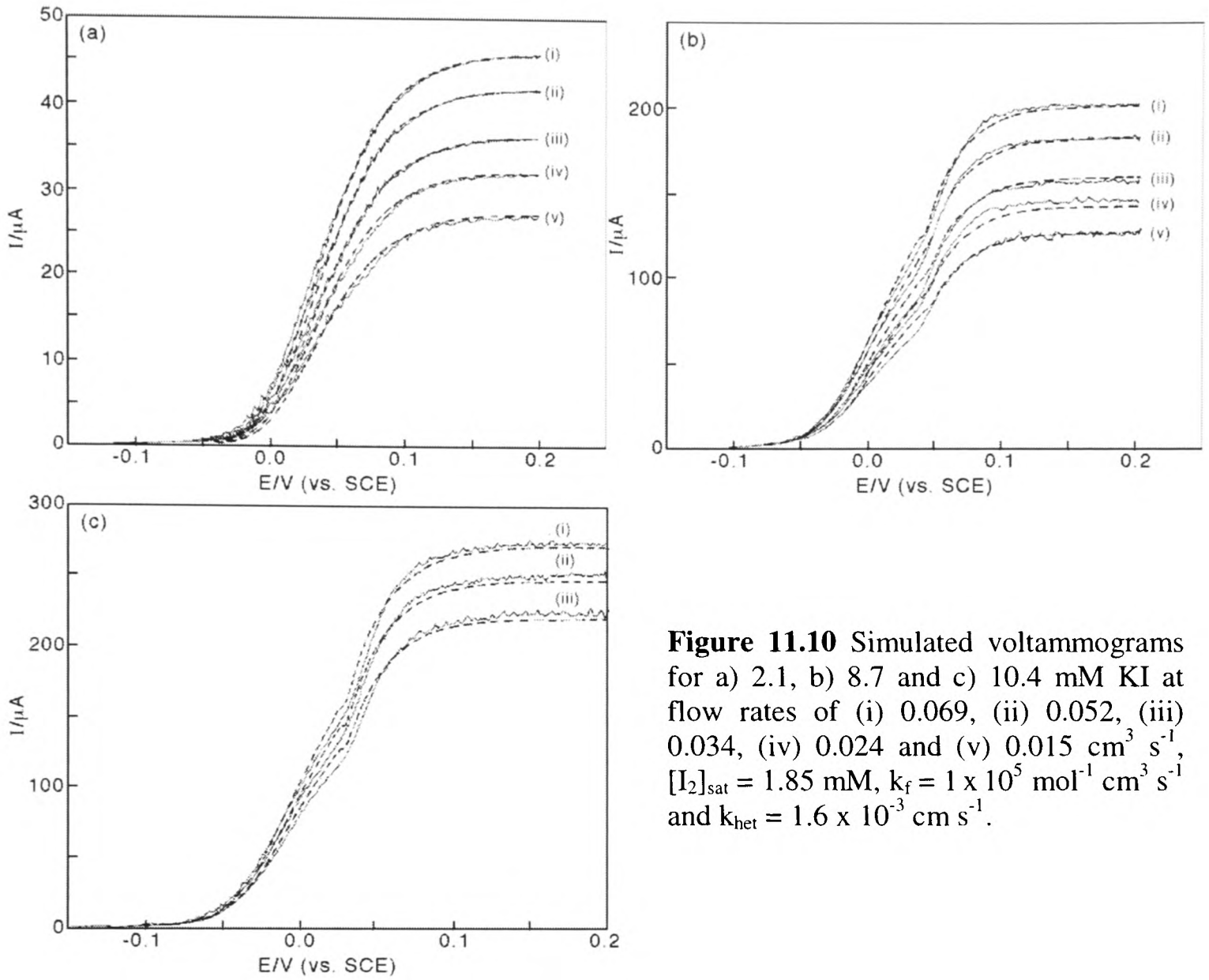

Figure 11.10 Simulated voltammograms for a) 2.1, b) 8.7 and c) 10.4 mM KI at flow rates of (i) 0.069, (ii) 0.052, (iii) 0.034, (iv) 0.024 and (v) 0.015 $cm^3\ s^{-1}$, $[I_2]_{sat}$ = 1.85 mM, $k_f = 1 \times 10^5\ mol^{-1}\ cm^3\ s^{-1}$ and $k_{het} = 1.6 \times 10^{-3}\ cm\ s^{-1}$.

modify the upper half of the voltammetric wave. Excellent agreement is seen between theory and experiment in terms of current magnitude, wave position and inflection giving good evidence for the proposed reaction mechanism and kinetic parameters.

11.6 CONCLUSIONS

The solid iodine formed at platinum electrodes by the electrochemical oxidation of aqueous potassium iodide has been examined by AFM and shown to be easily removed by laser activation (and previously in Chapter 7 by sono-emulsion techniques). By maintaining a clean electrode at steady-state, an oxidation mechanism is established as follows

$$2I^-(aq) - 2e^- \rightleftharpoons I_2(aq) \qquad \text{(i)}$$

$$I_2(aq) + I^-(aq) \rightleftharpoons I_3^-(aq) \qquad \text{(ii)}$$

$$I_2(aq) \rightleftharpoons I_2(s) \qquad \text{(iii)}$$

$$I^-(aq) + I_2(s) \rightarrow I_3^-(aq) \qquad \text{(iv)}$$

where the formal redox potential for reaction (i) is 0.358 V vs. SCE in 0.1 M H_2SO_4 and the equilibrium constant for reaction (ii) is 580 M^{-1}. Optimisation of other kinetic parameters was achieved by fitting the theory to steady-state laser activated waves under flow where solid iodine build up is controlled by laser illumination. Best-fit values of the k_f rate constant of 1×10^5 $mol^{-1}\,cm^3\,s^{-1}$, the solubility of I_2 (reaction (iii)) of 1.85×10^{-3} M, and the heterogeneous rate constant for reaction (iv), k_{het}, of 1.6×10^{-3} $cm\,s^{-1}$ are all of plausible magnitudes. The benefits of laser activation in studying electrode processes that produce surface active intermediates or products can be clearly seen. It is also evident that both laser activation with mass transport enhancement provided by gravity fed channel flow and the mass transport increase and emulsion induced by ultrasound described in Chapter 7 provide useful and parallel tools for probing the mechanism of iodide oxidation at platinum electrodes, particularly in the high concentration region.

11.7 CHAPTER 11: REFERENCES

[1] C. Lui, S. R. Snyder, A. J. Bard, *J. Phys. Chem. B* **1997**, *101*, 1180.

[2] Y. A. Yaraliyev, *Electrochim. Acta* **1984**, *29*, 1213.

[3] A. E. Thomas, A. Wieckowski, *J. Electroanal. Chem.* **1995**, *399*, 207.

[4] A. M. Bittner, J. Wintterlin, G. Ertl, *J. Electroanal. Chem.* **1995**, *388*, 225.

[5] F. Lu, G. N. Salaita, H. Baltruschat, A. T. Hubbard, *J. Electroanal. Chem.* **1987**, *222*, 305.

[6] F. C. Anson, J. J. Lingane, *J. Am. Chem. Soc.* **1957**, *79*, 1015.

[7] I. M. Kolthoff, J. Jordan, *J. Am. Chem. Soc.* **1953**, *75*, 1571.

[8] R. F. Lane, A. T. Hubbard, *J. Phys. Chem.* **1975**, *79*, 808.

[9] T. Bejerano, E. Gileadi, *J. Electrochem. Soc.* **1977**, *124*, 1720.

[10] T. Bejerano, E. Gileadi, *J. Electroanal. Chem.* **1977**, *82*, 209.

[11] P. G. Desideri, L. Lepri, D. Heimler, *Encyclopaedia of the Electrochemistry of the Elements* (Ed. A. J. Bard) Marcel Dekker, New York, **1976**; Vol. 1, Chapter 3.

[12] N. A. Zakhodyakina, M. A. Navitskii, L. A. Sokolov, P. D. Lukovtsev, *Elektrokhimiya* **1965**, *1*, 138 & 251.

[13] A. Y. Gokhshtein, *Elektrokhimiya* **1965**, *1*, 285 & 906.

[14] M. A. Tadayyoni, P. Gao, M. J. Weaver, *J. Electroanal. Chem.* **1986**, *198*, 125.

[15] M. F. Suárez, *D. Phil Thesis*, Oxford University, **1999**.

[16] X. Gao, M. J. Weaver, *J. Am. Chem. Soc.* **1992**, *114*, 8544.

[17] L. M. Dané, L. J. J. Janssen, J. G. Hoogland, *Electrochim. Acta* **1968**, *13*, 507.

[18] T. Hinoue, I. Watanabe, H. Watarai, *Chem. Letters* **1996**, *5*, 329.
[19] P. H. Chen, R. L. McCreery, *Anal. Chem.* **1996**, *68*, 3958.
[20] P. H. Chen, M. A. Frylung, R. L. McCreery, *Anal. Chem.* **1995**, *67*, 3115.
[21] R. K. Jaworski, R. L. McCreery, *J. Electrochem. Soc.* **1993**, *140*, 1360.
[22] R. L. McCreery, R. Bowling, R. Packard, M. Poon, *Abs. Pap. Am. Chem. Soc.* **1988**, *196*, 185.
[23] M. Poon, R. L. McCreery, R. Engstrom, *Anal. Chem.* **1988**, *60*, 1725.
[24] M. Poon, R. L. McCreery, *Anal. Chem.* **1987**, *59*, 1615.
[25] M. Poon, R. L. McCreery, *Anal. Chem.* **1986**, *58*, 2256.
[26] E. Hershenhart, R. L. McCreery, R. D. Knight, *Anal. Chem.* **1984**, *56*, 2745.
[27] R. Oltra, G. M. Indrianjafy, M. Keddam, H. Takenouti, *Corrosion Sci.* **1993**, *35*, 827.
[28] T. Hinoue, R. Harui, T. Izumi, I. Watanabe, H. Watarai, *Analytical Sci.* **1995**, *11*, 1.
[29] R. G. Compton, A. C. Fisher, G. H. W. Sanders, *Electroanalysis* **1993**, *5*, 615.
[30] M. S. Shuman, *Anal. Chem.* **1969**, *41*, 142.
[31] A. Jaworski, M. Donten, Z. Stojek, J. G. Osteryoung, *Anal. Chem.* **1999**, *71*, 243.
[32] R. G. Compton, M. B. G. Pilkington, G. M. Stearn, *J. Chem. Soc. Faraday Trans.* **1988**, *84*, 2155.
[33] M. J. Bidwell, J. A. Alden, R. G. Compton, *J. Electroanal. Chem.* **1996**, *417*, 119.
[34] M. Rudolph, *J. Electroanal. Chem.* **1991**, *314*, 13.
[35] M. Rudolph, *J. Electroanal. Chem.* **1992**, *338*, 85.
[36] J. A. Cooper, R. G. Compton, *Electroanalysis* **1998**, *10*, 141.
[37] H. Tang, A. Kitani, M. Shiotani, *J. Appl. Electrochem.* **1996**, *26*, 36.
[38] Y. Chen, H. Zhang, B. Wu, *J. Electroanal. Chem.* **1992**, *335*, 321.
[39] P. Beran, S. Bruckenstein, *Anal. Chem.* **1968**, *40*, 1044.
[40] S. Swathirajan, S. Bruckenstein, *J. Electroanal. Chem.* **1980**, *112*, 25.

12

DUAL ACTIVATION OF METHYLENE GREEN VOLTAMMETRY

CHAPTER 12: DUAL ACTIVATION OF METHYLENE GREEN VOLTAMMETRY

12.1 CONTENTS

This chapter studies methylene green voltammetry in aqueous solution using thermal, microwave, laser or ultrasonic activation at platinum electrodes. Some of the work detailed is reproduced in a paper accepted for publication in the *Journal of Physical Chemistry* in August 1999.

The voltammetry of the aqueous two-electron reduction of the phenothiazine dye methylene green, known to be passivating at platinum electrodes, is reported under simultaneous activation with each of the following techniques:

1. thermal activation in the temperature range 15 - 80°C,
2. pulsed microwave activation with a modified 800 W, 2.45 GHz domestic microwave oven,
3. 10 Hz pulsed laser activation with a Nd:YAG laser at 532 nm or
4. ultrasonic activation where a 20 kHz ultrasonic horn probe is employed to generate an aqueous/organic solvent emulsion.

The relative merits of the four methodologies are compared and discussed in terms of surface activation and cleaning, mass-transport enhancement and reduction mechanism elucidation. Comparisons are also drawn with the voltammetry of methylene blue; a dye of the same family. The structures of both molecules are given in the next section.

12.2 INTRODUCTION

The scope of electrochemical studies in aqueous systems where electrode passivation is commonplace can frequently be widely expanded by the use of *dual activation*, that is where a potential is applied to an electrode in tandem with some other mode of stimulation such as heating or photo-excitation. This chapter concentrates on four such secondary

techniques namely thermal activation, microwave activation, laser activation and ultrasonic activation. The first of these has been studied for many years, but recent advances have been made by examining the effects of very rapid local heating at wire electrodes by Gründler and colleagues [1-3].

A second example of in-situ activation of electrochemistry by external sources is by subjection to radiation. Until very recently the interaction of microwave radiation with electrochemical processes [4] was entirely unexplored, despite the widespread interest in microwave enhanced chemistry. The use of low power microwave radiation in electrochemical systems is of considerable importance in areas of research such as in-situ electrochemical EPR [5] (typically X-band, 9.5 GHz) and microwave reflectance characterisation [6] of semi-conducting electrodes. In these cases the activation of the electrochemical system due to absorption of microwave radiation can usually be ignored due to the low intensities used. However, microwave radiation is known to interact not only with molecules in the gas phase but also with condensed materials and interfaces with sufficient dielectric loss [7] and may therefore be employed to activate an electrochemical system.

The use of microwave radiation as an activation source leads to a considerable current enhancement, arising from a rapid heating effect which causes the temperature in the liquid phase at the electrode/solution interface to locally superheat [4].

Laser irradiation of electrodes is becoming popular. McCreery and colleagues have utilised high intensity infra-red laser pulses to activate the surface and increase heterogeneous electron-transfer kinetics at glassy carbon and platinum electrodes [8-13] whilst Watanabe and co-workers have subsequently employed a relatively high power infra-red laser source to maintain clean platinum and gold electrodes by ablating the top layer of the electrode surface every other second [14]. Oltra *et al.* have additionally used pulsed laser irradiation to depassivate an iron electrode under channel flow hydrodynamic conditions [15] whilst Hinoue *et al.* used an argon-ion laser to probe the effect of electrode heating on the electron transfer process of aqueous Fe (II/III) species in a flow system [16]. Importantly these experiments [8-16] used laser irradiation to activate or clean the electrode surface but not to

provide direct photochemical or photoelectrochemical effects [17] which are not discussed here.

Last we consider the introduction of power ultrasound into electrochemical methodologies. This has been widely studied over the last decade and has many benefits [18,19] including extremely enhanced mass transport resulting from acoustic streaming [20] or microjetting [21] and electrode activation arising from cavitational erosion [22]. In addition ultrasound has been used to permit the electrochemical study of essentially water-insoluble organic species in aqueous solution [23,24, Chapters 6 and 7]. Sonication is therefore a convenient and effective alternative to the use of high-speed stirring and/or detergents for the promotion of emulsions for electrochemistry [25].

Many potentially viable electrode processes are inhibited if not entirely passivated by the adsorption, precipitation or polymerisation of reaction products or intermediates on the electrode surface. This chapter addresses one such reaction in aqueous solution, the two-electron reduction of the phenothiazine dye methylene green (MG shown in Figure 12.1) [26-28] to leuco-methylene green (*l*-MG) at platinum electrodes and builds on the work presented in Chapter 7. This dye is similar to methylene blue (MB, also shown in Figure 12.1) which is studied for comparison. We report the use of the above activation techniques

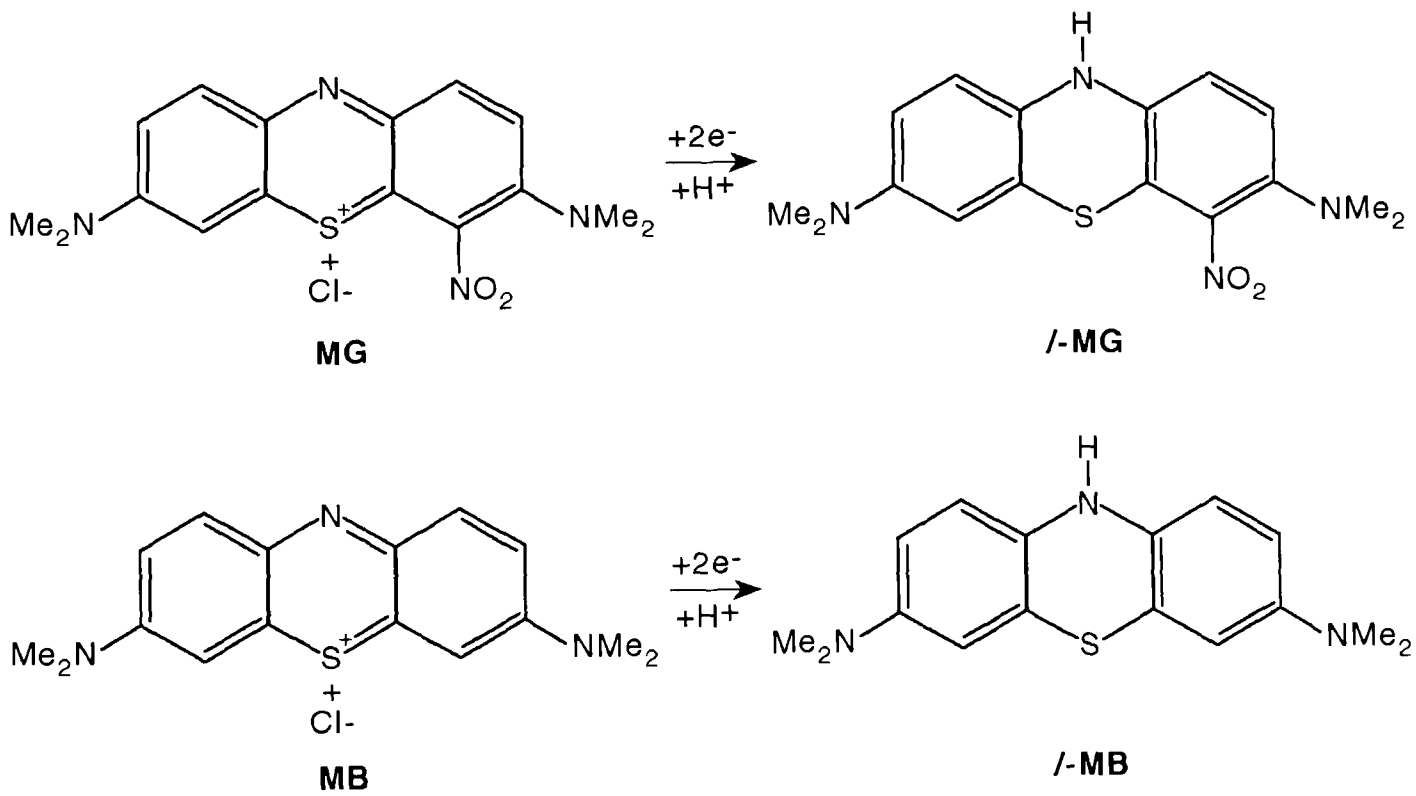

Figure 12.1 Structures of methylene green (MG), *leuco*-methylene green (*l*-MG), methylene blue (MB) and *leuco*-methylene blue (*l*-MB).

to explore and quantify the dual activation of a platinum electrode in the context of linear sweep and cyclic voltammetry of methylene green. Conventional thermostatted voltammetry, *microwave activated voltammetry* (hereafter referred to as MAV) using a modified 800 W, 2.45 GHz domestic microwave oven, *laser activated voltammetry* (LAV) using a 10 Hz pulsed Nd:YAG laser at 532 nm and *sonovoltammetry* using a 20 kHz ultrasonic horn are performed on aqueous solutions of methylene green to establish a comparison of the relative benefits of the different approaches.

12.3 EXPERIMENTAL

Channel flow voltammetry was conducted in the experimental apparatus shown in Figure 2.10 according to procedures outlined in section 2.6. The channel electrode cell employed a platinum working electrode (4 mm x 4 mm), an SCE and a platinum gauze counter electrode. Thermal activation experiments were performed in a divided cell of approximately 50 cm^3 total volume. This is shown in Figure 2.8 and employed a 25 μm diameter platinum disc as the working electrode in tandem with a combined reference and counter SCE connected via a solution bridge. The SCE was kept at a fixed temperature which was in the range 15 ± 2°C for all experiments. The temperature of the platinum electrode was raised in ca. 10°C steps by means of a small heating coil in a surrounding water bath. The two electrode cell used in the microwave activated experiments is shown in Figure 2.9. The cell volume was approximately 5 cm^3. Laser activated voltammetry in nominally stationary solution was conducted in the three-electrode cell shown in Figure 2.6. This utilised a 2 mm diameter platinum disc working electrode embedded in a Perspex window set in a Teflon mount. The cell volume was approximately 15 cm^3. The bulk solution temperature was 20 ± 2°C in all cases. The light source employed was the LAB 130 Q-switched Nd-YAG laser. The beam was reduced to 4.0 mm in diameter by means of passage through a fixed diameter aperture before being passed into the LAV cell. Typical experiments were performed in the range 0.1 to 0.8 W cm^{-2}. Sonovoltammetric experiments were conducted

using a 6 mm diameter platinum working electrode in a 250 ml cell at 20°C and are reported in detail in Chapter 7.

Atomic force microscopy (AFM) was employed to image the surface of a platinum disc before and after leuco-methylene green deposition at various temperatures.

12.4 RESULTS AND DISCUSSION

12.4.1 VOLTAMMETRY IN THE ABSENCE OF DUAL ACTIVATION

The voltammetry of methylene green (MG) [26-28] and methylene blue (MB) [29-30] at pHs in the range 1.7 to 7.3 was investigated at platinum electrodes using buffered 0.2 mM aqueous solutions of dye under channel flow conditions at a flow rate of 0.0104 $cm^3\ s^{-1}$. For methylene blue, a single mass-transport limited reduction wave was observed at all pHs, though the half-wave potential of the wave increased with decreasing pH. Half wave potentials over the above range of pH were measured and there were seen to be three distinct pH ranges where the slope of the $E_{1/2}$ vs. pH plot changed from ca. -90 to -60 to -30 mV $decade^{-1}$. This was directly analogous to the voltammetric behaviour of toluidine blue dye reported in both Chapter 10 and the literature [31]. For the two-electron reduction,

$$MB + mH^+ + 2e^- \rightleftharpoons \textit{l}\text{-}MB \qquad (12.1)$$

theory predicts that these gradients correspond directly to the uptake of three, two then one proton(s) during reduction respectively [32]. The pHs which marked the changeovers were ca. pH 5.0 and pH 6.0. This compares with previously reported work for methylene blue reduction on carbon fiber microdisk electrodes which gave three slopes as above at changeovers of ca. pH 5.4 and 6.0 [33].

In contrast the channel flow voltammetry of methylene green presented some interesting differences. At low pHs up to about pH 4.5, a single mass-transport limited wave was seen on reduction of an aqueous solution of the dye. In this pH region the slope of $E_{1/2}$ vs. pH was ca. -60 mV $decade^{-1}$, indicating the involvement of only two protons in the reduction process of Equation (12.1) with MB replaced by MG. This may reflect the

increased acidity of the protonated molecule owing to the nitro group on the ring. At higher pHs however the wave split into two. Some typical cathodic sweep voltammograms at pHs 3.86, 4.39 and 5.25 are shown in Figure 12.2 and illustrate this phenomenon. The plots of these separate half-wave potentials for the split wave against pH both have slopes of ca. -30 mV decade^{-1} at pHs higher than about 5.5 suggesting the uptake of a single proton during the reduction to form *l*-MG. Although the

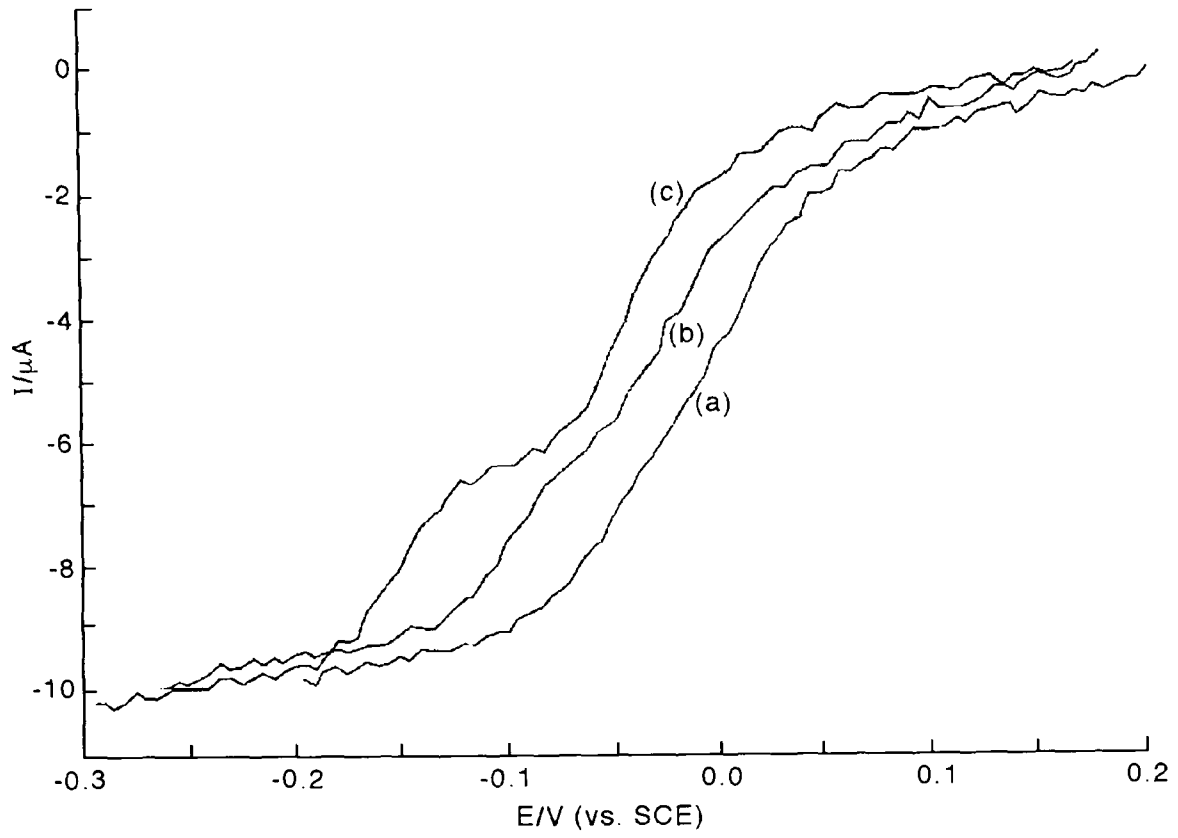

Figure 12.2 Linear sweep channel flow voltammograms on a 4 mm x 4 mm Pt electrode at a flow rate of 1.04 x 10^{-3} cm^3 s^{-1} for 0.2 mM MG buffered at a) pH 3.86, b) pH 4.39 and c) pH 5.25.

voltammetric response splits into two separate processes as discussed below, the total current observed in Figure 12.2 remains the same, indicating an *overall* two-electron process in all cases. Treating the total current passed as representing a two-electron reduction, the value of the diffusion coefficient, D, for methylene green was found to be 3.6 ± 0.2 x 10^{-6} cm^2 s^{-1}. The possibility that the split wave might be due to two *one-electron* processes was discounted both by the lack of any ESR signal which would be produced by the radical formed at intermediate potentials and also by virtue of Tafel analysis of the split wave which gave Tafel slopes of ca. 30 mV for each wave. The value of the gradients is that expected for a two-electron electrochemically reversible process. It is likely that because a two-electron reduction accompanied by the uptake of a single proton results in the formation of a neutral organic species that the wave is split because one process takes place in solution and the other on the electrode surface. Thus at pHs above about 4.5 the relevant equations for dilute concentrations of methylene green are:

$$MG(aq) + H^+ + 2e^- \rightleftharpoons l\text{-}MG(s) \quad (12.2)$$

$$MG(aq) + H^+ + 2e^- \rightleftharpoons l\text{-}MG(aq) \quad (12.3)$$

Further evidence for the above processes is suggested by the non-equality of the two waves in terms of current as has been reported previously [27] though this could be explained by different diffusion co-efficients for the dye and its one-electron reduction product.

We next focus on this split-wave voltammetry at higher pHs. Experiments were conducted in stationary solution using a 0.2 mM aqueous solution of methylene green in 0.1 M KCl buffered at pH 6.5 ± 0.1 with 0.1 M KH_2PO_4. Under dark conditions two reduction peaks are seen which can be attributed to the above processes. On the reverse scan a large 'stripping' peak is observed as shown in Figure 12.3 corresponding to the re-oxidation of the surface bound *l*-MG. At high concentrations (> ca. 2 mM in stationary solution) the second aqueous reduction wave largely disappears and this can be explained by the formation of a thick insulating surface bound layer of solid *l*-MG which largely passivates the electrode. This is shown for a microelectrode at room temperature in Figure 12.4.

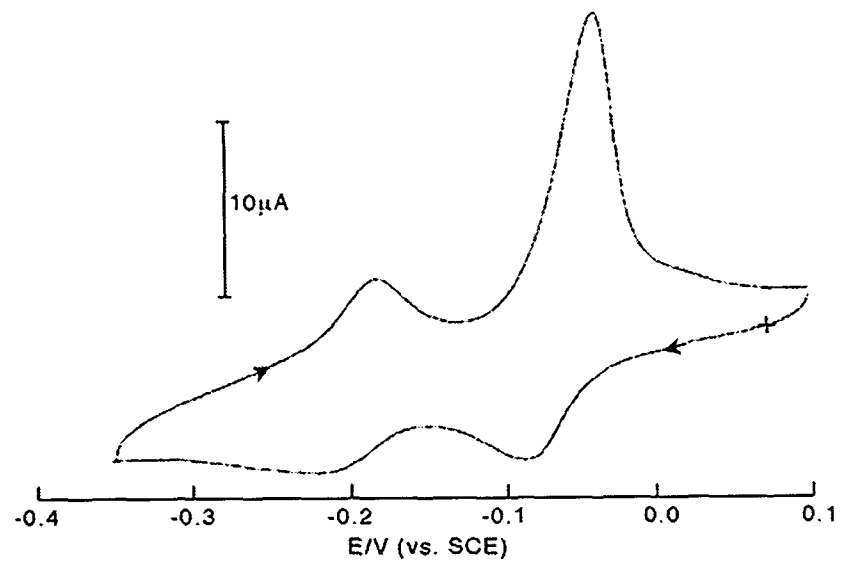

Figure 12.3 'Silent' CV of 0.2 mM MG in 0.1 M KCl / 0.2 M KH_2PO_4(aq) at pH 6.5. Scan rate was 10 mV s^{-1} at a 6 mm Pt disc working electrode.

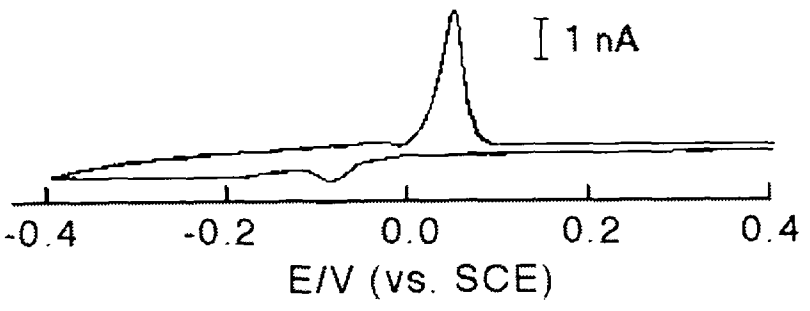

Figure 12.4 'Silent' CV of 2 mM MG in 0.1 M KCl / 0.2 M KH_2PO_4(aq) at pH 6.5. The scan rate was 10 mV s^{-1} at a 30 μm Pt disc working electrode.

12.4.2 THERMAL ACTIVATION OF METHYLENE GREEN VOLTAMMETRY

Cyclic voltammetry for a 2 mM aqueous solution of methylene green in KCl buffered at pH 6.5 ± 0.1 with 0.2 M KH_2PO_4 was performed in the apparatus shown in Figure 2.8. The temperature of the platinum electrode was raised in ca. 10°C steps by means of a small heating

coil in a surrounding water bath. Typical voltammograms at 17°C, 41°C, 59°C and 79°C are shown in Figure 12.5a-d. Initially, below ca. 70°C, as the temperature is raised the magnitude of the forward and backward peaks increases, corresponding to greater surface coverage probably as a result of increased mass transport and rates of nucleation and solid growth at the electrode. However, as the temperature rises to ca. 80°C two waves are clearly seen in the reduction sweep of the cyclic voltammogram recorded, as well as an extremely large 'stripping' peak upon re-oxidation (Figure 12.5d). Comparison with the results shown in Figure 12.3 leads to the conclusion that the second peak corresponds to the two-electron reduction of methylene green to form *leuco*-methylene green in the solution phase as given by Equation (12.3).

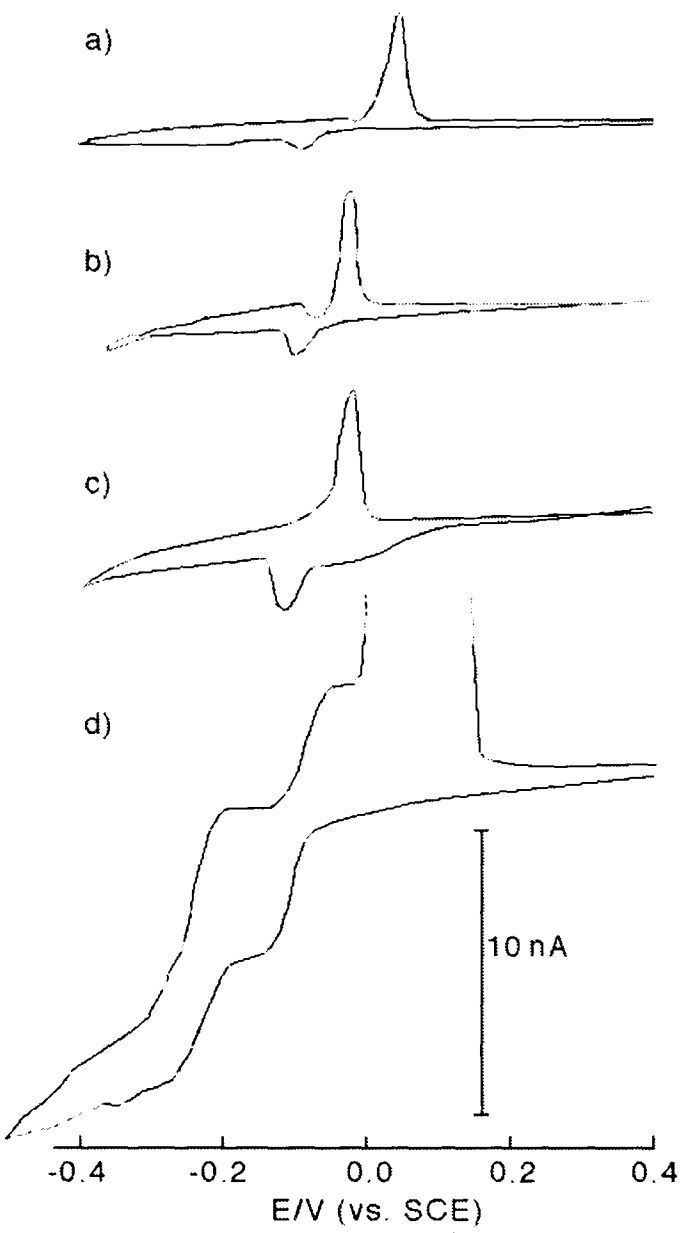

Figure 12.5 CVs at 10 mV s^{-1} at a 30 μm Pt disc electrode for 1.0 mM MG in 0.1 M KCl / 0.1 M KH_2PO_4(aq) (pH 6.5) at a) 17°C, b) 41°C, c) 59°C and d) 79°C.

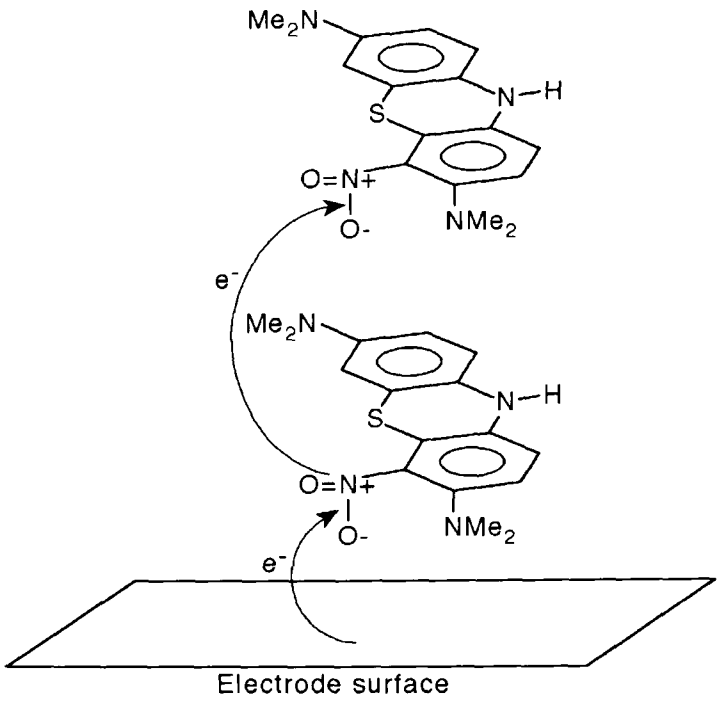

Figure 12.6 Schematic diagram of a possible 'electron hopping' mechanism for *leuco*-methylene green.

A possible explanation of why this second solution phase reaction is able to occur at higher temperatures is that the surface-bound *leuco*-methylene green becomes conducting via the thermally activated electron-hopping mechanism illustrated in Figure 12.6. This type of mechanism has been reported in liquid nitrobenzene [34] and the hypothesis is

supported by AFM measurements taken after 60 s deposition at -0.14 V vs. SCE (just beyond the potential for the surface reaction) at a range of temperatures (see Figure 12.7a-d). These images show that the higher the temperature the greater the surface coverage, and hence

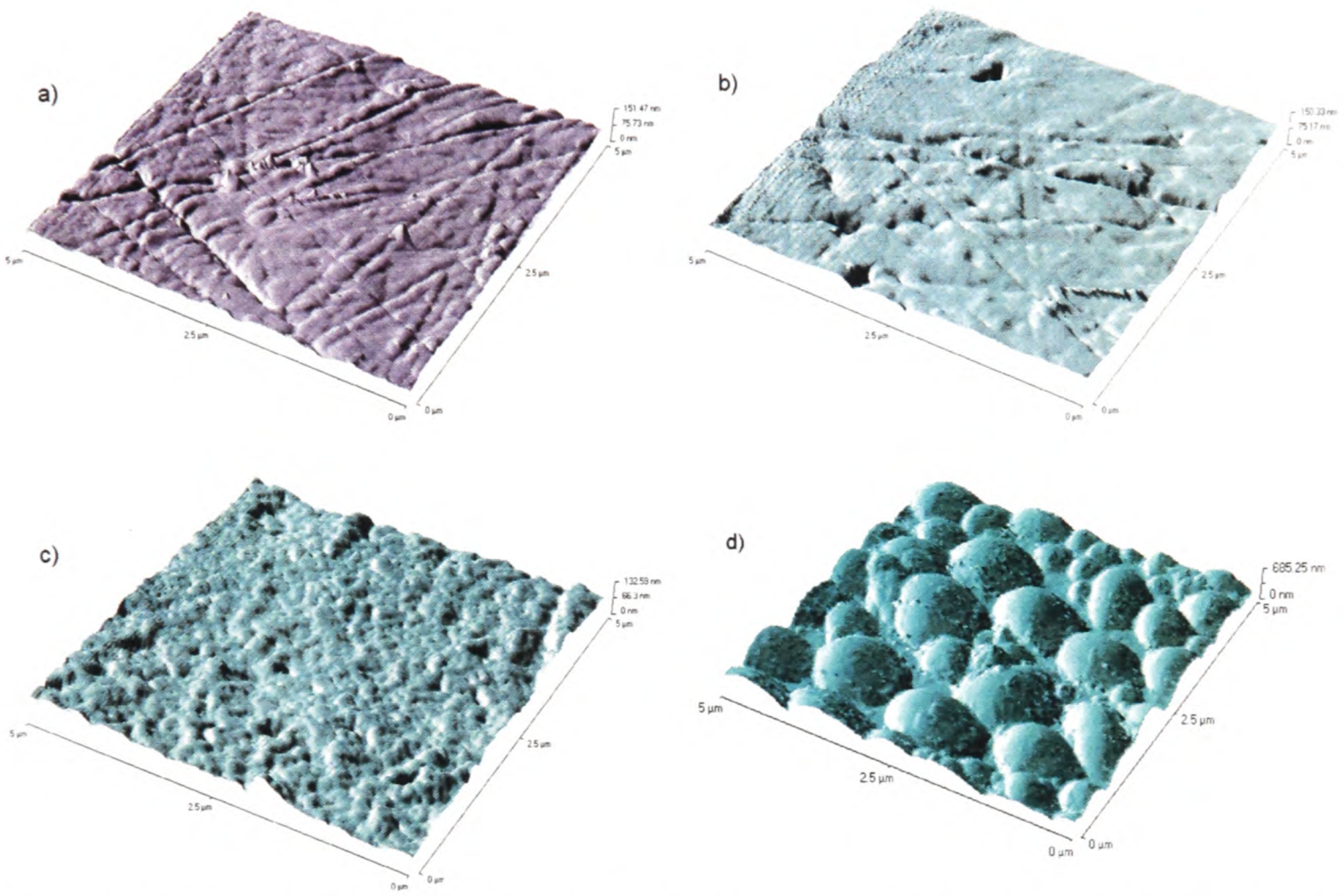

Figure 12.7 AFM images of a) a polished 4 mm diameter Pt disc electrode and the same electrode held at –0.14 V (vs. SCE) for 60 s in 1.0 mM MG at b) 17°C, c) 30°C and d) 85°C.

further reactions which occur must do so in the presence of this covered surface. Further evidence comes from the large stripping peak observed at high temperatures which shows that the surface species is still present in large amounts after the second process has occurred.

12.4.3 MICROWAVE ACTIVATED VOLTAMMETRY: OPTIMISATION

The activation of electrochemical systems by microwave radiation was until recently [4] entirely unexplored. Initially it was necessary to optimise the microwave experimental set-up to ensure that good reproducible results were obtained. First the effect of solution depth in the microwave cell shown in Figure 2.9 was investigated. This was carried out by allowing the cell to slowly fill up with solution whilst applying pulsed microwave radiation and recording the current response during anodic linear sweep voltammetry of a 2 mM aqueous solution of $K_4[Fe(CN)_6]$ in 0.1 M KCl. The voltammogram is shown in Figure

12.8 and clearly shows two solution levels where the current response due to microwave activation is greatest. The mid-point of the first volume was chosen as the experimental solution depth for at this level the current response was appreciable and fairly uniform over a small range of depth, therefore, small deviations would not result in large current deviations. Thus this level was marked on the cell wall and all following experiments were carried out with the solution up to this mark.

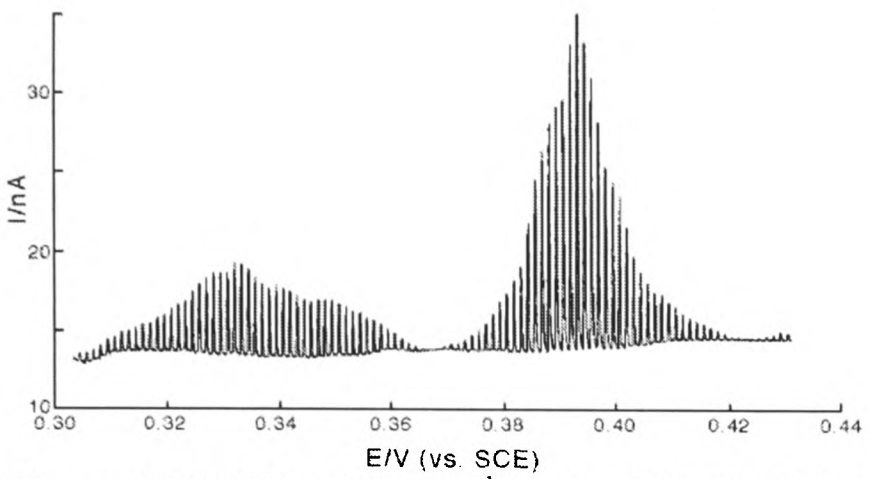

Figure 12.8 LSV at 20 mV s^{-1} for 2 mM $K_4[Fe(CN)_6]$ in 0.1 M KCl(aq) at a 50 µm Pt disc electrode during slow solution depth increase under pulsed microwave irradiation.

One further modification was made to the experimental procedure as a result of problems arising in reproducibility due to gas bubbles rising through the solution during scans. To eliminate this the solution was thoroughly degassed by bubbling argon through the solution via a thin capillary under high vacuum. This process removed most of the dissolved gases from the solution, leaving only a small amount of inert argon gas dissolved. Microwave power calibration was performed as described in section 2.5.2.

Current enhancement seen under microwave activation was ca. 10 fold for 2.5 W activation compared with 'dark' voltammetry and can be shown to be a result of rapid heating of the liquid phase at the solution/electrode interface by comparison with thermally activated ferrocyanide voltammetry. A typical microwave activated voltammogram for ferrocyanide oxidation is shown in Figure 12.9. The shift of half-wave potential with temperature (ca. -1.53 mV K^{-1}) has been previously reported [4]. Microwave activation at increasing powers also reduced the

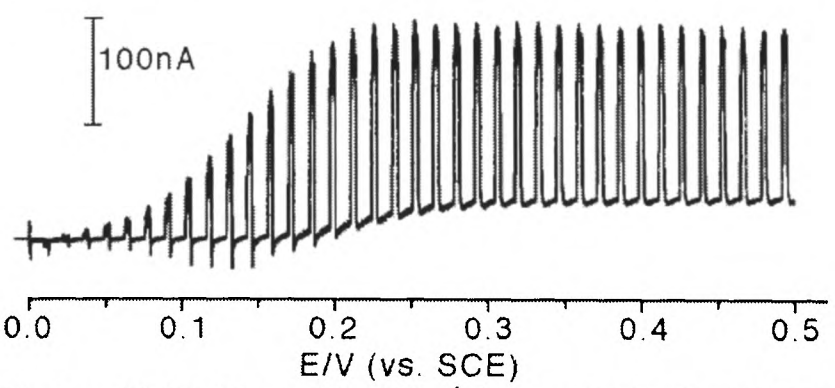

Figure 12.9 LSV at 20 mV s^{-1} for 2 mM $K_4[Fe(CN)_6]$ in 0.1 M KCl(aq) at a 50 µm Pt disc electrode under 2.5 W pulsed microwave irradiation.

half-wave potential of the ferrocyanide voltammetry. A plot of $E_{1/2}$ against microwave power had a slope of ca. –23 mV W^{-1}, which can be equated to an electrode temperature increase of approximately 15°C W^{-1}. By applying ca. 3.6 W of microwave power, we estimate that temperatures of almost 80°C were reached at the electrode-solution interface.

12.4.4 MICROWAVE ACTIVATED VOLTAMMETRY: METHYLENE GREEN

Cyclic voltammograms were recorded for a 0.2 mM aqueous solution of methylene green in 0.1 M KCl buffered at pH 6.5 ± 0.1 with 0.2 M KH_2PO_4 under microwave activation as outlined in the previous section. The scans show evidence of a sustained mass transport limited current at negative potentials. An example is shown in Figure 12.10. This agrees

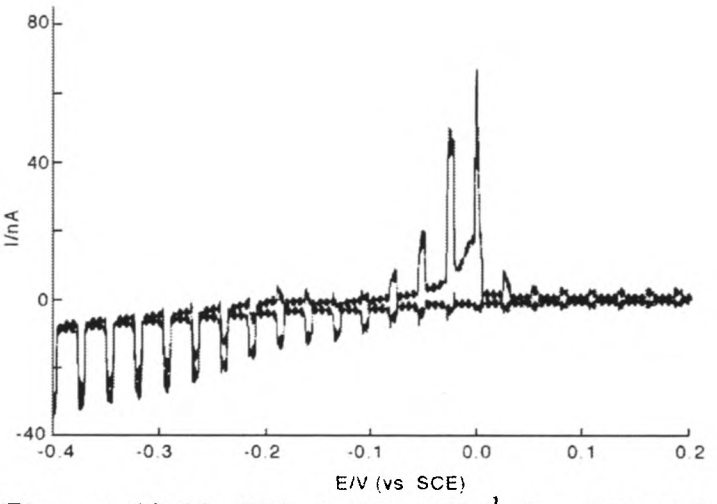

Figure 12.10 CV at 20 mV s^{-1} for 0.2 mM MG in 0.1 M KCl(aq) at pH 6.5 at a 50 µm Pt disc electrode under 3 W pulsed microwave irradiation.

with the high temperature results in section 12.4.2, as is expected from the thermal activation arising from the application of microwave radiation.

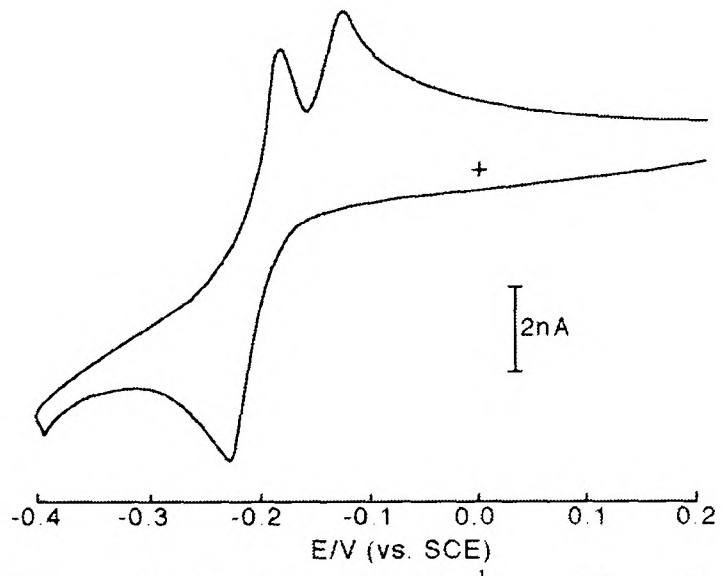

Figure 12.11 CV at 20 mV s^{-1} at a 50 µm Pt disc electrode for 1.0 mM MB in 0.1 M KCl / 0.1 M KH_2PO_4(aq) at pH 6.5.

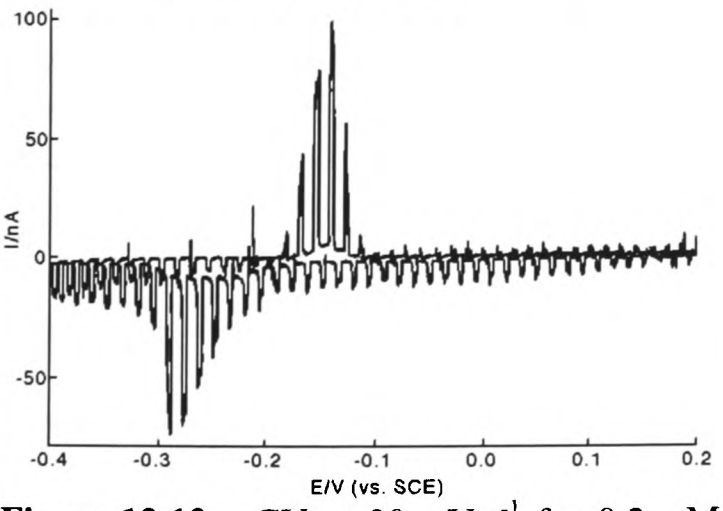

Figure 12.12 CV at 20 mV s^{-1} for 0.2 mM MB in 0.1 M KCl(aq) at pH 6.5 at a 50 µm Pt disc electrode under 3 W pulsed microwave irradiation.

A similar experiment was carried out for a 1 mM aqueous solution of methylene blue in 0.1 M KCl buffered at pH 6.5 ± 0.1 with 0.2 M KH_2PO_4. Figure 12.11 shows the cyclic voltammogram for methylene blue with no thermal activation, while Figure 12.12 shows the cyclic voltammogram under

microwave activation. Comparison of these results with those obtained for methylene green shows that in the case of methylene blue no sustained mass transport limiting current is seen during reduction under microwave activation. Instead, as in the absence of microwave activation, the current is seen to fall off at negative potentials due to surface passivation. This suggests that the surface bound *leuco*-methylene blue does not become conducting at high temperature, unlike *l*-MG. This may arise from the absence of the nitro group (NO_2) on the ring system of methylene blue, which may preclude the electron hopping mechanism. The structures of all four molecules are given in Figure 12.1.

12.4.5 LASER ACTIVATED VOLTAMMETRY

For laser activated cyclic voltammetry experiments a 0.2 mM aqueous solution of methylene green in 0.1 M KCl buffered at pH 6.6 ± 0.1 with 0.2 M KH_2PO_4 was used and scans were taken at 50 mV s^{-1}. Attention was focused on the first reduction wave attributed to the formation of surface bound *leuco*-methylene green given in Equation (12.2). Figure 12.13 shows the voltammetry at a 2 mm platinum disc electrode under varying conditions of laser illumination. It is evident that when greater laser activation is applied both the reduction and re-oxidation peaks are increasingly diminished, in contrast with the above results for thermal and microwave activation. A possible explanation of this is that the laser pulses remove methylene green nuclei on the surface preventing the growth of solid *l*-MG. Thus, these results provide good evidence for the surface cleaning effects of laser illumination.

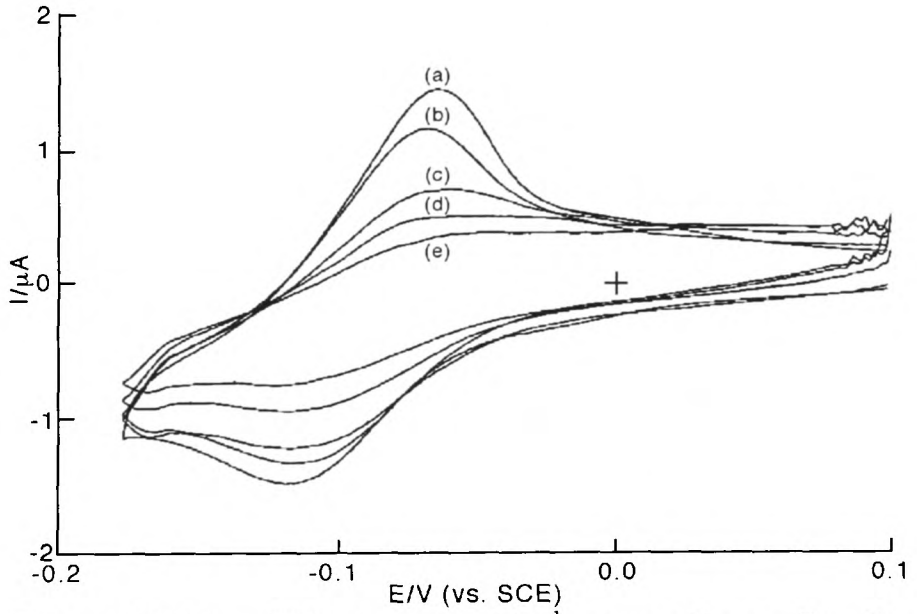

Figure 12.13 CVs at 50 mV s^{-1} at a 2 mm Pt disc electrode for 0.2 mM MG in 0.1 M KCl / 0.1 M KH_2PO_4(aq) at pH 6.6 under a) dark conditions, b) 160 mW cm^{-2}, c) 300 mW cm^{-2} d) 450 mW cm^{-2} and e) 560 mW cm^{-2} laser illumination (smoothed traces).

12.4.6 SONO-EMULSION VOLTAMMETRY

When 25 W cm^{-2} of power ultrasound is introduced to the cyclic voltammetry of a 0.2 mM aqueous solution of methylene green in 0.1 M KCl buffered at pH 6.6 ± 0.1 with 0.2 M KH_2PO_4, it changes markedly from the 'silent' behaviour seen in Figure 12.3 due to significantly enhanced mass transport. A cyclic voltammogram at a 6 mm platinum disc electrode at 20 mV s^{-1} is shown in Figure 12.14. First it can be observed that a much larger stripping peak is seen corresponding to the greater deposition resulting from the enhanced currents flowing due to the increased mass transport. Second whilst there is a mass-transport limited current relating to the two-electron processes, reflecting the constant flux of material due to steady-state convection/diffusion, the wave at the more negative potential shows a progressive decrease of signal at potentials negative of ca. –0.23 V (vs. SCE). This electrode passivation was also seen earlier both under silent conditions at higher concentrations and during hydrodynamic voltammetry at a channel electrode, effectively precluding the electrosynthetic generation of useful quantities of *leuco*-methylene green. However when voltammetry is conducted using a 20% (v/v) solution of toluene in water and 18 W cm^{-2} ultrasound is utilised to form an emulsion, the sonovoltammetry is very different as shown in Figure 12.15. Now, two sigmoidal reduction waves are observed with no evidence of a stripping peak on sweeps back to positive

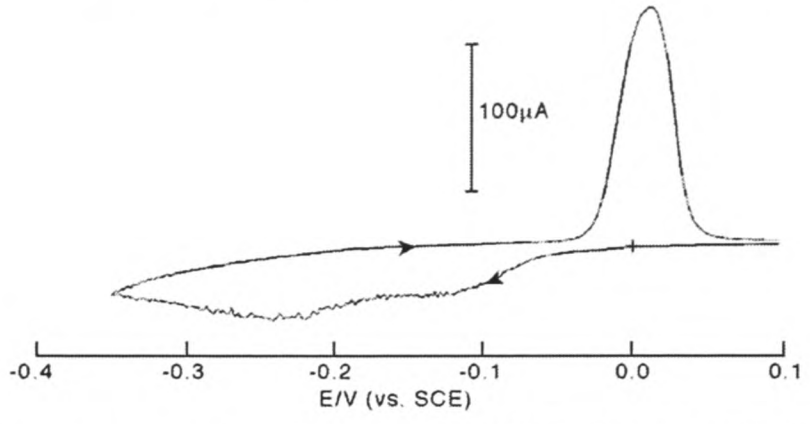

Figure 12.14 CV of 0.2 mM MG in 0.1 M KCl / 0.2 M KH_2PO_4(aq) at pH 6.5. 25 W cm^{-2} ultrasound was employed at a horn-to-electrode distance of 22 mm. Scan rate was 10 mV s^{-1} and the working electrode was a 6 mm diameter Pt disc.

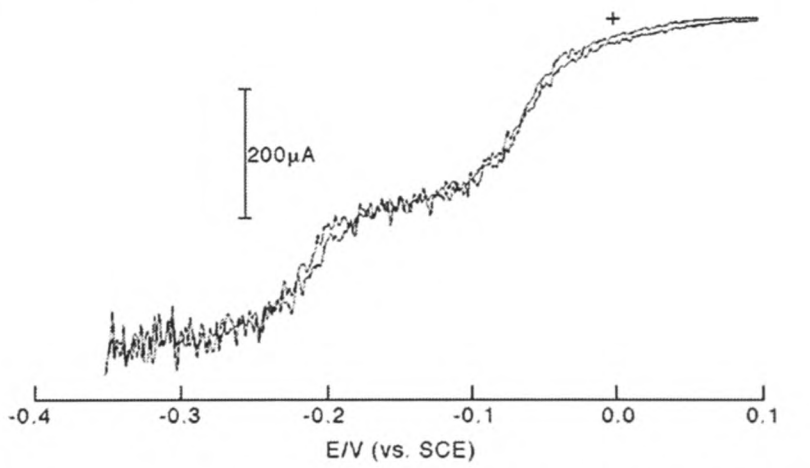

Figure 12.15 CV of 2 mM MG in 0.1 M KCl / 0.2 M KH_2PO_4(aq) at pH 6.5 and 20% (v/v) toluene (emulsified). 18 W cm^{-2} ultrasound was employed at a horn-to-electrode distance of 19 mm. Scan rate was 10 mV s^{-1} and the working electrode was a 6 mm diameter Pt disc.

potentials. Similar effects were seen using n-octane instead of toluene. We attribute this to the solubility of the reduction product in the emulsified organic phase that bathes the electrode surface. This was confirmed by employing a 30 minute sono-electrolysis experiment during which the potential of the solution (200 ml of 2 mM MG in 0.1 M KCl / 0.2 M KH_2PO_4 at pH 6.5 and 50 ml of toluene) was maintained at -0.35 V vs. SCE under 18 W cm^{-2} ultrasound. The toluene reaction mixture was then isolated under argon, evaporated to dryness and the product dissolved in octane for UV-visible characterisation of the *leuco* base via the peak at 263 nm [35].

Scrutiny of Figure 12.15 shows two non-equal waves attributed to the two-electron reduction of methylene green to give solid *l*-MG and aqueous phase *l*-MG respectively. The former, of course, is rapidly removed by the emulsion. The relative sizes of the two waves reflect the amount of material that can nucleate and adsorb in the case of the first wave and the fact that the overall magnitude of the two waves taken together reflects the total rate of mass transport of MG to the electrode surface. Tafel analysis of the two waves gave gradients of ca. 30 mV for each, again consistent with the two-electron reversible processes suggested in Equations (12.2) and (12.3) above. The scope for 'clean' electrochemical measurements in the presence of passivating redox species by using ultrasound is evident.

12.5 CONCLUSIONS

The comparison of the four dual activation methodologies gives insight into the nature of methylene green reduction at platinum electrodes. Below pH 4.5, reversible two-electron voltammetry is observed but at higher pH, a neutral, surface active product is generated giving rise to both surface and solution reduction processes. Both high concentrations and high rates of mass transport (for example as produced by power ultrasound) accelerate electrode passivation which can be overcome in the three following ways.

i) Sufficient temperature increase (to ca. 80°C) by either conventional or microwave heating allows the surface-deposited layer (as evidenced by AFM) to

become sufficiently conducting, possibly through an electron hopping mechanism, to resurrect the second aqueous reduction wave.

ii) Laser irradiation is shown to remove most surface adsorbed reactant before reduction can take place which may have benefits if competitive simultaneous reactions were present.

iii) The use of the sono-emulsion technique to depassivate the platinum electrode by dissolution of an insoluble reduction product in electrochemical systems promises much for synthetic, mechanistic and analytical studies and can be expected to considerably broaden the range of chemical systems amenable to electrochemical study.

12.6 CHAPTER 12: REFERENCES

[1] T. Zerihun, P. Gründler, *J. Electroanal. Chem.* **1998**, *441*, 57.

[2] P. Gründler, *Fresnius J. Anal. Chem.* **1998**, *362*, 180.

[3] T. Zerihun, P. Gründler, *J. Electroanal. Chem.* **1996**, *404*, 243.

[4] R. G. Compton, B. A. Coles, F. Marken, *Chem. Comm.* **1998**, 2595.

[5] R. G. Compton, A. M. Waller, *Spectroelectrochemistry: Theory and Practice*, Plenum Press, New York, **1988**, pg. 349.

[6] G. Schlichthörl, E. A. Ponomarev, L. M. Peter, *J. Electrochem. Soc.* **1995**, 142, 3062.

[7] C. Gabriel, S. Gabriel, E. H. Grant, B. S. J. Halstead, D. M. P. Mingos, *Chem. Soc. Rev.* **1998**, *27*, 213.

[8] P. H. Chen, R. L. McCreery, *Anal. Chem.* **1996**, *68*, 3958.

[9] P. H. Chen, M. A. Fryling, R. L. McCreery, *Anal. Chem.* **1995**, *67*, 3115.

[10] R. K. Jaworski, R. L. McCreery, *J. Electrochem. Soc.* **1993**, *140*, 1360.

[11] M. Poon, R. L. McCreery, *Anal. Chem.* **1987**, *59*, 1615.

[12] M. Poon, R. L. McCreery, *Anal. Chem.* **1986**, *58*, 2256.

[13] E. Hershenhart, R. L. McCreery, R. D. Knight, *Anal. Chem.* **1984**, *56*, 2745

[14] T. Hinoue, I. Watanabe, H. Watarai, *Chem. Letters* **1996**, *5*, 329.

[15] R. Oltra, G. M. Indrianjafy, M. Keddam, H. Takenouti, *Corrosion Sci.* **1993**, *35*, 827.

[16] T. Hinoue, R. Harui, T. Izumi, I. Watanabe, H. Watarai, *Analytical Sci.* **1995**, *11*, 1.

[17] R. G. Compton, R. A. W. Dryfe, *Prog. Reaction Kinetics* **1995**, *20*, 245.

[18] D. J. Walton, S. S. Phull, *Adv. Sonochem.* **1996**, *4*, 205.

[19] R. G. Compton, J. C. Eklund, F. Marken, *Electroanalysis* **1997**, *7*, 509.

[20] F. Marken, R. P. Akkermans, R. G. Compton, *J. Electroanal. Chem.* **1996**, *415*, 55.

[21] J. Klima, C. Bernard, C. Degrand, *J. Electroanal. Chem.* **1995**, *399*, 147.

[22] R. G. Compton, J. C. Eklund, S. D. Page, G. H. W. Sanders, J. Booth, *J. Phys. Chem.* **1994**, *98*, 12410.

[23] F. Marken, R. G. Compton, S. D. Bull, S. G. Davies, *J. Chem. Soc. Chem. Comm.* **1997**, 995.

[24] F. Marken, R. G. Compton, *Electrochim. Acta* **1998**, *43*, 2157.

[25] S. Schweizer, J. F. Rusling, Q. Huang, *Chemosphere* **1994**, *28*, 961.

[26] Q. Chi, S. Dong, *Anal. Chim. Acta* **1994**, *285*, 125.

[27] Y. Zhu, S. Dong, *Electrochim. Acta* **1990**, *35*, 1139.

[28] D.-M. Zhou, H.-Q. Fang, H.-Y. Chen, H.-X. Ju, Y. Wang, *Anal. Chim. Acta* **1996**, *329*, 41.

[29] J. Clavilier, V. Svetlicic, V. Zutic, *J. Electroanal. Chem.* **1996**, *402*, 129.

[30] V. Svetlicic, J. Clavilier, V. Zutic, J. Chevalet, *J. Electroanal. Chem.* **1991**, *312*, 205.

[31] J. A. Cooper, M. Wu, R. G. Compton, *Anal. Chem.* **1998**, *70*, 2922.

[32] P. Zuman, *The Elucidation of Organic Electrode Processes,* Academic Press, New York, **1969**.

[33] H.-X. Ju, J. Zhou, C.-X. Cai, H.-Y. Chen, *Electroanalysis* **1995**, *7*, 1165.

[34] J. D. Norton, S. A. Anderson, H. S. White, *J. Phys. Chem.* **1992**, *96*, 3.

[35] A. T. Vartanyan, *Optika i Spektroskopia* **1956**, *1*, 478.

12

CONCLUSIONS AND OUTLOOK

CHAPTER 13: CONCLUSIONS AND OUTLOOK

The work described in this thesis explores and expands on the relatively new methodology of 'dual activation' in electrochemistry and applies it to novel areas of research. Combined use of both ultrasound/electrochemistry and laser activation/electrochemistry in particular have found novel application in electroanalysis, electrosynthesis and mechanistic discrimination. The key findings in each area are now summarised.

13.1 SONO-ELECTROANALYSIS

13.1.1 USE OF 'SONOTRODES'

The work in Chapter 3 highlights the huge rates of mass transport achievable by use of 'sonotrodes' with diffusion layers of less than one micron being easily achievable. The cost of such extreme mass transport conditions is in the limited longevity of such delicate structures, making real world analytical usage difficult in comparison with the conventional 'face-on' electrode geometry approach. In addition, the deposition of mercury onto a platinum sonotrode is subject to a considerable amount of ablation through both cavitation at the electrode surface and mechanical shear forces affecting larger droplets. Nevertheless sufficient mercury adheres to allow formation of an amalgam when copper and lead are co-deposited and thus stripping signals can be seen for both these metals, even at very low concentrations. Thus sonotrodes and 'face-on' electrodes in particular provide an attractive alternative to the use of microelectrodes [1] for ASV. The high mass transport rates offered by sonication cause extremely efficient sono-preconcentration of ions. Consequently the useful working range of the technique (5 nM to 10 μM Pb^{2+}) is well suited to rapid analysis of lead levels in common liquid samples such as river water, drinks and blood where conventional electrochemical experiments may experience problems of electrode fouling which might be alleviated by the cleaning action of insonation. This is discussed in the next two sections.

13.1.2 ANALYSIS OF LEAD IN WINE

Sono-electroanalysis was found to be an extremely useful tool for the detection of aqueous lead in wine. The highly satisfactory level of agreement between the AAS and ASV results reported in Chapter 5 suggests that ASV can be reliably used as an alternative to the currently accepted analytical protocols [2-5] with the advantages of increased speed, reduced cost and greater simplicity of approach. When comparing the sono-electroanalytical technique with other electrochemical detection methods it can be observed that previous attempts to utilise ASV for lead detection have been only partially successful in that typically only about half of the lead levels detected by AAS were recorded [6]. Insonation both offers the maintenance of a largely clean, active electrode surface to ensure the uptake of metal from the range of complex lead cation species in solution and also likely aids the equilibration between 'free' and 'bound' ions as described by the equilibrium constant K_{eq}. A particular benefit of the procedure described in Chapter 5 is that the wine is analysed both rapidly and directly without the need for the removal or destruction of organic matter via elaborate and lengthy pre-treatment strategies [2,6]. In addition ongoing work within the Compton Group has realised the possibility of making portable electrochemical equipment for the reliable analysis of heavy metals in solution. In the next section, the merits of electroanalysis in a mixed phase system is judged.

13.1.3 ANALYSIS OF LEAD IN PETROL

The sono-electrochemical procedure outlined in Chapter 6 is shown to permit a quantitative determination of the *total* lead content in petrol in a total time of ca. 2 hours *without* any sample pre-treatment. The speed of the procedure relies pivotally on the optimisation of the cell to incorporate a large area (1.13 cm^2) electrode together with the minimisation of the total cell volume (9.0 ml). Currents as large as 1 mA corresponding to the stripping of lead present at levels of ca. 400 mg l^{-1} suggest that useful measurable signals could be obtained with significantly lower lead levels, possibly of as much as two orders of magnitude. This would be consistent with detection of the increasingly lower lead levels being required by legislation. Indeed unleaded petrol only is now available in, for example,

the Netherlands and Germany, and the use of leaded petrol will be phased out in the EU from 2000 [7]. It should be noted however that even 'unleaded' petrol contains up to 2% of the amount of lead reagents of conventional 4 star fuel [8].

The similarity between the AAS and ASV results reported in section 6.9 is very encouraging and suggests that sono-emulsion ASV can be reliably employed as an alternative to the presently accepted protocols [9-21] with the benefits of rapidity, lower cost and ease of approach. A particular advantage is the absence of *any* petrol sample pre-treatment. Again, the key to the whole technique is the rapid emulsification and mass transport afforded by the introduction of power ultrasound. The work in this thesis and previous literature reports [22,23] suggests that 'sono-electroanalysis' is an excellent tool for quantitative analysis especially in complex and / or 'dirty' media. Research into wider applications of the technique (for example monitoring the nitrite levels in egg white [24] and the copper levels in beer [25]) is current and has an extremely promising future. The comparison of sono-electroanalytical techniques with other methods of dual activation is the subject of discussion in section 13.4. In the next section we take a sideways step and summarise the utilisation of ultrasonically induced emulsions in the discipline of electrosynthesis.

13.2 SONO-ELECTROSYNTHESIS

In Chapters 6 and 7, sonication is found to be a convenient and effective alternative to the use of high-speed stirring and/or detergents for the promotion of emulsions for electrochemistry [26]. The advantage of using ultrasound lies in the fact that *no* sample pre-treatment is required. This both accelerates the procedure and eliminates the possible interferences caused by the addition of surfactants to the redox system in question. The use of the sono-emulsion technique to 'trap' insoluble reaction products in a small amount of organic solvent allows the sustained synthesis of otherwise passivating material. The redox reaction product can then be simply separated out and isolated from the organic phase. The resultant depassivation of electrodes promises much for synthetic, mechanistic and analytical studies and can be expected to considerably broaden the range of chemical systems amenable

to electrochemical study in the future. In the next section we turn our attention to characterisation of a parallel methodology for maintaining clean electrodes, namely laser activation, before comparing it directly with sonovoltammetry and other modes of dual activation in section 13.4 for the electroanalysis of ascorbic acid and methylene green dye.

13.3 LASER ACTIVATED VOLTAMMETRY

13.3.1 CHARACTERISATION OF LAV

The nature and scope of laser activated voltammetry is addressed in Chapter 10 through identification of mass transport and surface effects. Laser activation is shown to maintain a clean electrode by thermal desorption of adsorbed passivating species via the 'thermoelastic' effect [27,28]. This additionally results in enough thermal convection to maintain steady-state voltammetry on the newly cleaned electrode. The considerable potential for laser activation in electroanalysis is illustrated by the revitalisation of electrode activity for three separate conventionally passivating systems namely the reduction of toluidine blue dye, the oxidation of ferrocyanide in the presence of bovine albumin / fibrinogen and the oxidation of aqueous iodide. In the next section we seek to apply further use of laser illumination to scrutinise the oxidation of iodide at platinum electrodes and postulate a mechanism through comparison with theoretical computer simulation.

13.3.2 MECHANISTIC STUDIES BY LAV AND COMPUTER SIMULATION

In Chapter 11, the growth of solid iodine at platinum electrodes by the electrochemical oxidation of aqueous potassium iodide is both examined by AFM and shown to be easily removed by laser activation (and previously in Chapter 7 by sono-emulsion techniques). The removal of the non-conducting iodine by laser ablation during the anodic linear sweep voltammetric scan ensures that the electrode does not become passivated. By maintaining a clean electrode at steady-state in such a fashion, an oxidation mechanism is established as follows.

$$2I^- (aq) - 2e^- \rightleftharpoons I_2 (aq) \qquad \text{(i)}$$

$$I_2 (aq) + I^- (aq) \rightleftharpoons I_3^- (aq) \qquad \text{(ii)}$$

$$I_2\,(aq) \rightleftharpoons I_2\,(s) \qquad \text{(iii)}$$

$$I^-\,(aq) + I_2\,(s) \rightarrow I_3^-\,(aq) \qquad \text{(iv)}$$

where the formal redox potential for reaction (i) is 0.358 V vs. SCE in 0.1 M H_2SO_4 and the equilibrium constant for reaction (ii) is 580 M^{-1}. By fitting the theory to experimental steady-state laser activated waves under flow where solid iodine build up is controlled by laser illumination, optimisation of other kinetic parameters was achieved. Best-fit values of the k_f rate constant for reaction (ii) of 1 x 10^5 mol^{-1} cm^3 s^{-1}, the solubility of I_2 (reaction (iii)) of 1.85 x 10^{-3} M, and the heterogeneous rate constant for reaction (iv), k_{het}, of 1.6 x 10^{-3} cm s^{-1} are all of plausible magnitudes. The merits of laser activation for the study of electrode processes that produce surface active intermediates or products can be clearly seen.

It is evident that both the laser activation with mass transport enhancement provided by gravity fed channel flow detailed in Chapter 11 and the mass transport increase and emulsion induced by ultrasound described in Chapter 7, provide useful and parallel tools for probing the mechanism of iodide oxidation at platinum electrodes, particularly in the high concentration region. Further comparisons of these dual activation techniques are drawn in the next section.

13.4 COMPARISON OF DUAL ACTIVATION TECHNIQUES

In the specific case of ascorbic acid oxidation, the use of laser activation voltammetry is shown in Chapter 8 to provide a complementary approach to the utilisation of power ultrasound. Both techniques yield limiting currents that are proportional to the concentration of ascorbic acid present and are reproducible provided care is taken in the case of LAV with the laser alignment and intensity setting. Consequently both techniques offer the prospect of quantitative electroanalysis of AA which is time-consuming by non-electrochemical methods and irreproducible by conventional electrochemistry. The combination of the two methodologies to form the sono-LAV method showed only a small additional benefit in the case of ascorbic acid. Voltammetry is conducted that is not subject to electrode fouling and

hence particular application in systems that strongly passivate electrodes such as fruit juices or phenothiazine dye substrates was pursued.

It is shown in Chapter 9 that both pulsed sonovoltammetry and LAV can be reliably used for the electroanalysis of vitamin C at platinum electrodes in media where 'unaided' electrochemistry is precluded by passivation. Specifically the measurement of ascorbic acid levels in a commercially available fruit drink is achieved by these two methods and compared with values obtained by other procedures. Excellent agreement is observed. While the pulsed ultrasound technique offers higher mass transport and limiting currents the LAV technique gives better repeatability and surface cleaning provided the whole electrode is subject to continuous refreshment. As a consequence both techniques offer the prospect of quick and simple quantitative electroanalysis of ascorbic acid in Ribena® which is laborious by conventional non-electrochemical methods.

The comparison of the four dual activation methodologies in Chapter 12 gives insight into the nature of methylene green reduction at platinum electrodes. Below pH 4.5, reversible two-electron voltammetry is observed but at higher pH, a neutral, surface active product is generated giving rise to both surface and solution reduction processes. Both high concentrations and high rates of mass transport (for example as produced by power ultrasound) accelerate electrode passivation. This can be overcome by means of laser irradiation of the electrode surface which removes surface adsorbed reactants before reduction can take place. In contrast sonication of the electrode by means of 20 kHz ultrasound emitted from a horn probe located opposite to the electrode surface is, in itself, unsuccessful even at intensities as high as 52 W cm^{-2} in depassivating the methylene green system. However the use of the novel sono-emulsion technique in which a small quantity of organic material is emulsified in the presence of ultrasound and used to dissolve the insoluble reduction product is shown to permit quantitative voltammetry. This technique promises much for synthetic applications as discussed in section 13.2 above.

The use of electrode heating (up to ca. 80°C) by either conventional or microwave heating is, unlike laser activation or the sono-emulsion method, unsuccessful at removing

insoluble material formed in the reduction of methylene green. However the heating allows the surface-deposited layer (as evidenced by AFM) to become sufficiently conducting, possibly through an electron-hopping mechanism, to resurrect the second aqueous reduction wave. This use of microwave heating to change surface electrochemistry is thought to be entirely novel.

The contrasting benefits of the dual activation methodologies described will no doubt form the basis for much research in the future with the aim of unleashing the huge scope of electrochemistry in mechanistic discrimination, analysis and synthesis.

13.5 CHAPTER 13: REFERENCES

[1] S. Nomura, K. Nozaki, S. Okazaki, *Electroanalysis* **1991**, *3*, 617.
[2] P. B. Zeeman, L. R. P. Butler, *Appl. Spectrosc.* **1962**, *16*, 120.
[3] P. M. Bersier, J. Howell, C. Bruntlett, *Analyst* **1994**, *119*, 219.
[4] *Perkin Elmer A-Analyst™100 Instruction Manual*, PE, USA, **1996**.
[5] Office International de la Vigne et du Vin, *Recueil des Méthodes Internationales d'Analyse des Vins et des Mouts*, OIVV, Paris, **1990**.
[6] M. A. Baldo, C. Bragato, S. Daniele, *Analyst* **1997**, *122*, 1.
[7] Directive 98/70/EC of the European Parliament.
[8] Institute of Petroleum (Great Britain), *Standard Methods for Analysis and Testing of Petroleum and Related Products*, John Wiley, Chichester, UK, **1995**.
[9] *IP Standards for Petroleum and its Products*, Part 1. Vol. 1. Institute of Petroleum, London, **1985**.
[10] J. W. Robinson, *Anal. Chim. Acta.* **1961**, *24*, 451.
[11] R. M. Dagnall, T. S. West, *Talanta* **1964**, *11*, 1553.
[12] D. J. Trent, *Perkin-Elmer At. Abs. Newsletter* **1965**, *4 (9)*, 348.
[13] R. A. Mostyn, A. F. Cunningham, *J. Inst. Petrol.* **1967**, *53*, 101.
[14] M. Kashiki, S. Yamazoe, S. Oshima, *Anal. Chim. Acta.* **1971**, *53*, 95.
[15] E. Cardelli, M. Cifani, M. Mecozzi, G. Sechi, *Talanta* **1986**, *33*, 279.
[16] C. G. Taylor, J. M. Trevaskis, *Anal. Chim. Acta.* **1986**, *179*, 491.
[17] *Varian Instrument Applications* **1991**, *20*, 7.
[18] M. H. Pournaghi-Azar, A. H. Ansary-Fard, *Talanta* **1998**, *46*, 607.
[19] D. Jagner, L. Renman, Y. Wang, *Anal. Chim. Acta.* **1992**, *267*, 165.
[20] J.L. Guinón, R. Grima, *Analyst* **1988**, *113*, 613.
[21] A. Fontana, C. Braekman-Danheux, C. G. Jung, *Fuel Process. Tech.* **1996**, *48*, 107.
[22] F. Marken, T. O. Rebbitt, J. Booth, R. G. Compton, *Electroanalysis* **1997**, *9*, 19.
[23] F.-M. Matysik, S. Matysik, A. M. O. Brett, C. M. A. Brett, *Anal. Chem.* **1997**, *69*, 1651.
[24] J. Davis, R. G. Compton, *submitted for publication.*
[25] C. Agra-Gutiérrez, J. L. Hardcastle, J. C. Ball, R. G. Compton, *Analyst* **1999**, *124*, 1053.
[26] S. Schweizer, J. F. Rusling, Q. Huang, *Chemosphere* **1994**, *28*, 961.
[27] R. Oltra, G. M. Indrianjafy, J. P. Boquillon, *J. Phys. IV, Colloque C7, 769, Suppl. J. Phys. III* **1991**, 12.
[28] J. D. Aussel, A. Le Brun, J. C. Baboux, *Ultrasonics* **1988**, *26*, 245.

APPENDIX 1: FICK'S LAWS

A1.1 FICK'S FIRST LAW OF DIFFUSION

For the derivation of Fick's first law of diffusion, the following simplified model is employed. Consider a volume of electrolyte solution where the concentration of the diffusing ionic species is constant in the yz-plane, but varies in the x-direction (Figure A1.1). The parallelepiped of solution considered is then divided evenly into two compartments by an imaginary 'transit' plane, T, of area A. The diffusion occurs normal to this plane. The outer planes L and R are situated at a distance of $\sqrt{\langle x^2 \rangle}$ (the mean distance travelled by an ion in a time interval t) from the transit plane

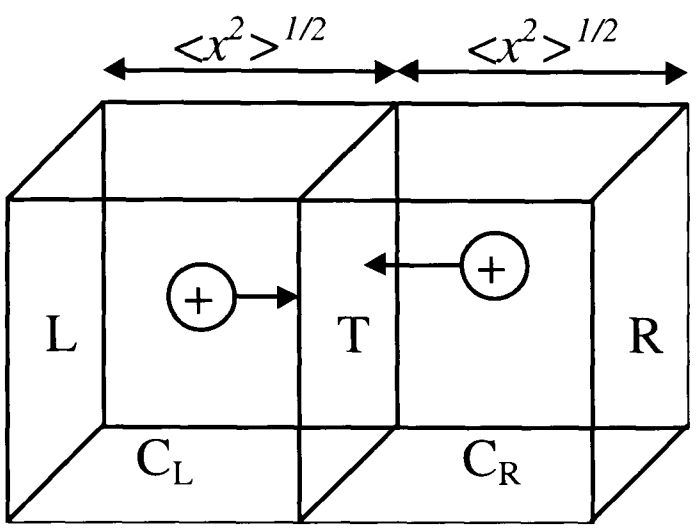

Figure A1.1 Parallelepiped of solution used to model random walk processes.

ensuring that, provided the ions are moving in the specified direction, all the ions in each compartment cross the 'transit' plane. As the ions are 'random walking', statistically only half the ions will be moving towards the plane T at any given time. Thus, in a time interval t,

$$\text{Number of ions making the L} \rightarrow \text{T crossing is } \frac{1}{2}\left(\sqrt{\langle x^2 \rangle} A C_L\right)$$

$$\text{Number of ions making the R} \rightarrow \text{T crossing is } \frac{1}{2}\left(\sqrt{\langle x^2 \rangle} A C_R\right)$$

where C_L and C_R are the concentrations of ions in the respective compartments. The total diffusive flux J (mol m^{-2} s^{-1}) of ions across the transit plane in the L → R direction is

$$J = \frac{1}{2}\frac{\sqrt{\langle x^2 \rangle}}{t}[C_L - C_R] \qquad \text{(A1.1)}$$

The concentration gradient (dc/dx) in the L → R direction can then be written

$$\frac{dc}{dx} = \frac{[C_R - C_L]}{\sqrt{\langle x^2 \rangle}} \equiv -\frac{[C_L - C_R]}{\sqrt{\langle x^2 \rangle}} \qquad \text{(A1.2)}$$

if the two expressions are then combined the following expression results

$$J = -\frac{1}{2}\frac{\langle x^2 \rangle}{t}\frac{dc}{dx} \tag{A1.3}$$

This is analogous to Fick's first law where $D = \frac{\langle x^2 \rangle}{2t}$ thus $\langle x^2 \rangle = 2Dt$ hence the parameters x and D are related.

A1.2 FICK'S SECOND LAW OF DIFFUSION

As for the first law only planar diffusion is considered (Figure A1.1). Considering a small region of volume Adx and the concentration changes which occur within this volume region in the time interval t and t + dt,

No. of moles in the region at time t+dt	-	No. of moles in the region at time t	=	No. of moles entering across plane at x	-	No. of moles leaving across plane at x+dx

or alternatively

$$c(x,t+dt)Adx - c(x,t)Adx = J(x,t)Adt - J(x+dx,t)Adt \tag{A1.4}$$

where J(x, t) is the flux in the x-direction (mol cm^{-2} s^{-1}) such that

$$[c(x,t+dt) - c(x,t)]dx = [J(x,t) - J(x+dx,t)]dt \tag{A1.5}$$

which when rearranged gives

$$\frac{\partial}{\partial t}c(x,t) + \frac{\partial}{\partial x}J(x,t) = 0 \tag{A1.6}$$

If J(x, t) is substituted for Fick's first law then Fick's second law is obtained as follows

$$\frac{\partial}{\partial t}c(x,t) = D\frac{\partial^2}{\partial x^2}c(x,t) \tag{A1.7}$$

Hence by using a simple statistical model the diffusion of molecules can be mathematically expressed in the form of Fick's first and second laws [1].

A1.3 APPENDIX 1: REFERENCES

[1] A. Fick, *Philosophical Magazine and Journal of Science* **1855**, *10*, 30.

APPENDIX 2: SONOLUMINESCENCE

A2.1 SONOLUMINESCENCE OF LUMINOL

Though the true phenomenon of sonoluminescence, where the high energy collapse of ultrasonically created bubbles results in the emission of light, is not observed at the relatively low ultrasound intensities employed in this thesis, the radicals produced by the sonolysis of water [1] during insonation of an aqueous solution of luminol are sufficient to drive a light-emitting reaction. Figure A2.1 shows the reaction scheme. The resultant sono-chemiluminescence can be seen in Figure A2.2.

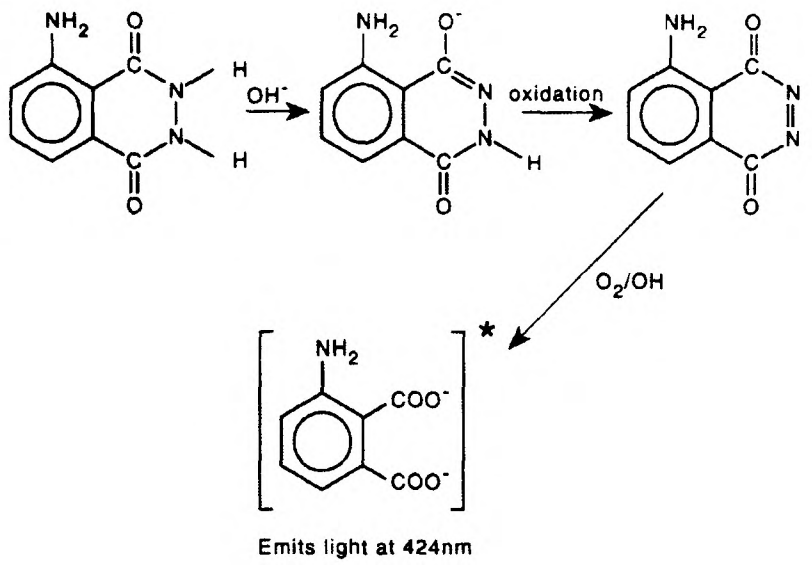

Figure A2.1 Reaction scheme for the process which causes chemiluminescence of luminol.

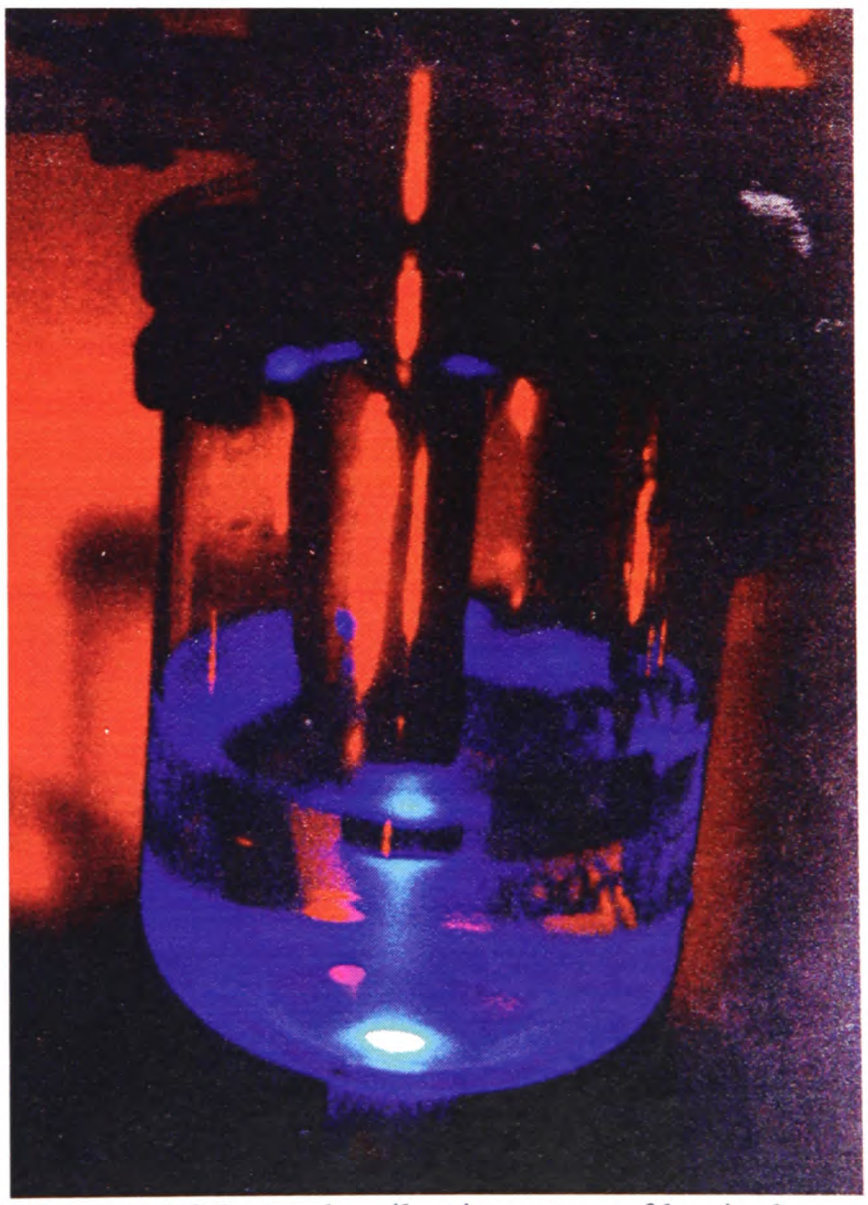

Figure A2.2 Sono-chemiluminescence of luminol.

A2.2 APPENDIX 2: REFERENCES

[1] K. S. Suslick, *Ultrasound, Its Chemical, Physical and Biological Effects*, VCH Weinheim, New York, **1988**.

[2] J. C. Eklund, *D. Phil. Thesis*, Oxford University, **1995.**

APPENDIX 3: SONO-ELECTROCHEMICAL APPARATUS

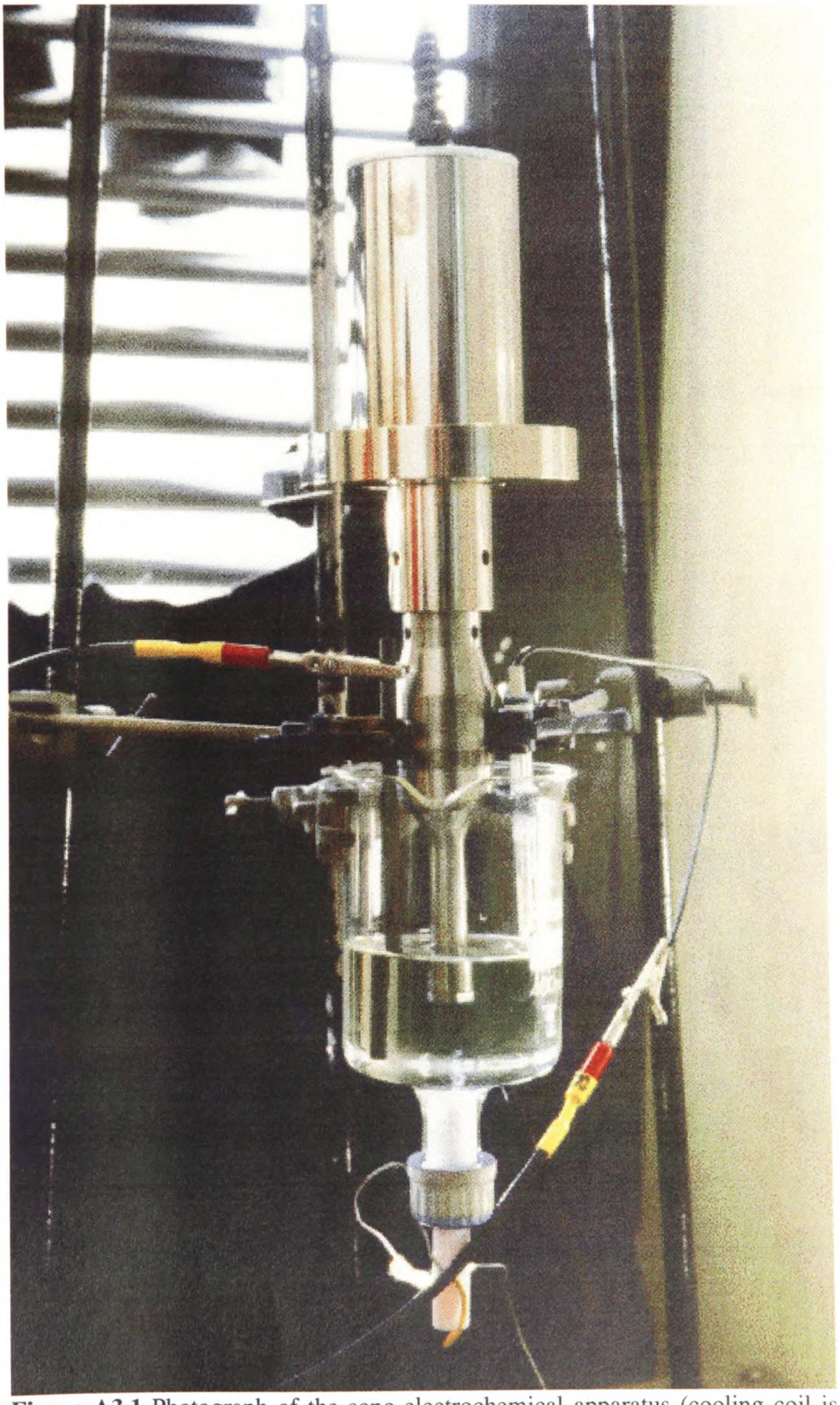

Figure A3.1 Photograph of the sono-electrochemical apparatus (cooling coil is omitted for clarity).

APPENDIX 4: 'FLOW PAST A PLATE' THEORY FOR A 'SIDE-ON SONOTRODE'

A4.1 THEORY FOR A 'SIDE-ON' SONOTRODE'

The flux, J, at a point on a planar 'side-on' electrode (x) in the geometry shown in Figures 3.1 and 3.2 has been previously calculated as [1]:

$$J(x) = \frac{3[X]_0 \beta^{2/3}}{24^{1/3}\Gamma(1/3)\sqrt{x}\left[1-\left(\frac{h_0}{x}\right)^{3/4}\right]^{1/3}} \qquad \text{(A4.1)}$$

where Γ is the gamma function ($\Gamma(1/3 = 2.67893)$, $[X]_0$ is the bulk concentration of electroactive species X, h_0 is the 'lead-in' length of plate before the electrode and the parameter β is given by [1]:

$$\beta = \frac{D(1.33/2)^{1/2}U^{3/4}}{\nu^{1/4}} \qquad \text{(A4.2)}$$

In Equation A4.2, D is the diffusion coefficient of species X, U is the ultrasonically induced bulk flow of solution and ν is the kinematic viscosity of the solution.

For the 'side-on sonotrode' geometry with a disc electrode of radius, r and area, A, h_0 becomes the submersion depth of the electrode where the acoustic streaming effectively begins. This is illustrated in Figure A4.1. Using Equation A4.1, the flux at the centre of the electrode, where $x = h_0 + r$, is given by:

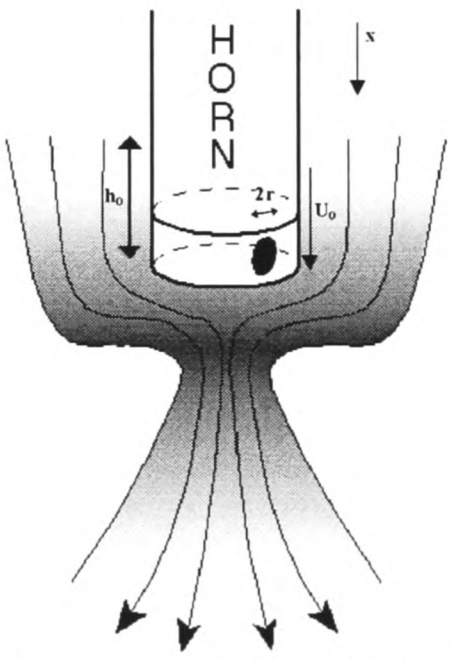

Figure A4.1 'Side-on sonotrode' flow parameters.

$$J(h_0 + r) = \frac{3[X]_0 \beta^{2/3}}{24^{1/3}\Gamma(1/3)\sqrt{h_0 + r}\left[1-\left(\frac{h_0}{h_0 + r}\right)^{3/4}\right]^{1/3}} \qquad \text{(A4.3)}$$

By rearranging Equation A4.3 using $\frac{h_0}{h_0+r} = \frac{1}{1+r/h_0}$, we get

$$J(h_0+r) = \frac{3[X]_0\beta^{2/3}}{24^{1/3}\Gamma(1/3)\sqrt{h_0+r}}\left[1-\left(1+\frac{r}{h_0}\right)^{-3/4}\right]^{-1/3} \quad \text{(A4.4)}$$

and since $r<<h_0$, $h_0 + r \approx h_0$, allowing a binomial expansion to be made as follows

$$J(h_0+r) = \frac{3[X]_0\beta^{2/3}}{24^{1/3}\Gamma(1/3)\sqrt{h_0}}\left[1-\left(1-\frac{3r}{4h_0}\right)\right]^{-1/3} \quad \text{(A4.5)}$$

which simplifies to

$$J(h_0+r) = \frac{3[X]_0\beta^{2/3}}{18^{1/3}\Gamma(1/3)h_0^{1/6}r^{1/3}} \quad \text{(A4.6)}$$

We next make the approximation that, as the electrode is small, this flux is the same to all points on the electrode. The sono-limiting current, I_{sono} is then calculated as:

$$I_{sono} = nFAJ(h_0+r) \quad \text{(A4.7)}$$

Substituting Equations A4.2 and A4.6 into Equation A4.7, we get

$$I_{sono} = \frac{3nF\pi r^2[X]_0}{18^{1/3}\Gamma(1/3)h_0^{1/6}r^{1/3}}\left(\frac{D(1.33/2)^{1/2}U^{3/4}}{\nu^{1/4}}\right)^{2/3} \quad \text{(A4.8)}$$

which simplifies to

$$I_{sono} = 0.373nF\pi r^{5/3}[X]_0 h_0^{-1/6}D^{2/3}U^{1/2}\nu^{-1/6} \quad \text{(A4.9)}$$

A4.2 APPENDIX 4: REFERENCES

[1] J. C. Eklund, F. Marken, D. N. Waller, R. G. Compton, *Electrochim. Acta* **1996**, *41*, 1541.

APPENDIX 5: 'VIBRATING ELECTRODE' THEORY FOR A 'SIDE-ON SONOTRODE'

A5.1 THEORY FOR A VIBRATING CYLINDER ELECTRODE

The mass transfer coefficient, k_m, to a cylindrical vibrating electrode of amplitude, a, length, L and radius R in the geometry shown in Figure A5.1 has been previously determined as [1]:

$$k_m = 1.295 D^{1/2} S_c^{-1/6} \left(\frac{a}{R}\right)^{2/3} f^{1/2} \qquad \text{(A5.1)}$$

where $S_c = \nu/D$ is the Schmidt number and f is the frequency of vibration. The corresponding mean current response, I_{vib}, is given by [2]:

$$I_{vib} = 2.580 \pi R L n F [X]_0 D^{1/2} S_c^{-1/6} \left(\frac{a}{r}\right)^{2/3} f^{1/2} \qquad \text{(A5.2)}$$

A5.2 THEORY FOR A 'SIDE-ON SONOTRODE'

In the case of the 'side-on' sonotrode, the cylindrical electrode area, $2\pi RL$ is replaced with the simple circular area πr^2 shown in Figure A5.2.

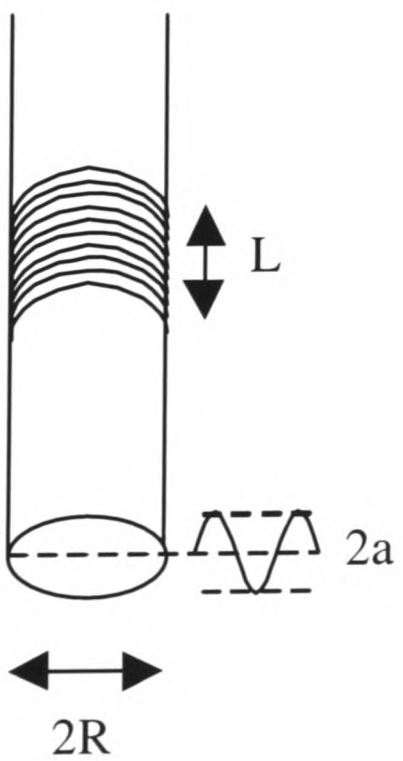

Figure A5.1 Parameters for a vibrating cylinder electrode.

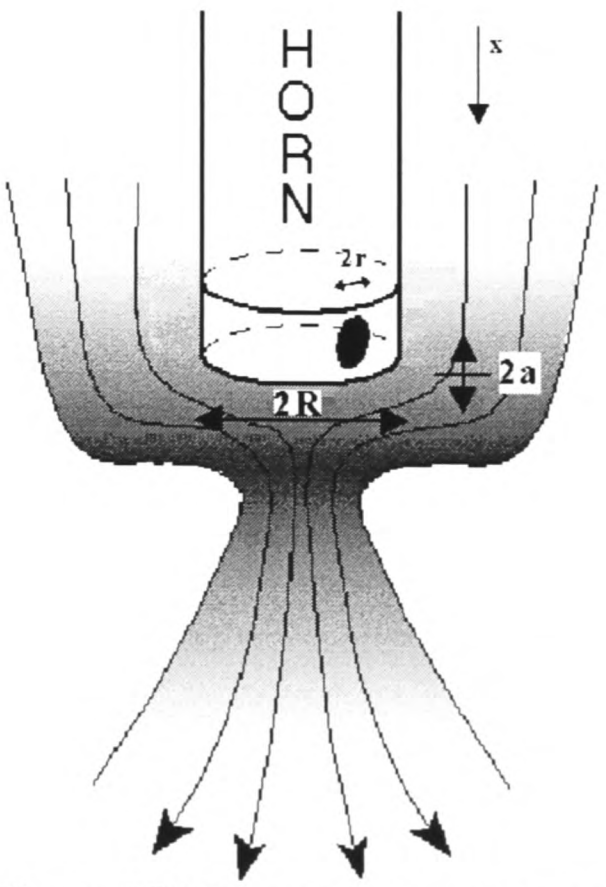

Figure A5.2 Parameters for a 'side-on sonotrode' vibrating electrode.

The corresponding mean current under sonication, I_{sono}, is therefore given by:

$$I_{sono} = 1.295\pi r^2 nF[X]_0 D^{2/3} \nu^{-1/6} \left(\frac{a}{r}\right)^{2/3} f^{1/2} \qquad \text{(A5.3)}$$

The theoretical equation A5.2 describes experimental results only for $R_e^{1/2} S_c^{1/3} \left(a/r\right)^{1/6} < 150$ [2], where $R_e = 2\pi faR/\nu$ is the Reynolds number (in practical terms $a/R \leq 0.06$ and frequency < 4 Hz). At larger values there was an enhancement of mass-transfer coefficient above that predicted. Thus, when applying this theory to insonated electrodes, both the $a/R \leq 0.06$ condition and the $f < 4$ Hz condition are not met since a/R = ca. 100 μm / 6.5 mm and f = 20 kHz! The resultant turbulent flow almost certainly results in further mass transport enhancement.

A5.3 APPENDIX 5: REFERENCES

[1] P. Dumargue, P. Humeau, *Electrochim. Acta* **1982**, *27*, 115.

[2] D. E. Williams, K. Ellis, A. Colville, S. J. Dennison, G. Laguillo, J. P. Larsen, *J. Electroanal. Chem.* **1997**, *432*, 159.

APPENDIX 6: CHANNEL FLOW THEORY FOR A DISC ELECTRODE

A6.1 CHANNEL FLOW THEORY FOR A DISC ELECTRODE

The Levich equation for the limiting current (I_{Levich} / A) in channel flow cell for a rectangular electrode is given by:

$$I_{Levich} = 0.925nF[X]w(Dx_e)^{2/3}(v_f / h^2 d)^{1/3} \quad \text{(A6.1)}$$

where n is the number of electrons transferred, F / C mol^{-1} is the Faraday constant, [X] / mol cm^{-3} is the bulk concentration of species X with diffusion coefficient D / cm^2 s^{-1}, w / cm is the width of the electrode of length x_e / cm in the flow direction, v_f / cm^3 s^{-1} is the solution flow rate, 2h / cm is the cell height and d / cm is the cell width. Next we consider a disc electrode of radius r and divide it up into incremental strips of width dz as illustrated in Figure A6.1. By Pythagoras' theorem, the length of these strips is given by,

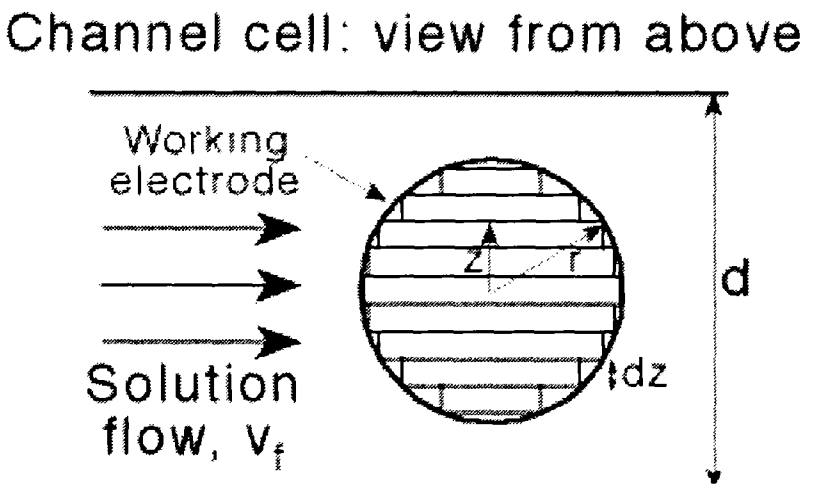

Figure A6.1 Top view of a channel flow disc electrode.

$$x_e = 2\sqrt{(r^2 - z^2)} \quad \text{(A6.2)}$$

so by substituting into Equation (A6.1) the corresponding limiting current of each strip (I_{strip}) is therefore given by,

$$I_{strip} = 0.925nF[X]D^{2/3}(v_f / h^2 d)^{1/3}[2(r^2 - z^2)^{1/2}]^{2/3}dz \quad \text{(A6.3)}$$

The total current (I_{Tot}) is then defined as the sum of the currents from all the individual strips, that is

$$I_{Tot} = \int_{-r}^{r} I_{strip} \quad \text{(A6.4)}$$

Since [1]

$$\int_{-r}^{r}(r^2 - z^2)^{1/3}\,dz = r^{5/3}\sqrt{\pi}\left[\Gamma(4/3)/\Gamma(11/6)\right], \qquad \text{(A6.5)}$$

$\Gamma(4/3) = 0.89338$ and $\Gamma(11/6) = 0.939692$ then a new Levich equation for the current at a disc electrode (I_{disc}) of radius, r, in a flow cell can be established as

$$I_{disc} = 2.474nF[X]r^{5/3}D^{2/3}(v_f / h^2 d)^{1/3} \qquad \text{(A6.6)}$$

Implicit in the above derivation is the neglect of diffusion in a direction orthogonal to x and y (see Figure 1.10) so that the above derivation is limited to conditions of relatively fast electrolyte flow. By comparing the calculated current for a circular electrode with that for a square electrode with the same area using the above formulae in Equations (A6.1) and (A6.6) we see that the circular electrode has only a ca. 2.3% larger current under channel flow.

A6.2 APPENDIX 6: REFERENCES

(1) S. Wolfram, *Mathematica A System for Doing Mathematics by Computer*, 2nd Ed., Addison-Wesley, New York, **1991**; software package.

(2) D. R. Lide, (Ed.-in-chief) *CRC Handbook of Chemistry and Physics,* 74th Ed., CRC Press, Boca Raton, Florida, **1993**.